In the Spotlight:

Bond Activation Reactions with Pyridyl–Triazolylidene Metal Complexes

Von der Fakultät 3 Chemie der Universität Stuttgart zur Erlangung der Würde des Doktors der Naturwissenschaften (Dr. rer. nat.) genehmigte Abhandlung.

Vorgelegt von

Tobias Bens

geboren in Bautzen

Hauptberichter:	Prof. Dr. Biprajit Sarkar
Mitberichter:	Prof. Dr. Michael R. Buchmeiser
Mitberichter:	Prof. Dr.-Ing. Elias Klemm

Tag der mündlichen Prüfung: 08.09.2023

Institut für Anorganische Chemie Universität Stuttgart

2023

The doctoral studies presented herein were begun in October 2018 at the Institute of Chemistry and Biochemistry of the Freie Universität Berlin under the supervision of Prof. Dr. Biprajit Sarkar. In April 2019, research was conducted under the supervision of Prof. Dr Janez Košmrlj during a research visit to the Univerza v Ljubljaniin. The work was continued at the Institute for Inorganic Chemistry of the University of Stuttgart from October 2019 onward and concluded in May 2023.

"Sorrow is so easy to express and yet so hard to tell."

Joni Mitchell

Dedicated to Julia

Declaration of Authorship

I hereby confirm that I have prepared this dissertation without the help of any impermissible resources. All citations are marked as such. The thesis has not been accepted in any previous doctorate degree procedure.

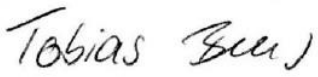

Tobias Bens

Stuttgart, Mai 2024

The results and discussion part of this dissertation have been published as follows:

1) *Chromium(0) and Molydenum(0) Complexes with a Pyridyl-Mesoionic Carbene Ligand: Structural, (Spectro)electrochemical, Photochemical, and Theoretical Investigations*
T. Bens, P. Boden, P. Di Martino-Fumo, J. Beerheus, U. Abold, S. Sobottka, N. I. Neuman, M. Gerhards, B. Sarkar*, Inorg. Chem*. **2020**, *59*, 20, 15504-15513.
DOI: 10.1021/acs.inorgchem.0c02537. (Chapter 3.3)

2) *Impact of Bidentate Pyridyl-Mesoionic Carbene Ligands: Structural, (Spectro)Electrochemical, Photophysical, and Theoretical Investigations on Ruthenium(II) Complexes*
T. Bens, J. A. Kübler, R. R. M. Walter, J. Beerhues, O. S. Wenger, B. Sarkar, *ACS Org. Inorg. Au* **2023**, *3*, 4, 184-198. (Chapter 3.2)
DOI: 10.1021/acsorginorgau.3c00005.

3) *The Best of Both Worlds: Combining the Power of MICs and WCAs to generate Stable and Crystalline Cr^{I}-tetracarbonyl Complexes with π −Accepting Ligands*
T. Bens, R. R. M. Walter, J. Beerhues, M. Schmitt, I. Krossing, B. Sarkar, *Chem. Eur. J.* **2023**, *29*, e202301205. (Chapter 3.4)
DOI: 10.1002/chem.202301205.

4) *A Different Perspective in Tuning the Photophysical and Photochemical Properties: The Influence of Constitutional Isomers in Group 6 Carbonyl Complexes with Pyridyl-Mesoionic Carbenes*

T. Bens, D. Marhöfer, P. Boden, S. T. Steiger, L. Suntrup, G. Niedner-Schatteburg, B. Sarkar, *Inorg. Chem*. **2023**, *62*, 16182-16195. (Chapter 3.5)

DOI: 10.1021/acs.inorgchem.3c02478.

5) *Investigations on the Influence of Two Pyridyl-Mesoionic Carbene Constitutional Isomers on the Electrochemical and Spectroelectrochemical Properties of Group 6 Metal Carbonyl Complexes*

T. Bens, B. Sarkar, *Inorganics* **2024**, *12*, 46. (Chapter 3.6)

DOI: 10.3390/inorganics12020046.

6) *Isolation, Characterization and Reactivity of Key Intermediates Relevant to Reductive (Electro)catalysis with Cp*Rh Complexes containing Pyridyl-MIC (MIC = Mesoionic Carbene) Ligands*

T. Bens, R. R. M. Walter, J. Beerhues, C. Lücke, J. Gabler, B. Sarkar, *Chem. Eur. J.* **2024**, *30*, e202302354. (Chapter 3.7)

DOI: 10.1002/chem.202302354.

Not included in this dissertation are the following publications:

1) *Oxidative Access via Aqua Regia to an Electrophilic, Mesoionic Dicobaltoceniumyltriazolylidene Gold(III) Catalyst*

S. Vanicek, J. Beerhues, **T. Bens**, V. Levchenko, K. Wurst, B. Bildstein, M. Tilset, B. Sarkar, *Organometallics* 2019, *38*, 22, 4383-4386.

DOI: 10.1021/acs.organomet.9b00616.

2) *NIR-Emissive Chromium(0), Molybdenum(0), and Tungsten(0) Complexes in the Solid State at Room Temperature*

P. Boden, P. Di Martino-Fumo, **T. Bens**, S. Steiger, U. Albold, Prof. Dr. Gereon Niedner-Schattenburg, Prof. Dr. M. Gerhards, Prof. Dr. B. Sarkar, *Chem Eur. J.* **2021**, *27*, 12959-12964.

DOI: 10.1002/chem.202102208.

3) *Fluorinated click-derived tripodal ligands drive spin crossover in both iron(II) and cobalt(II) complexes*

M. Nößler, D. Hunger, N. I. Neuman, M. Reimann, F. Reichert, M. Winkler, J. Klein, **T. Bens**, L. Suntrup, S. Demeshko, J. Stubbe, M. Kaupp, J. van Slageren, B. Sarkar, *Dalton Trans*. **2022**, *51*, 10507–10517.

DOI: 10.1039/D2DT01005D.

4) *Mechanistic and Kinetic Investigations of ON/OFF (Photo)Switchable Binding of Carbon Monoxide by Chromium(0), Molybdenum(0) and Tungsten(0) Carbonyl Complexes with a Pyridyl-Mesoionic Carbene Ligand*

P. J. Boden, P. Di Martino-Fumo, **T. Bens**, S. T. Steiger, D. Marhöfer, G. Niedner-Schattenburg, B. Sarkar, *Chem. Eur. J*. **2022**, e202201038.

DOI: 10.1002/chem.202201038.

5) *A crystalline cyclic (alkyl)(amino)carbene with a 1,1′-ferrocenylene backbone*

J. Volk, M. Heinz, M. Leibold, C. Bruhn, **T. Bens**, B. Sarkar, M. C. Holthausen, U. Siemeling, *Chem. Commun.* **2022**, *58*, 10396-10399.

DOI: 10.1039/D2CC03871D.

6) *Liquid crystalline self-assembly of azulene–thiophene hybrids and their applications as OFET materials*

F. Schulz, S. Takamaru, **T. Bens**, J. Hanna, B. Sarkar, S. Laschat, H. Iino, *Phys. Chem. Chem. Phys.* **2022**, *24*, 23481-23489.

DOI: 10.1039/D2CP03527H.

7) *Electrochemistry and Spin-Crossover Behaviour of Fluorinated Terpyridine-Based Co(II) and Fe(II) Complexes*

M. Nößler, R. Jäger, D. Hunger, M. Reimann, T. Bens, N. I. Neuman, A. Singha Hazari, M. Kaupp, J. van Slageren, B. Sarkar, *Eur. J. Inorg. Chem.* **2023**, *26*, e202300091.
DOI: 10.1002/ejic.202300091.

8) *Spin Crossover and Fluorine-Specific Interactions in Metal Complexes of Terpyridines with Polyfluorocarbon Tails*

M. Nößler, N. I. Neuman, L. Böser, R. Jäger, A. Singha Hazari, D. Hunger, Y. Pan, C. Lücke, **T. Bens**, J. van Slageren, B. Sarkar, *Chem. Eur. J.* **2023**, 29, e202301246.
DOI: 10.1002/chem.202301246.

Acknowledgments

I want to express my sincere gratitude to Prof. Dr. Biprajit Sarkar for the opportunity to work on this thesis in his research group and for years of fruitful discussions. Apart from the possibility to learn various new techniques, I want to express some personal thoughts: The ability to maintain a good heart and sympathy is nothing one should take for granted. I am grateful to be able to work with a supervisor who has not lost his faith in humanity during difficult years and was always available for personal discussions whenever needed. Thank you for that Bipro!

I am also grateful to Prof. Dr. Michael R. Buchmeiser for agreeing to be the 2nd reviewer for this thesis and I also want to thank Prof. Dr.-Ing. Elias Klemm for agreeing to be part of the committee.

The cooperation partners that contributed to this thesis are kindly acknowledged: Prof. Dr. Markus Gerhards (University Kaiserslautern), Prof. Dr. Gereon Niedner-Schatteburg (University Kaiserslautern), Prof. Dr. Ingo Krossing (University Freiburg) and Prof. Dr. Oliver S. Wenger (University Basel).

My sincere gratitude goes to all former and present members of the Sarkar group for filling the last years with joyful moments and unforgettable times inside and outside the lab. Special thanks go to all crystallographers Dr. Lisa Suntrup, Dr. Julia Beerhues, Dr. Uta Albold and Robert R. M. Walter for the single crystal XRD analysis and all the permanent staff at the Freie Universität Stuttgart and University of Stuttgart for performing measurements during the time. Especially, I want to thank Barbara Förtsch, Dr. Wolfgang Frey and Benjamin Rau.

I would like to thank Annette Kling and Lale Ötztürk for all their administrative support and for brightening my days whenever we got the chance to chat together. It was always delightful to share some personal experiences and thoughts.

I am sincerely grateful to Dr. Christopher Feil and Dr. Arijit Singha-Hazari for proofreading this thesis, the profound discussions we shared about life and the great times we spent during this period. I always appreciated your opinion and support, not only on a scientific but also on a personal basis.

Special thanks to Dr. Julia Beerhues and Dr. Shuhadeep Chandra for mastering the movement from Berlin to our Swabian labs and all the fun times we shared together.

I thank the whole Gudat group for the warm welcome and the fun wine tastings during that time.

Furthermore, I want to thank Clemens Lücke and Robert R. M. Walter for starting the adventure in Stuttgart with me and for the endless memories I will keep with me. I really enjoyed the late-night discussions with some beers, our Trash-TV evenings and fun moments. I can ensure that having you as friends enriched my life in many aspects. Thank you for being always there for me!

I would like to thank all my colleagues Fridolin Hennhöfer, Dr. Vasileios Filippou, Lasse Dettmann, Marie Leimkühler, Alok Mahata, Maren Neubrand, Maite Nößler, Manuel Pech, Tabea Pfister, Richard Rudolf, Felix Stein. You become more than just colleagues (now it is out!) and I really loved having such a great team with me. With you, everything seemed so much easier. Especially, I want to thank Fred for his emotional support and I hope you will take some time to take a deep breath and realize that everything will turn out fine, as we could prove it many times. Felix, I hope you will keep the sunshine in your heart that makes everyone happy.

Special thanks to all my students Cindy Odenwald, Ingo Schneider, Ivan Shestov, Jonas Genz and Julia Gabler and all they have contributed to the success of my thesis.

My deepest thanks go to Julia and the permanent support you gave me, all the beautiful moments and laughter we shared and it breaks my heart that we cannot share this moment together. There is not a single day passing by without thinking about you. You had the purest heart I have ever met and I will keep you always in mine.

Finally, I want to thank my family for their continuous support all my life. Most importantly, they made me the person I am today to build the strength and devotion for this thesis, knowing that they have my back, whatever happens. It makes me proud to be part of this family.

Abstract

The CuAAC reaction to transform organic azides and terminal alkynes into 1,4-triazoles as precursors for triazolium salts has been known for more than one decade. It comes as no surprise that the synthetic scope of 1,2,3-triazoles has expanded rather fast. To obtain heterocyclic triazolium salts in good yields, selective synthetic strategies are required. They build the fundament of the so-called mesoionic carbenes (MICs), a sub-class of the well-established NHCs. The classification results from the fact that 1,2,3-triazol-5-ylidenes cannot be drawn without a charge separation in their Lewis structure.

In the present work, new synthetic routes have been explored to access pyridyl-substituted 1,2,3-triazol-5-ylidenes (pyridyl-MIC) as bidentate ligands for transition metal complexes. The interplay between the strong σ–donating nature of the MIC and the good π–accepting properties of the ligand plays a crucial role in the photo- and electro-catalytic activity.

In chapter 3.2, a series of pyridyl–MIC (py–MIC) and 2,2'-bipyridine (bpy) containing Ru(II) complexes has been synthesized and characterized with techniques, such as ^{1}H and ^{13}C NMR spectroscopy, mass-spectrometry, elemental analysis and X-ray diffraction analysis. Moreover, (spectro)electrochemical measurements (SEC) were performed to explore the nature of different redox states with respect to the number of MIC moieties. Time-dependent density functional theory (TD-DFT) calculations were conducted to get insight into the photophysical properties of the complexes and their potential application as photocatalysts, while exited state lifetimes were investigated in cooperation with the group of Prof. Dr. Oliver Wenger.

Chapter 3.3 deals with pyridyl–MIC group 6 (Cr, Mo) carbonyl complexes. CO is an ideal probe to investigate the influence of the ligand at the transition metal complex, not only in the native but also in the oxidized and reduced form. IR-, EPR- and UV/Vis/NIR-SEC combined with TD-DFT were performed to get in-depth understanding of the electronic structure of corresponding redox states, while excitation leads to an unusual reversible binding of the CO ligand after leaving the photoproducts in the dark.

Surprisingly, the first stable $[M(py–MIC)(CO)_4]^+$ (M = Cr) fragment with π –accepting ligands could be isolated and characterized *via* single-crystal X-ray diffraction analysis (chapter 3.4). EPR-, IR- and UV/VIS-spectroscopy supported by theoretical investigations were performed to shine light on the rare electron-deficient nature of the isolated $[Cr(py–MIC)(CO)_4]^+$ complexes.

Furthermore, in chapter 3.5 all [M(py–MIC)(CO)$_4$] (M = Cr, Mo, W) complexes were investigated by step scan FTIR-spectroscopy and time-resolved spectroscopy in cooperation with the group of Prof. Dr. Gerhards and Prof. Dr. Niedner-Schatteburg. An unusual (photo)switchable ON/OFF binding of CO in solution was observed. Additionally, all complexes show a NIR-emission in the solid state.

In chapter 3.6, the reduced species [M(py–MIC)(CO)$_4$]$^-$ (M = Cr, Mo, W) were generated *in situ* and the reduction was assigned to be predominantly ligand-centered by various (spectro-)electrochemical and theoretical methods. Based on these results, electrochemical CO_2 reduction was performed under non-protic conditions.

(Spectro)electrochemistry can be a powerful tool to investigate reactive intermediates in electrocatalysis. In the last chapter 3.7, a series of [(py–MIC)Rh(Cp*)X]$^{n+}$ (X = Cl$^-$, MeCN; n = 1, 2) complexes was synthesized and fully characterized with several techniques. All complexes were tested in electrochemical H^+ reduction and a mechanism on the precatalyst formation was proposed. A number of intermediates was chemically isolated, investigated *via* single-crystal X-ray diffraction analysis and compared to the electrochemically generated species. Theoretical calculations further supported the precatalytic activation pathway.

The presented thesis provides an in-depth understanding of the impact of bidentate ligands with π −accepting and strong σ −donating ligands (pyridyl-MIC) in transition metal complexes for potential applications in the field of photochemistry and electrocatalysis. For the first time, detailed (spectro)electrochemical investigations, combined with theoretical calculations, of two constitutional isomers were conducted to explore the influence of the electronic structures in bond activation reactions. The investigations of the highly reactive (spectro)electrochemically generated and chemically isolated key intermediates enable a profound understanding of the tailor-made design in new potential transition metal-based photo- and electrocatalysts.

Kurzzusammenfassung

Die CuAAC-Reaktion zur Umwandlung organischer Azide und terminaler Alkine in 1,4-Triazole, als Vorstufen für Triazoliumsalze, ist seit mehr als einem Jahrzehnt bekannt. Es überrascht nicht, dass sich die synthetischen Möglichkeiten für 1,2,3-Triazole rasant weiterentwickelt haben. Um heterocyclische Triazoliumsalze in guter Ausbeute zu erhalten, sind selektive Synthesestrategien erforderlich. Sie bilden die Grundlage der so genannten mesoionischen Carbene (MICs), einer Unterklasse der bekannten NHCs. Die oben genannte Klassifizierung ergibt sich aus der Tatsache, dass 1,2,3-Triazol-5-ylidene nicht ohne Ladungstrennung in ihrer Lewis-Struktur gezeichnet werden können.

In der vorliegenden Arbeit wurden neue Synthesewege erforscht, um zu 1,2,3-Triazol-5-ylidenen mit Pyridyl-substituenten (Pyridyl–MIC) als zweizähnige Liganden für Übergangsmetallkomplexe zu gelangen. Das Zusammenspiel zwischen der stark σ −donierenden Natur des MIC und den guten π −akzeptierenden Eigenschaften des Liganden spielt eine entscheidende Rolle für die photo- und elektrokatalytische Aktivität. In Kapitel 3.2 wurde eine Reihe von Pyridyl–MIC (py-MIC) und 2,2'-Bipyridin (bpy) enthaltenden Ru(II)-Komplexen synthetisiert und mit Techniken wie ^{1}H- und ^{13}C-NMR-Spektroskopie, Massenspektrometrie, Elementaranalyse und Röntgenbeugungsanalyse charakterisiert. Darüber hinaus wurden (spektro)elektrochemische Messungen (SEC) durchgeführt, um die Art der verschiedenen Redoxzustände in Bezug auf die Anzahl der MIC-Einheiten zu untersuchen. Zeitabhängige Dichtefunktionaltheorie (TD-DFT) wurden durchgeführt, um einen Einblick in die photophysikalischen Eigenschaften der Komplexe und ihre potenzielle Anwendung als Photokatalysatoren zu erhalten, während die Lebensdauern der Ausgangszustände in Zusammenarbeit mit der Gruppe von Prof. Dr. Oliver Wenger untersucht wurden.

Kapitel 3.3 beschäftigt sich mit py-MIC basierten Gruppe 6 (Cr, Mo) Carbonylkomplexen. CO ist eine ideale Sonde, um den Einfluss des Liganden am Übergangsmetallkomplex nicht nur in der nativen, sondern auch in der oxidierten und reduzierten Form zu untersuchen. IR-, EPR- und UV/Vis/NIR-SEC in Kombination mit TD-DFT wurden durchgeführt, um ein tieferes Verständnis der elektronischen Struktur der Redoxzustände zu erhalten, während die Anregung der Komplexe zu einer ungewöhnlichen reversiblen Bindung des CO-Liganden führt, nachdem die Photoprodukte im Dunkeln gelassen wurden.

Überraschenderweise konnte das erste stabile $[M(py–MIC)(CO)_4]^+$ (M = Cr) Fragment mit π −akzeptierenden Liganden isoliert und mittels Röntgeneinkristallbeugungsanalyse

charakterisiert werden (Kapitel 3.4). EPR-, IR- und UV/VIS-Spektroskopie, unterstützt durch theoretische Untersuchungen, wurden durchgeführt um die seltene elektronenarme Natur der isolierten $[Cr(py{-}MIC)(CO)_4]^+$ Komplexe zu erschließen.

Darüber hinaus wurden in Kapitel 3.5 alle $[M(py{-}MIC)(CO)_4]$ (M = Cr, Mo, W) Komplexe mittels Step-Scan-FTIR-Spektroskopie und zeitaufgelöste Spektroskopie in Zusammenarbeit mit der Gruppe von Prof. Dr. Gerhards und Prof. Dr. Niedner-Schatteburg untersucht. Es wurde eine ungewöhnliche (photo)schaltbare ON/OFF-Bindung von CO in Lösung beobachtet. Zusätzlich zeigten alle Komplexe eine NIR-Emission im festen Zustand.

In Kapitel 3.6 wurden die reduzierte Spezies $[M(py{-}MIC)(CO)_4]^-$ *in-situ* erzeugt und die Reduktion durch verschiedene (spektro-)elektrochemische und theoretische Methoden als überwiegend ligandenzentriert eingestuft. Auf der Grundlage dieser Ergebnisse wurde eine elektrochemische CO_2-Reduktion unter nicht-protischen Bedingungen durchgeführt. Die (Spektro)elektrochemie stellt ein leistungsfähiges Instrument zur Untersuchung reaktiver Zwischenstufen in der Elektrokatalyse dar.

Im letzten Kapitel 3.7 wurde eine Reihe von $[(py{-}MIC)Rh(Cp^*)X]^{n+}$ (X = Cl^-, MeCN; n = 1, 2) Komplexen synthetisiert und mit verschiedenen Techniken vollständig charakterisiert. Alle Komplexe wurden in der elektrochemischen H^+ Reduktion getestet, und es wurde ein Mechanismus für die Bildung des Präkatalysators postuliert. Eine Reihe von Zwischenprodukten wurde chemisch isoliert, mittels Röntgeneinkristallbeugung untersucht und mit den elektrochemisch erzeugten Spezies verglichen. Theoretische Berechnungen untermauerten den präkatalytischen Aktivierungspfad.

Die vorliegende Arbeit vermittelt ein tiefgreifendes Verständnis der Auswirkungen von zweizähnigen Liganden mit π −akzeptierenden und stark σ −donierenden Liganden (py–MIC) in Übergangsmetallkomplexen für potenzielle Anwendungen im Bereich der Photochemie und Elektrokatalyse. Zum ersten Mal wurden detaillierte (spektro)elektrochemische Untersuchungen, kombiniert mit theoretischen Berechnungen, von zwei konstitutionellen Isomeren durchgeführt, um den Einfluss der elektronischen Strukturen in Bindungsaktivierungsreaktionen zu erforschen. Die Untersuchungen der hochreaktiven (spektro)elektrochemisch erzeugten und chemisch isolierten Schlüsselintermediate ermöglicht ein tiefgreifendes Verständnis für das maßgeschneiderte Design neuer potenzieller übergangsmetallbasierter Photo- und Elektrokatalysatoren.

Contents

List of Abbreviations

η	overpotential
aNHC	abnormal *N*-heterocyclic carbene
Bn	benzyl
bpy	2,2'-bipyridine
btz	3,3-dimethyl-1,1-bis(*p*-tolyl)-4,4-bis(1,2,3-triazol-5-ylidene)
^{t}Bu	*tert*-butyl
cat.	catalyzed
C-C	pyridyl-4-triazolylidene
C–N	pyridyl-1-triazolylidene
Cp*	pentamethylcyclopendatienyl
CuAAC	copper(I)-catalyzed alkyne-azide cycloaddition
CV	cyclic voltammetry/cyclic voltammogram
Cym	*p*-cymene
DCM	dichlormethane
DFT	density functional theory
Dipp	2,6-diisopropylphenyl
DMF	dimethylformamide
EC	electron-transfer/chemical reaction
EECC	electron-transfer/electron-transfer/chemical reaction/chemical reaction
EPR	electron paramagnetic resonance
ESI	electrospray ionization
Et	ethyl
FcH/FcH$^+$	ferrocene/ferrocenium couple
FE	Faradaic efficiency
GC	glassy carbon
HEP	Huynh's electronic parameter
HOMO	highest occupied molecular orbital
ILCT	intra-ligand charge transfer
IR	infrared
ISC	intersystem crossing
IVCT	intervalence charge transfer
LC	ligand-centered

LEP	ligand electrochemical parameter
LLCT	ligand-to-ligand charge transfer
LMCT	ligand-to-metal charge transfer
LUMO	lowest occupied molecular orbital
MeCN	acetonitrile
Me	methyl
Mes	mesityl/2,4,6-trimethylphenyl
MC	metal-centered
MIC	mesoionic carbene
MLCT	metal-to-ligand charge transfer
MO	molecular orbital
MS	mass spectrometry
NHC	*N*-heterocyclic carbene
NIR	near-infrared
nr	non-radiative
NMR	nuclear magnetic resonance
OTTLE	optically transparent thin-layer electrochemical
PCET	proton-coupled electron transfer
Ph	phenyl
ppy	2-phenylpyridine
^{i}Pr	isopropyl
py	pyridine
SCE	saturated calomel electrode
SEC	spectroelectrochemistry
SET	single-electron transfer
TEP	Tolman's electronic parameter
TDDFT	time-dependent density functional theory
THF	tetrahydrofuran
TOF	turnover frequency
Tol	tolyl
TON	turnover number
tetr	tetrazolate
tpy	2,2':6',2''-terpyridine

triaz	1,2,3-triazole
UV	ultraviolett
vis	visible
VC	vibrational cooling

1 Introduction

"*When the world is in trouble, chemistry comes to its rescue*."[1] With these simple yet so powerful words, Carolyn Bertozzi reacted to the announcement of the prestigious Nobel Prize awarded to her. In the face of rapidly evolving climate change, her words seem more relevant than ever.

The explosive growth of the world's population, progressive industrialization and the scarcity of fossil fuels for societal prosperity have sparked a global debate on resource-efficient access to environmentally friendly and sustainable materials.[2] Despite the tremendous achievements in energy efficiency and the integration of industrial processes into the modern economy, the continued exploitation of fossil fuels results in serious environmental and health concerns.[3]

In view of the global energy crisis looming, alternative energy sources such as wind, solar, nuclear and geothermal energy, biomass, dihydrogen and electrocatalytic refinery have been developed in recent decades.[4,5,6] However, according to recent data, 85% of the world's primary energy depends on fossil fuels, which inevitably release fairly unreactive greenhouse gas, such as CO_2 and methane,[5] giving rise to fundamental questions: What does it take to activate chemically inert bonds in small molecules to convert them into economically valuable products and what long-term strategies can be employed to store high energy material?[7,8] The answers appear simple from a chemical perspective – a catalytic transformation.

A catalyst is a substance that stabilizes the transition state ($\Delta G^{\ddagger}_{uncat.}$) of a reaction by lowering the energy barrier ($\Delta G^{\ddagger}_{cat.}$) between the starting material and the product without affecting the free enthalpy ΔG of the reaction (**Figure 1**). By definition, a catalyst is not consumed in the reaction and remains unaffected over across multiple transformations.[9]

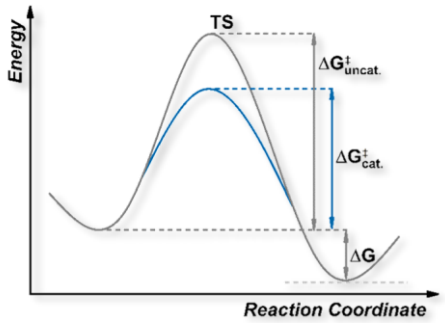

Figure 1. Energy profile of a one-step reaction (grey: uncatalyzed, blue: catalyzed).

Nature undoubtedly contains the most efficient catalysts for the activation of abundant small molecules such as O_2, N_2, H_2, CO_2, NO_x, and CH_4.[10,11,12] A variety of organisms make use of complex enzymes in metabolic processes, such as those found in respiratory processes[13] and photosynthesis,[10,14] overcoming the embedded kinetic and thermodynamic barriers in the multi-step catalytic conversion of chemically inert molecules. In a broader context, the complexity of the enzymes and the simplicity of the target molecules, have parallels to the battle between David and Goliath. Only this time Goliath retains the upper hand.

The key role of this outcome, apart from the global structure of the enzymes, can be addressed to the redox-active central metal ion. Indeed, from a (bio-)inorganic perspective, the catalytic activation of small molecules with transition metals forms the foundation of several fields of chemical science, such as heterogeneous catalysis,[15] homogeneous catalysis,[6,16,17] photocatalysis[18,19] and electrocatalysis (**Figure 2**).[20,21,22,23]

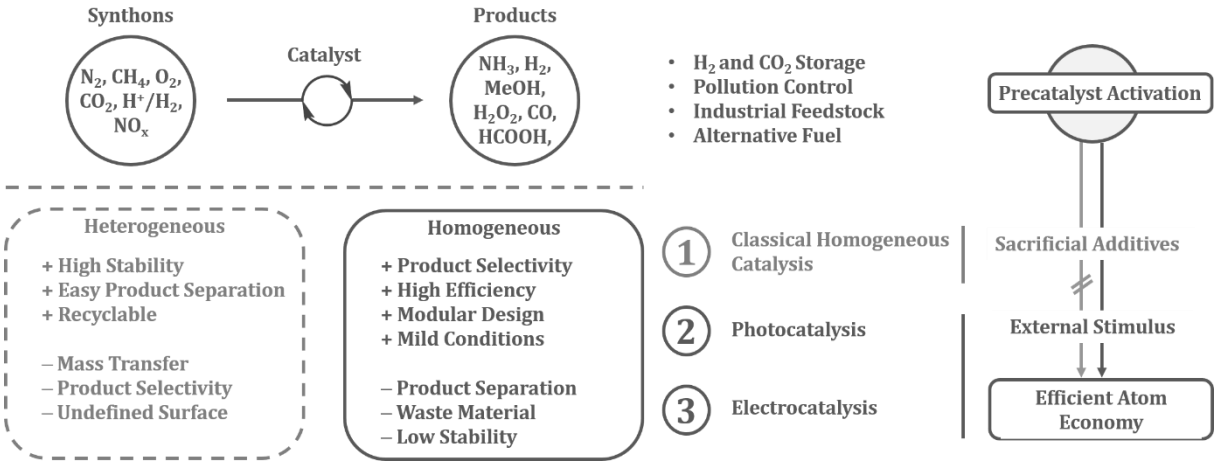

Figure 2. Overview of catalytic strategies for small molecule activation.

Plenty of industrial manufacturing processes are based on heterogeneous catalyst due to their high stability, easy product separation and excellent recovery. However, heterogeneous catalysts often display poor product selectivity, limited mass transfer, and an undefined catalytic surface precluding from detailed mechanistic studies. On the other hand, from a purely industrial viewpoint, homogeneous catalysts are less attractive considering the difficult product separation, the large amount of waste material, and the corrosion of the reactors. But what makes homogeneous catalysis so unique?

For some, homogeneous catalysis may be a purely academic challenge, but for others, it offers answers to the fundamental mechanistic understanding of small molecule activation in a well-defined molecular environment under relatively mild conditions, as observed in biological systems, such as enzymes. Understanding these complex mechanisms provides access to tailor-made molecular catalysts with extremely high efficiency and selectivity, requiring only low catalyst loadings.[24]

The extreme sensitivity of the catalytically active species make them difficult to handle and an appropriate choice of a stable precursor therefore is indispensable. In a classical approach, a homogeneous catalyst requires sacrificial additives to generate the highly reactive intermediate that converts the chemical synthons into valuable products, such as alcohols, formic acid, ammonia, dihydrogen, oxygen or carbon monoxide, to name a few.[5,6,8,12,17]

In the last few decades, enormous progress in the field of photo- and electrochemically induced activation of the precatalysts have been achieved to provide an atom economic access to the catalytically active species for the storage of high energy materials and the activation of small molecules.[22,23,25–27]

In view of the scope of this thesis and the vastness of the fields, the following discussion will focus on the conceptual design of the homogeneous molecular catalyst and its photo- and electrochemical precatalytic activation concerning small molecules, limited dominantly on bidentate heterocycles that contain *N*-donors.

1.1 Conceptual Design of Molecular Photocatalysts

Photochemistry is often associated in a vernacular sense, with photophysics in an interdisciplinary field that encompasses new synthetic strategies for the design of efficient molecular catalysts. In addition, it is usually accompanied by an in-depth understanding of the physical properties of the applied photocatalyst. The inclusion of rapidly advancing theoretical approaches provides a conceptual understanding of the interplay between the central metal ion and the ligand scaffold, leading to a tremendous development in the field of photocatalysis[18,25,26,28,29,30,31] and dye-sensitized solar cells.[32] In photochemistry, ground-breaking discoveries have been made in the field of supramolecular chemistry,[33] early[34–36] and late[28,29,36] transition metal complexes, due to the endless number of ligand frameworks, such as tripodal ligands[34–40] or cyclic ligands,[41] to name a few.

For the scope of this thesis, the following discussions will briefly focus on the octahedral group 8 transition metal complexes ($[M(bpy)_3]^{2+}$ with M = Ru, Fe) containing bidentate polypyridine ligands.

Photocatalysts are multi-electron systems and the resulting electronic wave functions (molecular orbital = MO) can be visualized in a Jablonski diagram according to their predominant atomic orbital contributions (**Figure 3**).

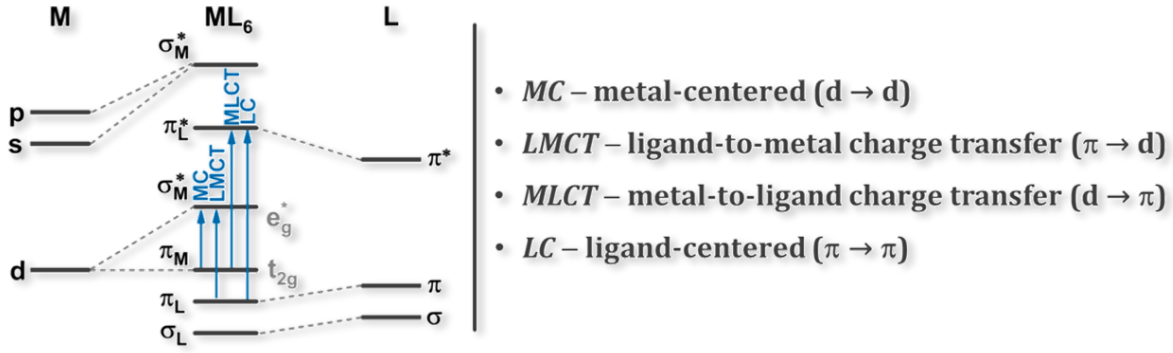

Figure 3. Molecular orbital diagram for an octahedral transition metal complex (arrows indicating electronic transitions).

Strongly bonding, predominantly ligand-centered orbitals are represented as σ_L for σ −bonding and π_L for π −bonding orbitals, while essentially non-bonding metal-centered orbitals of t_{2g} symmetry are depicted as π_M orbitals. The anti-bonding, predominantly metal-centered orbitals of e_g^* symmetry are classified as σ_M^* orbitals and the anti-bonding ligand-based orbitals as π_L^* orbitals.[42]

At relatively low ground state energies, electronic transitions of the type metal-centered (MC), ligand-to-metal charge transfer (LMCT), metal-to-ligand charge transfer (MLCT) and ligand-centered (LC) are expected. Although MC transitions are forbidden in octahedral complexes with inversion symmetry (Laporte's rule),[43] lowering the dynamic symmetry induces partially allowed transitions.

Octahedral complexes with a d^6 electron configuration typically have fully occupied σ_L and π_L orbitals, resulting in a closed-shell ground state configuration $^1A_{1g}$.

Since the electronic transitions from the ground state to the excited state occur instantaneously compared to their nuclear motions, the geometry of a metal complex does not change within the time scale of the electronic transition, according to the Franck-Condon principle.[42]

However, the spatial change in electron density induces a nuclear motion leading to a new minimum geometry of the excited complex.

The changes in the bond distances, angles and torsion angles are best described as a combination of normal modes (vibrational cooling, VC). Their intensity is proportional to the square of the overlap integral between the vibrational wave functions of the transitions involved (absorption and emission).[43]

To a first approximation, the electronic transitions and their vibronic modes represented by the potential energy surfaces (anharmonic oscillator) depends to a large extent on the nature of the metal center, the coordinated ligands and the overall symmetry of the molecule, defining the nature of the lowest excited state and multiplicity.[34,40]

These criteria form the basis for an efficient photocatalyst facilitating sufficient lifetime of the excited state. From a purely statistical perspective, an increased lifetime leads to a higher probability of efficient energy transfer or chemical reaction with the targeted molecule – but what factors limit the excited-state lifetime?

One of the well-established, yet so simple photocatalysts are the polypyridine complexes of group 8 $[M(bpy)_3]^{2+}$ (M = Ru, Fe) metals (**Figure 4**).[34,40,42] The higher homologue $[Ru(bpy)_3]^{2+}$ shows an excited-state lifetime of 890 ns at room temperature, while $[Fe(bpy)_3]^{2+}$ has only an excited-state lifetime of only 50 fs.[34,40] The drastic decrease in excited-state lifetime can be attributed to the central metal atom. After excitation from the $^1A_{1g}$ ground state to the excited ^{1}MLCT state and subsequent vibrational cooling, a rapid intersystem crossing (k_{ISC}) in the ^{3}MLCT state (nesting state) occurs in both complexes. However, the weaker ligand-field splitting of $[Fe(bpy)_3]^{2+}$, as a result of the smaller radial distribution of 3d electrons on the metal core,[44] allows access to energetically low-lying MC states, decreasing the energetic barrier (ΔE) for the internal conversion and initiating a non-radiative decay (k_{nr}) to the ground state.

The shift of the MC states can be attributed to the population of the anti-bonding e_g^* orbitals, resulting in the elongation of the metal-ligand bond. Therefore, to obtain long-lived emissive MLCT states, the non-emissive MC states must be shifted to higher energies. In this context, different conceptual strategies for ligand design have been explored to increase the thermal energy barrier between the MLCT and MC states.

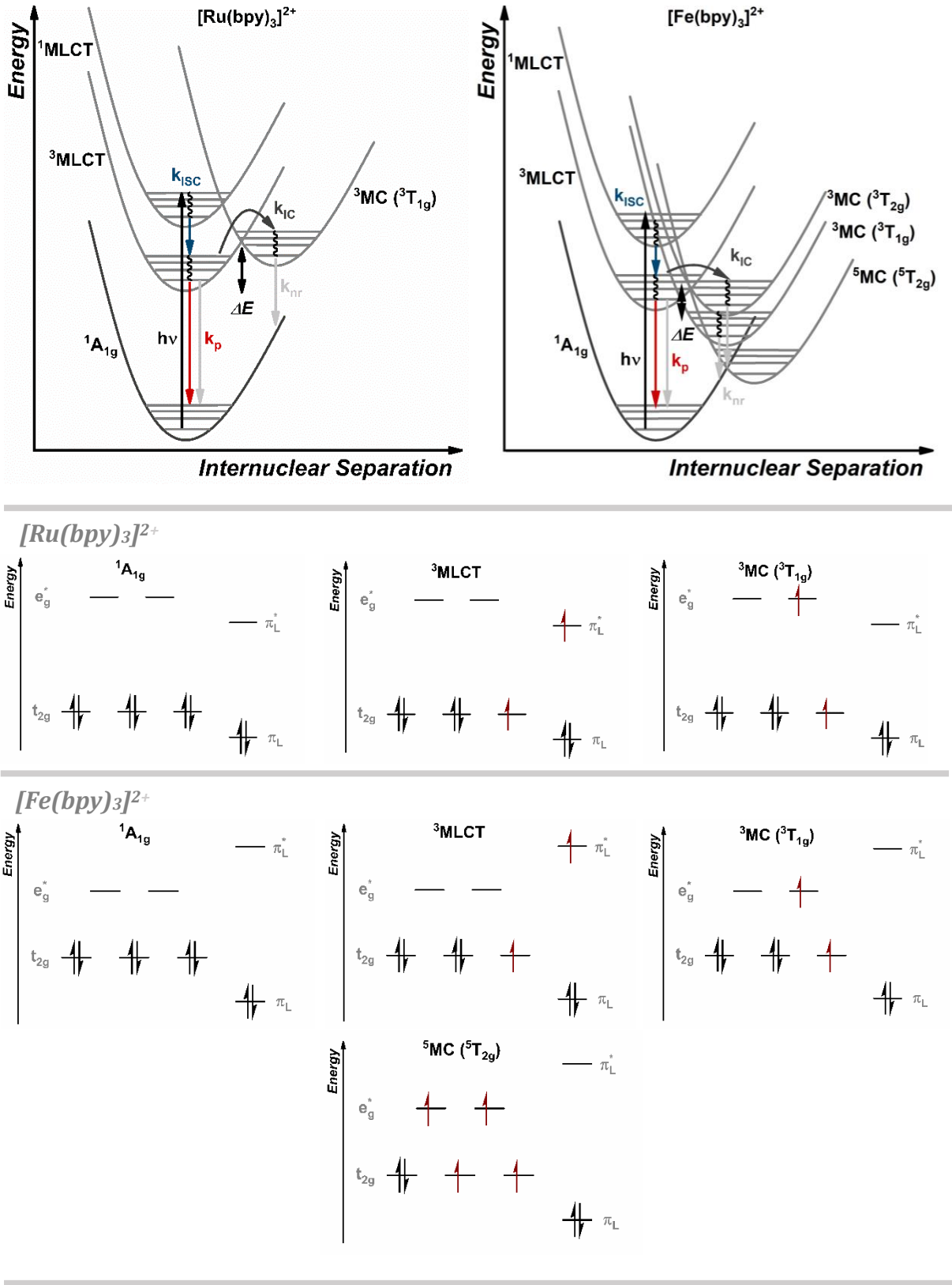

Figure 4. Schematic potential energy surface diagrams of $[M(bpy)_3]^{2+}$ (M = Ru, Fe) and their electronic states (excitation (hν): black, phosphorescence (k_p): red, intersystem crossing (k_{ISC}): blue, internal conversion (k_{IC}): dark grey, non-radiative decay (k_{nr}): light grey).[34]

Increasing the activation barrier between MLCT states and the MC states can be achieved by the inclusion of highly symmetric ligands, push-pull systems, highly strained complexes, strongly donating ligands or combined σ −donor and π −acceptor ligands (for detailed discussion see **Section 1.4**).[40]

In a more general perspective, the effect on ligand-field splitting is determined by the metal-ligand interaction according to ligand-field theory:

- σ −donor: overlap of the filled σ orbitals of the ligand with the metal-centered d–orbitals of σ −symmetry (d_{z^2}, $d_{x^2-y^2}$)
- π −donor: overlap of the filled π^* orbitals of the ligand with the metal-centered d–orbitals of π −symmetry (d_{xy}, d_{xz}, d_{yz})
- π −acceptor: overlap of an unoccupied π^* orbitals of the ligand with the metal-centered d–orbitals of π −symmetry (d_{xy}, d_{xz}, d_{yz}), so-called π −backbonding

A weak σ −donor ligand leads to a weak ligand-field splitting between the non-bonding t_{2g} orbitals and the anti-bonding e_g^* orbitals, while a strong σ −donor ligand destabilizes the anti-bonding e_g^* orbitals or in other words – the $^{3/5}$MC states (**Figure 5**). On the other hand, strong π −acceptor ligands decrease the energy of the t_{2g} orbitals and consequently the thermal barrier to internal conversion. A different situation is observed in the presence of a strong π −donor ligand. With a right choice of ligand, destabilization of the π orbitals can lead to a so-called HOMO inversion between the metal-centered and the ligand-centered orbitals and is currently state of the art.[45]

However, to achieve optimal ligand-field splitting, an ideal octahedral geometry of the N–M–N trans angles (= 180°) is required to maximize the overlap of the metal-ligand orbitals. Otherwise, a lowering of the symmetry in the metal center results in a degeneration of the participating orbitals and, consequently, to a decrease of the exited-state lifetime.[40]

Formally, the excitation in $[M(bpy)_3]^{2+}$ (M = Ru, Fe) complexes can be described as an oxidized metal center and a reduced ligand radical $[M^{III}(bpy)_2(bpy^{\cdot-})]^*$ in the ^{3}MLCT state.[44,46] The light-induced charge separation and the extended lifetime of the excited-state are essential for the activity of the photocatalyst in electron and energy transfer processes.

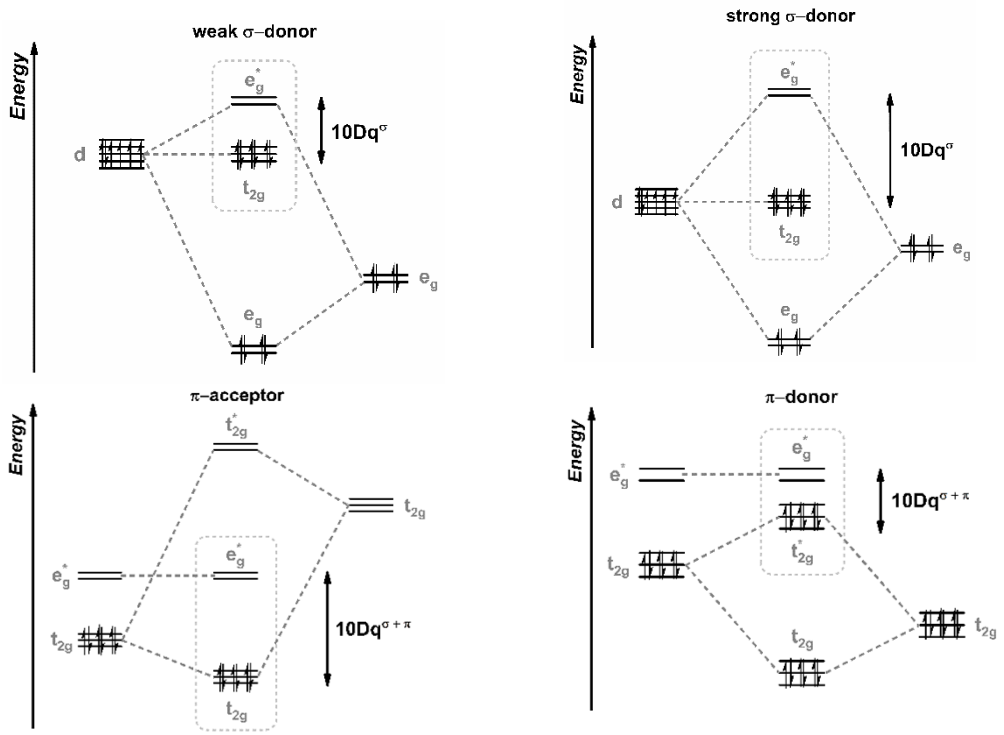

Figure 5. Ligand field effects between metal *d*–orbitals and ligand orbitals.[40]

The energy level of the generated electron-hole at the metal center and the excited ligand-centered electron can be tuned by the synergy between the metal center and the electronic properties of the incorporated ligand to provide an efficient photocatalyst for tailor-made applications.

To determine, whether the applied photocatalyst is a suitable candidate for chemical and energy transfer processes, Latimer diagrams have proven to be particularly useful.[31,47] The combination of the oxidative and reductive potentials of the ground state with the excited state energy (E_{00}) is frequently used to estimate the oxidative and reductive potentials of the excited state of the photocatalyst (**Scheme 1**).

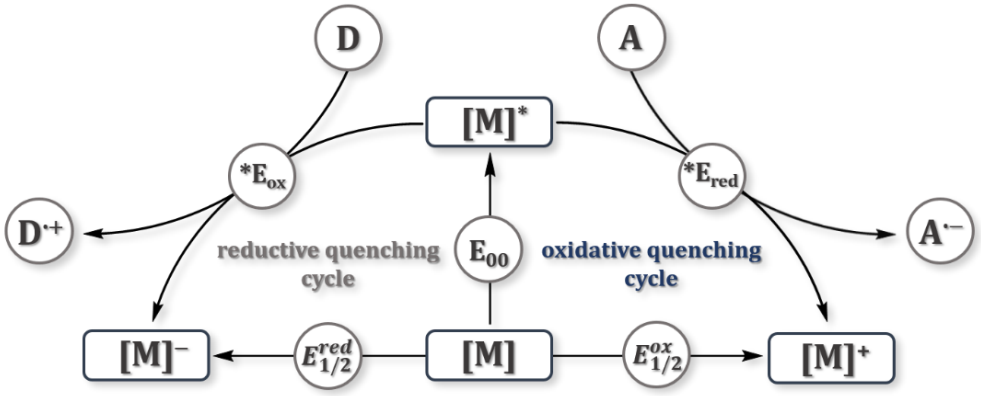

Scheme 1. Simplified Latimer-diagram for electron/energy transfer processes.

The ambivalence of the excited state, as a strong reductant and at the same time as a strong oxidant, leads to two different quenching pathways. One is the so-called reductive quenching cycle. After excitation, the photocatalyst $[M]^*$ can undergo an one-electron reduction in a bimolecular reaction with the substrate (D) to generate the singly-reduced species $[M]^-$ and $D^{\cdot+}$, while in the oxidative quenching cycle, the excited state transfers an electron to the substrate (A) of interest, forming the singly-oxidized species $[M]^+$ and $A^{\cdot-}$. It is important to mention, that the electron transfer rate competes with the radiative emission and vibrational relaxation (dynamic quenching) of the excited state and the interaction of the substrate with the photocatalyst (static quenching).[31] A sufficiently long-lived resting state is therefore crucial for an excellent catalytic performance.

So far, only non-catalytic conditions have been presented. In catalytic conditions, the native photocatalyst must be recovered from its oxidized or reduced form. In photocatalysis, sacrificial donors (or acceptors), such as amines,[31] are usually added to regenerate the catalyst. Once the catalytic conditions are fulfilled, the excited photocatalyst can either directly undergo a single-electron transfer (SET) to the substrate, to initiate a chemical reaction or act as a photosensitizer for a co-catalyst, to perform the redox-reaction (**Scheme 2**).

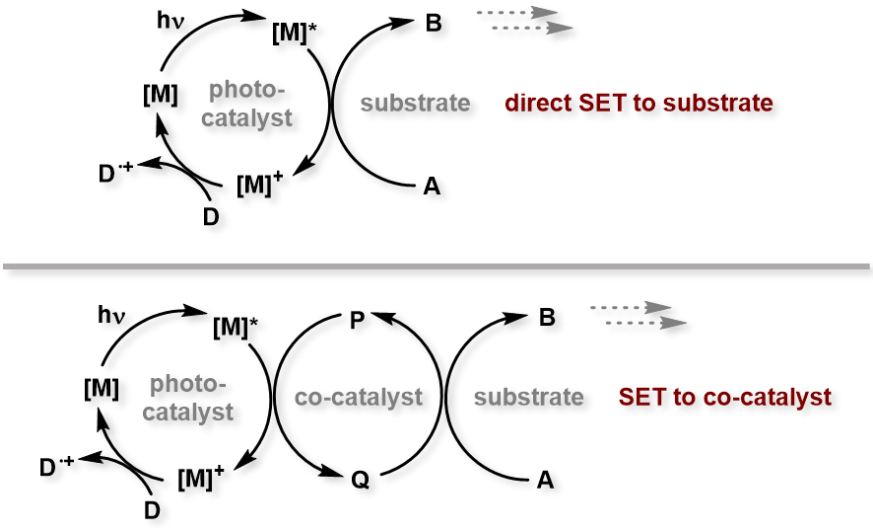

Scheme 2. Possible photocatalytic SET reactions in an oxidative quenching cycle (D = sacrificial donor).

The thermodynamic ability of the excited state to intervene in a bimolecular energy-transfer process follows the Marcus-theory[48] and the Franck-Condon factor.[49]

The non-radiative energy transfer can be described classically as combined effects of energy gradient and nuclear reorganization or quantum mechanically, as the thermally averaged sum of vibrational overlap integrals between the donor and acceptor molecule. They are divided into two mechanisms - the Coulomb mechanism, and the exchange mechanism (**Scheme 3**).[42] However, from a general perspective, the mechanism depends on the spin of the ground state, the excited state and the donor-acceptor distance.

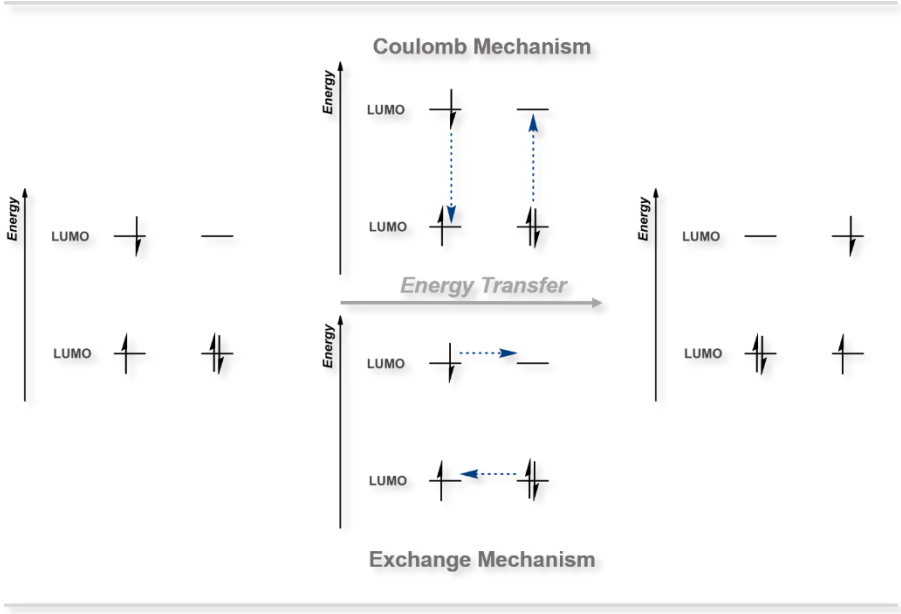

Scheme 3. Energy transfer mechanism (top: coulomb mechanism, bottom: exchange mechanism).[42]

The Coulomb (trough space) mechanism requires physical contact between the donor and acceptor molecules and a large dipole-dipole interaction. This mechanism is usually observed in singlet-singlet energy transfers with large aromatic systems.

On the other hand, the exchange mechanism strongly depends on the orbital overlap between the donor and acceptor molecules, typically mediated by a bridging fragment (trough bond). The energy transfer rate therefore increases with decreasing distance. Notably, the exchange mechanism allows spin-forbidden transitions to obey spin conservation, making a photocatalytic application particularly attractive.

Ideal photocatalysts show an absorption maximum in the visible spectrum ($\lambda_{max} = 390 - 700$ nm) to perform the catalytic transformation under mild conditions while avoiding substrate and product decomposition.[50]

They are of particular interest for the activation of small molecules, such as organohalides,[51] non-halogenated substrates (C–C bond cleavage,[52] C–H functionalization,[53] oxidative cyclization,[54,55] alkene reduction,[56] cyclcoaddition,[57] trifluormethylation[55,58]), in dehydrogenation reactions,[59,60] CO_2 reduction,[61,62,63] polymerization[64] and lignin degradation,[65] providing a wide range of products for synthetic transformations and sustainable energy conversion (**Figure 6**).

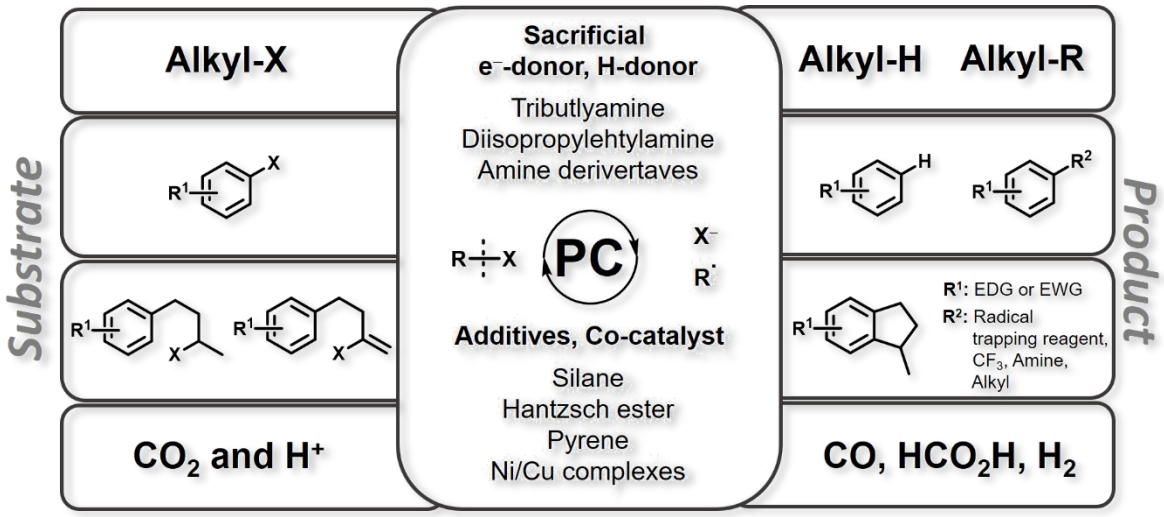

Figure 6. Photocatalytic small molecule activation.[31]

1.2 Molecular Electrocatalysts

The electrochemical conversion of low energy feedstocks, such as H_2O, H^+, and CO_2, has led to the discovery of an ever-growing number of homogeneous transition metal complexes to lower the kinetic barriers and to improve the selectivity for the generation of renewable energy sources.[66] However, non-trivial multi-electron conversion with high-energy intermediates allows for multiple reaction pathways and electrocatalyst degradation.[23,67,68] Therefore, the identification of the catalytically active species is of fundamental interest to optimize the stability and activity of the electrocatalyst.

In general, the homogeneous precatalyst (P) functions as electron shuttle between the electrode surface and the substrate (A) to induce the chemical reaction generating product B. The catalytically active species (Q) performs the substrate conversion in the diffusion layer of the electrochemical cell and requires lower energies ($E^0_{cat/2}$) compared to direct product formation at the electrode surface (E_{onset}) (**Scheme 4**).

The catalytically active species is therefore of fundamental interest to optimize the stability and activity of the electrocatalyst. However, the performance of the activated electrocatalyst is determined by the thermodynamic potential ($E^0_{A/B}$) of the product formation (A/B). In the case of $E^0_{cat/2} < E^0_{A/B}$, the chemical transformation from A→B is usually limited by the insufficient driving force of the catalyst. Hence, most of the reported electrocatalysts require additional energy, better known as overpotential (η).[23]

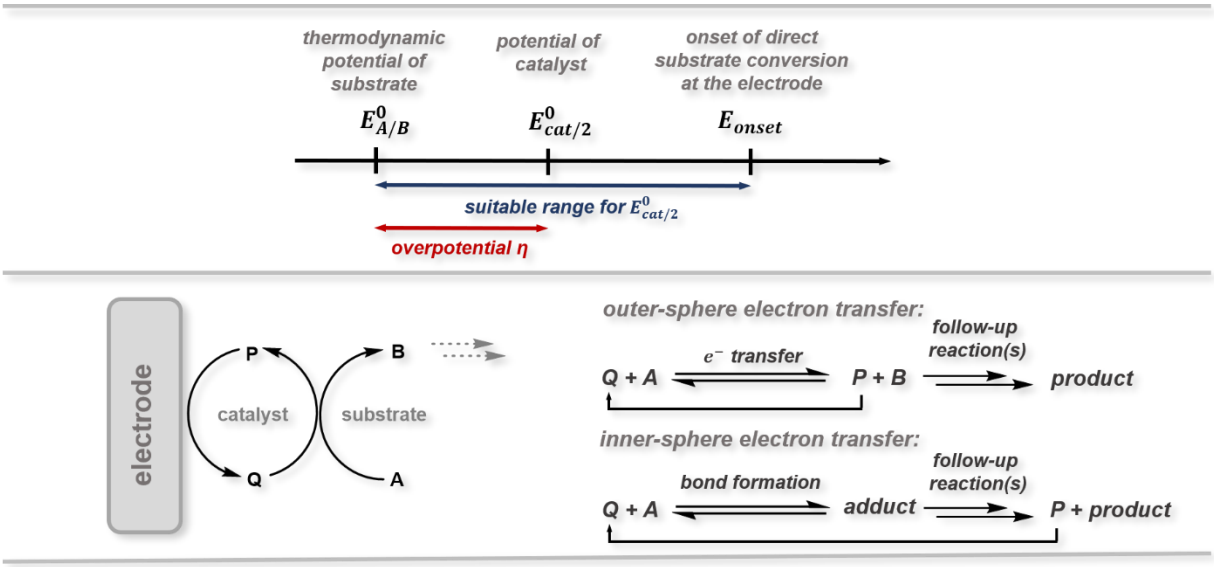

Scheme 4. Suitable range for a homogeneous electrocatalyst (top) and simplified electron transfer at the diffusion layer (bottom left) with a schematic inner- and outer-sphere mechanism (bottom right).

In an outer-sphere mechanism, the electrocatalyst acts as an electron-transfer reagent, that induces product formation, whereas in an inner-sphere mechanism, the electrocatalyst binds the substrate to produce an intermediate, which in turn undergoes a redox process to generate the desired product. But how can one assure that the precatalyst used is a suitable candidate under the electrocatalytic conditions?

One of the most popular techniques for evaluating the precatalyst is cyclic voltammetry. It not only provides information on the redox potentials to determine whether a catalyst can be used in an appropriate regime, but also in-depth kinetic and mechanistic details of the molecular (pre-)catalyst and its activity.[23,68,69]

However, the identification of the active species at the electrode surface is still relatively unexplored but is crucial for understanding the catalytic performance. The extreme potentials required for electrochemical transformation can lead to the decomposition or demetallation of the complex, resulting in catalytically active nanoparticles or heterogeneous species, that are adsorbed on the electrode surface.[68]

Given scope of this thesis, the following brief discussion will focus mainly on the precatalytic activation of the electrocatalyst and how the performance of the active species can be influenced by the metal center and the ligand framework.

In the absence of a substrate, molecular electrocatalysts exhibit individual redox processes, which, depending on the nature of the electrocatalyst, are either electrochemically reversible, quasi-reversible or irreversible. For the sake of simplicity, only electrochemically reversible processes in the presence of the substrate will be discussed here.

The first mathematical description of a one-electron, one-substrate reaction was described by Savéant and Su, who figuratively classified the limiting wave forms into eight kinetic zones.[70] According to their classification, catalysts under an ideal condition show a S-shaped (K or KS zone) response in the presence of the substrate (**Figure 7**, **I**). However, the shape strongly depends on the scan rate, electron transfer rate and individual substrate and catalyst concentrations in addition to competing with certain side phenomena such as substrate consumption, product inhibition and catalyst deactivation.[71]

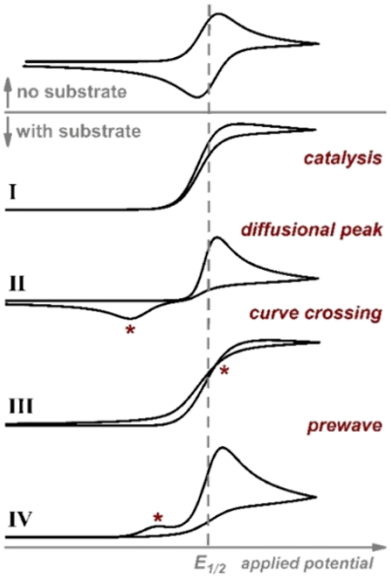

Figure 7. Qualitative cyclic voltammograms of catalyst transformation or decomposition adapted from Dempsey and co-workers.[68]

The complexity of catalytic systems has shown that direct translatability of kinetic zones is difficult to achieve due to multiple elementary steps and intermediates, that can undergo several reaction pathways. Some of the most common deviations from ideal S-shaped catalysis wave forms are shown in Figure 7.

In the one-electron, one-substrate catalytic reaction (**Figure 7**, **II**), a diffusion peak is observed after reversing the scan direction of the catalytic process. In this case, the redox event originates from a new homogeneous species, formed during the catalysis, as a consequence of a slow reaction rate constant or substrate consumption.[72] Additionally, the diffusion peak sometimes also indicate oxidation or reduction of the catalytic product, a decomposition product or even a feature of the active catalyst. Identifying the diffusional process can be challenging but can provide useful information about possible decomposition pathways, product formation or even important intermediates in the catalytic cycle.

The *in-situ* formation of the active catalyst is often accompanied by an induction period, manifested by the catalytic activity as a function of time. As the cyclic voltammogram (**Figure 7**, **III**) progresses, a higher concentration of the catalytically active species is produced. The accumulation of the active catalyst results in a continuous increase of the current, during reverse scan, causing a so-called "crossing curve". However, this phenomenon should not always be interpreted as the slow formation of the active species or as electrochemically induced autocatalysis,[73] but rather as possible electrodeposition at the electrode surface.[74]

Perhaps the most clear indication of precatalyst transformation is the appearance of an irreversible prewave (**Figure 7**, **IV**).[75–77] An electron transfer reaction can induce a chemical reaction leading to a catalytic intermediate that does not carry out the catalytic reaction immediately. In this case, the potential shift of the prewave $E_{1/2}$ strongly depends on the kinetics of the precatalyst formation. An anodic shift of the potential indicates a rapid formation of the precatalyst, while a cathodic shift is associated with a slow formation of the catalytic intermediate (**Figure 8**).

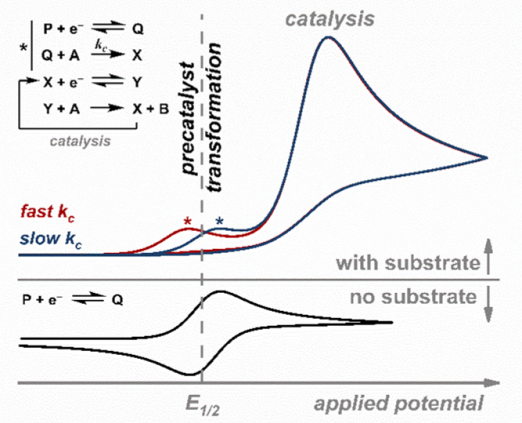

Figure 8. Kinetic influence of precatalytic formation in presence of the substrate.[68]

The investigation of the precatalytic wave plays a crucial role in understanding of the catalytic performance, considering the presence of competing chemical decomposition leading to the formation of heterogeneous intermediates.

During the past decades, various techniques have been developed to confirm the presence of a homogeneous (pre-)catalyst, such as mercury poisoning,[78,79] electrode surface analysis,[77,79–81] rotating ring-disc electrochemistry,[76,82] rinse tests[75,76,78,81,83] and spectroelectrochemistry.[84]

Each of the above-mentioned methods provide detailed insights into the nature of the electrochemically generated species. Particularly both rinse tests and spectroelectrochemistry are fruitful due to their simplicity and spectroelectrochemistry due to the scope to combine electrochemistry with classical spectroscopic techniques, such as UV/vis/NIR-, EPR- and IR-spectroscopy.[85,86]

The rinse test represents one of the most common methods for detecting a heterogeneous or heterogenized active catalyst. In this process, the electrode is rinsed and transferred into a freshly prepared substrate-only solution after stopping the cyclic voltammogram passing the precatalytic wave or the catalytic potential. The absence of any significant changes in the current beyond the background clearly exclude the formation of any heterogeneous particles or adsorption on the electrode surface.

However, correct handling of the rinse test determines whether a heterogeneous species can be detected or not. The observation of an additional current depends strongly on the metastable film, that forms on the electrode surface. Without the application of an appropriate potential during the rinse test to prevent the diffusion of decomposition of the molecular species at the electrode surface, the assignment of an electrodeposited catalyst could lead to a misinterpretation of the results.[81]

An excellent method to follow *in-situ* formation of the precatalyst, without transferring the electrode is spectroelectrochemistry (SEC). Real-time detection in the absence or presence of the substrate provides detailed information about the stability and electronic structure of the electrochemically generated precatalyst.[86]

However, from a purely electrochemical point of view the short-lived intermediates can undergo rapid follow-up reactions, even though they follow the criteria of a reversible electron transfer process in cyclic voltammetry (peak/peak current ratio = 1, peak/peak voltage difference = 59 mV for one-electron transfer at 298 K),[87]

In terms of spectroelectrochemistry, the time scale of bulk electrolysis competes with the rapid chemical transformation of a highly reactive intermediate generated during the fast sweep rate in cyclic voltammetry.

To shorten the bulk electrolysis time, narrow glass tubes (EPR-SEC) or optically transparent thin-layer electrodes (OTTLE) cells (UV/vis/NIR- or IR-SEC) are commonly used to increase the concentration of the electrochemically generated species at the electrode surface and consequently make detection of the electrochemically reduced or oxidized species more accessible.[86]

The stability of the electrochemically generated species is expressed by isosbestic points during controlled potential electrolysis and the complete recovery of the initial spectra after spectroelectrochemical measurements.[86] Any deviation from these criteria indicates electrochemically induced chemical transformation of the precatalyst.

The information that can be obtained from precatalytic wave formation paves the way for the optimal design of a highly active and stable catalyst.

An efficient electrocatalyst should be capable of performing multi-electron substrate conversion at low overpotential to access high energy materials, such as H_2, CO or HCOOH, to name a few.[88]

From a mechanistic point of view, the molecular catalyst can perform electron transfer steps directly at the metal center, in a combined metal-ligand pathway or exclusively at the ligand framework. This structure-reactivity relationship between the metal center and the ligand defines the catalytic performance of the electrocatalyst and is of great importance for modifying the catalytic activity – but nothing comes without a price.

The incorporation of an electron-withdrawing ligand is expected to lower the overpotential, by reducing the electron density at the active site of the metal center. This makes the electron uptake more accessible at mild potentials.

In contrast, electron-donating ligands increase the electron density at the electrocatalyst and thereby shift the electron uptake to higher potentials.

Activation of the precatalyst often follows subsequent substrate binding according to an inner-sphere mechanism. However, the initial step is strongly influenced by the electronic structure of the catalyst. Electron-withdrawing ligands, for instance, reduce the substrate affinity and thus the overall activity of the catalyst, while electron-donating ligands favor substrate binding. This contradiction between the requirement of a low overpotential and strong substrate activation is one of the major challenges in electrocatalysis. Savéant *et al.* described this paradox as the "iron law" of electrocatalysis.[89]

However, the modular synthesis of homogeneous electrocatalysts allows a tailor-made design for selective and highly efficient conversion of the substrate.

The nature of the active metal center plays probably the most obvious influence on the stability and activity of the electrocatalyst. Comparison of 3d metal centers with 4d and 5d metal centers reveals some interesting trends. First, 3d metals possess smaller atomic radii and consequently stronger Coulomb repulsion between the metal centers and the ligand frameworks, while 4d and 5d metals have more diffuse orbitals leading to better overlap (primogenic repulsion).[44] As a result, ligand dissociation is more likely in 3d metal complexes and usually (but not always)[90] higher overpotentials are observed due to the higher reorganization energies during electron transfer. The high geometric changes in 3 d metal complexes also reduce the electron transfer rate during the redox event.[88] However, this should be taken with great caution, as the relative energies of the d orbitals involved ($3d < 4/5d$) with respect to the incorporated ligand have a drastic effect on the activation of the substrate, reaction rate and activation of the precatalyst.[90]

Second, changing the oxidation state can affect product selectivity and overpotential. Higher oxidation states usually decrease the overpotential of the electrocatalyst as the overall charge of the complex decreases.

In 2015, Robert *et al*. showed that in a similar ligand framework the active metal center has a drastic impact on the product selectivity in electrochemical CO_2 reduction. The Fe(II) complexes, with an η^1 CO_2 binding mode selectively produced formic acid as a product, while in the corresponding Co(III) complex CO_2 was converted to CO. The product selectivity can be explained by the weaker π −backbonding in the Fe(II) complex leading to a weaker metal-carbon bond, which facilitates the isomerization from Fe–COOH to Fe–OCHO.[61]

However, the catalytic activity of the central metal atom is strongly influenced by the electronic and steric properties of the ligand framework.

The influence of the ligand system can be divided into two categories: the inner coordination sphere and the secondary coordination sphere (**Figure 9**). The inner-sphere primarily determines the electronic properties of the complex, as the ligands are directly bound to the active site, whereas in the outer-sphere the steric repulsions, weak bonding interactions and cooperative effects with the metal-bound substrate are decisive.

An extended π −system lowers the HOMO–LUMO energy gap and facilitates electron uptake, leading to lower overpotentials, while strongly electron-donating ligands increase the activity of the metal center, as mentioned earlier.

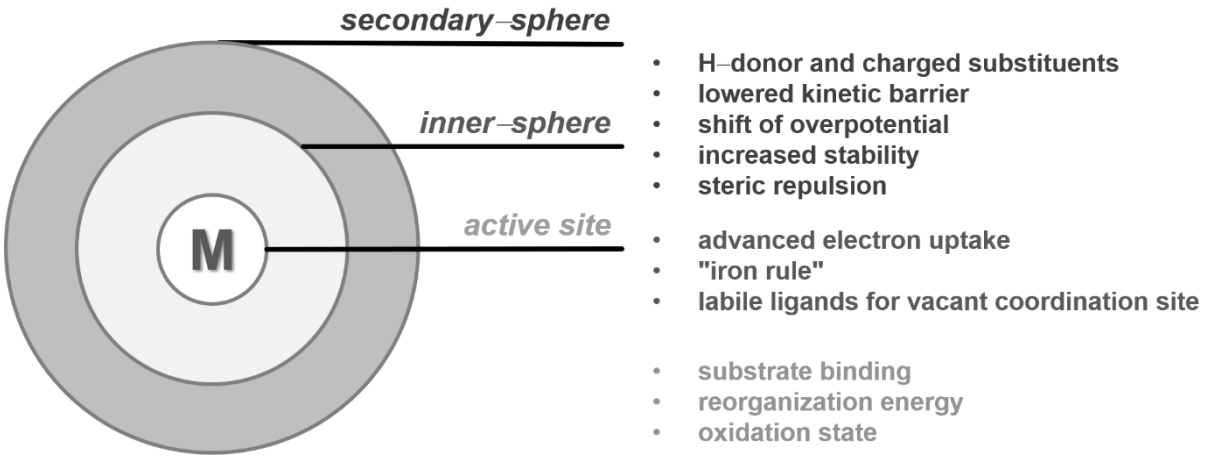

Figure 9. Schematic representation of a modular electrocatalyst.

The incorporation of a labile co-ligand, such as halides or solvent molecules, provides access to a vacant coordination site at the metal center for substrate binding. Contrary to halides, neutral ligands are easier to dissociate from the metal center under reductive conditions. As a result, electrocatalysts with neutral ligands have lower overpotentials compared to their halide-containing counterparts.[90]

A vacant coordination site can lead to the dimerization of the catalytic intermediate and consequently to a decrease in the catalytic rate. To prevent catalyst deactivation, sterically demanding substituents can be incorporated into the secondary-sphere of the ligand.[91]

In addition, the repulsive interaction of the ligand at the metal center can favor ligand dissociation of the labile co-ligand, lowering the overpotential for substrate binding and even altering the mechanism of electrocatalysis.[92]

Secondary-sphere effects have been shown to be effective in enhancing catalytic activity. Substitution of ligands with charged substituents or perfluorination of ligands lowers the overpotential of the catalyst, but the electronic changes induced by ligand substitution follows the "iron law".[89]

Another attempt is the inclusion of hydrogen bonding donor substituents. The hydrogen substrate interaction not only affects the stability and solubility of the complex, but also lowers the kinetic barrier for the substrate conversion and product selectivity.[89,90,93]

However, a strong ligand-substrate interaction in the secondary-sphere can lead to a decrease in the reaction rate, again highlighting the importance of a well-balanced interplay between the electrocatalyst and the substrate.[89]

1.3 1,2,3-Triazolylidene-based Ligands

A common motif for complexes based on transition metals are *N*–donor ligands, such as pyridine and bipyridine (**I**, **Figure 10**). The ligands exhibit both good σ −donor and π −acceptor properties, making them one of the most commonly used moieties for photocatalytic[34,39,40,44,59] and electrocatalytic applications.[20,23,91,94]

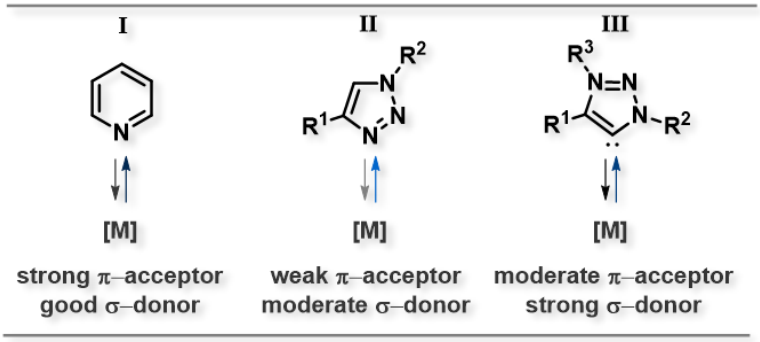

Figure 10. Relative donor/acceptor properties of the ligand classes utilized in this thesis.

Changing the type of the heterocycles that contain *N*-donors leads to new properties and has received growing interest in the field of organometallic chemistry. In particular, 1,2,3-triazoles have proven to be versatile ligands due to their modular synthesis and applicability in 'Click' chemistry (**II**, **Figure 10**).[37,39,95]

The five-membered heterocycle has a lower energy HOMO compared to pyridine, while the energy of the LUMO is higher, making it a weaker σ −donor and π −acceptor, respectively.[95]

1,2,3-Triazoles can be obtained by cycloaddition reactions of terminal alkynes and organic azides. However, thermally induced 1,3-dipolar cycloaddition (Huisgen cycloaddition) yields a mixture of the 1,4- and 1,5-regioisomers due to their similar energy profiles.[95]

In 2002, Sharpless[96] and Meldal[97] independently discovered the so-called copper(I)-catalyzed azide-alkyne cycloaddition (CuAAC), which produces exclusively the 1,4-regioisomer. The reaction proceeds under mild reaction conditions and has a very high functional group tolerance. Only three years later, Sharpless and co-workers again pioneered the development of synthetic protocol for the selective synthesis of the 1,5-regioisomer by a ruthenium-catalyzed cycloaddition.[98]

Within the same decade, an alternative synthetic protocol for the 1,5-regioisomer - the metal-free approach – was discovered, paving the way for a synthesis of a wide variety of ligand systems (**Scheme 5**).[99]

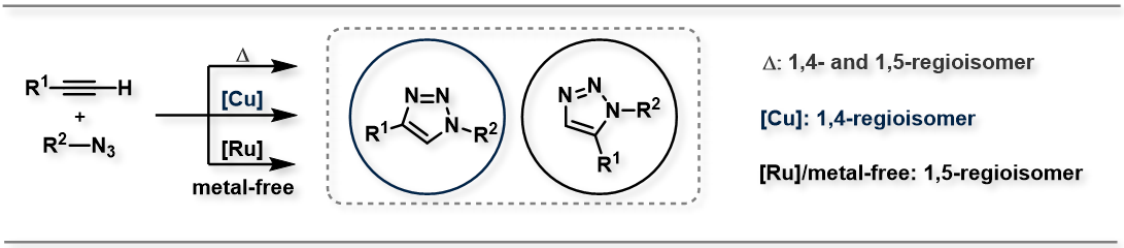

Scheme 5. Thermal and catalytic synthesis of 1,2,3-triazoles.

1,2,3-Triazoles are the most common precursor for the generation of 1,2,3-triazolylidenes (**III**, **Figure 10**), a subclass of *N*–heterocyclic carbenes (NHC). The term mesoionic carbene (MIC) or abnormal *N*–heterocyclic carbene (aNHC) was first coined by Crabtree and co-workers, who described that MICs cannot be formulated without a charge separation in their Lewis structure (**Scheme 6**).[37,39,100]

The ligand class exhibit great σ −donor properties and moderate but tunable π −acceptor capacities,[101] making them suitable candidates for wide-ranging applications, such as photochemistry,[34,37,40,102] electrocatalysis[103–107] and small molecule activation.[37]

MICs of the 1,2,3-triazolylidene type are usually accessed by alkylation[108,109] or arylation[110] of the 1,2,3-triazole at the N^3 position to generate the corresponding triazolium salt in nearly quantitative yields (**IV**, **Scheme 6**).

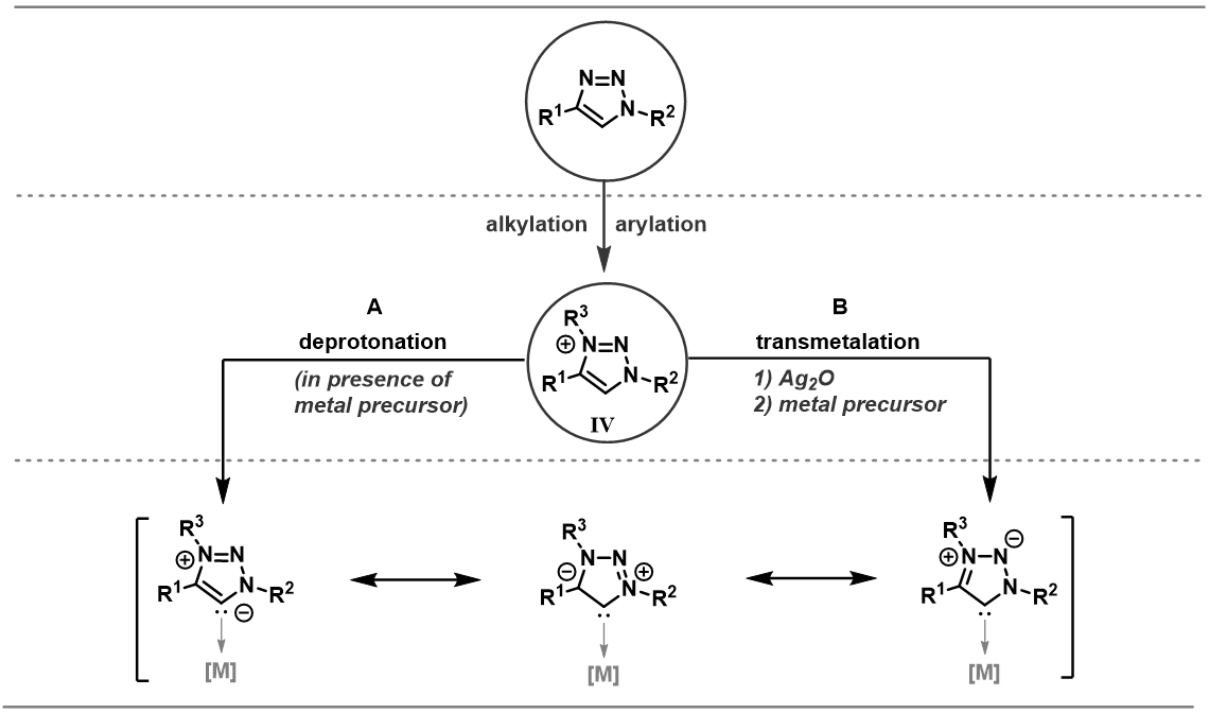

Scheme 6. Synthetic strategies to obtain MICs and possible resonance structures.

Direct deprotonation of the triazolium salt to obtain the free MIC is often accompanied by a methyl-shift from the N^3 to the C^5 atom.[108] In contrast, arylated MICs exhibit higher stability and can be stored at low temperatures under inert conditions.

A common strategy to avoid decomposition of the free MIC is the addition of a metal precursor (**A**, **Scheme 6**) after deprotonation of the triazolium salt for the *in-situ* formation of the desired transition metal complex. Alternatively, the well-established silver transmetalation route (**B**, **Scheme 6**) can be used. The *in-situ* generated silver-MIC complex can be further reacted with a metal precursor of choice under mild reaction conditions.[111]

The incorporation of MIC ligands into transition metal complexes is certainly interesting from many aspects, but the investigation of electronic properties is probably the most informative. Without the fundamental understanding of the electronic properties, structure-reactivity prediction for various (catalytic) applications would be challenging or even impossible.

Undoubtedly, Tolman's electronic parameter (TEP) is one of the milestones to probe the net donor strength of various ligands.[112] The concept of nickel phosphine complexes $[Ni(PR_3)CO)_3]$ was adapted by Gusev, by introducing the $[Ni(NHC)CO)_3]$ analogues.[113]

In 2003, the group of Crabtree reported a less-toxic alternative of the type [M(L)(CO)$_2$Br] (M = Rh, Ir) to convert the TEP to NHC-based systems using the average CO stretching frequencies as a probe for overall donor strength (**Figure 11**).[114]

Although all NHC ligands are considered fairly strong σ −donors, their MIC counterparts display even higher σ −donor properties, only surpassed by the mesoionic imidazolylidene ligands.[115]

In recent years, spectroscopic methods have emerged as a tool to differentiate between σ −donor and π −acceptor contributions of moieties. Huynh's group introduced a physical parameter named as Huynh's electronic parameter (HEP) for the determination of the σ −donor strength of the bound carbene in square planar palladium or linear gold NHC- and MIC-complexes (**Figure 11**).

The negligible π −backbonding in late transition metals facilitates the determination of the σ −donor ability of the ligand. As a result, the chemical shift of the *trans*-positioned benzimidazolylidene carbene in the ^{13}C NMR acts as an internal probe and is directly influenced by the change in electron density caused by the *trans*-influence of the ligand.

Notably, the HEPs for NHCs and MIC show a good correlation with the previously described σ −donor strength observed for the TEP.[116]

Based on these reports, Ganter and co-workers used the ^1J coupling constant of the C-H bond in the cationic NHC as an inexpensive and simple strategy to determine the σ −donor strength of the singlet carbene.[117]

Beerhues *et al*. demonstrated the spectroscopic approach for MICs which showed that the σ −donor strengths of the investigated triazoliums salts were in a similar range, irrespective of their substituents (**Figure 11**).[101]

Along this line, the group of Bertrand and Ganter introduced a method to determine the π −acceptor capacities of the ligand by ^{31}P and ^{77}Se NMR spectroscopy. The chemical shift of the main group adduct originates from the E(p_y)→E–NHC(π^*) (E = P, Se) backbonding and is in good agreement with the expected π −acceptor properties of the incorporated ligand (**Figure 11**).[117,118]

In 2020, Sarkar and co-workers investigated the mesoionic selones of the 1,2,3-triazolylidene type by ^{77}Se NMR spectroscopy. The π −acceptor ability of the corresponding MIC ligands is shown to be significantly influenced by the substituents at the N^1 and C^4 positions.[101]

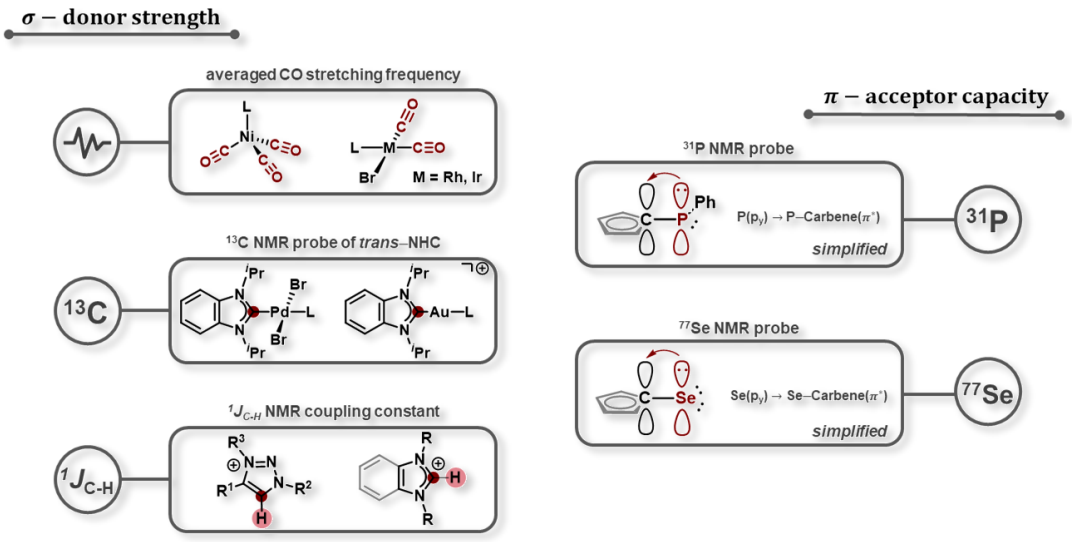

Figure 11. Spectroscopic methods for the determination of the σ −donor strength (left) and π −acceptor capacity (right) of **L** = NHC, MIC. The probe functionalities are highlighted in red.

The feasibility of incorporating a great variety of substituents on the 1,2,3-triazole and 1,2,3-triazolylidene moieties opened up a large toolbox for combining the electronic properties of each of the aforementioned classes of compounds in bi- and tridentate ligands. Despite the great developments of tridentate 1,2,3-triazole and 1,2,3-triazolylidene ligands, the following discussion will focus mainly on bidentate ligands.[37]

In 1990, Lever introduced an alternative method for determining the ligand redox properties of $Ru^{II/III}$ metal complexes using cyclic voltammetry. The ligand electrochemical parameter (LEP) describes the relative ability of ligands to stabilize a metal in a certain oxidation state and can be correlated with the overall σ −donor strength of the ligand. With the unambiguous assignment of a dominant ligand-centered reduction, the methodology can be applied to the π −acceptor capacities of the ligand. Dominantly metal-centered oxidation or ligand-centered reduction can be assigned by EPR- and IR-SEC in combination with theoretical calculations.[86]

In 2017, Suntrup *et al*. investigated *fac*-[(L–L)ReCl(CO)$_3$] complexes, bearing bidentate ligands with at least one 1,2,3-triazole (triaz) or 1,2,3-triazolylidene (MIC) containing moiety by EPR-, IR- and UV/vis/NIR-SEC, supported by DFT-calculations.[119] The results indicate a predominantly metal-centered oxidation and ligand-based reduction, which allows the determination of the σ −donor strengths by IR-spectroscopy and the π −acceptor properties by cyclic voltammetry (**Figure 12**).

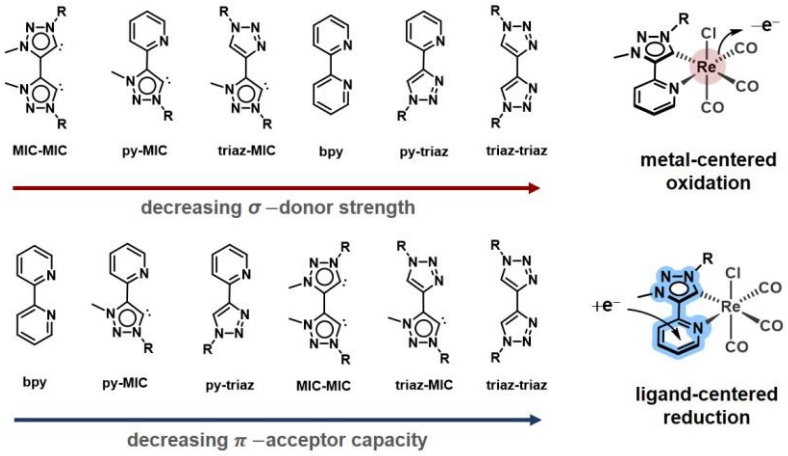

Figure 12. Comparison of σ −donor and π −acceptor properties in *fac*-[(L–L)ReCl(CO)$_3$].

Consistent with the aforementioned discussion, the incorporation of MICs drastically improved the σ −donor strength of the chelating ligands. The MIC-MIC ligand imparts greater stabilization of the oxidized metal-center, leading to an unusual reversible oxidation of the Re(I) central ion. Similar to its monodentate analogue, the triaz-triaz ligand shows the weakest σ −donor ability, followed by the well-established bpy ligand. While bpy exhibits the highest π −acceptor capacity, the triaz-triaz ligand shows the poorest π −acceptor properties among the ligands presented. Importantly, the inclusion of a pyridine ring drastically increases the π −acceptor ability of the bidentate ligands. This observation is significant in many ways, since the interplay between excellent π −acceptor and strong σ −donor properties leads to an increase in the thermal activation barrier (ΔE) of octahedral transition metal-based photocatalysts, resulting in a prolonged excited state lifetime and enhanced catalytic activity in a push-pull system (see section **1.1**).

In addition, according to the "iron law" (see section **1.2**), an increased π −acceptor ability lowers the overpotential of the electrocatalyst, while improving σ −donor strength enhances metal-substrate reactivity and hence catalytic activity.

The ideal candidate to fulfill these requirements is the pyridiyl-MIC ligand (py-MIC). The bidentate ligand combines the strong π −acceptor properties of the pyridine functionality with the excellent σ −donating ability of the MIC. The balanced synergy between the π −accepting pyridyl-moiety and the strong σ −donating MIC formed the basis for the present thesis.

1.4 Photochemistry Inspired by Mesoionic Carbenes

In the broad history of transition metal-based complexes in photochemistry, the conceptual design of the incorporated ligand has become increasingly important in recent decades due to the possibility of tailor-made tunability of the excited state properties.[34,36,40,120,121]

Mesoionic carbenes have shown to be particularly fruitful in increasing the excited state lifetimes of transition metal complexes, as their exceptional σ −donating properties are capable of increasing the ligand field strength in octahedral complexes and consequently the thermal barrier ΔE (see section **1.1**). The shift of MC states to higher energies becomes particularly important in transition metal complexes of the 3rd period, as the intrinsic weak ligand field splitting leads to a rapid population of non-radiative $^{3/5}$MC states.[34,36,40,44,121] Despite the large developments of main group adducts in photochemistry,[122] as well as in early[123] and late[124] transition metal complexes, the following discussion will focus on octahedral transition metal complexes of group 7-9 in context of this thesis.

In 2018, Wärnmark and co-workers reported an octahedral $[Fe(btz)_3]^{2+}$ (btz = 3,3-dimethyl-1,1-bis(*p*-tolyl)-4,4-bis(1,2,3-triazol-5-ylidene)) with an excellent excited-state lifetime of 528 ps (**4th generation**, **Figure 13**).[125] The complex shows a low oxidation potential of the Fe(II)/Fe(III) redox couple at −0.58 V, demonstrating significant impact of the strongly electron-donating MIC units. Indeed, the electron-rich nature of the MIC ligands enables the isolation of the oxidized $[Fe(btz)_3]^{3+}$ complex with an unusual ^{2}LMCT and an excited state lifetime of 100 ps at room temperature (**3rd generation**, **Figure 13**).[126] The oxidized Fe(III) complex shows great potential as a photooxidant with potentials of +1.5 V (^{2}LMCT) and +2.1 V (^{2}MLCT) *vs.* $Fc^{+/0}$, while the Fe(II) complex is a strong photoreductant with a potential of −1.6 V *vs.* $Fc^{+/0}$.[125,126]

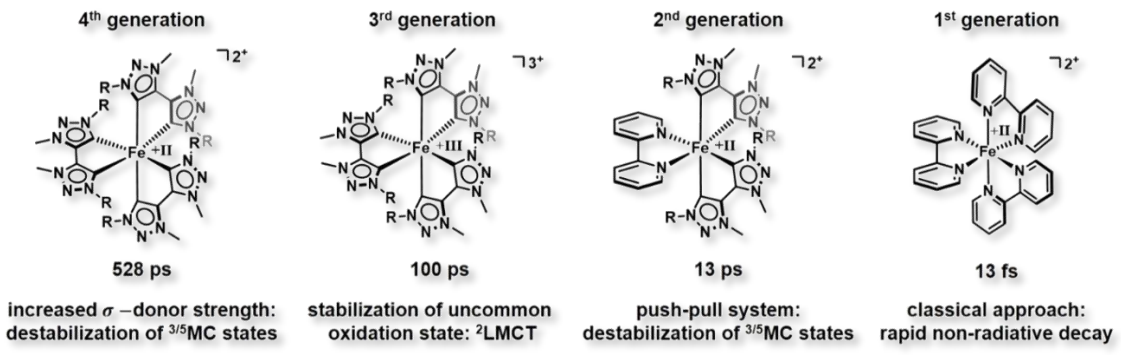

Figure 13. Recent developments in bidentate iron-MIC complexes (R = *p*-tolyl).

Replacing a btz-ligand with a π −acceptor ligand, such as bpy, leads to a push-pull system that has proven to be a key concept for enhancing the ligand field strength in various transition metal complexes.[34,40] The ^{3}MLCT excited state lifetime in $[Fe(btz)_2(bpy)]^{2+}$ (**2nd generation**, **Figure 13**)[127] could be increased by three orders of magnitude (13 ps) compared to the 'classical' $[Fe(bpy)_3]^{2+}$ complex (13 fs, **1st generation**, **Figure 13**)[128] and shows a remarkable photochemical stability in overnight laser experiments.

The photostability of transition metal complexes is often correlated with the distortion of the excited state. A common strategy to suppress excited-state distortion is to increase the structural rigidity by tridentate ligands and to expand the π −conjugation of the ligand framework. In addition, the higher symmetry of the chelating ligand optimizes the bite angle of the system, leading to increased overlap of the metal-ligand orbitals.[120]

Recently, a Fe(II) complex with two tridentate ligands containing two MIC units and a central pyridyl moiety with an extended π −system was studied photochemically (**I**, **Figure 14**). However, the tridentate ligands lead to stronger distortion of the ideal octahedral geometry compared to their bidentate counterparts, resulting in reduced ligand field splitting and excited state lifetimes ($\lambda_{ex}^{650\,nm} = 3.8–120$ ps; $\lambda_{ex}^{400\,nm} = 3.7–1910$ ps). At 400 nm, the population of an unusually long-lived dissociative ^{5}MC occurs, while excitation at 650 nm leads to the population of the ^{3}MLCT state.[129]

Photochemical investigations of Ru(II) MIC complexes are reported in great detail. Replacement of the one terpyridine ligand (tpy) with the MIC-derived pincer ligand produces a push-pull system **II** (**Figure 14**) with an excited state lifetime of $\tau > 600$ ns, 2500 times longer than observed for $[Ru(tpy)_2]^{2+}$ and similar to that reported for $[Ru(bpy)_3]^{2+}$. The ^{1}MLCT excitation is associated with the tpy ligand, whereas the ^{3}MLCT emission is attributed to the MIC ligand after the electronic redistribution during vibrational relaxation and ISC.[130]

Modification of the tpy ligand in **III**, *via* the insertion of an electron-withdrawing groups to increase the π −acceptor properties and the incorporation of long alkyl chains on the MIC-ligand, to reduce recombination reactions in dye-sensitized solar cells, leads to lifetimes of up to 410 ns (**Figure 14**).[131]

Further improvement of the MIC pincer ligand by replacing the substituents at the N^1-position of the MIC with aryl-units and extending the π −conjugation with furanyl-substituents in the para-position of the tpy ligand could drastically enhance the excited state lifetimes up to 7.9 μs (**IV**, **Figure 14**).[132]

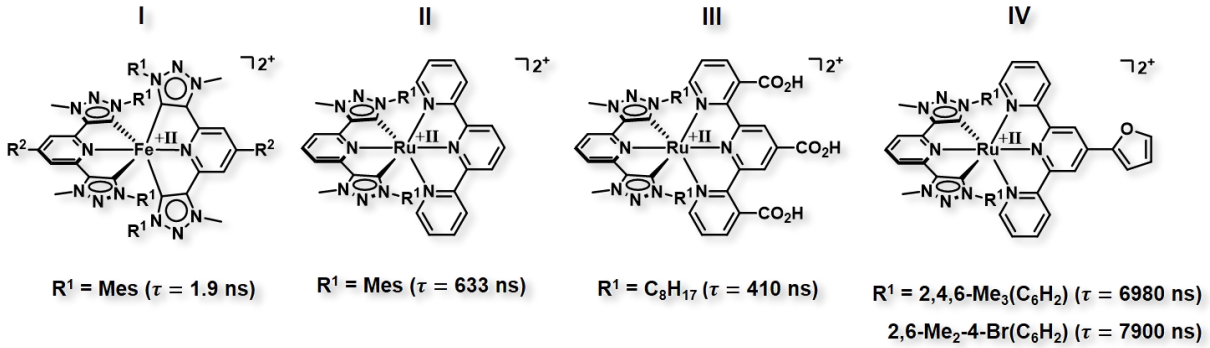

Figure 14. Excited state lifetimes of MIC-pyridyl-MIC pincer ligands in Fe(II)/Ru(II) complexes.

Ruthenium complexes with bidentate MIC ligands and their higher osmium analogues exhibit less impressive photophysical properties (**Figure 15**).[37] The excited state lifetimes usually do not exceed values of $\tau > 300$ ns and the quantum yields of 5.9% which are lower than those reported for $[Ru(bpy)_3]^{2+}$. However, natural transition orbitals analysis of $[Ru(di\text{-}MIC)(bpy)_2]^{2+}$ reveals that the Ru-bpy centered excited state can be significantly influenced by the MIC moieties.

The influence of the MIC moiety is particularly evident in the case of the photoredox properties, as observed in the Latimer diagrams of the investigated $[M(di\text{-}MIC)(bpy)_2]^{2+}$ and $[M(py\text{-}MIC)(bpy)_2]^{2+}$ complexes (M = Ru, Os). In comparison to the well-established $[M(bpy)_3]^{2+}$ (M = Ru, Os) complexes, the oxidative quenching potential ($^*E_{red}$) is increased by −400 mV after the incorporation of two MIC units, making MIC-based complexes attractive candidates for photoreductive applications.[133] Indeed, the MLCT lifetimes of the reported complexes are long enough to enable photoinduced electron transfer reactions in photocatalysis or electron injection into semiconductors.[134]

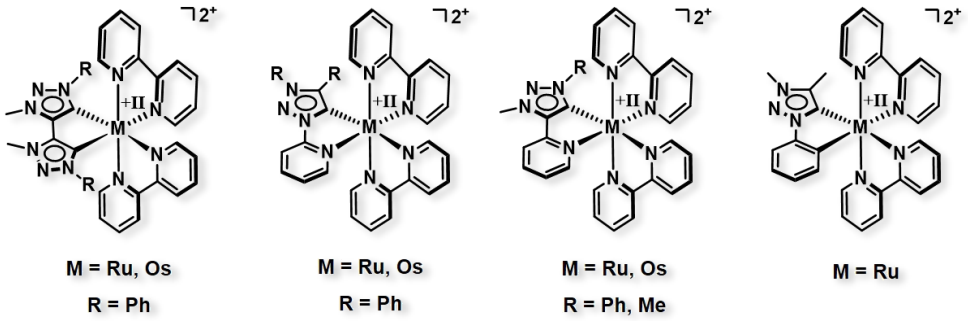

Figure 15. Investigated bidentate Ru(II) and Os(II) MIC complexes.

Iridium complexes play a prominent role in the area of photochemistry and photophysics, due to their high ligand field splitting, the large size of the d-orbitals and the higher ionic charge precluding non-emissive states and photodissociation and leading to a significant increase in excited state lifetimes. Cyclometallation of the chelating ligand, such as 2-phenylpyridine (= ppy), in $[Ir(ppy)_3]$, increases the covalency of the metal-ligand bond and contributes significantly to the metal-centered HOMO, while the LUMO is predominantly localized on the π −system of the ligand.[135]

In 2018, E. Matteucci *et al*. investigated a series of cyclometalated MIC ligands in $[Ir(L–MIC)(ppy)_2]^{0/+}$ (L = py, triaz, triazolide) as an alternative to standard chelating systems, such as 1,10-phenanthroline (= phen) and bpy (**Figure 16**). Unfortunately, the complexes $[Ir(py–MIC)(ppy)_2]^+$ and $[Ir(triaz–MIC)(ppy)_2]^+$ show very poor quantum yields of only 1% in acetonitrile. Theoretical calculations revealed that the luminescence is quenched by the lowest ^{3}MC state, leading to a reversible detachment of the metal-nitrogen bond, similar to the observations noted for the NHC counterparts.[136] In contrast, $[Ir(triazolid–MIC)(ppy)_2]$ shows quantum yields of up to 12% in acetonitrile, which could be attributed to the increased metal-triazolide bond strength. Accordingly, the beneficial bonding situation in $[Ir(triazolid–MIC)(ppy)_2]$ suppresses the non-radiative deactivation pathway *via* the dissociative ^{3}MC state.[137]

Earlier reports by Baschieri *et al*. with two py-MIC ligands and two chloride ligands in $[Ir(py–MIC)_2Cl_2]^+$ show luminescence from the LC state after excitation to the MLCT state. The replacement of the two chloride ligands by a bi-tetrazolate ligand (= bi-tetr) causes a blue shift of the emission (**Figure 16**). Both complexes exhibit quantum yields comparable to the archetypal $[Ir(ppy)_2(bpy)]^+$ and other chloride-containing Ir(III) complexes ranging from 1% to 12%.[138]

High quantum yields were obtained by Barnard and co-workers. They presented a new series of Ir(III) complexes, combining MICs with NHCs in $[Ir(NHC–MIC)(ppy)_2]^+$ (**Figure 16**). The complexes investigated showed quantum yields of up to 57%. Furthermore, preliminary studies as luminescent probes for cell imaging were also conducted, demonstrating the great potential of MIC-based Ir(III) complexes for biological applications.[139]

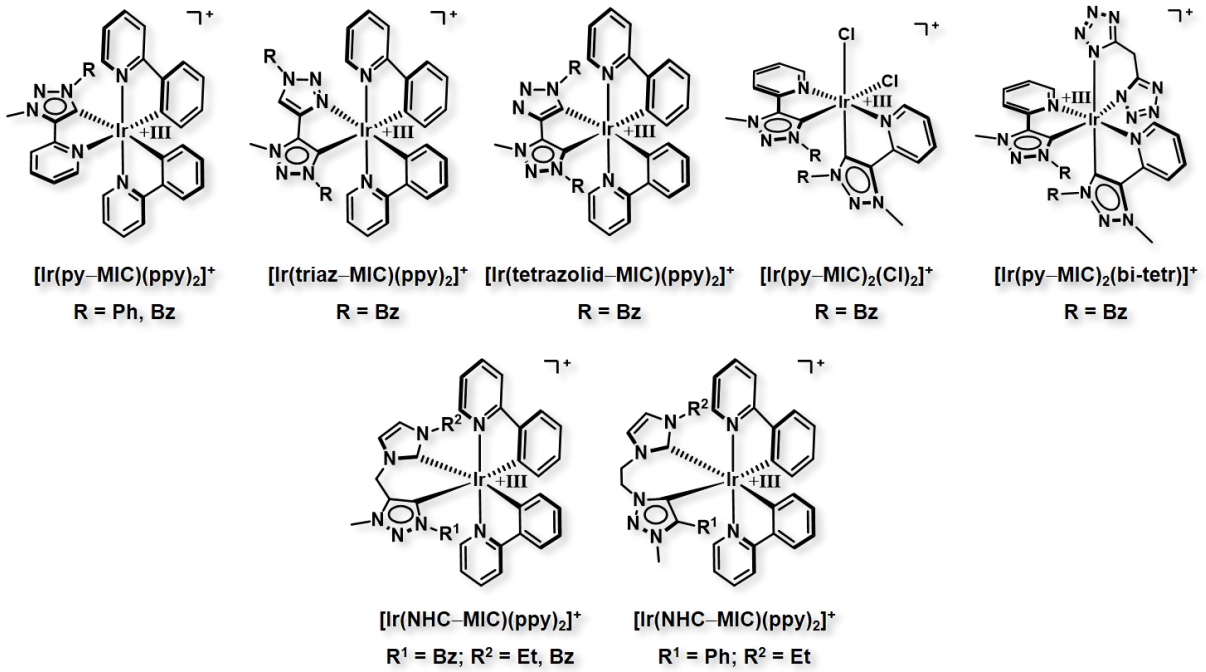

Figure 16. Selected Ir(III) complexes with MIC ligands.

Rhenium complexes of the *fac*-[Re(CO)$_3$X] (X = halide) type are excellent candidates for the photocatalytically conversion of CO_2,[140] since the metastable ^{3}MLCT state can induce the dissociation of the halide co-ligand by the thermal population of the ^{3}MC. However, the photo-induced ligand dissociation strongly depends on the excitation energy, temperature and the choice of solvent, giving access to long-lived emissive states.[141]

Recently, Suntrup *et al*. reported a series of py-MIC-based *fac*-[ReL(CO)$_3$Cl] complexes with different substituents at the N^1-positon (**Scheme 7**, section **1.5**). Irradiation at 360 nm in DMF at room temperature leads to excited state lifetimes of up to 56 ns, similar to those reported for [Re(bpy)(CO)$_3$Cl]. The insertion of the electron-donating MIC moiety shifts the emission to higher energies (550 nm) compared to the Re(I)-bpy counterpart (574 nm), demonstrating the appreciable influence of the MIC ligand.[106]

In addition, the investigated *fac*-[Re(py–MIC)(CO)$_3$Cl] complexes are catalytically active in the electrochemical conversion of CO_2 and show a high selectivity for the formation of CO under protic conditions, which will be the subject of the following section.

1.5 Recent Developments in MIC-based Electrocatalysis

Probably one of the best known molecular electrocatalysts reported so far is the so-called Lehn catalyst. The *fac*-[Re(bpy)(CO)$_3$Cl] complex shows an excellent Faradaic efficiency (FE) of 98% for the selective conversion of CO_2 to CO in a 9:1 DMF/H_2O mixture at mild potentials of –1.5 V *vs*. NHE with a turnover frequency of 21.4 h^{-1}.[142]

Nearly 40 years later, after Lehn's seminal discovery, Suntrup *et al*. investigated the analogous pyridyl-MIC *fac*-[Re(py–MIC)(CO)$_3$Cl] in electrochemical CO_2 reduction.[106] Earlier reports by the group of Sarkar and co-workers on the electronic structures of *fac*-[Re(py–MIC)(CO)$_3$Cl] allowed an in-depth characterization of the redox stability in different redox states by cyclic voltammetry, IR-, EPR- and UV/vis/NIR-SEC, combined with (TD-)DFT calculations.[119] At a later stage, IR-SEC measurements were performed in a CO_2-saturated DMF/Bu_4NPF_6 solution to obtain detailed information on the catalytic intermediates (**Scheme 7**).

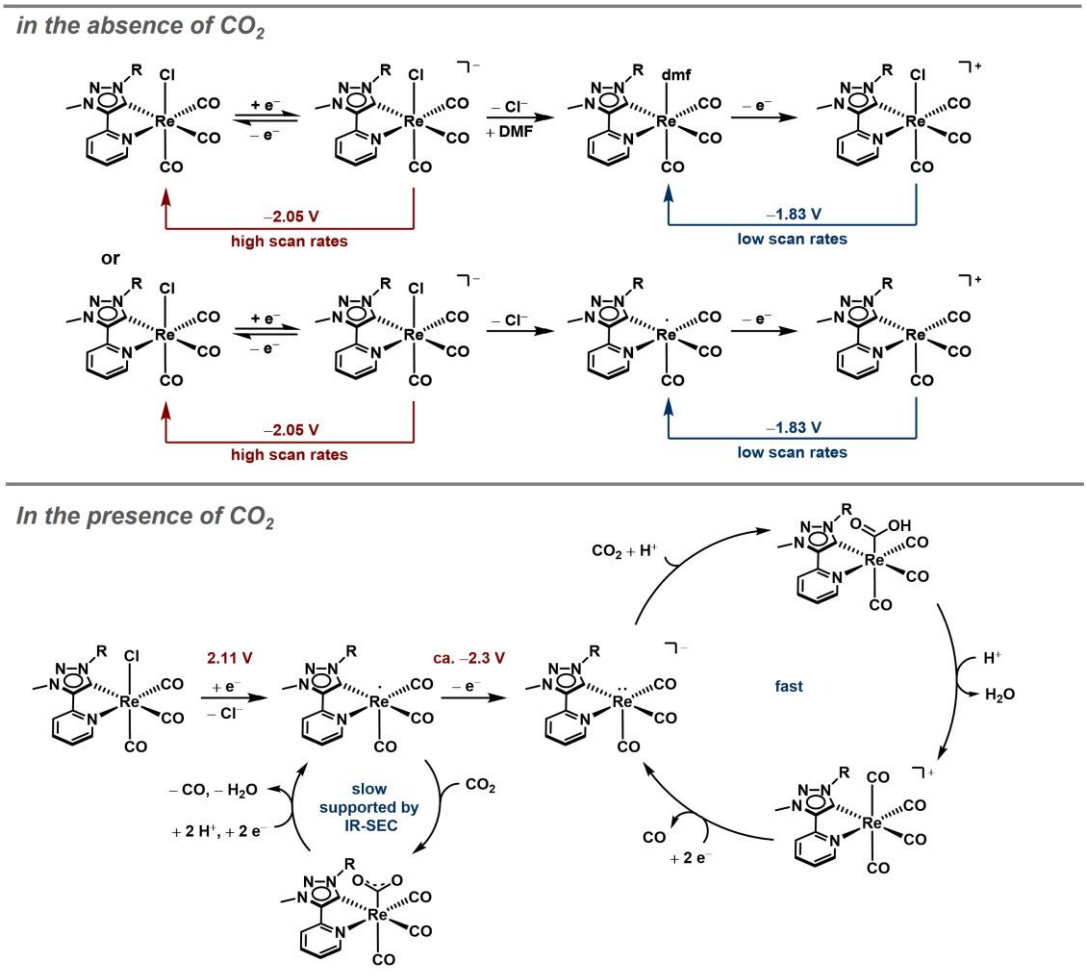

Scheme 7. Proposed pathways of *fac*-[Re(py–MIC)(CO)$_3$Cl] (R = dipp) in the absence (top, first reduction) and in the presence of CO_2 (bottom).

The first reduction was assigned to a ligand-centered reduction, as shown by the EPR-, UV/vis/NIR- and IR-SEC measurements and was further supported by TD-DFT calculations.

The scan rate dependency in cyclic voltammetry reveals an EC mechanism in the reduction, that can be attributed to the dissociation of chloride from the Re(I) metal center. Accordingly, the newly generated species detected at −1.83 V originates from either the solvent adduct *fac*-[Re(py–MIC)(CO)$_3$DMF] or the coordinatively unsaturated *fac*-[Re(py-MIC)(CO)$_3$] complex.

In addition, IR-SEC measurements supported the presence of an EC mechanism. The metal-bound CO ligands are ideal probes to provide detailed information about the electronic structure of the complexes, as their position is directly influenced by the changes in electron density. The small shift of the CO stretching frequencies of about 30 cm^{-1} to lower wavenumbers observed in *fac*-[Re(py–MIC)(CO)$_3$] indicates a ligand-centered reduction, since the increase in electron density is not directly induced by the metal center. However, prolonged electrolysis leads to dissociation of the chloride ligand, as shown by the absence of the isosbestic points and the appearance of several new CO bands.

The identification of an EC mechanism becomes particularly important in the electrochemical conversion of CO_2. Dissociation of the chloride ligand facilitates the metal-substrate interaction in *fac*-[Re(py–MIC)(CO)$_3$]. In the presence of CO_2, IR-SEC measurements showed exceptional reactivity of the singly-reduced species. In contrast to the archetypal Lehn catalyst, *fac*-[Re(py-MIC)(CO)$_3$Cl] is potentially capable of catalyzing CO_2 in a one-electron pathway without the need to generate the doubly reduced *fac*-[Re(py–MIC)(CO)$_3$]$^-$ species (two-electron pathway). The intense CO_2 band at 2338 cm^{-1} disappeared completely during the spectroelectrochemical measurement at −2.1 V *vs.* Fc/Fc$^+$ and the obtained CO bands are not identical with the aforementioned singly reduced species in the absence of CO_2. Spectral similarity was observed only after almost all CO_2 has been converted during electrolysis. The difference in the IR bands formed during the reduction in CO_2 and argon atmosphere suggests the formation of a CO_2-containing intermediate, such as *fac*-[Re(CO_2)(py–MIC)(CO)$_3$] or a CO_2-bridged dimer.[63,143] Other reactions, such as the Re-Re dimerization or the formation of the solvent adduct *fac*-[Re(py–MIC)(CO)$_3$DMF], are presumably suppressed in the presence of CO_2.

The electrochemical reduction of CO_2 was tested with two differently substituted *fac*-[Re(py–MIC)$(CO)_3$Cl] complexes in the presence and absence of methanol as a proton source in DMF at –2.3 V *vs*. Ag/$AgNO_3$. For comparison, the Lehn catalyst *fac*-[Re(bpy)$(CO)_3$Cl] was investigated under identical conditions at –1.9 V *vs*. Ag/$AgNO_3$. All complexes investigated exhibit high selectivity for the formation of CO. However, substitution at the MIC unit has a drastic effect on the catalytic activity, as indicated by the FE. The substitution with $–CH_2Ph^F$ shows a FE of only 64%, while the dipp-substituted *fac*-[Re(py–MIC)$(CO)_3$Cl] complex shows an excellent FE of 99%, outperforming the Lehn catalyst with 71% FE. The influence of the substitution at the MIC unit is also evident in the TON and TOF of the complexes studied. The fluorinated *fac*-[Re(py–MIC)$(CO)_3$Cl] complex shows a TON of 110 and a TOF of 0.03 s^{-1}, similar to the values observed for the *fac*-[Re(bpy)$(CO)_3$Cl] complex. In contrast, the dipp-substituted *fac*-[Re(py–MIC)$(CO)_3$Cl] complex shows a TON of 191 and a TOF of 0.08 s^{-1}, almost three times higher of that observed for archetypal Lehn catalyst.[106]

The groups of Piers and Royo investigated the lower homologues with the constitutional pyridyl-MIC isomers of the *fac*-[Mn(py–MIC)$(CO)_3$Br] type. In addition, Royo and co-workers studied the influence of the chelating ligand by replacing the pyridyl *N*-heterocycle with a 1,2,3-trizole and a MIC moiety in *fac*-[Mn(MIC–MIC)$(CO)_3$Br] and *fac*-[Mn(triaz–MIC)$(CO)_3$Br] (**Figure 17**).[104,105]

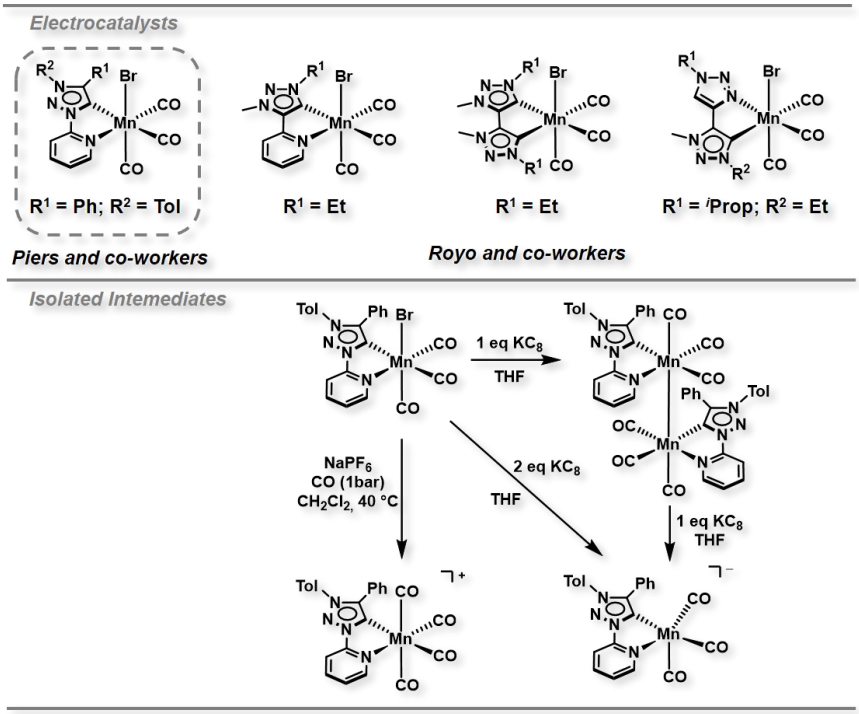

Figure 17. Investigated MIC-Mn(I) complexes (top) and isolated intermediates (bottom).

Manganese precatalysts are known to dimerize rapidly upon one-electron reduction.[144] The dimer itself can react catalytically by cleaving the Mn–Mn bond and subsequent insertion of CO_2.[145] However, dimerization of the Mn(0) species leads to an increase in the overpotential.[91,146] A common strategy to suppress dimerization is to incorporate bulky substituents near the metal center to slow the rate of dimerization and consequently to reduce the overpotential.

The electrocatalysts are extremely photosensitive because of the weak ligand field splitting, leading to rapid CO dissociation, as previously discussed in section **1.4**. The insertion of strongly σ −donating ligands, such as MICs facilitate the compensation of the electron deficiency of the formally oxidized metal center and increases the ligand field splitting, which is essential for the stability of the electrocatalyst.[147]

In the series of *fac*-[Mn(L)$(CO)_3$Br] complexes investigated by Royo and co-workers, only moderate catalytic activity was observed for the electrochemical reduction of CO_2 in MeCN and in the presence of H_2O. The low efficiency was attributed to the electrodeposition of the catalysts during the electrolysis experiment. The highest FE was observed for the *fac*-[Mn(MIC–MIC)$(CO)_3$Br] complex with 70%.

In contrast, Piers and co-workers investigated the C^{py}–N^{MIC} linked constitutional isomer and demonstrated that the *fac*-[Mn(py–MIC)$(CO)_3$Br] complex is robust under the experimental conditions and can operate at two well-separated potentials (ΔE = 400 mV) for electrochemical CO_2 reduction.[105]

In the low operating regime at −1.54 V, CO_2 is converted by a Mn(0) species to CO and CO_3^{2-} at a maximum rate of 7 s^{-1} for nearly 30.7 hours. The product analysis at a higher potential of −1.94 V displays the selective formation of CO and H_2O with a TOF of 200 s^{-1}. The catalytically active species was assigned to the *fac*-[Mn(py–MIC)$(CO)_3]^-$ species. However, the operating time is limited to 6.7 hours, which demonstrates the synergy in the structure-reactivity relationship of the electrocatalyst used.

The isolation of various predicted intermediates, such as the Mn–Mn dimer, the cationic *fac*-[Mn(py–MIC)$(CO)_4]^+$ complex and the two-electron reduced species, allowed an in-depth (spectro-)electrochemical analysis of the (pre-)catalytic activation pathway at the different operating potentials (**Scheme 8**).

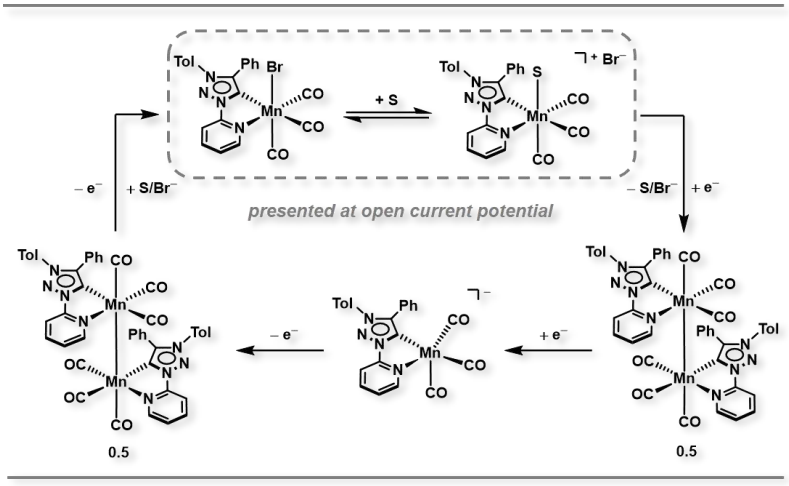

Scheme 8. Illustration of the redox chemistry in the *fac*-[Mn(py–MIC)(CO)$_3$Br] complex based on isolated intermediates (adapted from Piers and co-workers).[105]

Cyclic voltammetry *fac*-[Mn(py–MIC)(CO)$_3$Br] reveals rich redox chemistry. In particular, the cyclic voltammogram in MeCN shows a 120 mV shift in the first reduction ($E_{pc,1}$ = –1.57 V) to a more anodic potential compared to the cyclic voltammogram recorded in DMF ($E_{pc,1}$ = –1.69 V), indicating a rapid halide/solvent dissociation in MeCN. Accordingly, the first reduction can be assigned to the halide/solvent dissociation of the *fac*-[Mn(py–MIC)(CO)$_3$Br] and/or *fac*-[Mn(py–MIC)(CO)$_3$S] complex (S = MeCN, DMF), leading to the radical Mn(0) species.

The radical Mn(0) species can undergo rapid dimerization to the Mn–Mn complex. Electrochemical investigation of the isolated dimer confirmed this observation, as indicated by the consistent reduction potential at –1.87 V, leading to the monoanionic complex [Mn(py–MIC)(CO)$_3$]$^-$. Reverse anodic scan leads to the formation of the Mn(0) radical species, followed by subsequent dimerization.

Finally, oxidation of the dimer leads to the formation of the solvent adduct *fac*-[Mn(py–MIC)(CO)$_3$S] (S = MeCN, DMF) or the respective starting complex *fac*-[Mn(py–MIC)(CO)$_3$Br] in the presence of an excess of bromide.

IR-SEC in the presence of CO_2 and a proton source indicated the formation of CO and carbonates at lower reduction potentials, which was further confirmed by the precipitation of $MgCO_3$ after prolonged electrolysis.

In contrast, electrolysis at higher potentials shows selective formation of CO and H_2O *via* an EECC mechanism, yielding *fac*-[Mn(py–MIC)(CO)$_4$] after the consumption of CO_2, as mentioned earlier.

The exceptional properties of the pyridyl-MIC ligand were also investigated by Sarkar and co-workers in the electrochemical H^+ reduction with a $[Co(Cp^*)(py–MIC)Cl]^+$ complex (**Scheme 9**). The complex exhibits a low overpotential (130 mV) and a TOF of $4 \cdot 10^2\ s^{-1}$ with a glassy carbon electrode. The TON was determined at about 650 000 during the 30 min bulk electrolysis experiment and the Co(III) complex shows remarkable stability towards acidic acid due to the unique robustness of the metal-MIC bond. On basis of the electrochemical data, a (catalytic) mechanism was proposed.[107]

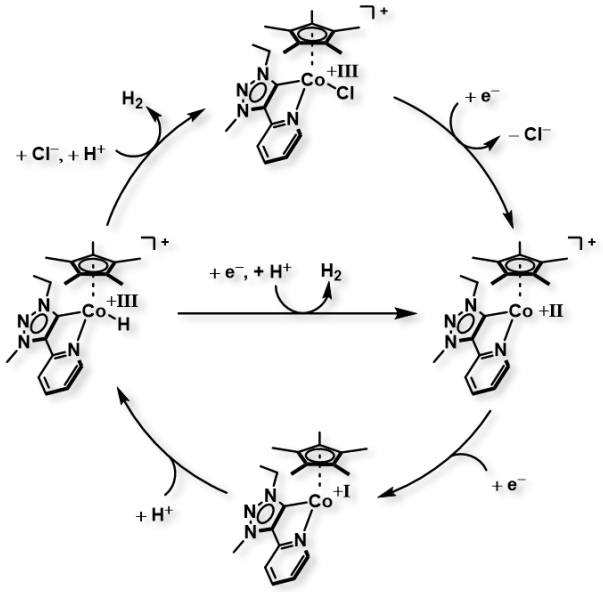

Scheme 9. Proposed mechanism for electrochemical H^+ reduction for a Co(III)-MIC catalyst.[107]

Upon reduction, an electron-transfer/chemical reaction (EC) mechanism, accompanied by dissociation of the chloride ligand, is proposed. Similar observations have been made for $[Co(Cp^*)(bpy)Cl]^+$ complexes.[148] The first reduction at –1.1 V vs. Fc/Fc^+ is metal-centered, as indicated by the similar potential for the investigated Co(III) MIC–MIC and triaz–py counterparts. The second reduction shifts according to the π –acceptor capacities of the ligands, indicating a 'non-innocent' nature of the ligand, followed by an electron density distribution to produce an active Co(I) metal center. In the presence of a proton source, the formation of a Co(III)-hydride species is postulated, which can facilitate dihydrogen formation by a proton-coupled electron transfer (PCET) to the Co(II) species or regeneration of the starting complex after chloride coordination. The electrochemical studies revealed first-order dependence on the catalyst and a second-order for acetic acid, further corroborating the proposed mechanism.

References

[1] Nobel Prize Outreach AB 2023, "Carolyn Bertozzi – Facts – 2022", can be found under https://www.nobelprize.org/prizes/chemistry/2022/bertozzi/interview/, **2023**.

[2] a) N. Armaroli, V. Balzani, *Energy for a Sustainable World*. *From the Oil Age to a Sun-Powered Future*, Wiley-VCH, Weinheim, Germany, **2011**; b) T. B. Johansson, *Global Energy Assessment*. *Toward a Sustainable Future*, Cambridge Univ. Press, Cambridge, **2012**.

[3] J. Lelieveld, A. Pozzer, U. Pöschl, M. Fnais, A. Haines, T. Münzel, *Cardiovasc. Res.* **2020**, *116*, 1910–1917.

[4] a) M. Dittmar, *Energy* **2012**, *37*, 35–40; b) J. W. Eerkens, *The Nuclear Imperative*, Springer, Dordrecht, **2010**; c) R. Wengenmayr, *Renewable Energy*. *Sustainable Concepts for the Energy Change*, Wiley-VCH, Weinheim, **2013**.

[5] A. Kumar, P. Daw, D. Milstein, *Chem. Rev.* **2022**, *122*, 385–441.

[6] K. Sordakis, C. Tang, L. K. Vogt, H. Junge, P. J. Dyson, M. Beller, G. Laurenczy, *Chem. Rev.* **2018**, *118*, 372–433.

[7] B. Milani, G. Licini, E. Clot, M. Albrecht, *Dalton Trans.* **2016**, *45*, 14419–14420.

[8] P. W. Roesky, A. R. Fout, *Inorg. Chem.* **2021**, *60*, 13757–13758.

[9] R. Poli, *Comments Inorg. Chem.* **2009**, *30*, 177–228.

[10] M. Y. Darensbourg, A. Llobet, *Inorg. Chem.* **2016**, *55*, 371–377.

[11] a) N. Lehnert, J. C. Peters, *Inorg. Chem.* **2015**, *54*, 9229–9233; b) S. Amanullah, P. Saha, A. Nayek, M. E. Ahmed, A. Dey, *Chem. Soc. Rev.* **2021**, *50*, 3755–3823; c) C. W. Koo, A. C. Rosenzweig, *Chem. Soc. Rev.* **2021**, *50*, 3424–3436; d) N. Lehnert, B. W. Musselman, L. C. Seefeldt, *Chem. Soc. Rev.* **2021**, *50*, 3640–3646; e) C. J. Reed, Q. N. Lam, E. N. Mirts, Y. Lu, *Chem. Soc. Rev.* **2021**, *50*, 2486–2539; f) X.-P. Zhang, A. Chandra, Y.-M. Lee, R. Cao, K. Ray, W. Nam, *Chem. Soc. Rev.* **2021**, *50*, 4804–4811; g) M. R. A. Blomberg, *Chem. Soc. Rev.* **2020**, *49*, 7301–7330.

[12] F. Meyer, W. B. Tolman, *Inorg. Chem.* **2015**, *54*, 5039.

[13] a) G. T. Babcock, M. Wikström, *Nature* **1992**, *356*, 301–309; b) A. J. Gow, H. Ischiropoulos, *J. Cell Physiol.* **2001**, *187*, 277–282; c) M. Wikström, V. Sharma, V. R. I. Kaila, J. P. Hosler, G. Hummer, *Chem. Rev.* **2015**, *115*, 2196–2221.

[14] J. Barber, P. D. Tran, *J. R. Soc. Interface* **2013**, *10*, 20120984.

[15] a) C. Descorme, P. Gallezot, C. Geantet, C. George, *ChemCatChem* **2012**, *4*, 1897–1906; b) I. Fechete, Y. Wang, J. C. Védrine, *Catal.* **2012**, *189*, 2–27; c) X. Jiang, X. Nie, X. Guo, C.

Song, J. G. Chen, *Chem. Rev.* **2020**, *120*, 7984–8034; d) J. M. Thomas, *ChemSusChem* **2014**, *7*, 1801–1832; e) S. Liu, M. Wang, Q. Cheng, Y. He, J. Ni, J. Liu, C. Yan, T. Qian, *ACS Nano* **2022**, *16*, 17911–17930.

[16] a) D. Ar, A. F. R. Kilpatrick, B. Cula, C. Herwig, C. Limberg, *Inorg. Chem.* **2021**, *60*, 13844–13853; b) L. Chen, G. Chen, C.-F. Leung, C. Cometto, M. Robert, T.-C. Lau, *Chem. Soc. Rev.* **2020**, *49*, 7271–7283; c) M. Gennari, C. Duboc, *Acc. Chem. Res.* **2020**, *53*, 2753–2761; d) R. Latifi, T. D. Palluccio, W. Ye, J. L. Minnick, K. S. Glinton, E. V. Rybak-Akimova, S. P. de Visser, L. Tahsini, *Inorg. Chem.* **2021**, *60*, 13821–13832; e) L. C. Lewis, H. S. Shafaat, *Inorg. Chem.* **2021**, *60*, 13869–13875; f) Q. Liang, J. C. DeMuth, A. Radović, N. J. Wolford, M. L. Neidig, D. Song, *Inorg. Chem.* **2021**, *60*, 13811–13820; g) M. Springborg, J.-O. Joswig (Eds.) *Chemical Modelling*, Royal Society of Chemistry, Cambridge, **2019**; h) J. I. van der Vlugt, *Eur. J. Inorg. Chem.* **2012**, *2012*, 363–375; i) R. L. Meyer, P. Miró, W. W. Brennessel, E. M. Matson, *Inorg. Chem.* **2021**, *60*, 13833–13843.

[17] F. Möller, S. Piontek, R. G. Miller, U.-P. Apfel, *Chem. Eur. J.* **2018**, *24*, 1471–1493.

[18] L. Lindh, P. Chábera, N. W. Rosemann, J. Uhlig, K. Wärnmark, A. Yartsev, V. Sundström, P. Persson, *Catalysts* **2020**, *10*, 315.

[19] a) Y. Wang, H. Suzuki, J. Xie, O. Tomita, D. J. Martin, M. Higashi, D. Kong, R. Abe, J. Tang, *Chem. Rev.* **2018**, *118*, 5201–5241; b) Y. Yao, X. Gao, Z. Li, X. Meng, *Catalysts* **2020**, *10*, 335.

[20] D.-M. Feng, Y.-P. Zhu, P. Chen, T.-Y. Ma, *Catalysts* **2017**, *7*, 373.

[21] a) C. Finn, S. Schnittger, L. J. Yellowlees, J. B. Love, *Chem. Commun.* **2012**, *48*, 1392–1399; b) N. Kaeffer, W. Leitner, *JACS Au* **2022**, *2*, 1266–1289; c) C. Tang, Y. Zheng, M. Jaroniec, S.-Z. Qiao, *Angew. Chem. Int. Ed. Engl.* **2021**, *60*, 19572–19590; d) X. Yin, J. R. Moss, *Coord. Chem. Rev.* **1999**, *181*, 27–59; e) L.-H. Zhang, S. Mathew, J. Hessels, J. N. H. Reek, F. Yu, *ChemSusChem* **2021**, *14*, 234–250; f) R. Zhang, J. J. Warren, *ChemSusChem* **2021**, *14*, 293–302.

[22] W.-H. Wang, Y. Himeda, J. T. Muckerman, G. F. Manbeck, E. Fujita, *Chem. Rev.* **2015**, *115*, 12936–12973.

[23] R. Francke, B. Schille, M. Roemelt, *Chem. Rev.* **2018**, *118*, 4631–4701.

[24] a) M. E. Ali, M. M. Rahman, S. M. Sarkar, S. B. A. Hamid, *J. Nanomater.* **2014**, *2014*, 1–23; b) A. Z. Fadhel, P. Pollet, C. L. Liotta, C. A. Eckert, *Molecules* **2010**, *15*, 8400–8424.

[25] A. J. Esswein, D. G. Nocera, *Chem. Rev.* **2007**, *107*, 4022–4047.

[26] T. Stoll, C. E. Castillo, M. Kayanuma, M. Sandroni, C. Daniel, F. Odobel, J. Fortage, M.-N. Collomb, *Coord. Chem. Rev.* **2015**, *304-305*, 20–37.

[27] G. Knör, *Coord. Chem. Rev.* **2015**, *304-305*, 102–108.

[28] K. P. S. Cheung, S. Sarkar, V. Gevorgyan, *Chem. Rev.* **2022**, *122*, 1543–1625.

[29] L. Guillemard, J. Wencel-Delord, *Beilstein J. Org. Chem.* **2020**, *16*, 1754–1804.

[30] a) C. K. Prier, D. A. Rankic, D. W. C. MacMillan, *Chem. Rev.* **2013**, *113*, 5322–5363; b) D. M. Schultz, T. P. Yoon, *Science* **2014**, *343*, 1239176; c) F. Strieth-Kalthoff, F. Glorius, *Chem* **2020**, *6*, 1888–1903.

[31] J.-H. Shon, T. S. Teets, *Comments Inorg. Chem.* **2020**, *40*, 53–85.

[32] B. O'Regan, M. Grätzel, *Nature* **1991**, *353*, 737–740.

[33] a) R. Ham, C. J. Nielsen, S. Pullen, J. N. H. Reek, *Chem. Rev.* **2023**, *9*, 5225–5261; b) M. Schulz, M. Karnahl, M. Schwalbe, J. G. Vos, *Coord. Chem. Rev.* **2012**, *256*, 1682–1705; c) H. Kumagai, Y. Tamaki, O. Ishitani, *Acc. Chem. Res.* **2022**, *55*, 978–990.

[34] C. Förster, K. Heinze, *Chem. Soc. Rev.* **2020**, *49*, 1057–1070.

[35] S. Treiling, C. Wang, C. Förster, F. Reichenauer, J. Kalmbach, P. Boden, J. P. Harris, L. M. Carrella, E. Rentschler, U. Resch-Genger, C. Reber, M. Seitz, M. Gerhards, K. Heinze, *Angew. Chem. Int. Ed. Engl.* **2019**, *58*, 18075–18085.

[36] C. Wegeberg, O. S. Wenger, *JACS Au* **2021**, *1*, 1860–1876.

[37] R. Maity, B. Sarkar, *JACS Au* **2022**, *2*, 22–57.

[38] P. A. Scattergood, A. Sinopoli, P. I. Elliott, *Coord. Chem. Rev.* **2017**, *350*, 136–154.

[39] D. Schweinfurth, L. Hettmanczyk, L. Suntrup, B. Sarkar, *Z. Anorg. Allg. Chem.* **2017**, *643*, 554–584.

[40] O. S. Wenger, *Chem. Eur. J.* **2019**, *25*, 6043–6052.

[41] a) R. Costa E Silva, L. Da Oliveira Silva, A. de Andrade Bartolomeu, T. J. Brocksom, K. T. de Oliveira, *Beilstein J. Org. Chem.* **2020**, *16*, 917–955; b) V. N. Gopalakrishnan, J. Becerra, E. F. Pena, M. Sakar, F. Béland, T.-O. Do, *Green Chem.* **2021**, *23*, 8332–8360; c) J. Min Park, J. H. Lee, W.-D. Jang, *Coord. Chem. Rev.* **2020**, *407*, 213157; d) E. Nikoloudakis, I. López-Duarte, G. Charalambidis, K. Ladomenou, M. Ince, A. G. Coutsolelos, *Chem. Soc. Rev.* **2022**, *51*, 6965–7045.

[42] V. Balzani, P. Ceroni, A. Juris, *Photochemistry and Photophysics*. *Concepts, Research, Applications*, Wiley-VCH, Weinheim, Germany, **2014**.

[43] P. S. Wagenknecht, P. C. Ford, *Coord. Chem. Rev.* **2011**, *255*, 591–616.

[44] J. K. McCusker, *Science* **2019**, *363*, 484–488.

[45] S. Mukherjee, D. E. Torres, E. Jakubikova, *Chem. Sci.* **2017**, *8*, 8115–8126.

[46] W. Gawelda, M. Johnson, F. M. F. de Groot, R. Abela, C. Bressler, M. Chergui, *J. Am. Chem. Soc.* **2006**, *128*, 5001–5009.

[47] L. Schmid, C. Kerzig, A. Prescimone, O. S. Wenger, *JACS Au* **2021**, *1*, 819–832.

[48] T. P. Silverstein, *J. Chem. Educ.* **2012**, *89*, 1159–1167.

[49] S. H. Lin, *J. Chem. Phys.* **1970**, *53*, 3766–3767.

[50] T. P. Yoon, M. A. Ischay, J. Du, *Nat. Chem.* **2010**, *2*, 527–532.

[51] a) J. W. Beatty, C. R. J. Stephenson, *Acc. Chem. Res.* **2015**, *48*, 1474–1484; b) E. B. Corcoran, M. T. Pirnot, S. Lin, S. D. Dreher, D. A. DiRocco, I. W. Davies, S. L. Buchwald, D. W. C. MacMillan, *Science* **2016**, *353*, 279–283; c) J. J. Devery, J. D. Nguyen, C. Dai, C. R. J. Stephenson, *ACS Catal.* **2016**, *6*, 5962–5967; d) J. A. Kautzky, T. Wang, R. W. Evans, D. W. C. MacMillan, *J. Am. Chem. Soc.* **2018**, *140*, 6522–6526; e) H. Kim, C. Lee, *Angew. Chem. Int. Ed. Engl.* **2012**, *51*, 12303–12306; f) C. Le, T. Q. Chen, T. Liang, P. Zhang, D. W. C. MacMillan, *Science* **2018**, *360*, 1010–1014; g) J. D. Nguyen, E. M. D'Amato, J. M. R. Narayanam, C. R. J. Stephenson, *Nat. Chem.* **2012**, *4*, 854–859; h) P. Zhang, C. C. Le, D. W. C. MacMillan, *J. Am. Chem. Soc.* **2016**, *138*, 8084–8087.

[52] S. Cai, X. Zhao, X. Wang, Q. Liu, Z. Li, D. Z. Wang, *Angew. Chem. Int. Ed. Engl.* **2012**, *51*, 8050–8053.

[53] a) Y. Cheng, J. Yang, Y. Qu, P. Li, *Org. Lett.* **2012**, *14*, 98–101; b) A. McNally, C. K. Prier, D. W. C. MacMillan, *Science* **2011**, *334*, 1114–1117.

[54] S. Maity, M. Zhu, R. S. Shinabery, N. Zheng, *Angew. Chem. Int. Ed. Engl.* **2012**, *51*, 222–226.

[55] X. Pan, N. Malhotra, J. Zhang, K. Matyjaszewski, *Macromolecules* **2015**, *48*, 6948–6954.

[56] C. Pac, M. Ihama, M. Yasuda, Y. Miyauchi, H. Sakurai, *J. Am. Chem. Soc.* **1981**, *103*, 6495–6497.

[57] a) J. Du, T. P. Yoon, *J. Am. Chem. Soc.* **2009**, *131*, 14604–14605; b) S. Lin, M. A. Ischay, C. G. Fry, T. P. Yoon, *J. Am. Chem. Soc.* **2011**, *133*, 19350–19353; c) E. L. Tyson, E. P. Farney, T. P. Yoon, *Org. Lett.* **2012**, *14*, 1110–1113.

[58] a) P. V. Pham, D. A. Nagib, D. W. C. MacMillan, *Angew. Chem. Int. Ed. Engl.* **2011**, *50*, 6119–6122; b) N. Iqbal, J. Jung, S. Park, E. J. Cho, *Angew. Chem.* **2014**, *126*, 549–552.

[59] C. Bachmann, M. Guttentag, B. Spingler, R. Alberto, *Inorg. Chem.* **2013**, *52*, 6055–6061.

[60] a) P. Du, J. Schneider, F. Li, W. Zhao, U. Patel, F. N. Castellano, R. Eisenberg, *J. Am. Chem. Soc.* **2008**, *130*, 5056–5058; b) J. I. Goldsmith, W. R. Hudson, M. S. Lowry, T. H. Anderson, S. Bernhard, *J. Am. Chem. Soc.* **2005**, *127*, 7502–7510; c) Z. Han, F. Qiu, R. Eisenberg, P. L.

Holland, T. D. Krauss, *Science* **2012**, *338*, 1321–1324; d) S. Metz, S. Bernhard, *Chem. Commun.* **2010**, *46*, 7551–7553; e) A. Petronilho, J. A. Woods, S. Bernhard, M. Albrecht, *Eur. J. Inorg. Chem.* **2014**, *2014*, 708–714; f) T. S. Teets, D. G. Nocera, *Chem. Commun.* **2011**, *47*, 9268–9274; g) J. Torres, M. C. Carrión, J. Leal, F. A. Jalón, J. V. Cuevas, A. M. Rodríguez, G. Castañeda, B. R. Manzano, *Inorg. Chem.* **2018**, *57*, 970–984; h) D. R. Whang, K. Sakai, S. Y. Park, *Angew. Chem. Int. Ed. Engl.* **2013**, *52*, 11612–11615; i) J. A. Woods, R. Lalrempuia, A. Petronilho, N. D. McDaniel, H. Müller-Bunz, M. Albrecht, S. Bernhard, *Energy Environ. Sci.* **2014**, *7*, 2316–2328; j) Z.-T. Yu, Y.-J. Yuan, J.-G. Cai, Z.-G. Zou, *Chem. Eur. J.* **2013**, *19*, 1303–1310.

[61] L. Chen, Z. Guo, X.-G. Wei, C. Gallenkamp, J. Bonin, E. Anxolabéhère-Mallart, K.-C. Lau, T.-C. Lau, M. Robert, *J. Am. Chem. Soc.* **2015**, *137*, 10918–10921.

[62] a) P. L. Cheung, C. W. Machan, A. Y. S. Malkhasian, J. Agarwal, C. P. Kubiak, *Inorg. Chem.* **2016**, *55*, 3192–3198; b) A. Genoni, D. N. Chirdon, M. Boniolo, A. Sartorel, S. Bernhard, M. Bonchio, *ACS Catal.* **2017**, *7*, 154–160; c) H. Takeda, C. Cometto, O. Ishitani, M. Robert, *ACS Catal.* **2017**, *7*, 70–88; d) V. S. Thoi, N. Kornienko, C. G. Margarit, P. Yang, C. J. Chang, *J. Am. Chem. Soc.* **2013**, *135*, 14413–14424.

[63] A. J. Morris, G. J. Meyer, E. Fujita, *Acc. Chem. Res.* **2009**, *42*, 1983–1994.

[64] a) B. P. Fors, C. J. Hawker, *Angew. Chem. Int. Ed. Engl.* **2012**, *51*, 8850–8853; b) Q. Yang, F. Dumur, F. Morlet-Savary, J. Poly, J. Lalevée, *Macromolecules* **2015**, *48*, 1972–1980.

[65] a) I. Bosque, G. Magallanes, M. Rigoulet, M. D. Kärkäs, C. R. J. Stephenson, *ACS Cent. Sci.* **2017**, *3*, 621–628; b) M. D. Kärkäs, B. S. Matsuura, T. M. Monos, G. Magallanes, C. R. J. Stephenson, *Org. Biomol. Chem.* **2016**, *14*, 1853–1914; c) C. Li, X. Zhao, A. Wang, G. W. Huber, T. Zhang, *Chem. Rev.* **2015**, *115*, 11559–11624; d) J. D. Nguyen, B. S. Matsuura, C. R. J. Stephenson, *J. Am. Chem. Soc.* **2014**, *136*, 1218–1221; e) J. D. Nguyen, B. Reiss, C. Dai, C. R. J. Stephenson, *Chem. Commun.* **2013**, *49*, 4352–4354; f) J. Zhang, X. Jiang, X. Ye, L. Chen, Q. Lu, X. Wang, C. Dong, *J. Therm. Anal. Calorim.* **2016**, *123*, 501–510.

[66] R. J. Detz, J. N. H. Reek, B. C. C. van der Zwaan, *Energy Environ. Sci.* **2018**, *11*, 1653–1669.

[67] D. L. DuBois, *Inorg. Chem.* **2014**, *53*, 3935–3960.

[68] K. J. Lee, B. D. McCarthy, J. L. Dempsey, *Chem. Soc. Rev.* **2019**, *48*, 2927–2945.

[69] a) A. M. Appel, M. L. Helm, *ACS Catal.* **2014**, *4*, 630–633; b) C. Costentin, M. Robert, J.-M. Savéant, *Chem. Soc. Rev.* **2013**, *42*, 2423–2436; c) E. S. Rountree, B. D. McCarthy, T. T. Eisenhart, J. L. Dempsey, *Inorg. Chem.* **2014**, *53*, 9983–10002; d) J.-M. Savéant, *Elements*

of Molecular and Biomolecular Electrochemistry, John Wiley & Sons, Inc, Hoboken, NJ, USA, **2006**; e) J.-M. Savéant, *Chem. Rev.* **2008**, *108*, 2348–2378; f) J.-M. Savéant, *Energy Environ. Sci.* **2012**, *5*, 7718.

[70] J. M. Savéant, K. B. Su, *J. Electroanal. Chem.* **1984**, *171*, 341–349.

[71] G. M. Jacobsen, J. Y. Yang, B. Twamley, A. D. Wilson, R. M. Bullock, M. Rakowski DuBois, D. L. DuBois, *Energy Environ. Sci.* **2008**, *1*, 167.

[72] E. S. Rountree, D. J. Martin, B. D. McCarthy, J. L. Dempsey, *ACS Catal.* **2016**, *6*, 3326–3335.

[73] A. Houmam, E. M. Hamed, I. W. J. Still, *J. Am. Chem. Soc.* **2003**, *125*, 7258–7265.

[74] M. Fang, M. H. Engelhard, Z. Zhu, M. L. Helm, J. A. S. Roberts, *ACS Catal.* **2014**, *4*, 90–98.

[75] E. Anxolabéhère-Mallart, C. Costentin, M. Fournier, S. Nowak, M. Robert, J.-M. Savéant, *J. Am. Chem. Soc.* **2012**, *134*, 6104–6107.

[76] N. Kaeffer, A. Morozan, J. Fize, E. Martinez, L. Guetaz, V. Artero, *ACS Catal.* **2016**, *6*, 3727–3737.

[77] D. J. Martin, B. D. McCarthy, C. L. Donley, J. L. Dempsey, *Chem. Commun.* **2015**, *51*, 5290–5293.

[78] V. Artero, M. Fontecave, *Chem. Soc. Rev.* **2013**, *42*, 2338–2356.

[79] J. A. Widegren, R. G. Finke, *J. Mol. Catal. A Chem.* **2003**, *198*, 317–341.

[80] Bard, Faulkner, White, *Electrochemical Methods*. *Fundamentals and Applications*, Wiley & Sons, Hoboken, **2022**.

[81] B. D. McCarthy, C. L. Donley, J. L. Dempsey, *Chem. Sci.* **2015**, *6*, 2827–2834.

[82] N. D. Schley, J. D. Blakemore, N. K. Subbaiyan, C. D. Incarvito, F. D'Souza, R. H. Crabtree, G. W. Brudvig, *J. Am. Chem. Soc.* **2011**, *133*, 10473–10481.

[83] a) S. M. Barnett, K. I. Goldberg, J. M. Mayer, *Nat. Chem.* **2012**, *4*, 498–502; b) R. H. Crabtree, *Chem. Rev.* **2015**, *115*, 127–150; c) D. J. Martin, B. D. McCarthy, N. A. Piro, J. L. Dempsey, *Polyhedron* **2016**, *114*, 200–204.

[84] L. Chen, G. Chen, C.-F. Leung, S.-M. Yiu, C.-C. Ko, E. Anxolabéhère-Mallart, M. Robert, T.-C. Lau, *ACS Catal.* **2015**, *5*, 356–364.

[85] S. Best, A. Crumbliss, S. Dhungana, L. Dunsch, M.-A. Haga, F. Hartl, W. Kaim, A. Klein, C. Kubiak, P. Murray, C. Salsman, R. Winter, L. Yellowlees, *Spectroelectrochemistry*, Royal Society of Chemistry, Cambridge, **2008**.

[86] W. Kaim, J. Fiedler, *Chem. Soc. Rev.* **2009**, *38*, 3373.

[87] A. M. Bond, *Broadening Electrochemical Horizons*. *Principles and Illustrations of Voltammetric and Related Techniques*, Oxford University Press, New York, **2002**.

[88] B. Das, A. Thapper, S. Ott, S. B. Colbran, *Sustain. Energy Fuels* **2019**, *3*, 2159–2175.

[89] C. Costentin, J.-M. Savéant, *Nat. Rev. Chem.* **2017**, *11*, 1–8.

[90] C. Jiang, A. W. Nichols, C. W. Machan, *Dalton Trans.* **2019**, *48*, 9454–9468.

[91] M. D. Sampson, A. D. Nguyen, K. A. Grice, C. E. Moore, A. L. Rheingold, C. P. Kubiak, *J. Am. Chem. Soc.* **2014**, *136*, 5460–5471.

[92] B. A. Johnson, S. Maji, H. Agarwala, T. A. White, E. Mijangos, S. Ott, *Angew. Chem. Int. Ed. Engl.* **2016**, *55*, 1825–1829.

[93] C. Hou, J. Jiang, S. Zhang, G. Wang, Z. Zhang, Z. Ke, C. Zhao, *ACS Catal.* **2014**, *4*, 2990–2997.

[94] a) M. L. Clark, K. A. Grice, C. E. Moore, A. L. Rheingold, C. P. Kubiak, *Chem. Sci.* **2014**, *5*, 1894–1900; b) J. D. Blakemore, E. S. Hernandez, W. Sattler, B. M. Hunter, L. M. Henling, B. S. Brunschwig, H. B. Gray, *Polyhedron* **2014**, *84*, 14–18; c) S. I. Johnson, H. B. Gray, J. D. Blakemore, W. A. Goddard, *Inorg. Chem.* **2017**, *56*, 11375–11386.

[95] B. Schulze, U. S. Schubert, *Chem. Soc. Rev.* **2014**, *43*, 2522–2571.

[96] V. V. Rostovtsev, L. G. Green, V. V. Fokin, K. B. Sharpless, *Angew. Chem.* **2002**, *114*, 2708–2711.

[97] C. W. Tornøe, C. Christensen, M. Meldal, *J. Org. Chem.* **2002**, *67*, 3057–3064.

[98] L. Zhang, X. Chen, P. Xue, H. H. Y. Sun, I. D. Williams, K. B. Sharpless, V. V. Fokin, G. Jia, *J. Am. Chem. Soc.* **2005**, *127*, 15998–15999.

[99] a) S. W. Kwok, J. R. Fotsing, R. J. Fraser, V. O. Rodionov, V. V. Fokin, *Org. Lett.* **2010**, *12*, 4217–4219; b) Z. Monasterio, A. Irastorza, J. I. Miranda, J. M. Aizpurua, *Org. Lett.* **2016**, *18*, 2511–2514; c) Y.-C. Wang, Y.-Y. Xie, H.-E. Qu, H.-S. Wang, Y.-M. Pan, F.-P. Huang, *J. Org. Chem.* **2014**, *79*, 4463–4469.

[100] a) R. H. Crabtree, *Coord. Chem. Rev.* **2013**, *257*, 755–766; b) Á. Vivancos, C. Segarra, M. Albrecht, *Chem. Rev.* **2018**, *118*, 9493–9586.

[101] J. Beerhues, H. Aberhan, T.-N. Streit, B. Sarkar, *Organometallics* **2020**, *39*, 4557–4564.

[102] B. Sarkar, L. Suntrup, *Angew. Chem. Int. Ed. Engl.* **2017**, *56*, 8938–8940.

[103] S. Bertini, M. Rahaman, A. Dutta, P. Schollhammer, A. V. Rudnev, F. Gloaguen, P. Broekmann, M. Albrecht, *Green Chem.* **2021**, *23*, 3365–3373.

[104] S. Friães, S. Realista, C. S. B. Gomes, P. N. Martinho, B. Royo, *Molecules* **2021**, *26*.

[105] T. Scherpf, C. R. Carr, L. J. Donnelly, Z. S. Dubrawski, B. S. Gelfand, W. E. Piers, *Inorg. Chem.* **2022**, *61*, 13644–13656.

[106] L. Suntrup, F. Stein, J. Klein, A. Wilting, F. G. L. Parlane, C. M. Brown, J. Fiedler, C. P. Berlinguette, I. Siewert, B. Sarkar, *Inorg. Chem.* **2020**, *59*, 4215–4227.

[107] M. van der Meer, E. Glais, I. Siewert, B. Sarkar, *Angew. Chem. Int. Ed. Engl.* **2015**, *54*, 13792–13795.

[108] G. Guisado-Barrios, J. Bouffard, B. Donnadieu, G. Bertrand, *Angew. Chem. Int. Ed. Engl.* **2010**, *49*, 4759–4762.

[109] P. Mathew, A. Neels, M. Albrecht, *J. Am. Chem. Soc.* **2008**, *130*, 13534–13535.

[110] a) T. Lv, Z. Wang, J. You, J. Lan, G. Gao, *J. Org. Chem.* **2013**, *78*, 5723–5730; b) M. Virant, J. Košmrlj, *J. Org. Chem.* **2019**, *84*, 14030–14044.

[111] L. Suntrup, M. Kleoff, B. Sarkar, *Dalton Trans.* **2018**, *47*, 7992–8002.

[112] C. A. Tolman, *Chem. Rev.* **1977**, *77*, 313–348.

[113] D. G. Gusev, *Organometallics* **2009**, *28*, 6458–6461.

[114] A. R. Chianese, X. Li, M. C. Janzen, J. W. Faller, R. H. Crabtree, *Organometallics* **2003**, *22*, 1663–1667.

[115] H. V. Huynh, *Chem. Rev.* **2018**, *118*, 9457–9492.

[116] a) Q. Teng, H. V. Huynh, *Dalton Trans.* **2017**, *46*, 614–627; b) D. Yuan, H. V. Huynh, *Organometallics* **2012**, *31*, 405–412.

[117] K. Verlinden, H. Buhl, W. Frank, C. Ganter, *Eur. J. Inorg. Chem.* **2015**, *2015*, 2416–2425.

[118] a) O. Back, M. Henry-Ellinger, C. D. Martin, D. Martin, G. Bertrand, *Angew. Chem. Int. Ed. Engl.* **2013**, *52*, 2939–2943; b) S. V. C. Vummaleti, D. J. Nelson, A. Poater, A. Gómez-Suárez, D. B. Cordes, A. M. Z. Slawin, S. P. Nolan, L. Cavallo, *Chem. Sci.* **2015**, *6*, 1895–1904.

[119] L. Suntrup, S. Klenk, J. Klein, S. Sobottka, B. Sarkar, *Inorg. Chem.* **2017**, *56*, 5771–5783.

[120] N. Sinha, O. S. Wenger, *J. Am. Chem. Soc.* **2023**, *145*, 4903–4920.

[121] O. S. Wenger, *J. Am. Chem. Soc.* **2018**, *140*, 13522–13533.

[122] P. Pinter, C. M. Schüßlbauer, F. A. Watt, N. Dickmann, R. Herbst-Irmer, B. Morgenstern, A. Grünwald, T. Ullrich, M. Zimmer, S. Hohloch, D. M. Guldi, D. Munz, *Chem. Sci.* **2021**, *12*, 7401–7410.

[123] T. Maulbetsch, D. Kunz, *Angew. Chem. Int. Ed. Engl.* **2021**, *60*, 2007–2012.

[124] a) L. Cao, S. Huang, W. Liu, H. Zhao, X.-G. Xiong, J.-P. Zhang, L.-M. Fu, X. Yan, *Chem. Eur. J.* **2020**, *26*, 17222–17229; b) L. Hettmanczyk, S. J. P. Spall, S. Klenk, M. van der Meer, S. Hohloch, J. A. Weinstein, B. Sarkar, *Eur. J. Inorg. Chem.* **2017**, *2017*, 2112–2121; c) G. Kleinhans, A. K.-W. Chan, M.-Y. Leung, D. C. Liles, M. A. Fernandes, V. W.-W. Yam, I. Fernández, D. I. Bezuidenhout, *Chem. Eur. J.* **2020**, *26*, 6993–6998; d) M. Monticelli, M. Baron, C. Tubaro, S. Bellemin-Laponnaz, C. Graiff, G. Bottaro, L. Armelao, L. Orian, *ACS omega* **2019**, *4*, 4192–4205; e) A. R. Naziruddin, C.-S. Lee, W.-J. Lin, B.-J. Sun, K.-H. Chao, A. H. H. Chang, W.-S. Hwang, *Dalton Trans.* **2016**, *45*, 5848–5859; f) J. Soellner, T. Strassner, *Chem. Eur. J.* **2018**, *24*, 5584–5590; g) J. Soellner, T. Strassner, *ChemPhotoChem* **2019**, *3*, 554–558; h) S. K. Verma, P. Kumari, S. N. Ansari, M. O. Ansari, D. Deori, S. M. Mobin, *Dalton Trans.* **2018**, *47*, 15646–15650; i) Á. Vivancos, D. Bautista, P. González-Herrero, *Chem. Eur. J.* **2019**, *25*, 6014–6025.

[125] P. Chábera, K. S. Kjaer, O. Prakash, A. Honarfar, Y. Liu, L. A. Fredin, T. C. B. Harlang, S. Lidin, J. Uhlig, V. Sundström, R. Lomoth, P. Persson, K. Wärnmark, *J. Phys. Chem. Lett.* **2018**, *9*, 459–463.

[126] P. Chábera, Y. Liu, O. Prakash, E. Thyrhaug, A. E. Nahhas, A. Honarfar, S. Essén, L. A. Fredin, T. C. B. Harlang, K. S. Kjær, K. Handrup, F. Ericson, H. Tatsuno, K. Morgan, J. Schnadt, L. Häggström, T. Ericsson, A. Sobkowiak, S. Lidin, P. Huang, S. Styring, J. Uhlig, J. Bendix, R. Lomoth, V. Sundström, P. Persson, K. Wärnmark, *Nature* **2017**, *543*, 695–699.

[127] Y. Liu, K. S. Kjaer, L. A. Fredin, P. Chábera, T. Harlang, S. E. Canton, S. Lidin, J. Zhang, R. Lomoth, K.-E. Bergquist, P. Persson, K. Wärnmark, V. Sundström, *Chem. Eur. J.* **2015**, *21*, 3628–3639.

[128] G. Auböck, M. Chergui, *Nat. Chem.* **2015**, *7*, 629–633.

[129] S. S. Nair, O. A. Bysewski, S. Kupfer, M. Wächtler, A. Winter, U. S. Schubert, B. Dietzek, *Inorg. Chem.* **2021**, *60*, 9157–9173.

[130] B. Schulze, D. Escudero, C. Friebe, R. Siebert, H. Görls, U. Köhn, E. Altuntas, A. Baumgaertel, M. D. Hager, A. Winter, B. Dietzek, J. Popp, L. González, U. S. Schubert, *Chem. Eur. J.* **2011**, *17*, 5494–5498.

[131] S. Sinn, B. Schulze, C. Friebe, D. G. Brown, M. Jäger, E. Altuntaş, J. Kübel, O. Guntner, C. P. Berlinguette, B. Dietzek, U. S. Schubert, *Inorg. Chem.* **2014**, *53*, 2083–2095.

[132] D. G. Brown, N. Sanguantrakun, B. Schulze, U. S. Schubert, C. P. Berlinguette, *J. Am. Chem. Soc.* **2012**, *134*, 12354–12357.

[133] L. Suntrup, F. Stein, G. Hermann, M. Kleoff, M. Kuss-Petermann, J. Klein, O. S. Wenger, J. C. Tremblay, B. Sarkar, *Inorg. Chem.* **2018**, *57*, 13973–13984.

[134] F. Cao, G. Oskam, G. J. Meyer, P. C. Searson, *J. Phys. Chem.* **1996**, *100*, 17021–17027.

[135] F. Monti, A. Baschieri, L. Sambri, N. Armaroli, *Acc. Chem. Res.* **2021**, *54*, 1492–1505.

[136] F. Kessler, R. D. Costa, D. Di Censo, R. Scopelliti, E. Ortí, H. J. Bolink, S. Meier, W. Sarfert, M. Grätzel, M. K. Nazeeruddin, E. Baranoff, *Dalton Trans.* **2012**, *41*, 180–191.

[137] E. Matteucci, F. Monti, R. Mazzoni, A. Baschieri, C. Bizzarri, L. Sambri, *Inorg. Chem.* **2018**, *57*, 11673–11686.

[138] A. Baschieri, F. Monti, E. Matteucci, A. Mazzanti, A. Barbieri, N. Armaroli, L. Sambri, *Inorg. Chem.* **2016**, *55*, 7912–7919.

[139] R. E. Karmis, S. Carrara, A. A. Baxter, C. F. Hogan, M. D. Hulett, P. J. Barnard, *Dalton Trans.* **2019**, *48*, 9998–10010.

[140] H. Takeda, K. Koike, H. Inoue, O. Ishitani, *J. Am. Chem. Soc.* **2008**, *130*, 2023–2031.

[141] S. Sato, O. Ishitani, *Coord. Chem. Rev.* **2015**, *282-283*, 50–59.

[142] J. Hawecker, J.-M. Lehn, R. Ziessel, *J. Chem. Soc., Chem. Commun.* **1984**, 328–330.

[143] J. Agarwal, E. Fujita, H. F. Schaefer, J. T. Muckerman, *J. Am. Chem. Soc.* **2012**, *134*, 5180–5186.

[144] a) D. C. Grills, J. A. Farrington, B. H. Layne, S. V. Lymar, B. A. Mello, J. M. Preses, J. F. Wishart, *J. Am. Chem. Soc.* **2014**, *136*, 5563–5566; b) C. Riplinger, M. D. Sampson, A. M. Ritzmann, C. P. Kubiak, E. A. Carter, *J. Am. Chem. Soc.* **2014**, *136*, 16285–16298.

[145] a) M. Bourrez, M. Orio, F. Molton, H. Vezin, C. Duboc, A. Deronzier, S. Chardon-Noblat, *Angew. Chem. Int. Ed. Engl.* **2014**, *53*, 240–243; b) G. Neri, P. M. Donaldson, A. J. Cowan, *Phys. Chem. Chem. Phys.* **2019**, *21*, 7389–7397.

[146] M. D. Sampson, C. P. Kubiak, *J. Am. Chem. Soc.* **2016**, *138*, 1386–1393.

[147] a) W. C. Henke, C. J. Otolski, W. N. G. Moore, C. G. Elles, J. D. Blakemore, *Inorg. Chem.* **2020**, *59*, 2178–2187; b) H.-Y. Kuo, T. S. Lee, A. T. Chu, S. E. Tignor, G. D. Scholes, A. B. Bocarsly, *Dalton Trans.* **2019**, *48*, 1226–1236.

[148] W. Kaim, R. Reinhardt, E. Waldhör, J. Fiedler, *J. Organomet. Chem.* **1996**, *524*, 195–202.

2 Scope of this Thesis

1,2,3-Triazolylidenes (= MIC) and in particular mesoionic carbenes with a pyridyl-moiety have proven as excellent candidates to fulfill the synergy between strongly σ −donating and excellent π −accepting properties to tune the photophysical properties of transition metal complexes and to improve the stability and activity of potential electrocatalysts. Given the scope of the thesis, the impact of bidentate pyridyl-MIC ligands compared to classical polypyridine ligands, such as bpy and diamine ligands, is repeatedly highlighted to provide detailed insights into the structure-reactivity relationship in different transition metal complexes for the potential activation of small molecules based on (spectro-)electrochemical, theoretical and photophysical methods. In a more profound context, the effects of two constitutional isomers (C–N *vs*. C–C), which have received less attention in the field of photo- and electrocatalysis, are discussed (**Figure 18**).

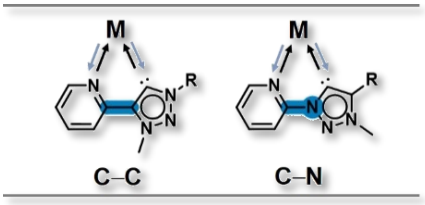

Figure 18. Investigated constitutional isomers of the pyridyl-MIC type.

In the first part (Chapter 3.2), the electrochemical and photophysical properties of a new Ru(II) polypyridine series are discussed. The successive replacement of a bpy ligand by a pyridyl-MIC ligand in $[Ru(bpy)_3]^{2+}$ leads to new excited-state properties for potential photocatalytic applications. (Spectro-)electrochemical investigations, supported by theoretical calculations, provide detailed insights into the different redox state properties concerning the total number of incorporated MICs in such systems (**Figure 19**).

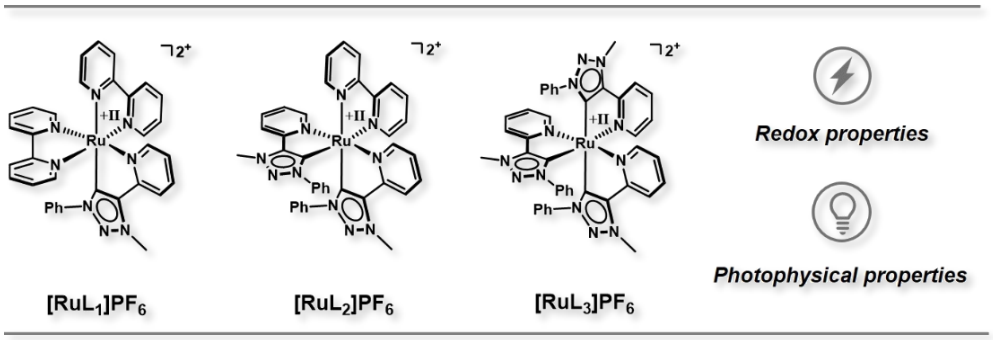

Figure 19. Pyridyl–MIC Ru(II) polypyridine complexes as potential photocatalysts.

In analogy to the well-established Lehn-type catalyst, the isostructural and isoelectronic group 6 carbonyl complexes bearing a bidentate ligand are attractive candidates for the electrochemical conversion of CO_2 and exhibit exciting photochemical properties. The incorporation of two constitutional isomers in $[M(py–MIC)(CO)_4]$ (M = Cr, Mo, W) offers the opportunity to investigate not only the potential application as an electrocatalyst for electrochemical CO_2 reduction but also the photophysical properties and photochemical reactivity in view of the different connectivity in the pyridyl–MIC ligand (**Figure 20,** Chapters 3.3–3.6).

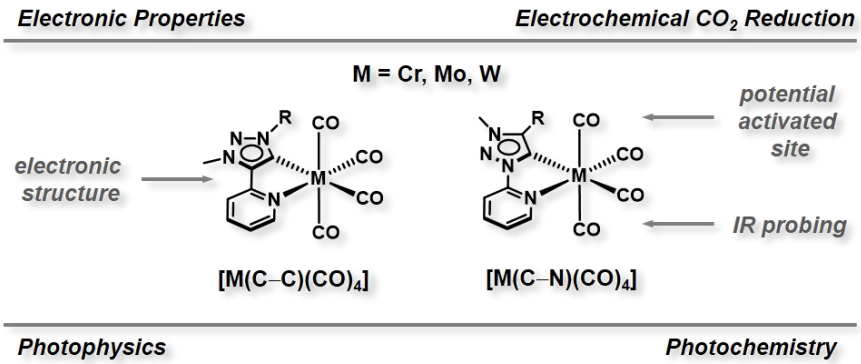

Figure 20. $[M(py–MIC)(CO)_4]$ (M = Cr, Mo, W) complexes as a model system for electronic properties, potential electrocatalysis and photochemical investigations.

The pyridyl-MIC ligand has been shown to significantly enhance the catalytic activity in electrochemical proton reduction with Co(III) half-sandwich complexes. However, the mechanism of this reaction is still debated. In the present thesis, a detailed mechanistic study of the precatalytic activation of the corresponding pyridyl-MIC Rh(III) complexes (Chapter 3.7) for the electrochemical proton reduction is discussed using (spectro-)electrochemistry and theoretical methods (**Figure 21**).

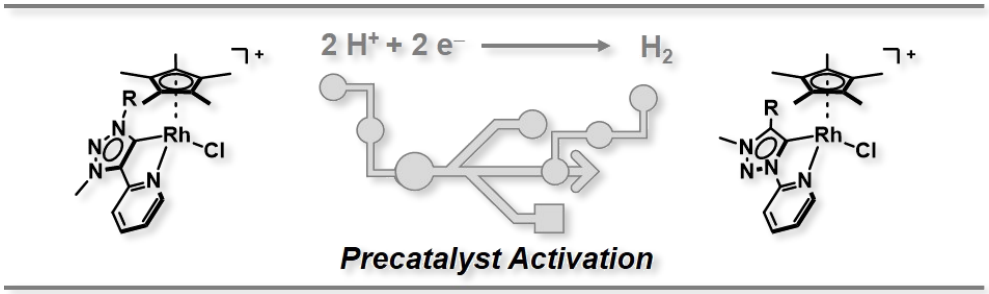

Figure 21. Rh(III) pyridyl-MIC complexes used for the mechanistic studies on the precatalytically activation in electrochemical proton reduction.

3 Results & Discussion

3.1 Summary and Conclusion

Undoubtedly, nature represents the most efficient homogeneous catalysts in highly structurally defined, selective and robust enzymes for the conversion of small molecules at ambient conditions. The unique synergy between structural complexity and reactivity has motivated scientists all around the globe to mimic the tremendous and exceptional performance of enzymes in organometallic chemistry. However, it is difficult to realize the well-defined enzymatic structures and extensive environment for a homogeneous catalyst in an industrial approach operating under mild conditions. New strategies have been developed to enhance the performance of homogeneous catalysts at low energy costs and widely accessible synthetic methods.

The utilizing of external triggers, such as light or electric sources, activate homogeneous precatalysts and generates the highly reactive catalytic active species without using sacrificial additives. Homogeneous catalysts that take advantage of such external stimuli are referred to as photo- or electrocatalysts. Their catalytic performance strongly depends on their structural confinement. Therefore, it is no surprise that a well-defined ligand design plays a crucial role in creating efficient and robust photo- and/or electrocatalysts.

In recent decades, various strategies in the conceptual ligand design of new and highly reactive photo- and electrocatalysts have been discovered. Homogeneous photocatalysts, for instance, have shown outperforming lifetimes and quantum yields by combining strong π −acceptor ligands with highly σ −donating ligands, despite the fact that each of the ligand classes itself shows a great impact on the photophysical properties in octahedral transition metal complexes. The strong π −acceptor properties of the ligand energetically stabilize the so-called metal-to-ligand charge transfer ($^{1/3}$MLCT) excited states, while highly σ −donating ligands destabilize the metal-centered (MC) states, which are prone to undergo non-radiative decay of the photochemical excited states.

The synergy between good π −acceptor ligands and strong σ −donating ligands is also represented in the so-called "iron law" for electrocatalysts. Ideal electrocatalysts should be highly efficient, robust and capable of performing the substrate conversion at mild over-potentials.

Increasing the π −acceptor capacity of the ligand system in reductive processes leads to low operating potential, but the decreased electron density at the metal center results in a limited catalytic rate. On the other hand, incorporating electron-rich ligands manifests an increased catalytic conversion, but the corresponding electrocatalyst operates at higher potentials and is consequently less attractive in terms of total energy costs.

A simple, yet powerful strategy to overcome the "iron law" in electrocatalysis is to combine good π −acceptor capacities with high σ −donor properties in a single bidentate ligand.

An excellent candidate to fulfill the criteria for a good photo- and electrocatalyst is the pyridyl–1,2,3-triazolylidene ligand (py–MIC). The insertion of a pyridyl moiety drastically increases the π −acceptor properties of the strong electron-donating mesoionic carbene (MIC) ligand, as earlier reported in the *fac*-[Re(py–MIC)$(CO)_3$Cl] complex. A direct comparison in the electrochemical CO_2 reduction with the well-established Lehn catalyst *fac*-[Re(bpy)$(CO)_3$Cl] revealed the great potential of the ligand system. The exchange of the bpy ligand with the strong σ −electron-donating and good π −accepting pyridyl-MIC ligand leads to enhanced catalytic performance at similar operating potentials.

Despite the great developments in the conceptual ligand design, a direct comparison of the impact of constitutional isomers in the field of photo- and electrochemistry has gained limited to no attention (**Figure 22**).

The present thesis provides insights into the electronic and photophysical influence of pyridyl-MIC ligands in potential homogeneous photo- and electrocatalytic systems. The analogy to well-established polypyridine and diamine ligands facilitates an in-depth understanding of tuning the electronic and photophysical properties based on pyridyl-MIC containing transition metal complexes.

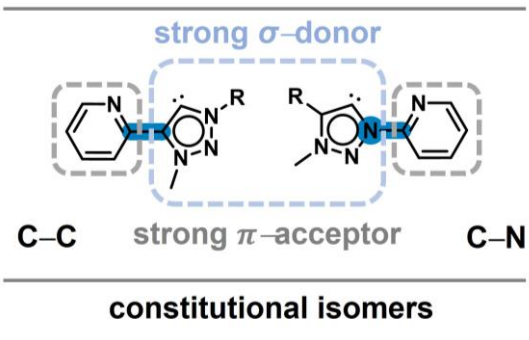

Figure 22. Ligand design for constitutional isomers of the pyridyl–1,2,3-triazolylidene type (left: **C–C** linked isomer; right: **C–N** linked isomer).

$[Ru(bpy)_3]^{2+}$ represents one of the most prominent homogeneous photocatalysts. The archetypical complex has been intensively studied with various ligand modifications, such as substitution at the ligand backbone, the extension of the π −system or the replacement of one of the bpy ligands with tailor-made ligands to enhance the photophysical properties of such systems.

Ru(II) complexes bearing strong σ −donating ligands, such as NHCs or MICs, have shown excellent photophysical properties and are well-established in photocatalytic applications. However, a systematic study based on the total number of carbenes incorporated in Ru(II) complexes with polypyridine ligands has not been investigated.

In the first part of this thesis (Chapter 3.2), a series of three new Ru(II) complexes with the **C–C** linked pyridyl–MIC ligand was synthesized and fully characterized via ^{1}H and ^{13}C NMR spectroscopy, mass spectrometry, elemental analysis and single crystal X-ray diffraction analysis. All complexes were investigated by cyclic voltammetry, EPR- and UV/vis/NIR-SEC, supported by (TD-)DFT calculations, and compared to the archetypal $[Ru(bpy)_3]^{2+}$ complex.

The successive replacement of a bpy ligand by a pyridyl–MIC ligand shifts the metal-centered oxidation by ~160 mV to more cathodic potential. The oxidation at the metal center was assigned by low-temperature EPR spectroelectrochemistry, supported by spin density calculations.

The UV/vis spectra of the native complexes showed absorption bands in the range between 300–550 nm. TD-DFT calculations assigned the electronic transitions to a metal-to-ligand-charge transfer (MLCT). Upon oxidation, the great influence of the total number of incorporated py–MIC ligands becomes particularly prominent.

Moving from the Ru(II) complex with one pyridyl-MIC ligand to the complexes bearing two and three pyridyl-MIC ligands shifted the mixed metal-ligand-to-ligand charge transfer (MLMCT) to a dominant ligand-to-metal charge transfer (LMCT) transition. The stronger σ −donating nature of the incorporated pyridyl–MIC ligands generates predominantly ligand-centered HOMO-orbitals. The presented results reveal that the HOMO-orbitals of the oxidized Ru(III) complexes can be tuned by the strong electron-donating pyridyl–MIC ligands. This observation is interesting from many perspectives, as the copper-catalyzed-alkin-azide cyclization (CuAAC) to generate the respective triazoles as precursor for the MICs allows a broad substrate scope for tailor-made tuning of the electronic properties and is not exclusively limited by the central metal atom anymore.

The extrapolation of the total number of MIC moieties incorporated in the Ru(II) complex might provide the opportunity to isolate stable Ru(III) metal complexes with exciting new photophysical properties, such as LMCT and long-lived excited states. Earlier reported by Wärnmark and co-workers showed excited state lifetimes in a homoleptic tris-(MIC–MIC) Fe(III) complex of 528 ps. The unusual Ru(III) complexes could act as strong photooxidants for photocatalytic applications with even longer excited state lifetimes.

In addition, EPR-SEC measurements and spin density calculations revealed a bpy-centered first reduction. The Ru(II) complex with only one py–MIC ligand showed an isotropic signal without any hyperfine coupling of the ^{14}N in the bpy ligand due to the energetically close-lying bpy-centered LUMO-orbitals. In contrast, the incorporation of two py–MIC ligands shows a well-defined isotropic EPR signal with hyperfine splitting of the ^{14}N at the bpy ligand. These results clearly demonstrate that the electronic properties of the Ru(II) complexes for a potential application as photocatalysts can be tuned by the right choice of the incorporated ligands.

Interestingly, the first bpy-centered reduction shifts by ~100 mV to more anodic potential after the replacement of one bpy ligand with the pyridyl-MIC ligand. The replacement of all bpy ligands by the electron-rich MIC-containing ligands leads to a shift of the first reduction up to 250 mV. The detailed electrochemical studies in combination with the transient spectroscopy and theoretical calculations allowed us to estimate the photocatalytic properties of the presented complexes.

All presented complexes showed emission spectra typical for polypyridine Ru(II) complexes in the range of 600–900 nm. Photoluminescence quantum yields $\Phi_{em} \approx 1\%$ were obtained and the excited state lifetimes were in the range between 26–344 ns. The lower photoluminescence quantum yields and excited state lifetimes τ compared to the archetypal $[Ru(bpy)_3]^{2+}$ complex are likely a consequence of the population of the metal-centered ^3MC state from the $^{1/3}MLCT$ state leading to the dissociation of one of the electron-rich pyridyl-MIC ligand arms. However, the excited state lifetimes are sufficiently long-lived enough to potentially allow photo-induced electron-transfer reactions in photocatalysis or for electron injection into semiconductors.

The calculated excited state energies E_{00} of the ^3MLCT state showed that the incorporation of the py–MIC ligands does not significantly change the relative energy of E_{00}.

Combining the reduction and oxidation potentials of the ground states with the ^{3}MLCT energies (E_{00}) allowed us to estimate the oxidative $^*E_{ox}$ and reductive $^*E_{red}$ quenching potentials for photocatalytic applications or as photosensitizers. The Latimer diagram showed that an increased number of MIC within the Ru(II) complexes decreases the photooxidative potential. However, the strong electron-donating properties of the MIC moiety generate strong photoreductants for potential photocatalytic transformations (**Figure 23**).

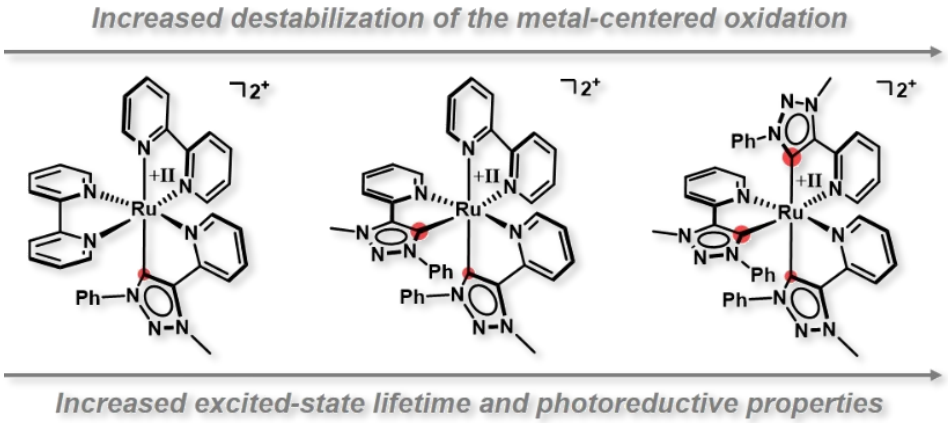

Figure 23. Electronic and photophysical investigated Ru(II) complexes with pyridyl–MIC ligands.

However, the noble metals as elements with a low natural abundance provides challenges for an industrial application. The geopolitical problems caused by mining low-abundant metals, such as ruthenium, lead to high energy costs and extensive water consumption. Consequently, the use of earth-abundant transition metals would be more suitable. The metals of the group 6 Cr, Mo and W all have a high natural abundance.

Chapter 3.3 presents in-depth investigations of the electronic properties in [M(**C–N**)(CO)$_4$] (M = Cr, Mo) as inexpensive and earth-abundant alternatives. The high redox stability is a crucial criterion for generating robust and highly efficient photo- and electrocatalysts and was highlighted in the following chapter 3.3.

(Spectro)electrochemistry is a powerful technique to investigate the redox stability of the presented group 6 carbonyl complexes.

Cyclic voltammetric, IR- and UV/vis/NIR-SEC measurements revealed an unusually reversible chromium-centered oxidation under ambient conditions, and served as the first indication of the exceptionally strong σ −donor properties of the pyridyl-MIC ligand to compensate for the electron-deficiency at the metal center.

In contrast, the higher homologue [Mo(**C–N**)$(CO)_4$] showed an irreversible oxidation. The electrochemical irreversibility can be explained by considering the properties of the central metal atom.

Metals of the 4th period are able to form complexes with higher coordination numbers. Upon oxidation, the coordinating solvent can bind to the metal center in an associative mechanism, which results in the dissociation of one of the CO ligands. Therefore, it was shown that the right choice of the metal center plays an important role to generate highly redox-stable metal complexes.

In addition, a reversible ligand-centered reduction could be observed for the first time on MIC-containing ligands for both complexes. The ligand-centered reduction could be assigned by IR- and EPR-SEC. The small shift of the CO stretching frequencies in the IR spectra ($\Delta\tilde{\nu} \approx 20$ cm^{-1}) is a consequence of the pyridyl-MIC-ligand-centered reduction, as the electron density within the [M$(CO)_4$] fragment is only indirectly influenced by the ligand-centered reduction. In contrast, the drastic change in electron density caused by the metal-centered oxidation leads to a strong shift of the CO stretching frequencies by about 120 cm^{-1}.

The high redox stability of the presented complexes emphasizes the great synergy between the good π −acceptor properties of the pyridyl moiety and the strong σ −donating properties of the MIC unit, making this ligand class an attractive candidate for potential photo- and electrocatalysts. Therefore, we investigated the photochemical properties of the presented [M(**C–N**)$(CO)_4$] (M = Cr, Mo) complexes in close cooperation with the groups of Gerhards and Niedner-Schattenburg.

Upon irradiation, step-scan FTIR spectroscopy indicated an uncommon reversible dark back reaction of the dissociated CO ligand. The generated photoproducts are stable for hours under ambient conditions. The observation of such robust photoswitchable systems can open new perspectives in chemical transformations by an inner-sphere mechanism for atom transfer radical additions (ATRA).

The unusual photochemical reactivity of the [M(**C–N**)(CO)$_4$] complexes inspired us to further investigate the photophysical properties of the group 6 tetracarbonyl complexes (**Scheme 10**). Only recently, the isoelectronic and isostructural group 6 metal complexes have experienced a renaissance in photochemistry and are able to compete with transition metal complexes of the 7th, 8th and 9th groups.

All presented [M(**C–N**)(CO)$_4$] complexes (M = Cr, Mo, W) exhibit room temperature emission in the solid state reaching the NIR region demonstrating the exceptional photophysical and photochemical properties induced by the pyridyl–MIC ligand.

NIR emitters are of particular interest in the field of photon-upconversion reactions to generate highly energetic material, biosensing or photodynamic therapy. The presented results give access to a new class of NIR emitters.

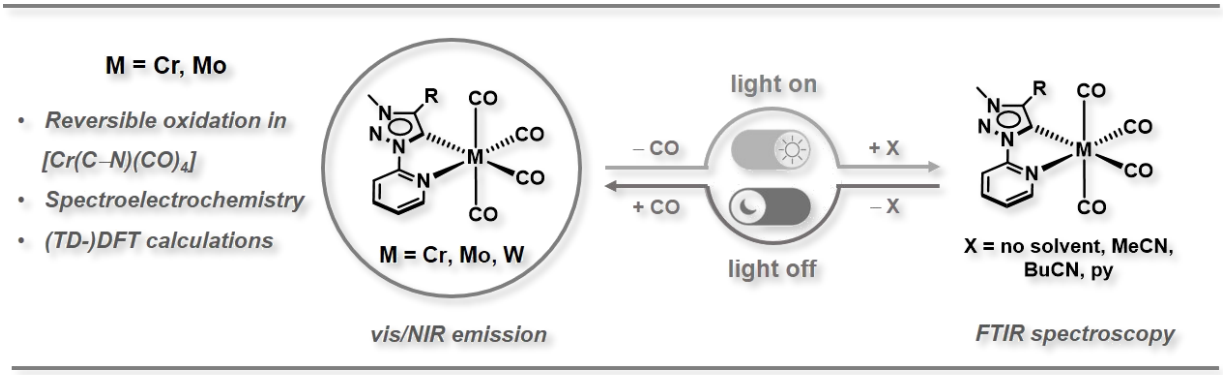

Scheme 10. (Spectro)electrochemical studies on [M(**C–N**)(CO)$_4$] (M = Cr, Mo) together with photophysical and photochemical investigations (M = Cr, Mo, W).

Excitation in analogous group 6 α −diimine and polypyridine tetracarbonyl complexes [M(CO)$_4$] results in a MLCT – the formal oxidation of the metal center and the formal reduction of the chelating ligand. Oxidation of the metal center leads to a decreased CO–backbonding from the metal center to the CO ligands. The weakening of the metal–CO bond is often accompanied by an irreversible loss of a CO ligand, leading to various decomposition pathways. Consequently, the excited MLCT state in group 6 carbonyl complexes is prone to undergo CO dissociation.

The demand for a profound understanding of the oxidized [M(CO)$_4$]$^+$ fragment to optimize new generations of photocatalysts and the unusual reversible chromium-centered oxidation in [Cr(**C–N**)(CO)$_4$] built the fundament for the next chapter 3.4.

For the first time, the isolation of the oxidized chromium tetracarbonyl complexes with π −accepting ligands was described. Analogous transition metal complexes with classical α −diimine and polypyridine ligands typically undergo rapid decomposition, as the π −accepting nature of the ligands leads to a decreased electron density at the metal center and consequently to the destabilization of the $[M(CO)_4]^+$ fragment.

However, the excellent σ −donating properties of the MIC moiety are capable of compensating for the electron deficiency at the oxidized metal center, while retaining their excellent π −acceptor properties.

The great synergy between the σ −donor strength of the MIC moiety and the π −acceptor capacity of the ligand facilitated in-depth investigations of the fragile $[M(CO)_4]^+$ fragment. The oxidized $[Cr(py–MIC)(CO)_4]^+$ complexes with both constitutional isomers could be isolated after the addition of mild oxidation reagents at ambient temperatures.

The right choice of the embedded counterion played a crucial role in obtaining single crystals of the Cr(I) species suitable for X-ray diffraction analysis.

Strong interactions of the cationic fragment with the counterion can induce the decomposition of the labile $[Cr(py–MIC)(CO)_4]^+$ complexes. A common strategy to overcome CO dissociation, substitution or dimerization of the so-called (super-)electrophiles is to take advantage of weak coordinating anions, such as $[Al(OR^F)_4]^-$ (with $R^F = C(CF_3)_3$) or BAr^{F-} (= tetrakis(3,5-bis(trifluoromethyl)-phenyl)borate).

The single crystal structure of $[Cr(\mathbf{C–C})(CO)_4]^+$ indicated fluorine-specific interactions of the CF_3 group in BAr^{F-} with the axial CO ligand, while no such interactions were present in $[Cr(\mathbf{C–N})(CO)_4]^+$ with the $[Al(OR^F)_4]^-$ counterion. These results clearly show the importance of the ion pairing effect for the isolation of new complexes with an electron-poor metal center and labile bond ligands.

The chemically isolated $[Cr(py–MIC)(CO)_4]^+$ complexes were compared with the electrochemically generated species to verify the stability in solution. Notably, the UV/vis spectra of the Cr(I) complexes supported by TD-DFT calculations revealed that the oxidized complexes retain most of their MLCT character, due to the electron-rich nature of the ligands. In addition, an uncommon ligand-to-metal charge transfer (LMCT) from various MIC-based orbitals to the oxidized Cr(I) center was observed at higher excitation energies. These results provide indirect evidence of the stabilizing effect of the MIC moieties on the oxidized metal center.

Furthermore, EPR spectroscopy of the oxidized species revealed detailed information about the influence of the constitutional isomers, as indicated by the strong hyperfine coupling of the pyridyl-*N* in [Cr(**C–C**)$(CO)_4$]$^+$ and its [Cr(**C–N**)$(CO)_4$]$^+$ counterpart. The **C–N** linkage in the pyridyl-MIC ligand leads to a decreased nucleophilicity of the pyridyl-*N* induced by the negative inductive effect (–I effect) of the N^1-triazolylidene moiety.
The weaker nucleophilicity of the pyridyl-moiety in **C–N** linked ligand and the anodic shift of the chromium-centered oxidation observed in cyclic voltammetry combined with the shift to higher wavenumbers in the IR spectrum allowed us to assign the **C–N** linked ligand as a weaker σ −donor compared to its **C–C** linked counterpart (**Figure 24**).

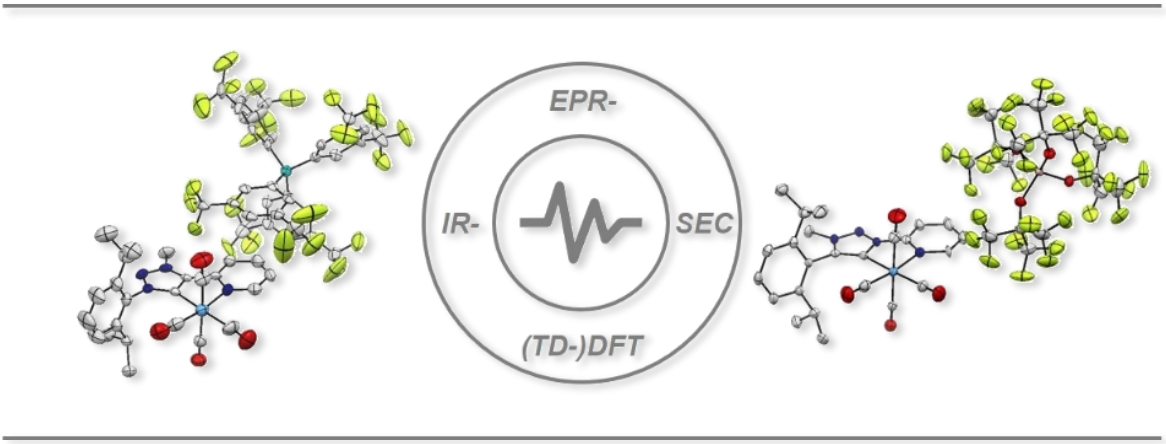

Figure 24. Isolated and *in-situ* generated [Cr(py–MIC)$(CO)_4$]$^+$ complexes investigated by IR, EPR and (spectro)electrochemistry.

The impact of the different connectivity between the pyridyl- and MIC-moiety accompanied by the changes in the electronic properties are presented in chapter 3.5. The chapter highlighted the influence of the two constitutional isomers on the photophysical and photochemical properties in group 6 carbonyl complexes.
The excitation-dependent duality in tetracarbonyl group 6 metal complexes between the excited state emission and the photo-induced CO cleavage leads to unique photophysical and photochemical properties of the presented substance class.
High excitation energies result in the population of the excited ^{1}MLCT state from the metal center to the axial CO ligand (M → CO) with a small vibronic barrier inducing CO dissociation.

Changing the excitation energy to low energies results in the population of the energetic lower ^{1}MLCT state (M → L) by a metal-to-ligand charge transfer from the metal center to the chelating ligand. A fast intersystem crossing (ISC) from the ^{1}MLCT state leads to the emissive ^{3}MLCT state.

The influence of the constitutional isomers of the pyridyl-MIC ligand in [M(**C–C**)(CO)$_4$] *vs.* [M(**C–N**)(CO)$_4$] (M = Cr, Mo, W) was in particular evident in the photochemical and photophysical properties of the higher homologous.

In the first part of this chapter, the quantum yields Φ_{em} and the exited state lifetimes τ in [M(**C–C**)(CO)$_4$] were determined and compared with the previously reported in [M(**C–N**)(CO)$_4$] complexes. The insertion of the more electron-donating **C–C** linked isomer resulted in a drastic increase of the quantum yields from $1.7 \cdot 10^{-4}$ in [W(**C–N**)(CO)$_4$] to 0.29 in [W(**C–C**)(CO)$_4$]. To the best of our knowledge these are the highest quantum yields reported for tetracarbonyl group 6 complexes so far.

At lower temperatures, the [W(**C–C**)(CO)$_4$] complex shows excited state lifetimes of 3000 ns in the solid state. In contrast, the [W(**C–N**)(CO)$_4$] complex shows excited state lifetime of only 290 ns. However, all presented complexes outperform the well-established α −diimine and polypyridine tetracarbonyl complexes.

Interestingly, an unusual emission at room temperature in solution was observed for [W(**C–C**)(CO)$_4$]. Unfortunately, the nature of the emission could not be assigned at this point. The results show a new strategy for the design of long-lived emissive group 6 carbonyl complexes based on mesoionic carbenes. Additionally, the simple change in the connectivity between the pyridyl and MIC moiety has a drastic influence of the photoluminescence quantum yields and the excited state lifetimes.

In the second part of this chapter, the photodissociation quantum yields Φ_{diss} in [M(**C–C**)(CO)$_4$] were investigated and compared to the [M(**C–N**)(CO)$_4$] analogs.

The incorporation of the more electron-rich **C–C** linked ligand leads to a decrease in the photodissociation quantum yields Φ_{diss} of the axial CO ligand. The increased electron density at the metal center results in a stronger metal–CO bond, disfavoring the CO dissociation compared to the less electron-donating **C–N** linked ligand. Low-temperature FTIR-step scan spectroscopy supported by quantum chemical calculations facilitated the characterization of the highly reactive [W(**C–C**)(CO)$_3$] complex with a vacant axial coordination site.

In solution, subsequent solvent coordination results in the respective solvato complexes. Leaving the complexes in the dark initiates the dark reverse reaction to recover the starting complexes, as previously observed in [M(**C–N**)$(CO)_4$] (M = Cr, Mo, W).

In the case of [M(**C–C**)$(CO)_4$], higher kinetic rates for the dark reverse reactions were observed, compared to the **C–N** analogues. The increased electron density in within the [M(**C–C**)$(CO)_3$S] (S = solvent) presumably leads to faster binding of the dissociated CO ligand and to a destabilization of the respective solvato complexes.

In a more general perspective, the stabilizing effect induced by the two pyridyl–MIC ligands facilitates new strategies to access long-lived intermediates for potential photocatalytic applications in an inner-sphere mechanism. The stability and reactivity of the activated complex can be tuned by the different connectivity within constitutional pyridyl–MIC-based isomers.

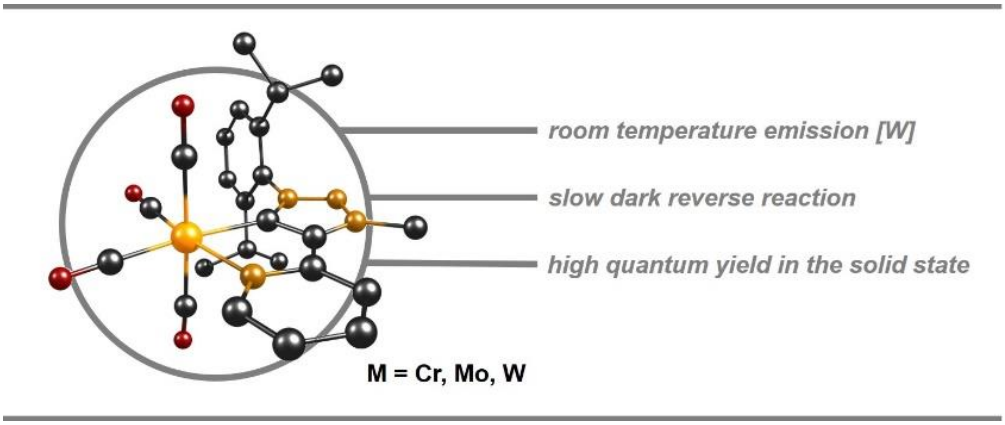

Figure 25. Photophysical and photochemical investigated [M(**C–C**)$(CO)_4$] (M = Cr, Mo, W) complexes.

The extraordinary influence on the (photo)chemical and photophysical properties of the two constitutional isomers incorporated in [M$(CO)_4$] (M = Cr, Mo, W) prompted us to further investigate the complexes by (spectro)electrochemical and theoretical methods. In chapter 3.6, the reductive processes have been highlighted with a focus on the electrochemical activation of CO_2.

The greenhouse gas represents a non-toxic, cheap and abundant C_1 feedstock for the chemical industry. However, the high thermodynamic stability and high kinetic barrier to generate CO, MeOH or formic acid remains challenging and requires an efficient electrocatalyst to overcome the inertness of CO_2.

One of the most prominent electrocatalysts for the electrochemical conversion of CO_2 is the so-called Lehn catalysts *fac*-[Re(bpy)$(CO)_3$Cl]. The one-electron reduction at the bpy ligand leads to the dissociation of the chloride ligand. The second ligand-centered reduction generates the monoanionic catalytically active [Re(bpy)$(CO)_3]^-$ species capable of overcoming the kinetic and thermodynamic barrier for the activation of CO_2.

In protic media, CO_2 binds to the metal center and the resulting CO_2 adduct selectively generates CO and H_2O under mild conditions making the Lehn catalyst one of the best-known and efficient molecular electrocatalysts for the electrochemical CO_2 reduction so far. However, the group 7 electrocatalyst contains rhenium as a low-abundant and expensive metal center limiting an industrial application for the electrochemical conversion of CO_2.

In contrast, the more earth-abundant and inexpensive group 6 metal complexes are attractive candidates for the electrochemical conversion of CO_2 because of their presence in biochemical systems, such as molybdenum represented in the active site of enzymes capable of converting CO_2 to formate.

Recent reports have demonstrated that the isoelectronic and isostructural group 6 metal tetracarbonyl complexes with polypyridine ligands are electrocatalytically active in the electrochemical conversion of CO_2 under non-protic conditions.

With the series of [M(**C–C**)$(CO)_4$] and [M(**C–N**)$(CO)_4$] (M = Cr, Mo, W) in hand, chapter 3.6 highlighted the precatalytic activation of the presented complexes by (spectro-)electrochemical and theoretical methods in the absence and in the presence of CO_2.

All presented complexes showed a reversible ligand-centered first reduction, which shifts according to the π −acceptor properties of the ligands and the incorporated metal center. The results demonstrated that the **C–N** linked pyridyl–MIC ligand represents a slightly better π −acceptor but a weaker σ −donor compared to its **C–C** linked counterpart.

The ligand-centered reduction could be further confirmed by IR- and EPR-SEC supported by theoretical calculations. The EPR data showed that in the case of the [M(**C–C**)$(CO)_4$] complexes, the electron spin is more delocalized within the pyridyl–MIC framework. In contrast, in the series of [M(**C–N**)$(CO)_4$] a stronger localization of the electron spin at the MIC moiety is observed, as indicated by the higher coupling constants of the ^{14}N atoms within the MIC and the stronger coupling to the ^{1}H atoms of the methyl group at the MIC.

The stronger delocalization of the electron within the pyridyl–MIC of [M(**C–C**)$(CO)_4$] is supported by the broad absorption bands between 650–2000 nm in the UV/vis/NIR spectrum of the singly reduced species. In the case of [M(**C–N**)$(CO)_4]^-$, more discrete absorption bands in the range of 500–750 nm are observed, indicating a higher localization of the free electron.

However, the marginal differences in the electronic properties lead to a drastic influence on the bond activation in the series of [M(**C–C**)$(CO)_4$] and [M(**C–N**)$(CO)_4$].

According to the IR- and UV/vis/NIR-spectroelectrochemical measurements, the first reduction leads to CO dissociation in the series of [M(**C–C**)$(CO)_4$].

A new IR band around 2030 cm^{-1} was observed, which could be assigned to free CO within the electrochemical OTTLE cell. The dissociation of CO is a consequence of the prolonged electrolysis time during the spectroelectrochemical measurements. In contrast, the reduction of the [M(**C–N**)$(CO)_4$] complexes appeared completely reversible as indicated by the isosbestic points.

The one-electron reduction in [M(**C–C**)$(CO)_4$] and [M(**C–N**)$(CO)_4$] showed that the different linkage in the constitutional isomers can have a drastic influence on the bond activation within the presented complex class. These results provide an essential concept in bond activation mechanisms to further improve future electrocatalysts.

Based on these observations, all presented complexes were tested with different electrode materials (Au/GC) in the electrochemical CO_2 reduction.

The electrochemical CO_2 reduction with an Au working electrode showed that all presented complexes were capable of activating CO_2 after the first reduction. This contractionary observation within the series of the [M(**C–N**)$(CO)_4$] could be a consequence of only traces of catalytic active species formed during the reduction. Unfortunately, the high potentials applied for electrochemical CO_2 reduction limited the in-depth investigation of the respective electrocatalysts.

Changing the working electrode to a GC working electrode did not lead to an electrochemical activation of CO_2 after the first reduction in the series of [M(**C–C**)$(CO)_4$] and [M(**C–N**)$(CO)_4$]. Only the chromium complex [Cr(**C–C**)$(CO)_4$] showed an increased current after the first reduction. However, electrodeposition could not fully be excluded at this point.

In the series of [M(**C–C**)(CO)$_4$], an adduct formation after the second irreversible reduction was observed, as indicated by the cathodic shift of the second reduction. In analogous polypyridine [M(CO)$_4$] complexes, the formation of a metal-bound CO_2 intermediate is reported. However, the dissociation of one of the electron-rich ligand arms and subsequent reaction with CO_2 cannot be fully ruled out at this point.

In contrast, in the series of [M(**C–N**)(CO)$_4$] an increase in the current was observed after the second reduction. Unfortunately, the high operating potential prevented us from further investigations of the electrochemical transformation. However, the complexes are potential candidates for the electrochemical CO_2 reduction.

In conclusion, the (spectro)electrochemical results demonstrated that the right choice of the incorporated ligand and the electrode material can indeed tune the electrochemical activation of CO_2 in group 6 metal complexes.

In the series of [M(**C–C**)(CO)$_4$] and [M(**C–N**)(CO)$_4$], further optimizations have to be carried out to generate an efficient electrocatalyst suitable for the electrochemical CO_2 reduction at lower operating potentials (**Figure 26**).

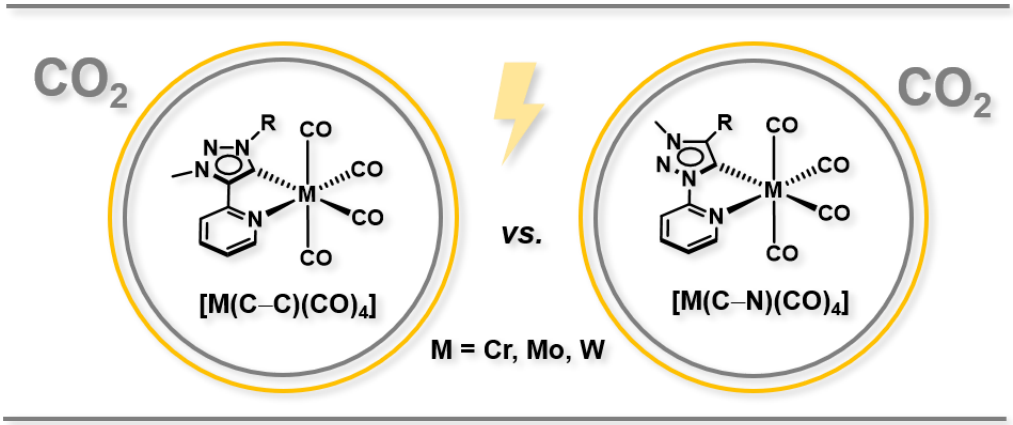

Figure 26. Group 6 carbonyl complexes probed for the electrochemical CO_2 reduction with an Au and a GC working electrode, respectively.

The rise of atmospheric CO_2 associated with global warming has raised significant awareness to develop alternative green energy sources. One of the most promising alternative feedstocks has gained increasing attention during the past decades – H_2. Dihydrogen has the highest energy per mass of any fuel. However, the temperature density at ambient conditions results in a low energy per unit volume.

The urgent need to develop an advanced storage system to release H_2 selectively seems more prominent than ever. One strategy is to make use of a robust homogeneous electrocatalyst that generates significant amounts of H_2 from a simple proton source under mild conditions. Unfortunately, various homogeneous electrocatalysts are not sufficiently stable enough under the applied electrocatalytic conditions. The electrochemically generated highly reactive intermediates can undergo rapid decomposition pathways. Therefore, the investigation of the key intermediates within the electrocatalytic cycle is crucial to optimize the homogeneous electrocatalyst and to increase the stability of the highly reactive intermediates.

In the last part of this thesis (chapter 3.7), detailed mechanistic studies on the precatalytic activation path in the electrochemical H^+ reduction with pyridyl-MIC containing [RhCp*] complexes were presented.

Under non-catalytic conditions, the combined (spectro)electrochemical and theoretical methods revealed a two-electron reduction for the chlorido [RhCp*] complexes generating the electron-rich Rh(I) complexes after chloride dissociation. The Rh(I) species can undergo another electron-transfer step to form the 19 VE species.

In the case of the [RhCp*] solvato complexes, a stepwise one-electron reduction was observed to generate the Rh(I) species. The first one-electron reduction could be assigned to a metal-centered reduction, as indicated by the identical reduction potentials.

The second reduction is shifted according to the π −acceptor properties of the ligands. Therefore, the second reduction can be assigned to a ligand-centered reduction.

In-depth spectroelectrochemical and theoretical calculations have been performed to identify the nature of the respective intermediates. The UV/vis/NIR-SEC measurement showed intense absorption bands in the range of 380–800 nm after the first reduction. TD-DFT calculations were performed on the singly reduced $[RhCp^*]^-$ solvato complexes and the cationic coordinatively unsaturated $[RhCp^*]^+$ species. The calculated absorption spectra of the cationic $[RhCp^*]^+$ are in good agreement with experimentally observed UV/vis spectra. Consequently, dissociation of the acetonitrile ligand in the [RhCp*] solvato complex occurs upon reduction to generate a rare coordinatively unsaturated Rh(II) species.

The chemical isolation of the [RhCp*] hydride complexes allowed us to further investigate the unusual Rh(II) species. The addition of the organic radical TEMPO (=(2,2,6,6-tetramethylpiperidin-1-yl)oxyl) resulted in an abstraction of a $H^{\cdot}$ and the *in-situ* formation of the 17 VE species. Isotropic signals at *g*-values of 2.06 were observed for both complexes. The high *g*-values are characteristic for paramagnetic species with a significant metal contribution. Spin density calculations of the postulated intermediates could further confirm the formation of the coordinatively unsaturated Rh(II) species.

These results show that the electron-rich nature of the MIC moiety is capable of stabilizing the electron-deficient coordinatively unsaturated Rh(II) center by the strong σ −electron-donating properties, while the good π −acceptor capacities generating a beneficial conjugation between the electron-donating Cp* ligand, the metal center and the chelating ligand.

Under electrocatalytic conditions, an ECCE mechanism in the [RhCp*] hydride formation with acetic acid was proposed. The vacant coordination site of the Rh(II) species results in a rapid formation of the [RhCp*] hydride complexes, as indicated by UV/vis/NIR-SEC and TD-DFT calculations.

The chemical isolation of the [RhCp*] hydride complexes allowed us to further investigate the reactive intermediate. Fortunately, we were able to obtain single crystals suitable for X-ray diffraction analysis of the **C–N** linked isomer, representing a rare example of this complex class and the first reported structurally characterized MIC–based hydride complex.

In contrast to earlier literature reports, no hydride migration to the Cp* moiety was observed over a broad temperature regime in the ^{1}H-NMR spectra. Instead, an ambivalent H^+, $H^{\cdot}$ and H^- reactivity is presented, which was confirmed by different reactivity studies and spectroscopic measurements.

In a first approximation, the pK_a values, bond dissociation free energy (BDFE) and hydricity ($\Delta G^0_{H^-}$) were determined.

Both [RhCp*] hydride complexes display strong $\Delta G^0_{H^-}$ values compared to analogous polypyridine [RhCp*] hydride complexes as a direct consequence of the strong electron-donating nature of the pyridyl-MIC ligands. The BDFE was estimated to be in a similar range as observed for cyclometalated-phenyl-pyridyl [RhCp*] hydride complexes.

Interestingly, UV/vis spectroscopy of the isolated [RhCp*] hydride complexes revealed an equilibrium between the reduced Rh(I) species and the Rh(III) hydride species. The equilibrium was further supported by the low pK_a values determined for both complexes. The low pK_a values emphasize a beneficial stabilization of the conjugated base. Indeed, the **C–N** linked Rh(I) species was sufficiently stable enough to obtain single crystals suitable for X-ray diffraction analysis and represents the first structurally characterized MIC-based complex of its kind.

The observation of these unusual equilibrium opens new perspectives in the field of precatalytic activation in the presented substance class for tailor-made chemical transformations, such as $NADP^+$ reduction or homogeneous reductive catalysis.

An additional electron transfer step is required to initiate the electrochemical H^+ reduction with acetic acid. At lower acid concentrations a continuous increase in the current was observed. However, the limited potential window of the acetic acid prevented us from further investigations of the electrochemical H_2 generation.

The reduction of the cationic [RhCp*] hydride complexes could lead to neutral [RhCp*] hydride complexes, directly reacting with the proton source to generate H_2 in an electrocatalytic manner or recombine with the cationic [RhCp*] hydride complex to form H_2 in a sub-stochiometric amount (**Scheme 11**).

The high stability of the [RhCp*] complexes facilitates future studies with a different proton source to shine a light on the electrocatalytic formation of H_2 to generate an efficient electrocatalyst. However, under the applied electrocatalytic conditions modification of the electrocatalysts is necessary to shift the electrocatalysis to more anodic potentials.

Interestingly, during the UV/vis/NIR-SEC measurements of the [RhCp*] hydride complexes a rapid gas formation was observed, which we would like to attribute to the formation of H_2. The light-induced generation of H_2 could shift the operating potential about 850 mV to more anodic potential and consequently bypassing the limitations of the electrochemical H^+ reduction with the presented complexes under the experimental conditions.

In addition, the uncommon equilibrium between the [RhCp*] hydride complexes and the electron-rich Rh(I) species and the ambivalent reactivity of the [RhCp*] hydride complexes paves the way for a better mechanistic understanding of carbene-based homogeneous catalysts in reductive processes and to further improve the applied reaction conditions of such systems.

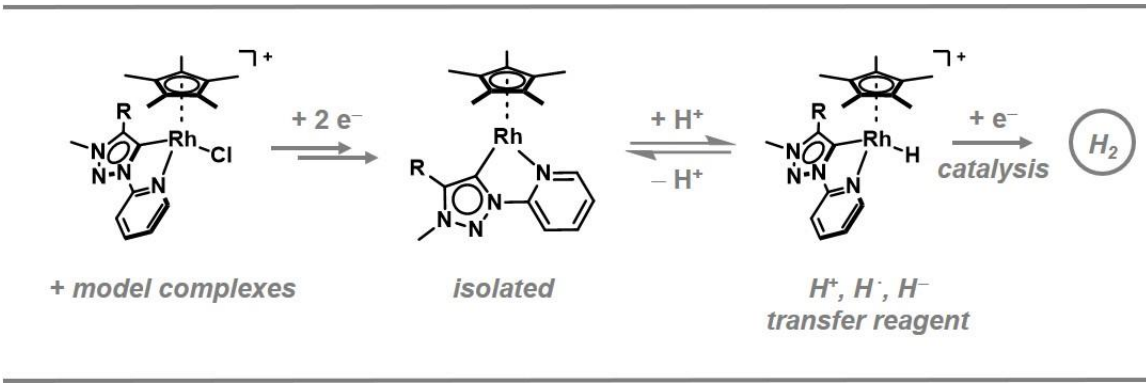

Scheme 11. Simplified mechanistic proposal for electrocatalytical proton reduction with pyridyl–MIC [RhCp*] complexes.

In conclusion, the presented thesis highlights the extraordinary properties of pyridyl-1,2,3-triazolylidene ligands in organometallic chemistry.

The ligand class exhibits strong σ −donor properties, facilitating the stabilization of uncommon oxidation states (e.g. Cr^{I} or Rh^{II}) by the MIC moiety, while the pyridyl unit induces excellent π −acceptor capacities. The well-balanced synergy between the σ −donor and π −acceptor properties builds the fundament for various transition metal complexes with potential applications in photo- and electrocatalysis.

A series of three new Ru(II) polypyridine complexes with the **C–C** linked ligand has been investigated. The strong electron-donating properties of the MIC moiety could give access to a new class stable of Ru(III) complexes with unusual LMCT emissions, whereas the respective Ru(II) complexes are attractive candidates for photoreductive catalysis.

However, the high cost and low abundance of ruthenium-based photocatalysts prohibit industrial applications. Therefore, more earth-abundant group 6 tetracarbonyl complexes represent an excellent alternative to the precious 4d and 5d metals of the groups 8 and 9.

The [M(**C–C**)(CO)$_4$] and [M(**C–N**)(CO)$_4$] complexes (M = Cr, Mo, W) show remarkable redox stability, which is also reflected in the prolonged excited state lifetimes and photoluminescence quantum yields. However, the influence of constitutional isomers has not received much attention in this regard.

The **C–C** linked constitutional isomer leads to excited state lifetimes nearly 100 times higher compared to the **C–N** linked counterpart and quantum yields as high as 29% in the solid state.

The excellent electron-donating properties of the two constitutional isomers in [M(**C–C**)(CO)$_4$] and [M(**C–N**)(CO)$_4$] are also capable of stabilizing highly reactive [M(CO)$_3$] intermediates with a vacant coordination site after irradiation with high excitation energy. The resulting solvato complexes show remarkable stability making them attractive candidates for inner-sphere mechanisms for photocatalytic applications, such as atom transfer radical addition (ATRA). Furthermore, an unusual dark reverse reaction of the dissociated CO ligand was observed, representing rare cases of photoswitchable transition metal complexes.

The series of [M(**C–C**)(CO)$_4$] and [M(**C–N**)(CO)$_4$] were further investigated (spectro-)electrochemical methods. The simple change in the connectivity between the pyridyl and MIC moiety leads in the **C–C** constitutional isomer [M(**C–C**)(CO)$_4$] to CO dissociation during the first ligand-centered reduction. In contrast, the complexes based on the **C–N** linked isomer [M(**C–N**)(CO)$_4$] remain intact during the first reduction.

The present thesis revealed that the marginal change in the connectivity can result in an entirely different bond activation reactivity. EPR spectroscopy and spin density calculations in the series of [M(**C–C**)(CO)$_4$] indicated a stronger delocalization of the electron spin within the pyridyl-MIC fragment. In contrast, the electron spin in [M(**C–N**)(CO)$_4$] was shown to be more localized at the MIC moiety.

Even though all complexes are capable of the electrochemical activation of CO_2 under the experimental conditions, optimization of the pyridyl–MIC-based group 6 carbonyl complexes must be carried out to generate an efficient electrocatalyst for the electrocatalytic CO_2 reduction at low operating potentials. A common strategy to optimize homogeneous electrocatalysts is to investigate the highly reactive intermediates generated during the electrocatalytic cycle.

In-depth theoretical and (spectro)electrochemical have been performed on [RhCp*] complexes for the electrochemical H^+ reduction containing both constitutional pyridyl–MIC isomers. All key intermediates could be isolated and characterized by various spectroscopical methods. The [RhCp*] hydride complexes can act as a transferring reagent for H^+, $H^\cdot$ or H^- opening various opportunities in homogeneous reductive catalysis.

The observation of the unusual equilibrium of the [RhCp*] hydride complexes will improve the fundamental mechanistic understanding of homogeneous catalysis and assist to adjust the catalytic conditions to optimize the substrate conversion.

Taking all results into account, this thesis provided an extensive understanding of the fine-tuning of the electronic properties induced by pyridyl-MIC based ligands and their constitutional isomers, leading to new perspectives on the structure-reactivity relationship for small molecule activation in electro- and photocatalysis (**Figure 27**).

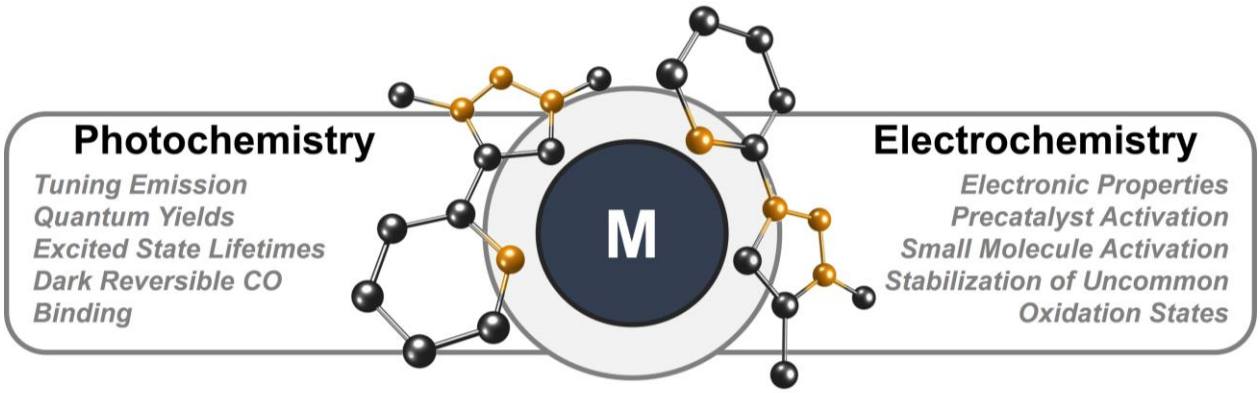

Figure 27. Overview of the investigated key points in the present thesis.

3.2 The Impact of Bidentate Pyridyl-Mesoionic Carbene Ligands: Structural, (Spectro)Electrochemical, Photophysical, and Theoretical Investigations on Ruthenium(II) Complexes

T. Bens,[†,§] J. A. Kübler,[‡] R. R. M. Walter,[†] J. Beerhues,[†,§,^] Prof. Dr. O. S. Wenger,[‡] Prof. Dr. B. Sarkar[†,§,*]

[†]Institut für Anorganische Chemie, Universität Stuttgart, Pfaffenwaldring 55, D-70569 Stuttgart, Germany, Email: biprajit.sarkar@iac.uni-stuttgart.de

[§]Institut für Chemie und Biochemie, Freie Universität Berlin, Fabeckstraße 34-36, 14195, Berlin, Germany.

[^]Current Address: Institute of Chemical Research of Catalonia (ICIQ), Barcelona Institute of Science and Technology (BIST), Av. Països Catalans 16, 43007 Tarragona, Spain.

[‡]Department of Chemistry, University of Basel, 4056 Basel, Switzerland; Email: oliver.wenger@unibas.ch

This article was published and is reprinted with permission from ACS:

T. Bens, J. A. Kübler, R. R. M. Walter, J. Beerhues, O. S. Wenger, B. Sarkar, *ACS Org. Inorg. Au* **2023**, *3*, 184-198.

DOI: 10.1021/acsorginorgau.3c00005 (© 2023 American Chemical Society).

The **Supporting Information** is available free of charge at https://pubs.acs.org/doi/10.1021/acsorginorgau.3c00005.

Autor contribution: The project was designed by Biprajit Sarkar. The complexes were synthesized and fully characterized by Tobias Bens. All (spectro)electrochemical measurements and theoretical calculation were performed by Tobias Bens. The photophysical properties were investigated by Jasmin A. Kübler. X-Ray diffraction analysis was carried out by Robert R. R. Walter and Julia Beerhues. The manuscript was written by Tobias Bens and Biprajit Sarkar.

ACS ORGANIC & INORGANIC Au
AN OPEN ACCESS JOURNAL OF THE AMERICAN CHEMICAL SOCIETY

pubs.acs.org/orginorgau Article

Impact of Bidentate Pyridyl-Mesoionic Carbene Ligands: Structural, (Spectro)Electrochemical, Photophysical, and Theoretical Investigations on Ruthenium(II) Complexes

Tobias Bens, Jasmin A. Kübler, Robert R. M. Walter, Julia Beerhues, Oliver S. Wenger, and Biprajit Sarkar*

Cite This: ACS Org. Inorg. Au 2023, 3, 184–198 Read Online

ACCESS | Metrics & More | Article Recommendations | Supporting Information

ABSTRACT: We present here new synthetic strategies for the isolation of a series of Ru(II) complexes with pyridyl-mesoionic carbene ligands (MIC) of the 1,2,3-triazole-5-ylidene type, in which the bpy ligands (bpy = 2,2′-bipyridine) of the archetypical $[Ru(bpy)_3]^{2+}$ have been successively replaced by one, two, or three pyridyl-MIC ligands. Three new complexes have been isolated and investigated via NMR spectroscopy and single-crystal X-ray diffraction analysis. The incorporation of one MIC unit shifts the potential of the metal-centered oxidation about 160 mV to more cathodic potential in cyclic voltammetry, demonstrating the extraordinary σ-donor ability of the pyridyl-MIC ligand, while the π-acceptor capacities are dominated by the bpy ligand, as indicated by electron paramagnetic resonance spectroelectrochemistry (EPR-SEC). The replacement of all bpy ligands by the pyridyl-MIC ligand results in an anoidic shift of the ligand-centered reduction by 390 mV compared to the well-established $[Ru(bpy)_3]^{2+}$ complex. In addition, UV/vis/NIR-SEC in combination with theoretical calculations provided detailed insights into the electronic structures of the respective redox states, taking into account the total number of pyridyl-MIC ligands incorporated in the Ru(II) complexes. The luminescence quantum yield and lifetimes were determined by time-resolved absorption and emission spectroscopy. An estimation of the excited state redox potentials conclusively showed that the pyridyl-MIC ligand can tune the photoredox activity of the isolated complexes to stronger photoreductants. These observations can provide new strategies for the design of photocatalysts and photosensitizers based on MICs.

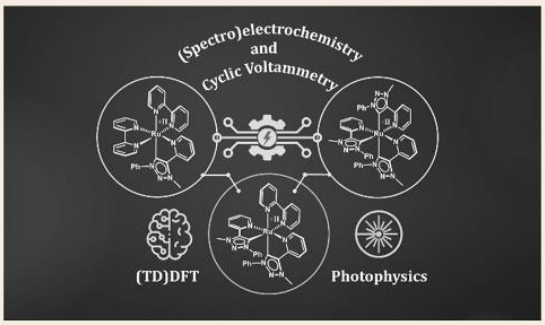

KEYWORDS: *mesoionic carbenes, (spectro)electrochemistry, photochemistry, ruthenium, bipyridine, metal to ligand charge transfer*

INTRODUCTION

In recent years, mesoionic carbenes (MICs) of the 1,2,3-triazole-5-ylidene type have attracted increasing attention due to the versatility in ligand design and tunability of electronic properties. In comparison to their classical NHC counterparts, MICs feature stronger σ-donating properties and higher π-acceptor abilities leading to extensive utilization in both transition metal and main group chemistry.[1−8] The incorporation of an additional donor substituent to the existing ligand backbone enables a bridge between the famous 2,2′-bipyridine (bpy, Figure 1) and newly designed tailor-made bidentate MIC-based ligands for transition metal complexes.

Recently, some of us investigated the overall σ-donor- and π-acceptor properties of chelating click-derived triazole and triazolylidene ligands in rhenium(I) complexes, combining cyclic voltammetry and IR spectroscopy (Figure 1).[9] The study revealed a comparatively weaker σ-donor and π-acceptor ability of the bis-triazole ligand (triaz-triaz) in comparison to bpy, while the bis-MIC ligand (MIC-MIC) exhibits moderate π-acceptor and strong σ-donor strength. Including a single pyridyl moiety (triaz-py and py-MIC) in such ligands already drastically increases their π-acceptor capacities. In the case of the pyridyl-MIC (R = 2,6-diisopropylphenyl), the outstanding tunability of this class of ligands can be revealed. The ligand shows strong overall σ-donor and high π-acceptor properties, making it a suitable candidate for electrocatalytic and photocatalytic applications.

The growing interest in MICs is particularly evident in the photo-[10−23] and redox-active chemistry,[9,24−31] providing access to various applications in homogeneous catalysis[2−4,7,32] and dyes for dye-sensitized solar cells.[33,34] The modular synthesis

Received: February 13, 2023
Revised: April 19, 2023
Accepted: April 19, 2023
Published: May 3, 2023

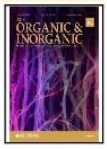

https://doi.org/10.1021/acsorginorgau.3c00005
ACS Org. Inorg. Au 2023, 3, 184–198

ACS Organic & Inorganic Au pubs.acs.org/orginorgau Article

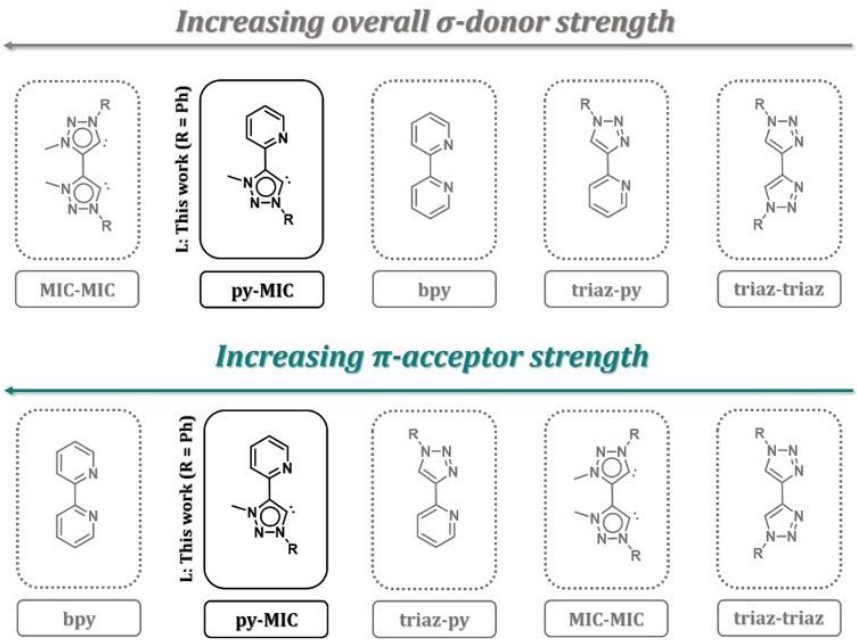

Figure 1. Comparison of the overall σ-donor properties and π-acceptor abilities in click-derived triazole and triazolylidene *fac*-$[ReCl(CO)_3]$ complexes by Suntrup et al.[9] including the reported photoredox investigations in Fe(II)/(III) or Ru(II) complexes with the respective ligands.[10,13,16,17,35−37,39,40,42−45,47]

Scheme 1. Synthetic Strategies for $[RuL_1]^{2+}$, $[RuL_2]^{2+}$, and $[RuL_3]^{2+}$[a]

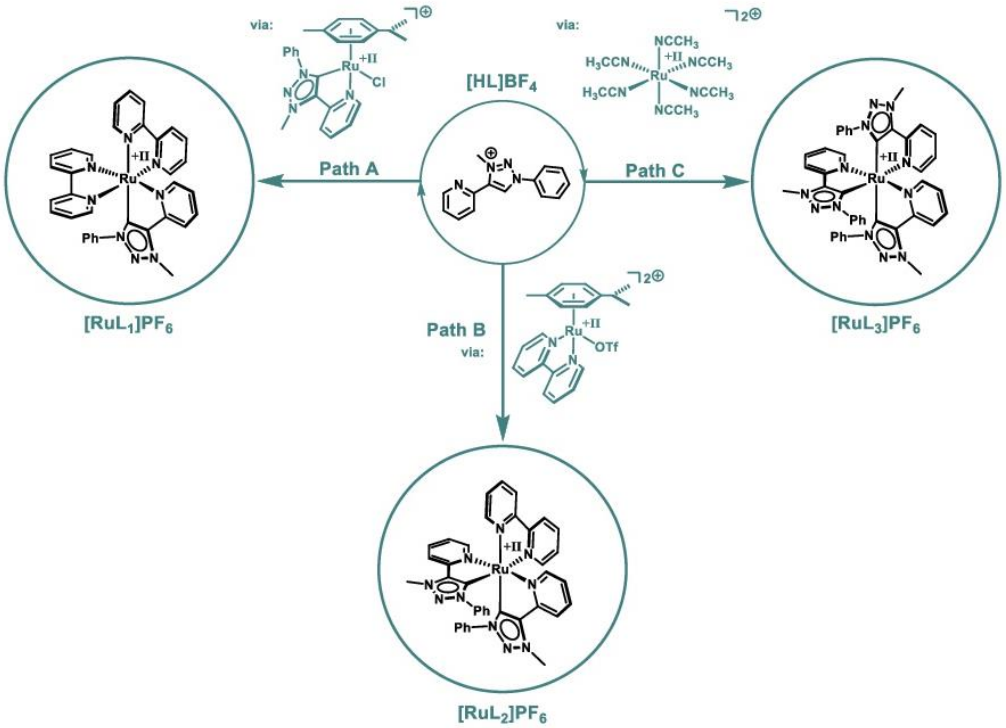

[a]Path A: [**HL**]**BF**$_4$, Ag_2O, CH_3CN, rt, 4 days; $[Ru(p\text{-cymene})Cl_2]_2$, rt, 2 h (74%);[52] bpy, $AgPF_6$, ethylene glycol, 150 °C, 12 h; aq KPF_6 (74%).[17] Path B: $[Ru(p\text{-cymene})Cl_2]_2$, bpy, MeOH, 2 h, rt; aq NH_4PF_6, 1 h (72%);[55] HOTf, DCM, rt, 12 h (83%);[56] [**HL**]**BF**$_4$, ethylene glycol, 180 °C, 12 h; aq KPF_6 (49%, crude after workup); 2 weeks under *hν* in acetone/Et_2O (16%).[57] Path C: modified: $RuCl_3{\cdot}3H_2O$, Zn(act), CH_3CN, reflux, 2 days; $AgBF_4$, CH_3CN, reflux, 12 h (81%);[58] modified: [**HL**]**BF**$_4$, K_2CO_3, ethylene glycol, 160 °C, 16 h; aq NH_4PF_6 (46%).[57]

https://doi.org/10.1021/acsorginorgau.3c00005
ACS Org. Inorg. Au 2023, 3, 184−198

ACS Organic & Inorganic Au pubs.acs.org/orginorgau Article

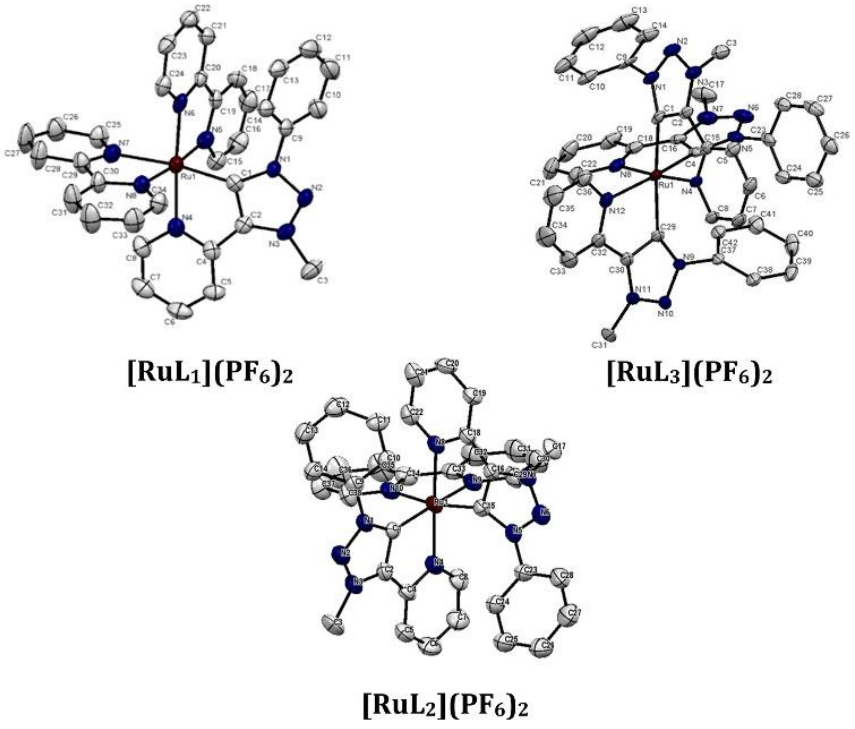

Figure 2. ORTEP representation of top left: $[\mathbf{RuL_1}](\mathbf{PF_6})_2$, bottom center: $[\mathbf{RuL_2}](\mathbf{PF_6})_2$, and top right: $[\mathbf{RuL_3}](\mathbf{PF_6})_2$ (hydrogen atoms and counter ions are omitted for clarity). Ellipsoids are drawn with 50% probability.

and tunability of the electronic structure of the redox- and photoactive metal centers enable new generations of photoredox catalysts that have different properties compared to the well-established $[Ru(bpy)_3]^{2+}$.[32,35−47]

The lifetime of the photoactive ^{3}MLCT state in the aforementioned complexes is primarily influenced by the ligand field splitting imparted by the coordination environment and high symmetry. Excellent reviews on the conceptual design of the ligand framework to increase the ligand field splitting have been published by several different working groups, showing the significant contributions in the past decades.[7,15,48−50] Therefore, it is not surprising that the easily modulable bidentate triazoles and triazolylidene ligands have been investigated with various Ru(II) complexes to enhance their photophysical and photoredox properties.

Elliot and Skoglund first reported on triazole-containing ligands (triaz-triaz and triaz-py) and showed that excitation of the corresponding Ru(II) complexes leads to a destabilization of the ^{3}MLCT state and a rapid depopulation via the nonradiatively deactivating ^{3}MC state. Therefore, to generate luminescent metal complexes, the excitation of unoccupied triazole-based orbitals is not desirable due to their luminescence quenching character.[10,37,39,46]

In 2013, Albrecht and co-workers investigated the pyridyl-MIC ligand (R = Me) in the complex $[Ru(bpy)_2(py\text{-}MIC)]^{2+}$.[40] They showed that the strong electron-donating nature of the MIC-based ligand resulted in the destabilization of the metal-centered highest occupied molecular orbital (HOMO), as indicated by the shift of the first metal-centered oxidation to more cathodic potential in cyclic voltammetry. According to the first ligand-centered reduction, the π-acceptor property of the pyridyl-MIC ligand leads to a minor destabilization of the lowest unoccupied molecular orbital (LUMO) orbital compared to the well-established $[Ru(bpy)_3]^{2+}$ complex.

Moreover, Wärnmark and Sundström in successive reports revealed the unique photophysical properties of MIC-containing transition metal complexes.[13,16,44] The homoleptic tris-(MIC−MIC) Fe(III)[13] complex was shown to be stabilized by the extreme electron-donating nature of the bidentate MIC ligands, resulting in an outstanding lifetime of 100 ps at room temperature, originating from an unusual LMCT.

In addition, a record-breaking MLCT lifetime of 528 ps was observed for the corresponding Fe(II) complex,[16] which was only to be surpassed by the scorpion-type tris-NHC Fe(III) complex published in 2019 by Wärnmark and co-workers. The octahedral complex with two mono-anionic ligands showed a remarkable LMCT lifetime of 2.0 ns at room temperature.[51]

The immense influence of MICs on the photoredox properties of transition metal complexes has motivated us to conduct systematical studies on $[Ru(L)_n(bpy)_m]^{2+}$ (n = 1−3, m = 0−2) complexes containing the pyridyl-MIC ligand **L**. Complexes $[\mathbf{RuL_1}]^{2+}$, $[\mathbf{RuL_2}]^{2+}$, and $[\mathbf{RuL_3}]^{2+}$ were isolated and characterized by spectroscopic and crystallographic methods (Scheme 1 and Figure 2). Additionally, cyclic voltammetry, density functional theory (DFT), UV/Vis/NIR, and electron paramagnetic resonance−(EPR) spectroelectrochemistry (SEC) were performed to investigate the redox stability in different redox states as a function of the number of MIC units bound to the Ru(II) center. Time-resolved absorption and emission spectroscopic studies were performed

https://doi.org/10.1021/acsorginorgau.3c00005
ACS Org. Inorg. Au 2023, 3, 184−198

to explore the influence of the MIC moiety on the electronic structure, with the aim to assess their potential application as photocatalysts in the future.

RESULTS AND DISCUSSION

Synthesis and Characterization

The synthesis of $[\mathbf{HL}]\mathbf{BF_4}$ as ligand precursor was performed according to a modified literature procedure.[52] The reductive cleavage of the *N*-oxide at the pyridyl-triazole, after methylation with Meerwein's salt, was realized using activated zinc in refluxing methanol overnight, instead of the expensive and toxic $[Mo(CO)_6]$, yielding nearly quantitative yields of 91% (see Supporting Information, Scheme S1).[53]

In order to obtain the complexes $[\mathbf{RuL_1}]^{2+}$, $[\mathbf{RuL_2}]^{2+}$, and $[\mathbf{RuL_3}]^{2+}$, different synthetic strategies were used (Path **A**, Path **B**, and Path **C**, Scheme 1). $[\mathbf{RuL_1}]^{2+}$ was synthesized based on a previously reported route.[17,54] In the first step, the ligand **L** is generated in situ and transferred to form the respective $[(\mathbf{L})Ru(p\text{-cymene})Cl](PF_6)$ complex via the well-established silver(I)-transmetalation route. After purification by column chromatography on alumina, the 1,2,3-triazolylidene half-sandwich complex was further reacted with bpy in the presence of $AgPF_6$ in ethylene glycol at 150 °C.

Aqueous workup with KPF_6, followed by column chromatography on alumina gave $[\mathbf{RuL_1}]^{2+}$ in 74% yield (see Supporting Information, Section S2.30). These results are in good agreement with the previously described yields for 1,2,3-triazolylidene-based Ru(II) bpy complexes.[17,40,54]

In contrast, synthetic access to $[\mathbf{RuL_2}]^{2+}$ and $[\mathbf{RuL_3}]^{2+}$ has proven to be challenging. The isolation of $[\mathbf{RuL_2}]^{2+}$, following the well-established synthetic approaches for similar reported NHC-based Fe(II) and Ru(II) complexes, resulted in a poor selectivity and purity of the crude product, making the isolation of $[\mathbf{RuL_2}]^{2+}$ difficult.[59−66] Therefore, we changed our strategy accordingly to Path **B**.[55−57]

The resulting crude product (see Supporting Information, Section S2.40) points to the formation of at least two regioisomers as indicated by ^{1}H NMR and $^{13}C\{H\}$ NMR spectroscopy, elemental analysis, and ESI-ToF-MS. Two well-separated methyl groups of two chemical inequivalent **L** at 4.52 and 4.40 ppm are observed in the ^{1}H NMR spectra, while the $^{13}C\{H\}$ NMR spectra show two signals of the methyl groups at 39.98 and 39.50 ppm besides two MIC-carbene signals at 188.29 and 186.62 ppm.

Upon recrystallization in acetone/Et_2O by slow diffusion at room temperature, the main product decomposes in the presence of light, indicated by a drastic color change from orange to dark brown. After one month single crystals suitable for X-ray diffraction were isolated from the crude product mixture (16%, see Supporting Information, Section S2.40). Complete characterization of the isolated product indicated the isolation of the minor product of higher symmetry. The two methyl groups of **L** show a total integral of 6 H at 4.42 ppm and one methyl group at 39.65 ppm in the $^{13}C\{H\}$ NMR next to the MIC-carbene signal at 185.09 ppm. The total number of 17 carbon signals underlines the higher symmetry of isolated $[\mathbf{RuL_2}]^{2+}$. Unfortunately, ^{1}H NMR spectroscopy of the remaining crude product solution clearly shows the decomposition of the main product during crystallization. Any attempt to identify the nature of the decomposition product remained unsuccessful.

Direct synthesis of $[\mathbf{RuL_3}]^2$, starting from $RuCl_3{\cdot}xH_2O$ as described by Son et al.,[57] resulted in a crude reaction mixture. We were not able to isolate the pure product due to the decomposition of $[\mathbf{RuL_3}]^{2+}$ during column chromatography (SiO_2 and basic/neutral aluminum oxide). Therefore, we focused our attention on the right choice of precursor to achieve good product selectivity combined with an easy workup of the crude product.

As a precursor, we chose the homoleptic $[Ru(MeCN)_6]^{2+}$ complex (see Supporting Information, Section S2.50). Starting from $RuCl_3{\cdot}xH_2O$, activated zinc in acetonitrile was added as a reducing agent. The reaction mixture was refluxed for 2 days. After filtration, $AgBF_4$ was added to abstract the chloride ligand in the remaining $[RuCl_2(MeCN)_4]$, yielding 81% of $[Ru(MeCN)_6](BF_4)_2$.[58]

With the precursor in hand, we started reinvestigating the literature procedure of Son et al.[57] and observed a higher product selectivity for $[\mathbf{RuL_3}]^{2+}$. The addition of K_2CO_3 led to an even higher selectivity and allowed milder reaction temperatures of 160 °C. Direct crystallization (slow diffusion/vapor diffusion) of the crude product in common solvents at room temperature, close to 0 °C, or lower temperatures (up to −20 °C) failed.

To avoid precipitation, the crude product was dissolved in acetone and cooled with liquid nitrogen until the mixture solidified. Et_2O was added and cooled with liquid nitrogen until it solidified, too. The capped flask was transferred to a freezer to avoid decomposition in the presence of light and stored for 1 month at −20 °C resulting in dark orange crystals (46%) suitable for single X-ray diffraction analysis.

In the molecular structure of the crystal, all complexes $[\mathbf{RuL_1}]^{2+}$, $[\mathbf{RuL_2}]^{2+}$, and $[\mathbf{RuL_3}]^{2+}$ display a distorted octahedral geometry (Figure 2). All bond angles along the axis in the Ru(II) center range between 169 and 177°, while the C−Ru−N and N−Ru−N angles are between 77 and 79°. The Ru-bond lengths are in the range of 2.05−2.16 Å, slightly longer than the respective Ru−C bond lengths (1.99−2.06 Å). Interestingly, the M−C bonds in $[\mathbf{RuL_3}]^{2+}$, which are trans to each other show longer bond distances (2.06 Å) compared to the M−C (1.99 Å) bond trans to the M−N bond (2.17 Å). A plausible explanation is the increased trans-influence caused by the strong σ-donating properties of the MIC-carbenes. The bond length and angles of the chelating ligands are within the expected range.[9,17,19,24,67,68]

(Spectro)Electrochemistry and (TD)DFT Calculations

Cyclic Voltammetry. To investigate the influence of the total number of pyridyl-MICs in the complexes $[\mathbf{RuL_1}]^{2+}$, $[\mathbf{RuL_2}]^{2+}$, and $[\mathbf{RuL_3}]^{2+}$, cyclic voltammetry, UV/Vis/NIR-, EPR-SEC, and (TD)DFT calculations were performed. The electrochemical investigations provide further evidence for the HOMO/LUMO gap in the presented pyridyl-MIC-containing Ru(II) complexes.

All complexes exhibit redox-rich cyclic voltammograms with one reversible oxidation and multiple reductions (Figures 3 and S13−S15).

In the reported complexes, oxidation can be assigned to a predominantly metal-centered Ru(II)/Ru(III) redox couple (see Figure 7, EPR-SEC). The incorporation of one or more MIC units shifts the oxidation potential to more cathodic potential. Taking the archetypical complex $[\mathbf{Ru(bpy)_3}]^{2+}$ into account, a shift between 140 and 190 mV per MIC unit can be estimated for the oxidation (Figures 3, 4, and Table 1).[17,69,70]

https://doi.org/10.1021/acsorginorgau.3c00005
ACS Org. Inorg. Au 2023, 3, 184−198

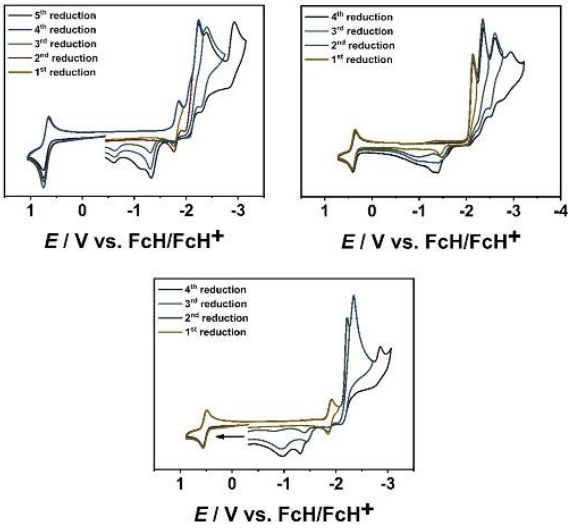

Figure 3. Cyclic voltammograms of $[\mathbf{RuL_1}]^{2+}$ (top left), $[\mathbf{RuL_1}]^{2+}$ (bottom center), and $[\mathbf{RuL_3}]^{2+}$ (top right) in CH_3CN and 0.1 M Bu_4NPF_6 with a scan rate of 100 mV/s.

This is in good agreement with previously reported oxidation potentials for MIC-containing Ru(II) complexes.[17] Considering earlier reports by Albrecht and co-workers, the replacement of the phenyl substituent by an electron-donating methyl substituent at the N^1 position further destabilizes the metal-centered HOMO, as indicated by the decreased oxidation potential.[40]

The first reduction is primarily determined by the π-acceptor properties of the ligand. Since bpy is a better π-acceptor than the pyridyl-MIC ligand **L**, the first reduction processes in $[\mathbf{RuL_1}]^{2+}$ and $[\mathbf{RuL_2}]^{2+}$ are bpy-based (Figure 7, EPR-SEC), resulting in a reversible first reduction around −1.85 V. Similar observations have been made for bpy-containing Ru(II)MIC complexes.[17,40] The influence of **L** on the reduction potential is particularly evident in the complex $[\mathbf{RuL_3}]^{2+}$, containing only **L**. The reduction potentials display a cathodic shift from $[\mathbf{Ru(bpy)_3}]^{2+}$ to $[\mathbf{RuL_1}]^{2+}$ and $[\mathbf{RuL_2}]^{2+}$ by about 100 mV. Going from $[\mathbf{RuL_2}]^{2+}$ to $[\mathbf{RuL_3}]^{2+}$, a shift of 250 mV in the reduction potential is observed, indicating a strong change in the π-acceptor properties of the complex. However, $[\mathbf{RuL_3}]^{2+}$ displays only irreversible reduction processes. The electron-rich nature of $[\mathbf{RuL_3}]^{2+}$ could lead to dissociation of the ligand arm upon reduction, as described for analogous electron-rich Ru(II) terpyridine complexes.[71]

UV/Vis/NIR- and EPR-SEC. To gain a detailed insight into the redox stability and the nature of the metal-centered oxidation, as well as the ligand-centered reduction, EPR-, and UV/Vis/NIR-SEC were performed on $[\mathbf{RuL_1}]^{2+}$, $[\mathbf{RuL_2}]^{2+}$, and $[\mathbf{RuL_3}]^{2+}$.

In the native form, all three complexes exhibit MLCT bands in the region of 300−550 nm as described for similar systems (Figure 4).[17,42,61,69] Time-dependent density functional theory (TD-DFT) calculations (see Supporting Information, Sections S7.10−S7.30) assign the electronic transitions from a metal d-orbital to a uniformly distributed ligand-centered charge transfer (d(Ru) → π^*(L)) to all ligands.

Upon oxidation, all MLCT bands diminish and new bands appear in the 535−830 nm range (Figure 5). In the case of $[\mathbf{RuL_1}]^{3+}$, the bands can be assigned to a metal−ligand to metal (MLMCT) charge transfer (see Supporting Information, Section S7.10). However, the picture changes drastically when moving from $[\mathbf{RuL_1}]^{3+}$ to $[\mathbf{RuL_2}]^{3+}$ and $[\mathbf{RuL_3}]^{3+}$. The metal contribution significantly decreases, shifting the mixed MLMCT to a dominant ligand to metal (LMCT) charge transfer in the case of $[\mathbf{RuL_3}]^{3+}$ (Figure 6, see Supporting Information, Section S7.30).

Similar observations were made by Kalyanasundaram and co-workers.[72] The incorporation of strong σ-donating ligands with good π-accepting ligands in Ru(III) complexes leads to a

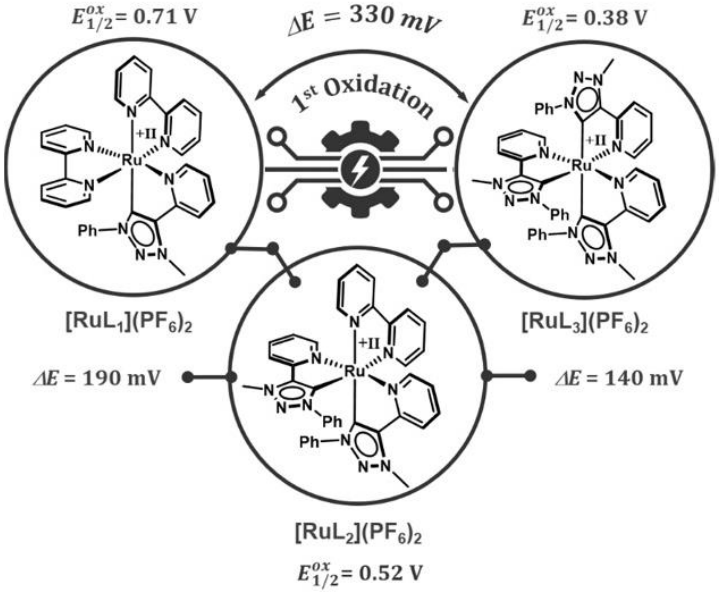

Figure 4. Effect of incorporating MIC moieties on the oxidation potential in $[\mathbf{RuL_1}]^{2+}$, $[\mathbf{RuL_2}]^{2+}$, and $[\mathbf{RuL_3}]^{2+}$.

https://doi.org/10.1021/acsorginorgau.3c00005
ACS Org. Inorg. Au 2023, 3, 184−198

ACS Organic & Inorganic Au pubs.acs.org/orginorgau Article

Table 1. Redox Potentials of $[RuL_1]^{2+}$, $[RuL_2]^{2+}$, $[RuL_3]^{2+}$, and $[Ru(bpy)_3]^{2+}$[69,70] in CH_3CN and 0.1 M NBu_4PF_6 at 100 mV/s vs FcH/FcH^+

	$E^{ox}_{1/2}$ (ΔE) (V)	$E^{red1}_{1/2}$(ΔE) (V)	E^{red2}_{P} (V)	E^{red3}_{P} (V)	E^{red4}_{P} (V)	E^{red5}_{P} (V)
$[RuL_1]^{2+}$	0.71(0.11)	−1.81(0.09)	−2.02	−2.11	−2.34	−2.89
$[RuL_2]^{2+}$	0.52(0.10)	−1.89(0.08)	−2.22	−2.34	−2.86	
$[RuL_3]^{2+}$	0.38(0.08)	−2.14[a]	−2.31	−2.56	−2.85	
$[Ru(bpy)_3]^{2+}$	0.89	−1.73	−1.92	−2.16		

[a] $E^{red1}_{1/2} = E^{red1}_{P}$.

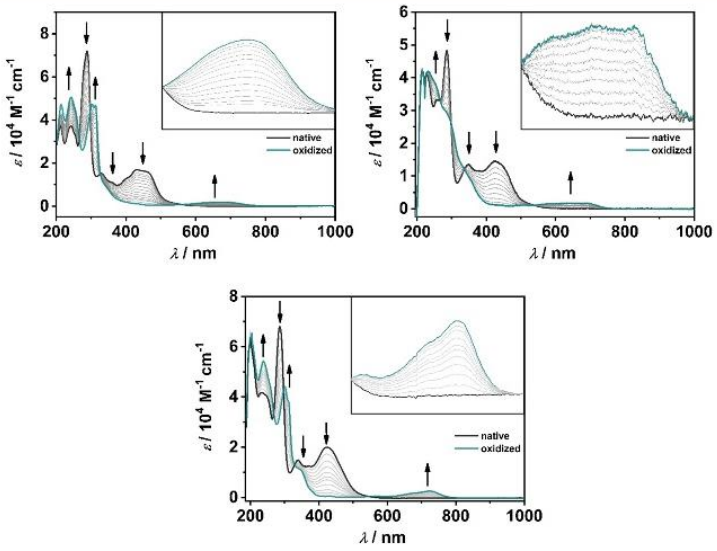

Figure 5. Changes in the UV/vis/NIR spectra of $[RuL_1]^{2+}$ (top left, inset: 560−810 nm), $[RuL_2]^{2+}$ (bottom center, inset: 550−830 nm), and $[RuL_3]^{2+}$ (top right, inset: 535−780 nm) in CH_3CN/0.1 M Bu_4NPF_6 during the first oxidation with a Au working electrode.

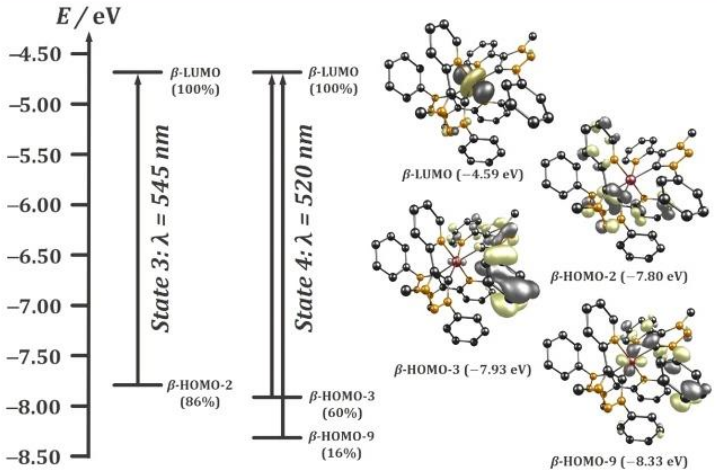

Figure 6. Involved molecular orbitals in LMCT of complex $[RuL_3]^{3+}$ calculated by TD-DFT (PBE0/RIJCOSX/D3(BJ)/def2-TZVP/CPCM, iso value = 0.052).

larger mixing of the metal d(π)-orbitals with the π^*-orbitals of the π-accepting ligand. The resulting HOMO-orbitals display a stronger mixed-metal−ligand character. In contrast, electron-rich ligands with weak π-acceptor properties result in predominantly ligand-centered HOMO-orbitals of the homoleptic Ru(III).

Interestingly, the contribution in the LMCT is not only limited to the pyridyl-MIC framework but also to the phenyl substituent on the triazolylidene moiety, revealing the strong impact of the substituents on the stability and photoredox chemistry in $[RuL_2]^{3+}$ and $[RuL_3]^{3+}$.[13,44] Notably, the reduction of the oxidized $[RuL_1]^{3+}$, $[RuL_2]^{3+}$, and $[RuL_3]^{3+}$ restores the starting spectra indicating a completely reversible

https://doi.org/10.1021/acsorginorgau.3c00005
ACS Org. Inorg. Au 2023, 3, 184−198

Table 2. Spectroscopic Data of $[RuL_1]^{2+}$, $[RuL_2]^{2+}$, $[RuL_3]^{2+}$, and $[Ru(bpy)_3]^{2+}$ in MeCN

	λ_{em} (nm)	τ_{abs} (ns)	Φ_{em} (%)	E_{00} (eV)	τ_{em} (ns)
$[RuL_1]^{2+}$	594, 649	71[a]	0.88[e]	2.21	62[f]
$[RuL_2]^{2+}$	597, 640	99[b], 103[c]	1.05[e]	2.07	99[g]
$[RuL_3]^{2+}$	610, 653	26, 344[d,i]	0.64[e]	2.07	28, 288[h,i]
$[Ru(bpy)_3]^{2+}$	611[80]	890[80]	5.9[80]	2.10[69]	890[80]

[a]At λ = 368 nm (λ_{ex} = 460 nm). [b]λ = 370 nm (λ_{ex} = 430 nm). [c]λ = 420 nm (λ_{ex} = 430 nm). [d]at λ = 420 nm (λ_{ex} = 435 nm). [e]Average out of 5 measurements. [f]At λ = 620 nm (λ_{ex} = 460 nm). [g]At λ = 660 nm (λ_{ex} = 370 nm). [h]At λ = 644 nm (λ_{ex} = 435 nm). [i]The biexponential decay behavior is tentatively attributed to a photodegradation process (Figure S68).

$[RuL_1]^{2+}$, $[RuL_2]^{2+}$, and $[RuL_3]^{2+}$ show emission spectra with typical vibrational structures for polypyridine Ru(II) complexes in the 600−900 nm range.[79] Such systems typically show a fast intersystem crossing (k_{isc}) from the ^{1}MLCT state to the ^{3}MLCT state upon excitation. The thermal population (E_a) of the ^{3}MC state from the $^{1/3}$MLCT nesting states results in a nonradiative decay (k_{nr}). MICs as strong σ-donor ligands can destabilize the metal-centered ^{3}MC state, while the π-acceptor properties of the pyridyl moiety lead to the stabilization of the $^{1/3}$MLCT state. Consequently, the energy barrier for E_a increases, disfavoring quenching of the ^{3}MLCT state.[48−50]

However, the incorporation of pyridyl-MIC ligands leads to a decrease in the lifetimes of the ^{3}MLCT excited state (τ_{abs}) in all three cases compared to the well-established $[Ru(bpy)_3]^{2+}$ (Table 2).[17,40,80] The same trend is observed for the photoluminescence quantum yields.

After irradiation of $[RuL_3]^{2+}$, decomposition products emitting in the range of 400−550 nm are formed (Figure S64), featuring luminescence lifetimes in the order of 16−28 ns (Figure S67). This decomposition process is significantly less prevalent at lower temperatures. It seems plausible that the thermal population of the ^{3}MC state plays a decisive role in the photo-decomposition of $[RuL_3]^{2+}$. The population of the e_g^*-orbitals can result in dissociation of the electron-rich pyridyl-MIC ligand, while steric bulk and an unsymmetrical geometry (Table S1) around the Ru(II) center can potentially further lower the ligand field strength, giving access to a fast population of the ^{3}MC state.[48,49,71,81−83]

The MLCT excited state lifetimes of $[RuL_1]^{2+}$, $[RuL_2]^{2+}$, and $[RuL_3]^{2+}$ at 293 K are long enough to allow for photo-induced electron transfer reactions in photocatalysis, or for electron injection into semiconductors.[84,85] Interestingly, comparison of the excited state ^{3}MLCT energies (E_{00}) of $[RuL_1]^{2+}$, $[RuL_2]^{2+}$, and $[RuL_3]^{2+}$ with $[Ru(bpy)_3]^{2+}$ shows that the incorporation of the pyridiyl-MIC ligand does not significantly change the relative energy of E_{00}.

Combining the oxidation or reduction potentials of the ground states with the excited state ^{3}MLCT energies (E_{00}) allows us to estimate the potentials for the oxidative $^*E_{red}$ and reductive $^*E_{ox}$ quenching of the ^{3}MLCT states to assess the application potential of the presented complexes as photocatalysts or photosensitizers, as illustrated in a Latimer diagram (Table 3).

These results indicate that the redox potentials of the excited states of such ruthenium complexes can indeed be tuned over a broad range, making metal complexes containing MIC ligands interesting candidates for photocatalytic applications.

CONCLUSIONS

In summary, a series of three new pyridyl-MIC-based Ru(II) complexes were synthesized and fully characterized by ^{1}H and ^{13}C NMR spectroscopy, mass spectrometry, elemental analysis, and single-crystal X-ray diffraction. Cyclic voltammetry reveals an interesting trend: the incorporation of an MIC moiety in the Ru(II) polypyridine complex shifts the metal-centered reversible oxidation by ∼160 mV to a more cathodic potential, while the first bpy-centered reduction shifts by ∼100 mV to a more negative potential after an additional MIC unit is incorporated. The replacement of all bpy ligands by the strongly electron-donating pyridyl-MIC ligand **L** shifts the reduction potential up by 250 mV. The changes in the electronic structures of the different redox states were further investigated using EPR- and UV/Vis/NIR-SEC and supported by (TD)DFT. Upon oxidation, the MLLCT character of $[RuL_1]^{3+}$ is reverted to a dominant LMCT going to $[RuL_3]^{3+}$. Our photophysical investigations showed that within the series

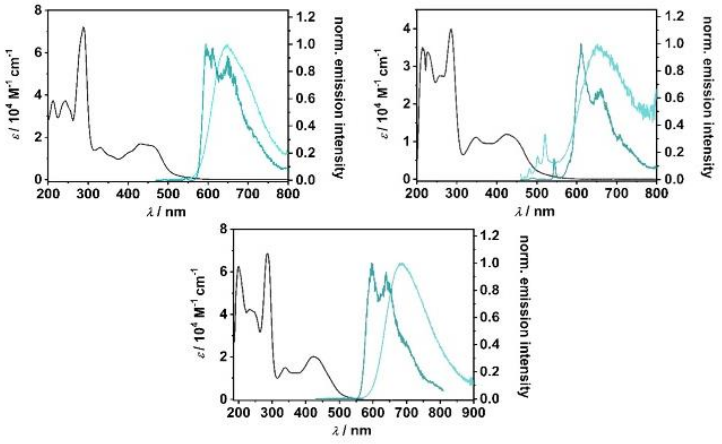

Figure 9. UV/Vis absorption (black) at 293 K and normalized emission spectra at 293 K (light blue line) and 77 K (dark blue line) of $[RuL_1]^{2+}$ (top left, excited at 460 nm), $[RuL_2]^{2+}$ (bottom center, excited at rt: 460 nm and 77 K: 420 nm), and $[RuL_3]^{2+}$ (top right, excited at 450 nm).

https://doi.org/10.1021/acsorginorgau.3c00005
ACS Org. Inorg. Au 2023, 3, 184−198

Table 2. Spectroscopic Data of $[RuL_1]^{2+}$, $[RuL_2]^{2+}$, $[RuL_3]^{2+}$, and $[Ru(bpy)_3]^{2+}$ in MeCN

	λ_{em} (nm)	τ_{abs} (ns)	Φ_{em} (%)	E_{00} (eV)	τ_{em} (ns)
$[RuL_1]^{2+}$	594, 649	71[a]	0.88[e]	2.21	62[f]
$[RuL_2]^{2+}$	597, 640	99[b], 103[c]	1.05[e]	2.07	99[g]
$[RuL_3]^{2+}$	610, 653	26, 344[d,i]	0.64[e]	2.07	28, 288[h,i]
$[Ru(bpy)_3]^{2+}$	611[80]	890[80]	5.9[80]	2.10[69]	890[80]

[a]At λ = 368 nm (λ_{ex} = 460 nm). [b]λ = 370 nm (λ_{ex} = 430 nm). [c]λ = 420 nm (λ_{ex} = 430 nm). [d]at λ = 420 nm (λ_{ex} = 435 nm). [e]Average out of 5 measurements. [f]At λ = 620 nm (λ_{ex} = 460 nm). [g]At λ = 660 nm (λ_{ex} = 370 nm). [h]At λ = 644 nm (λ_{ex} = 435 nm). [i]The biexponential decay behavior is tentatively attributed to a photodegradation process (Figure S68).

$[RuL_1]^{2+}$, $[RuL_2]^{2+}$, and $[RuL_3]^{2+}$ show emission spectra with typical vibrational structures for polypyridine Ru(II) complexes in the 600−900 nm range.[79] Such systems typically show a fast intersystem crossing (k_{isc}) from the ^{1}MLCT state to the ^{3}MLCT state upon excitation. The thermal population (E_a) of the ^{3}MC state from the $^{1/3}$MLCT nesting states results in a nonradiative decay (k_{nr}). MICs as strong σ-donor ligands can destabilize the metal-centered ^{3}MC state, while the π-acceptor properties of the pyridyl moiety lead to the stabilization of the $^{1/3}$MLCT state. Consequently, the energy barrier for E_a increases, disfavoring quenching of the ^{3}MLCT state.[48−50]

However, the incorporation of pyridyl-MIC ligands leads to a decrease in the lifetimes of the ^{3}MLCT excited state (τ_{abs}) in all three cases compared to the well-established $[Ru(bpy)_3]^{2+}$ (Table 2).[17,40,80] The same trend is observed for the photoluminescence quantum yields.

After irradiation of $[RuL_3]^{2+}$, decomposition products emitting in the range of 400−550 nm are formed (Figure S64), featuring luminescence lifetimes in the order of 16−28 ns (Figure S67). This decomposition process is significantly less prevalent at lower temperatures. It seems plausible that the thermal population of the ^{3}MC state plays a decisive role in the photo-decomposition of $[RuL_3]^{2+}$. The population of the e_g^*-orbitals can result in dissociation of the electron-rich pyridyl-MIC ligand, while steric bulk and an unsymmetrical geometry (Table S1) around the Ru(II) center can potentially further lower the ligand field strength, giving access to a fast population of the ^{3}MC state.[48,49,71,81−83]

The MLCT excited state lifetimes of $[RuL_1]^{2+}$, $[RuL_2]^{2+}$, and $[RuL_3]^{2+}$ at 293 K are long enough to allow for photo-induced electron transfer reactions in photocatalysis, or for electron injection into semiconductors.[84,85] Interestingly, comparison of the excited state ^{3}MLCT energies (E_{00}) of $[RuL_1]^{2+}$, $[RuL_2]^{2+}$, and $[RuL_3]^{2+}$ with $[Ru(bpy)_3]^{2+}$ shows that the incorporation of the pyridyl-MIC ligand does not significantly change the relative energy of E_{00}.

Combining the oxidation or reduction potentials of the ground states with the excited state ^{3}MLCT energies (E_{00}) allows us to estimate the potentials for the oxidative $^*E_{red}$ and reductive $^*E_{ox}$ quenching of the ^{3}MLCT states to assess the application potential of the presented complexes as photocatalysts or photosensitizers, as illustrated in a Latimer diagram (Table 3).

These results indicate that the redox potentials of the excited states of such ruthenium complexes can indeed be tuned over a broad range, making metal complexes containing MIC ligands interesting candidates for photocatalytic applications.

CONCLUSIONS

In summary, a series of three new pyridyl-MIC-based Ru(II) complexes were synthesized and fully characterized by ^{1}H and ^{13}C NMR spectroscopy, mass spectrometry, elemental analysis, and single-crystal X-ray diffraction. Cyclic voltammetry reveals an interesting trend: the incorporation of an MIC moiety in the Ru(II) polypyridine complex shifts the metal-centered reversible oxidation by ∼160 mV to a more cathodic potential, while the first bpy-centered reduction shifts by ∼100 mV to a more negative potential after an additional MIC unit is incorporated. The replacement of all bpy ligands by the strongly electron-donating pyridyl-MIC ligand **L** shifts the reduction potential up by 250 mV. The changes in the electronic structures of the different redox states were further investigated using EPR- and UV/Vis/NIR-SEC and supported by (TD)DFT. Upon oxidation, the MLLCT character of $[RuL_1]^{3+}$ is reverted to a dominant LMCT going to $[RuL_3]^{3+}$. Our photophysical investigations showed that within the series

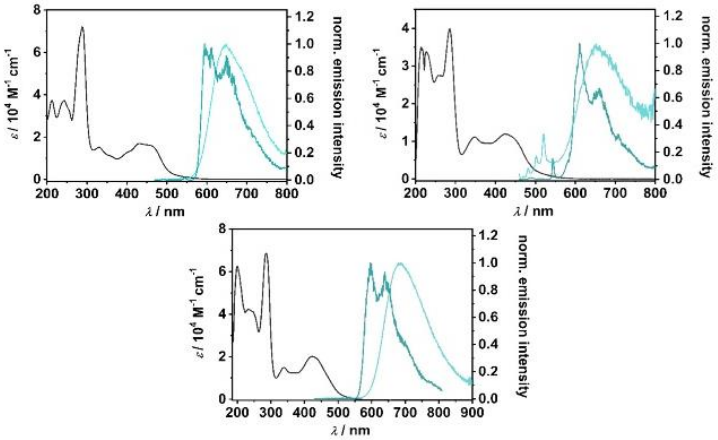

Figure 9. UV/Vis absorption (black) at 293 K and normalized emission spectra at 293 K (light blue line) and 77 K (dark blue line) of $[RuL_1]^{2+}$ (top left, excited at 460 nm), $[RuL_2]^{2+}$ (bottom center, excited at rt: 460 nm and 77 K: 420 nm), and $[RuL_3]^{2+}$ (top right, excited at 450 nm).

https://doi.org/10.1021/acsorginorgau.3c00005
ACS Org. Inorg. Au 2023, 3, 184−198

ACS Organic & Inorganic Au pubs.acs.org/orginorgau Article

Table 3. Latimer Diagram with Relevant Potentials for Photoexcitation[86,a,b]

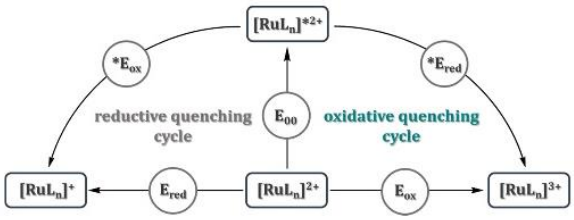

	E_{red} (V)	E_{ox} (V)	$^*E_{red}$ (V)	$^*E_{ox}$ (V)	E_{00} (eV)
$[RuL_1]^{2+}$	−1.43	1.09	1.12	−0.78	2.21
$[RuL_2]^{2+}$	−1.51	0.90	1.17	−0.56	2.07
$[RuL_3]^{2+}$	−1.76	0.76	1.29	−0.29	2.05
$[Ru(bpy)_3]^{2+}$[69]	−1.34	1.27	0.83	−0.76	2.10

[a]The data in the table shows that $^*E_{red}$ follow the trend $[Ru(bpy)_3]^{2+} < [RuL_1]^{2+} < [RuL_2]^{2+} < [RuL_3]^{2+}$. A similar observation was already described by Suntrup et al. exploring the influence of pyridyl-MICs and bi-MICs on Ru(II) and Os(II) bipyridine complexes. Increasing the number of MICs within the transition metal complexes results in higher $^*E_{red}$,[17] making them in particular attractive as photoreductant, while the oxidative quenching potential $^*E_{ox}$ follows the trend $[Ru(bpy)_3]^{2+} \approx [RuL_1]^{2+} > [RuL_2]^{2+} > [RuL_3]^{2+}$, demonstrating the strong electron-donating nature of the MIC ligands. [b]All potentials with FcH/FcH^+ were converted vs SCE = 0.38 V in MeCN/0.1 M NBu_4PF_6 at room temperature.

from $[RuL_1]^{2+}$ to $[RuL_2]^{2+}$, and $[RuL_3]^{2+}$, the excited-state reduction potential $^*E_{red}$ increases and the excited-state oxidation potential $^*E_{ox}$ becomes less negative. The MLCT lifetimes are within the expected range and in combination with the electrochemical data, a new series of potential photocatalysts could be developed. The presented complexes are in particular interesting as photoreductants, while the incorporation of the strongly σ-donating pyridyl-MIC ligands decreases the photooxidative capability. Extrapolation of the total number of MICs incorporated in Ru(II) complexes could even lead to stable Ru(III) metal complexes opening up new opportunities for photosensitizers and photocatalytic applications.

EXPERIMENTAL SECTION

General Procedures, Materials, and Instrumentation

Caution!: Compounds containing azides are potentially explosive. Although we never experienced any problems during synthesis or analysis, all compounds should be synthesized only in small quantities and handled with great care!

Unless otherwise noted, all reactions were carried out using standard Schlenk line techniques under an inert atmosphere of argon (Linde Argon 4.8, purity 99.998%). All reactions which require heating were performed with an oil bath.

Commercially available chemicals were used without further purification. The solvents used for metal complex synthesis and catalysis were available from MBRAUN MB-SPS-800 solvent system and degassed by standard techniques prior to use. The identity and purity of compounds were established via ^1H and $^{13}C\{H\}$ NMR spectroscopy, elemental analysis, and mass spectrometry.

Solvents for cyclic voltammetry and UV/vis- and EPR-spectroelectrochemical measurements were dried and distilled under argon and degassed by common techniques prior to use. Column chromatography was performed over silica 60 M (0.04−0.063 mm).

^1H and $^{13}C\{^1H\}$ NMR spectra were recorded on a Bruker Avance 500 spectrometer at 19−22 °C. Chemical shifts are reported in ppm referenced to the residual solvent peaks.[87]

The following abbreviations are used to represent the multiplicity of the signals: s (singlet), d (doublet), t (triplet), q (quartet), p (pentet), sept (septet).

Mass spectrometry was performed on an Agilent 6210 ESI-TOF.

Elemental analyses were performed with an Elementar Micro Cube elemental analyzer.

X-ray Diffraction

X-ray data were collected on a BRUKER Smart AXS, BRUKER D8 Venture, or Bruker Kappa Apex2duo system. Data were collected at 100(2) or 140(2) K, respectively, using graphite-monochromatic Mo Kα radiation (λ_α = 0.71073 Å). The strategy for the data collection was evaluated by using the APEX2 or Smart software. The data were collected by standard "ω scan techniques" or "$\omega-\varphi$ scan techniques" and were scaled and reduced using APEX2, SAINT+, and SADABS software.

The structures were solved by direct methods using SHELXL-97 or intrinsic phasing using SHELXL-2014/7 and refined by full-matrix least squares with SHELXL-2014/7, refining on F^2. Nonhydrogen atoms were refined anisotropically. If it is noted, bond length and angles were measured with Mercury, version 3.8.[88−95]

Electrochemistry

Cyclic voltammograms were recorded with a Metrohm Autolab potentiostat (PGSTAT 204) with a conventional three-electrode configuration consisting of a glassy carbon working electrode, a platinum auxiliary electrode, and a coiled silver wire as a pseudo reference electrode. The (decamethyl)ferrocene/(decamethyl)-ferrocenium couple was used as internal reference. All measurements were performed at room temperature with a scan rate between 25 and 1000 mV s^{-1}. The experiments were carried out in absolute acetonitrile containing 0.1 M Bu_4NPF_6 (Sigma-Aldrich, ≥99.0%, electrochemical grade) as the supporting electrolyte.

Spectroelectrochemistry

UV/vis spectra were recorded with a J&M TIDAS spectrometer. UV/vis-spectroelectrochemical measurements were carried out in an optically transparent thin-layer electrochemical (OTTLE)[96] cell (CaF_2 windows) with a gold-mesh working electrode, a platinum-mesh counter electrode, and a silver-foil pseudo reference. EPR spectra at the X-band frequency (ca. 9.5 GHz) were obtained with a Magnettech MS-5000 benchtop EPR spectrometer equipped with a rectangular TE 102 cavity and a TC HO4 temperature controller. The measurements were carried out in synthetic quartz glass tubes. For EPR spectroelectrochemistry, a three-electrode setup was employed using two Teflon-coated platinum wires (0.005 in. bare and 0.008 in. coated) as the working and counter electrodes and a Teflon-coated silver wire (0.005 in. bare and 0.007 in. coated) as the pseudo reference electrode. The low-temperature EPR spectra were recorded at −175 °C. The experiments were carried out in absolute acetonitrile or CH_2Cl_2 containing 0.1 M Bu_4NPF_6 as the supporting electrolyte. The same solvents as for the CV measurements were used for each compound.

DFT

The program package ORCA 4.1. was used for all DFT calculations.[97] Starting from the molecular structure obtained from X-ray diffraction geometry optimizations were carried out using the PBE0[98] functional and no symmetry restrictions were imposed during the optimization. All calculations were performed with empirical van der Waals correction (D3).[99−102] The restricted and unrestricted DFT methods were employed for closed- and open-shell molecules, respectively, unless stated otherwise. Convergence criteria were set to default for geometry optimization (OPT), and tight for SCF calculations (TIGHTSCF). Triple-ζ-valence basis sets (def2-TZVP)[103] were employed for all atoms. Calculations were performed using resolution of the identity approximation[104−110] with matching auxiliary basis sets[111,112] for geometry optimizations and numerical frequency calculations and the RIJCOSX (combination of the resolution of the identity and chain of spheres algorithms) approximation for single-point calculations using the PBE0 functional.[98] Low-lying

https://doi.org/10.1021/acsorginorgau.3c00005
ACS Org. Inorg. Au 2023, 3, 184−198

excitation energies were calculated with time-dependent DFT (TD-DFT). Solvent effects were taken into account with the conductor-like polarizable continuum model, CPCM.[113] Spin densities were calculated according to the Mulliken population analysis.[114] The absence of imaginary frequency spin densities, molecular orbitals, and difference densities were visualized with the Chemcraft 1.8 program.[115] All molecular orbitals are illustrated with an iso value of 0.052. All calculated TD-DFT spectra are Gaussian broadened with a bandwidth of 25 nm at half-height.

Photophysical Measurements

Steady-state luminescence spectra at room temperature and 77 K were measured using a Fluorolog-3-22 instrument from Horiba Jobin-Yvon. Transient absorption and kinetic emission and absorption measurements were performed on an LP920-KS instrument from Edinburgh Instruments in MeCN. Excitation source was a pulsed Quantel Brilliant b ND:YAG laser equipped with a Rainbow optical parameter oscillator (OPO) with a pulse energy of 13 mJ at 435 nm and 20 mJ at 460 nm. The solutions typically had an optical density below 0.4 and were deaerated through three cycles of freeze−pump−thaw. The quantum yields were measured on a Hamamatsu absolute photoluminescence quantum yield spectrometer C11347 Quantaurus QY with a sample concentration of 2.5×10^{-5} M, and the solutions were deaerated by bubbling Ar for 10 min.

SYNTHETIC PROCEDURES

Synthetic Strategy for $[HL]BF_4$

According to a modified procedure, the triazole-containing *N*-oxide [HL−O] (1.04 g, 3.21 mmol) was dissolved in 20 mL of CH_2Cl_2. Me_3OBF_4 (1.04 g, 7.03 mmol) was added, and the mixture was stirred at room temperature for 5 days. The solvent was evaporated and the residue was suspended in abs. MeOH (80 mL). Activated zinc (0.835 g, 12.84 mmol) was added and heated under reflux overnight. The reaction mixture was filtered through celite and purified by column chromatography CH_2Cl_2/MeOH (10:1) to obtain the product as an off-white solid (0.74 g, 2.92 mmol, 91%). ^{1}H NMR (400 MHz, CD_3CN) δ (ppm) = 9.23 (s, 1H), 8.89−8.82 (m, 1H), 8.10 (td, J = 7.8, 1.7 Hz, 1H), 8.03−7.89 (m, 3H), 7.80−7.72 (m, 3H), 7.68−7.62 (m, 1H), 4.66 (s, 3H); ^{13}C {^{1}H} NMR (101 MHz, CD_3CN) δ (ppm) = 151.4, 143.9, 142.7, 139.4, 136.0, 133.2, 131.6, 128.3, 127.2, 125.7, 122.7, 42.1; Anal. calcd for $C_{14}H_{13}BF_4N_4$: C, 51.89, H, 4.04, N, 17.29; found: C, 51.99, H, 4.15, N, 17.29.[52,53]

Synthetic Strategy for $[RuL_1](PF_6)_2$

In a 15 mL Schlenk flask, the respective [Ru(L)(*p*-cymene)-Cl]BF_4 (50 mg, 0.084 mmol, 1 equiv), bipyridine (26 mg, 0.169 mmol, 2 equiv), and $AgPF_6$ (43 mg, 0.169 mmol, 2 equiv) were dissolved in degassed ethylene glycol (4 mL). The reaction mixture was capped and heated to 150 °C for 12 h. After cooling to room temperature, the resulting dark orange mixture was treated with aqueous KPF_6 and extracted with CH_2Cl_2 (3 × 40 mL). The organic phase was washed with water (5 × 50 mL) and dried over Na_2SO_4. Additional crystallization from slow diffusion of Et_2O into a concentrated solution of $[RuL_1](PF_6)_2$ dissolved in CH_2Cl_2 yielded in an orange crystalline solid of $[RuL_1](PF_6)_2$ (57 mg, 0.061 mmol, 72%). In the case of an insufficient conversion, purification by column chromatography (aluminum oxide, activated with 5 wt % water; CH_2Cl_2/acetone 100:0 → 100:15) resulted in pure $[RuL_1](PF_6)_2$.

Single crystals suitable for X-ray diffraction were obtained by slow vapor diffusion of Et_2O into a concentrated solution of $[RuL_1](PF_6)_2$ in acetone at 4 °C.

^{1}H NMR (500 MHz, CD_3CN) δ (ppm) = 8.45 (d, J = 8.2 Hz, 1H), 8.42 (d, J = 8.1 Hz, 1H), 8.35 (d, J = 5.6 Hz, 1H), 8.27 (d, J = 8.1 Hz, 1H), 8.16 (d, J = 8.1 Hz, 1H), 8.06−7.95 (m, 5H), 7.70−7.68 (m, 1H), 7.67 (d, J = 5.6 Hz, 1H), 7.61−7.56 (m, 2H), 7.43−7.36 (m, 3H), 7.27−7.21 (m, 2H), 7.20−7.16 (m, 1H), 7.08 (t, J = 8.0 Hz, 2H), 6.92 (dd, J = 8.4, 1.1 Hz, 2H), 6.82 (ddd, J = 7.3, 5.7, 1.3 Hz, 1H), 4.58 (s, 3H); ^{13}C{^{1}H} NMR (126 MHz, CD_3CN) δ (ppm) = 185.6, 158.0, 157.6, 157.5, 156.5, 156.5, 153.9, 153.0, 152.5, 152.1, 150.5, 146.8, 139.2, 139.0, 138.5, 138.1, 137.7, 137.2, 131.2, 130.3, 128.6, 128.3, 128.0, 127.4, 126.0, 125.912, 125.1, 124.8, 124.4, 124.1, 122.6, 39.9; HRMS (ESI) m/z: $[RuL_1](PF_6)^+$ calcd for $[C_{34}H_{27}F_6N_8PRu]^+$ 795.1126; found 795.1120, $[RuL_1]^{2+}$ calcd for $[C_{34}H_{28}N_8Ru]^{2+}$ 325.0739; found 325.0731; Anal. calcd for $C_{34}H_{28}F_{12}N_8P_2Ru$: C, 43.46, H, 3.00, N, 11.93; found: C, 43.60, H, 3.06, N, 11.60.

Synthetic Strategy for $[RuL_2](PF_6)_2$

In a 15 mL Schlenk flask, [Ru(bpy)(*p*-cymene)OTf]OTf (34 mg, 0.049 mmol, 1 equiv) and $[HL]BF_4$ (30 mg, 0.093 mmol, 2 equiv) were dissolved in degassed ethylene glycol (4 mL). The reaction mixture was capped and heated to 180 °C for 12 h. After cooling to room temperature, the resulting dark orange mixture was treated with aqueous KPF_6 and extracted with CH_2Cl_2 (3 × 40 mL). The organic phase was washed with water (5 × 50 mL) and dried over Na_2SO_4. The crude product was dry-loaded on Celite and purified by column chromatography (inversed column, interchim puriFlash XS 520 Plus, column: PF-15C18AQ-F0040; H_2O/CH_3CN 100:0 → 80:20). The crude product was extracted with CH_2Cl_2 (3 × 40 mL) and dried over Na_2SO_4. The solvent was removed under reduced pressure, and the remaining dark orange solid (23 mg, 0.022 mmol, 46% crude) was dissolved in $(CH_3)_2CO$ (3 mL) and overlayed with Et_2O under light. The dark orange solution turned dark brown after 2 days, and after 1 month, single crystals suitable for X-ray diffraction have been obtained.

The collected crystals were used as seed crystals to induce crystallization from the crude product in the follow-up reactions. The resulting red crystals (7.8 mg, 0.077 mmol, 16%) were used without further purification.

^{1}H NMR (700 MHz, CD_3CN) δ (ppm) = 8.42 (d, J = 7.0 Hz, 2H), 8.29 (d, J = 6.5 Hz, 2H), 8.00 (td, J = 8.1, 1.5 Hz, 2H), 7.58 (d, J = 8.0 Hz, 2H), 7.53 (td, J = 7.9, 1.4 Hz, 2H), 7.42 (ddd, J = 7.5, 5.5, 1.2 Hz, 2H), 7.28−7.23 (m, 4H), 7.11−7.08 (m, 4H), 7.05 (dd, J = 8.4, 1.2 Hz, 4H), 6.71 (ddd, J = 7.3, 5.7, 1.4 Hz, 2H), 4.42 (s, 6H); ^{13}C{^{1}H} NMR (176 MHz CD_3CN) δ (ppm) = 185.1, 156.6, 154.4, 153.3, 151.6, 145.6, 139.1, 138.5, 137.0, 131.2, 130.0, 128.3, 125.9, 124.8, 124.8, 121.6, 39.6; HRMS (ESI) m/z: $[RuL_2](PF_6)^+$ calcd for $[C_{38}H_{32}F_6N_{10}PRu]^+$ 875.1491; found 875.1487, $[RuL_2]^{2+}$ calcd for $[C_{38}H_{32}N_{10}Ru]^{2+}$ 365.0922; found 365.0925; Anal. calcd for $C_{38}H_{32}F_{12}N_{10}P_2Ru$: C, 44.76, H, 3.16, N, 13.74; found: C, 44.71, H, 3.20, N, 13.40.

Synthetic Strategy for $[RuL_3](PF_6)_2$

In a 15 mL Schlenk flask, $[Ru(CH_3CN)_6](BF_4)_2$ (54 mg, 0.103 mmol, 1 equiv), $[HL]BF_4$ (100 mg, 0.310 mmol, 3 equiv), and K_2CO_3 (47 mg, 0.341 mmol, 3.3 equiv) were dissolved in degassed ethylene glycol (4 mL). The reaction mixture was capped and heated to 160 °C for 16 h. After cooling to room temperature, the resulting dark red mixture was treated with aqueous NH_4PF_6, whereas a dark orange precipitate was formed. The orange solid was filtered off and extensively washed with H_2O, EtOAc, and Et_2O. The

https://doi.org/10.1021/acsorginorgau.3c00005
ACS Org. Inorg. Au 2023, 3, 184−198

remaining solid was dissolved in acetone (15 mL), cooled down with liquid nitrogen, overlayed with Et_2O, and cooled down with liquid nitrogen, too. The capped flask was stored at −20 °C for 1 month inducing crystallization of dark orange crystals suitable for X-ray diffraction analysis. The remaining crystalline solid was vigorously washed with Et_2O and decanted to remove the remaining brownish solid yielding a dark orange crystalline solid of $[RuL_3](PF_6)_2$ (52 mg, 0.047 mmol, 46%).

^{1}H NMR (500 MHz, CD_3CN) δ (ppm) = 8.25 (d, J = 5.4 Hz, 1H), 8.13 (d, J = 8.1 Hz, 1H), 7.99 (td, J = 7.9, 1.5 Hz, 1H), 7.82 (d, J = 5.5 Hz, 1H), 7.60−7.47 (m, 5H), 7.46−7.39 (m, 3H), 7.34−7.23 (m, 2H), 7.19 (t, J = 7.0 Hz, 1H), 7.14−7.04 (m, 4H), 7.04−6.98 (m, 4H), 6.75 (dddd, J = 13.2, 7.3, 5.8, 1.8 Hz, 2H), 6.51 (dd, J = 8.4, 1.1 Hz, 2H), 4.55 (s, 3H), 4.43 (s, 3H),4.30 (s, 3H); $^{13}C\{^1H\}$ NMR (126 MHz, CD_3CN) δ (ppm) = 191.1, 187.0, 186.6, 157.8, 156.0, 153.7, 151.9, 151.4, 150.9, 147.1, 146.3, 144.1, 140.0, 139.3, 139.0, 138.4, 136.6, 135.8, 131.4, 130.8, 130.6, 129.99, 129.96, 129.6, 126.5, 126.1, 125.5, 125.3, 124.7, 124.2, 122.2, 121.49, 121.1, 39.9, 39.6, 39.3; HRMS (ESI) m/z: $[RuL_3](PF_6)^+$ calcd for $[C_{42}H_{36}F_6N_{12}PRu]^+$ 995.1866; found 995.1874, $[RuL_2]^{2+}$ calcd for $[C_{42}H_{36}N_{12}Ru]^{2+}$ 405.1113; found 405.115; Anal. calcd for $C_{42}H_{36}F_{12}N_{12}P_2Ru$: C, 45.87, H, 3.30, N, 15.28; found: C, 45.52, H, 3.34, N, 15.00.

■ ASSOCIATED CONTENT

Data Availability Statement

The data underlying this study are available in the published article and its Supporting Information.

Supporting Information

The Supporting Information is available free of charge at https://pubs.acs.org/doi/10.1021/acsorginorgau.3c00005.

Synthesis; ^{1}H and $^{13}C\{H\}$ NMR spectroscopy; single X-ray diffraction data; cyclic voltammetry; differential pulsed voltammetry; UV/vis/NIR and EPR spectroelectrochemistry; (TD)DFT calculations; and photophysical measurments (PDF)

Accession Codes

CCDC 2075647, 2075649, and 2220128 contain the supplementary crystallographic data for this paper. These data can be obtained free of charge via www.ccdc.cam.ac.uk/data_request/cif, or by emailing data_request@ccdc.cam.ac.uk, or by contacting The Cambridge Crystallographic Data Centre, 12 Union Road, Cambridge CB2 1EZ, UK; fax: +44 1223 336033.

CCDC 2075647, 2220128, and 2075649 ($[\mathbf{RuL_1}](\mathbf{PF_6})_2$, $[\mathbf{RuL_2}](\mathbf{PF_6})_2$, and $[\mathbf{RuL_1}](\mathbf{PF_6})_2$) contain the supplementary crystallographic data for this paper. These data can be obtained free of charge via www.ccdc.cam.ac.uk/data_request/cif, by emailing data_request@ccdc.cam.ac.uk, or by contacting The Cambridge Crystallographic Data Centre, 12 Union Road, Cambridge CB2 1EZ, UK; fax: +44 1223 336033.

■ AUTHOR INFORMATION

Corresponding Author

Biprajit Sarkar − *Institut für Anorganische Chemie, Universität Stuttgart, D-70569 Stuttgart, Germany; Institut für Chemie und Biochemie, Freie Universität Berlin, 14195 Berlin, Germany;* orcid.org/0000-0003-4887-7277; Email: biprajit.sarkar@iac.uni-stuttgart.de

Authors

Tobias Bens − *Institut für Anorganische Chemie, Universität Stuttgart, D-70569 Stuttgart, Germany; Institut für Chemie und Biochemie, Freie Universität Berlin, 14195 Berlin, Germany*

Jasmin A. Kübler − *Department of Chemistry, University of Basel, 4056 Basel, Switzerland*

Robert R. M. Walter − *Institut für Anorganische Chemie, Universität Stuttgart, D-70569 Stuttgart, Germany*

Julia Beerhues − *Institut für Anorganische Chemie, Universität Stuttgart, D-70569 Stuttgart, Germany; Institut für Chemie und Biochemie, Freie Universität Berlin, 14195 Berlin, Germany;* Present Address: Institute of Chemical Research of Catalonia (ICIQ), Barcelona Institute of Science and Technology (BIST), Av. Països Catalans 16, 43007 Tarragona, Spain

Oliver S. Wenger − *Department of Chemistry, University of Basel, 4056 Basel, Switzerland;* orcid.org/0000-0002-0739-0553

Complete contact information is available at: https://pubs.acs.org/10.1021/acsorginorgau.3c00005

Author Contributions

CRediT: **Tobias Bens** conceptualization (equal), data curation (lead), formal analysis (lead), investigation (lead), methodology (lead), visualization (lead), writing-original draft (lead); **Jasmin A. Kübler** data curation (equal), formal analysis (equal), visualization (supporting), writing-original draft (supporting); **Robert R. M. Walter** data curation (supporting), formal analysis (supporting), visualization (supporting); **Julia Beerhues** data curation (supporting), formal analysis (supporting); **Oliver S. Wenger** formal analysis (supporting), funding acquisition (supporting), resources (supporting), software (supporting), supervision (supporting), writing-original draft (supporting), writing-review & editing (supporting); **Biprajit Sarkar** conceptualization (lead), formal analysis (equal), funding acquisition (lead), project administration (lead), resources (lead), software (lead), supervision (lead), writing-original draft (equal), writing-review & editing (lead).

Notes

The authors declare no competing financial interest.

■ ACKNOWLEDGMENTS

The authors kindly acknowledge the German Science Foundation (DFG, Priority Program SPP 2102 "Light-controlled reactivity of metal complexes", SA 1840/7-1 and SA 1840/7-2) for financial support. They further thank B. Förtsch for elemental analyses and Dr. W. Frey (Institut für Organische Chemie) for collecting the X-ray data sets and the support by the state of Baden-Württemberg through bwHPC and the German Research Foundation (DFG) through grant no. INST 40/575-1 FUGG (JUSTUS 2 cluster).

■ REFERENCES

(1) Mathew, P.; Neels, A.; Albrecht, M. 1,2,3-Triazolylidenes as versatile abnormal carbene ligands for late transition metals. *J. Am. Chem. Soc.* **2008**, *130*, 13534−13535.

(2) Guisado-Barrios, G.; Bouffard, J.; Donnadieu, B.; Bertrand, G. Crystalline 1*H*-1,2,3-triazol-5-ylidenes: new stable mesoionic carbenes (MICs). *Angew. Chem., Int. Ed.* **2010**, *49*, 4759−4762.

(3) Schweinfurth, D.; Hettmanczyk, L.; Suntrup, L.; Sarkar, B. Metal Complexes of Click-Derived Triazoles and Mesoionic Carbenes:

Electron Transfer, Photochemistry, Magnetic Bistability, and Catalysis. *Z. Anorg. Allg. Chem.* **2017**, *643*, 554−584.
(4) Guisado-Barrios, G.; Soleilhavoup, M.; Bertrand, G. 1*H*-1,2,3-Triazol-5-ylidenes: Readily Available Mesoionic Carbenes. *Acc. Chem. Res.* **2018**, *51*, 3236−3244.
(5) Vivancos, Á.; Segarra, C.; Albrecht, M. Mesoionic and Related Less Heteroatom-Stabilized N-Heterocyclic Carbene Complexes: Synthesis, Catalysis, and Other Applications. *Chem. Rev.* **2018**, *118*, 9493−9586.
(6) Neururer, F. R.; Liu, S.; Leitner, D.; Baltrun, M.; Fisher, K. R.; Kopacka, H.; Wurst, K.; Daumann, L. J.; Munz, D.; Hohloch, S. Mesoionic Carbenes in Low- to High-Valent Vanadium Chemistry. *Inorg. Chem.* **2021**, *60*, 15421−15434.
(7) Maity, R.; Sarkar, B. Chemistry of Compounds Based on 1,2,3-Triazolylidene-Type Mesoionic Carbenes. *JACS Au* **2022**, *2*, 22−57.
(8) Wittwer, B.; Dickmann, N.; Berg, S.; Leitner, D.; Tesi, L.; Hunger, D.; Gratzl, R.; van Slageren, J.; Neuman, N. I.; Munz, D.; Hohloch, S. A mesoionic carbene complex of manganese in five oxidation states. *Chem. Commun.* **2022**, *58*, 6096−6099.
(9) Suntrup, L.; Klenk, S.; Klein, J.; Sobottka, S.; Sarkar, B. Gauging Donor/Acceptor Properties and Redox Stability of Chelating Click-Derived Triazoles and Triazolylidenes: A Case Study with Rhenium(I) Complexes. *Inorg. Chem.* **2017**, *56*, 5771−5783.
(10) Welby, C. E.; Armitage, G. K.; Bartley, H.; Wilkinson, A.; Sinopoli, A.; Uppal, B. S.; Rice, C. R.; Elliott, P.I.P. Photochemistry of Ru^{II} 4,4′-bi-1,2,3-triazolyl (btz) complexes: crystallographic characterization of the photoreactive ligand-loss intermediate *trans*-[Ru(bpy)-(κ^2-btz)(κ^1-btz)(NCMe)]$^{2+}$. *Chem. - Eur. J.* **2014**, *20*, 8467−8476.
(11) Baschieri, A.; Monti, F.; Matteucci, E.; Mazzanti, A.; Barbieri, A.; Armaroli, N.; Sambri, L. A Mesoionic Carbene as Neutral Ligand for Phosphorescent Cationic Ir(III) Complexes. *Inorg. Chem.* **2016**, *55*, 7912−7919.
(12) Soellner, J.; Tenne, M.; Wagenblast, G.; Strassner, T. Phosphorescent Platinum(II) Complexes with Mesoionic 1*H*-1,2,3-Triazolylidene Ligands. *Chem. - Eur. J.* **2016**, *22*, 9914−9918.
(13) Chábera, P.; Liu, Y.; Prakash, O.; Thyrhaug, E.; Nahhas, A. E.; Honarfar, A.; Essén, S.; Fredin, L. A.; Harlang, T.C.B.; Kjær, K. S.; Handrup, K.; Ericson, F.; Tatsuno, H.; Morgan, K.; Schnadt, J.; Häggström, L.; Ericsson, T.; Sobkowiak, A.; Lidin, S.; Huang, P.; Styring, S.; Uhlig, J.; Bendix, J.; Lomoth, R.; Sundström, V.; Persson, P.; Wärnmark, K. A low-spin Fe(III) complex with 100-ps ligand-to-metal charge transfer photoluminescence. *Nature* **2017**, *543*, 695−699.
(14) Hettmanczyk, L.; Spall, S.J.P.; Klenk, S.; van der Meer, M.; Hohloch, S.; Weinstein, J. A.; Sarkar, B. Structural, Electrochemical, and Photochemical Properties of Mono- and Digold(I) Complexes Containing Mesoionic Carbenes. *Eur. J. Inorg. Chem.* **2017**, *2017*, 2112−2121.
(15) Sarkar, B.; Suntrup, L. Illuminating Iron: Mesoionic Carbenes as Privileged Ligands in Photochemistry. *Angew. Chem., Int. Ed.* **2017**, *56*, 8938−8940.
(16) Chábera, P.; Kjaer, K. S.; Prakash, O.; Honarfar, A.; Liu, Y.; Fredin, L. A.; Harlang, T.C.B.; Lidin, S.; Uhlig, J.; Sundström, V.; Lomoth, R.; Persson, P.; Wärnmark, K. Fe^{II} Hexa N-Heterocyclic Carbene Complex with a 528 ps Metal-to-Ligand Charge-Transfer Excited-State Lifetime. *J. Phys. Chem. Lett.* **2018**, *9*, 459−463.
(17) Suntrup, L.; Stein, F.; Hermann, G.; Kleoff, M.; Kuss-Petermann, M.; Klein, J.; Wenger, O. S.; Tremblay, J. C.; Sarkar, B. Influence of Mesoionic Carbenes on Electro- and Photoactive Ru and Os Complexes: A Combined (Spectro-)Electrochemical, Photochemical, and Computational Study. *Inorg. Chem.* **2018**, *57*, 13973−13984.
(18) Kleinhans, G.; Chan, A.K.-W.; Leung, M.-Y.; Liles, D. C.; Fernandes, M. A.; Yam, V.W.-W.; Fernández, I.; Bezuidenhout, D. I. Synthesis and Photophysical Properties of T-Shaped Coinage-Metal Complexes. *Chem. - Eur. J.* **2020**, *26*, 6993−6998.
(19) Suntrup, L.; Stein, F.; Klein, J.; Wilting, A.; Parlane, F.G.L.; Brown, C. M.; Fiedler, J.; Berlinguette, C. P.; Siewert, I.; Sarkar, B. Rhenium Complexes of Pyridyl-Mesoionic Carbenes: Photochemical Properties and Electrocatalytic CO_2 Reduction. *Inorg. Chem.* **2020**, *59*, 4215−4227.
(20) Boden, P. J.; Di Martino-Fumo, P.; Bens, T.; Steiger, S. T.; Marhöfer, D.; Niedner-Schatteburg, G.; Sarkar, B. Mechanistic and Kinetic Investigations of ON/OFF (Photo)Switchable Binding of Carbon Monoxide by Chromium(0), Molybdenum(0) and Tungsten(0) Carbonyl Complexes with a Pyridyl-Mesoionic Carbene Ligand. *Chem. - Eur. J.* **2022**, *28*, No. e202201038.
(21) Brown, D. G.; Sanguantrakun, N.; Schulze, B.; Schubert, U. S.; Berlinguette, C. P. Bis(tridentate) ruthenium-terpyridine complexes featuring microsecond excited-state lifetimes. *J. Am. Chem. Soc.* **2012**, *134*, 12354−12357.
(22) Schulze, B.; Schubert, U. S. Beyond click chemistry - supramolecular interactions of 1,2,3-triazoles. *Chem. Soc. Rev.* **2014**, *43*, 2522−2571.
(23) Mejuto, C.; Ibáñez-Ibáñez, L.; Guisado-Barrios, G.; Mata, J. A. Visible-Light-Promoted Iridium(III)-Catalyzed Acceptorless Dehydrogenation of N-Heterocycles at Room Temperature. *ACS Catal.* **2022**, *12*, 6238−6245.
(24) Hettmanczyk, L.; Manck, S.; Hoyer, C.; Hohloch, S.; Sarkar, B. Heterobimetallic complexes with redox-active mesoionic carbenes as metalloligands: electrochemical properties, electronic structures and catalysis. *Chem. Commun.* **2015**, *51*, 10949−10952.
(25) Maity, R.; van der Meer, M.; Sarkar, B. Redox-active multinuclear Pd(II) complexes with bis- and tris-mesoionic carbenes. *Dalton Trans.* **2015**, *44*, 46−49.
(26) Hettmanczyk, L.; Suntrup, L.; Klenk, S.; Hoyer, C.; Sarkar, B. Heteromultimetallic Complexes with Redox-Active Mesoionic Carbenes: Control of Donor Properties and Redox-Induced Catalysis. *Chem. - Eur. J.* **2017**, *23*, 576−585.
(27) Klenk, S.; Rupf, S.; Suntrup, L.; van der Meer, M.; Sarkar, B. The Power of Ferrocene, Mesoionic Carbenes, and Gold: Redox-Switchable Catalysis. *Organometallics* **2017**, *36*, 2026−2035.
(28) Vanicek, S.; Podewitz, M.; Stubbe, J.; Schulze, D.; Kopacka, H.; Wurst, K.; Müller, T.; Lippmann, P.; Haslinger, S.; Schottenberger, H.; Liedl, K. R.; Ott, I.; Sarkar, B.; Bildstein, B. Highly Electrophilic, Catalytically Active and Redox-Responsive Cobaltoceniumyl and Ferrocenyl Triazolylidene Coinage Metal Complexes. *Chem. - Eur. J.* **2018**, *24*, 3742−3753.
(29) Vanicek, S.; Beerhues, J.; Bens, T.; Levchenko, V.; Wurst, K.; Bildstein, B.; Tilset, M.; Sarkar, B. Oxidative access via aqua regia to an electrophilic, mesoionic dicobaltoceniumyltriazolylidene gold(III) catalyst. *Organometallics* **2019**, *38*, 4383−4386.
(30) Beerhues, J.; Neubrand, M.; Sobottka, S.; Neuman, N. I.; Aberhan, H.; Chandra, S.; Sarkar, B. Directed Design of a Au^{I} Complex with a Reduced Mesoionic Carbene Radical Ligand: Insights from 1,2,3-Triazolylidene Selenium Adducts and Extensive Electrochemical Investigations. *Chem. - Eur. J.* **2021**, *27*, 6557−6568.
(31) Bens, T.; Boden, P.; Di Martino-Fumo, P.; Beerhues, J.; Albold, U.; Sobottka, S.; Neuman, N. I.; Gerhards, M.; Sarkar, B. Chromium(0) and Molydenum(0) Complexes with a Pyridyl-Mesoionic Carbene Ligand: Structural, (Spectro)electrochemical, Photochemical, and Theoretical Investigations. *Inorg. Chem.* **2020**, *59*, 15504−15513.
(32) Crowley, J. D.; Lee, A.-L.; Kilpin, K. J. 1,3,4-Trisubtituted-1,2,3-Triazol-5-ylidene 'Click' Carbene Ligands: Synthesis, Catalysis and Self-Assembly. *Aust. J. Chem.* **2011**, *64*, 1118−1132.
(33) Eymann, L. Y. M.; Scopelliti, R.; Tirani, F. F.; Severin, K. Synthesis of Azo Dyes from Mesoionic Carbenes and Nitrous Oxide. *Chem. - Eur. J.* **2018**, *24*, 7957−7963.
(34) Liu, Y.; Varava, P.; Fabrizio, A.; Eymann, L. Y. M.; Tskhovrebov, A. G.; Planes, O. M.; Solari, E.; Fadaei-Tirani, F.; Scopelliti, R.; Sienkiewicz, A.; Corminboeuf, C.; Severin, K. Synthesis of aminyl biradicals by base-induced Csp^3-Csp^3 coupling of cationic azo dyes. *Chem. Sci.* **2019**, *10*, 5719−5724.
(35) Fink, D. W.; Ohnesorge, W. E. Temperature effects on charge-transfer luminescence intensity of some transition metal ion chelates. *J. Am. Chem. Soc.* **1969**, *91*, 4995−4998.

https://doi.org/10.1021/acsorginorgau.3c00005
ACS Org. Inorg. Au 2023, 3, 184−198

(36) Damrauer, N. H.; Cerullo, G.; Yeh, A.; Boussie, T. R.; Shank, C. V.; McCusker, J. K. Femtosecond Dynamics of Excited-State Evolution in $[Ru(bpy)_3]^{2+}$. *Science* **1997**, *275*, 54−57.
(37) Fletcher, J. T.; Bumgarner, B. J.; Engels, N. D.; Skoglund, D. A. Multidentate 1,2,3-Triazole-Containing Chelators from Tandem Deprotection/Click Reactions of (Trimethylsilyl)alkynes and Comparison of Their Ruthenium(II) Complexes. *Organometallics* **2008**, *27*, 5430−5433.
(38) Felici, M.; Contreras-Carballada, P.; Vida, Y.; Smits, J. M.; Nolte, R. J.; de Cola, L.; Williams, R. M.; Feiters, M. C. Ir(III) and Ru(II) complexes containing triazole-pyridine ligands: luminescence enhancement upon substitution with beta-cyclodextrin. *Chem. - Eur. J.* **2009**, *15*, 13124−13134.
(39) Welby, C. E.; Grkinic, S.; Zahid, A.; Uppal, B. S.; Gibson, E. A.; Rice, C. R.; Elliott, P. I. P. Synthesis, characterisation and theoretical study of ruthenium 4,4′-bi-1,2,3-triazolyl complexes: fundamental switching of the nature of S_1 and T_1 states from MLCT to MC. *Dalton Trans.* **2012**, *41*, 7637−7646.
(40) Leigh, V.; Ghattas, W.; Lalrempuia, R.; Müller-Bunz, H.; Pryce, M. T.; Albrecht, M. Synthesis, photo-, and electrochemistry of ruthenium bis(bipyridine) complexes comprising a N-heterocyclic carbene ligand. *Inorg. Chem.* **2013**, *52*, 5395−5402.
(41) Thompson, D. W.; Ito, A.; Meyer, T. J. $[Ru(bpy)_3]^{2+*}$ and other remarkable metal-to-ligand charge transfer (MLCT) excited states. *Pure Appl. Chem.* **2013**, *85*, 1257−1305.
(42) Hohloch, S.; Schweinfurth, D.; Sommer, M. G.; Weisser, F.; Deibel, N.; Ehret, F.; Sarkar, B. The redox series $Ru(bpy)_2(L)n$, n = +3, +2, +1, 0, with L = bipyridine, ″click″ derived pyridyl-triazole or bis-triazole: a combined structural, electrochemical, spectroelectrochemical and DFT investigation. *Dalton Trans.* **2014**, *43*, 4437−4450.
(43) Auböck, G.; Chergui, M. Sub-50-fs photoinduced spin crossover in $[Fe(bpy)_3]^{2+}$. *Nat. Chem.* **2015**, *7*, 629−633.
(44) Liu, Y.; Kjaer, K. S.; Fredin, L. A.; Chábera, P.; Harlang, T.; Canton, S. E.; Lidin, S.; Zhang, J.; Lomoth, R.; Bergquist, K.-E.; Persson, P.; Wärnmark, K.; Sundström, V. A Heteroleptic Ferrous Complex with Mesoionic Bis(1,2,3-triazol-5-ylidene) Ligands: Taming the MLCT Excited State of Iron(II). *Chem. - Eur. J.* **2015**, *21*, 3628−3639.
(45) Lo, W. K. C.; Huff, G. S.; Cubanski, J. R.; Kennedy, A. D. W.; McAdam, C. J.; McMorran, D. A.; Gordon, K. C.; Crowley, J. D. Comparison of inverse and regular 2-pyridyl-1,2,3-triazole ″click″ complexes: structures, stability, electrochemical, and photophysical properties. *Inorg. Chem.* **2015**, *54*, 1572−1587.
(46) Scattergood, P. A.; Elliott, P. I. P. An unexpected journey from highly tunable phosphorescence to novel photochemistry of 1,2,3-triazole-based complexes. *Dalton Trans.* **2017**, *46*, 16343−16356.
(47) Happ, B.; Friebe, C.; Winter, A.; Hager, M. D.; Hoogenboom, R.; Schubert, U. S. 2-(1*H*-1,2,3-triazol-4-yl)-Pyridine Ligands as Alternatives to 2,2′-Bipyridines in Ruthenium(II) Complexes. *Chem. - Asian J.* **2009**, *4*, 154−163.
(48) Wenger, O. S. Is Iron the New Ruthenium? *Chem. - Eur. J.* **2019**, *25*, 6043−6052.
(49) Förster, C.; Heinze, K. Photophysics and photochemistry with Earth-abundant metals - fundamentals and concepts. *Chem. Soc. Rev.* **2020**, *49*, 1057−1070.
(50) Wegeberg, C.; Wenger, O. S. Luminescent First-Row Transition Metal Complexes. *JACS Au* **2021**, *1*, 1860−1876.
(51) Kjær, K. S.; Kaul, N.; Prakash, O.; Chábera, P.; Rosemann, N. W.; Honarfar, A.; Gordivska, O.; Fredin, L. A.; Bergquist, K.-E.; Häggström, L.; Ericsson, T.; Lindh, L.; Yartsev, A.; Styring, S.; Huang, P.; Uhlig, J.; Bendix, J.; Strand, D.; Sundström, V.; Persson, P.; Lomoth, R.; Wärnmark, K. Luminescence and reactivity of a charge-transfer excited iron complex with nanosecond lifetime. *Science* **2019**, *363*, 249−253.
(52) Bolje, A.; Košmrlj, J. A selective approach to pyridine appended 1,2,3-triazolium salts. *Org. Lett.* **2013**, *15*, 5084−5087.
(53) Rajesh, Y. B. R. D. An Improved Rapid and Mild Deoxygenation of Amine N-oxides. *J. Heterocycl. Chem.* **2018**, *55*, 486−491.
(54) Bolje, A.; Hohloch, S.; Urankar, D.; Pevec, A.; Gazvoda, M.; Sarkar, B.; Košmrlj, J. Exploring the Scope of Pyridyl- and Picolyl-Functionalized 1,2,3-Triazol-5-ylidenes in Bidentate Coordination to Ruthenium(II) Cymene Chloride Complexes. *Organometallics* **2014**, *33*, 2588−2598.
(55) Mutua, G. K.; Bellam, R.; Jaganyi, D.; Mambanda, A. The role of *N,N*-chelate ligand on the reactivity of (η^6-*p*-cymene)Ru(II) complexes: kinetics, DNA and protein interaction studies. *J. Coord. Chem.* **2019**, *72*, 2931−2956.
(56) Queyriaux, N.; Giannoudis, E.; Lefebvre, J.-F.; Artero, V.; Chavarot-Kerlidou, M. Synthesis of Ruthenium Tris-Diimine Photosensitizers Substituted by Four Methylphosphonate Anchoring Groups for Dye-Sensitized Photoelectrochemical Cell Applications. *Eur. J. Inorg. Chem.* **2019**, *2019*, 2154−2161.
(57) Son, S. U.; Park, K. H.; Lee, Y.-S.; Kim, B. Y.; Choi, C. H.; Lah, M. S.; Jang, Y. H.; Jang, D.-J.; Chung, Y. K. Synthesis of Ru(II) complexes of N-heterocyclic carbenes and their promising photoluminescence properties in water. *Inorg. Chem.* **2004**, *43*, 6896−6898.
(58) Abbas, M. A.; McMillen, C. D.; Brumaghim, J. L. Synthesis, characterization, and structures of ruthenium(II) complexes with multiple solvato ligands. *Inorg. Chim. Acta* **2017**, *468*, 308−315.
(59) Krause, R. A. Synthesis of Mixed Complexes of Ruthenium(II) with 2,2′-Dipyridyl. *Inorg. Chim. Acta* **1977**, *22*, 209−213.
(60) Petroni, A.; Slep, L. D.; Etchenique, R. Ruthenium(II) 2,2′-Bipyridyl Tetrakis Acetonitrile Undergoes Selective Axial Photocleavage. *Inorg. Chem.* **2008**, *47*, 951−956.
(61) Bernet, L.; Lalrempuia, R.; Ghattas, W.; Mueller-Bunz, H.; Vigara, L.; Llobet, A.; Albrecht, M. Tunable single-site ruthenium catalysts for efficient water oxidation. *Chem. Commun.* **2011**, *47*, 8058−8060.
(62) Gupta, S. K.; Choudhury, J. A Mixed N-Heterocyclic Carbene/2,2′-Bipyridine-Supported Robust Ruthenium(II) Oxidation Precatalyst for Benzylic C−H Oxidation. *ChemCatChem* **2017**, *9*, 1979−1984.
(63) Oliveira, K. M.; Liany, L.-D.; Corrêa, R. S.; Deflon, V. M.; Cominetti, M. R.; Batista, A. A. Selective Ru(II)/lawsone complexes inhibiting tumor cell growth by apoptosis. *J. Inorg. Biochem.* **2017**, *176*, 66−76.
(64) Zheng, Y.; Tan, Y.; Harms, K.; Marsch, M.; Riedel, R.; Zhang, L.; Meggers, E. Octahedral Ruthenium Complex with Exclusive Metal-Centered Chirality for Highly Effective Asymmetric Catalysis. *J. Am. Chem. Soc.* **2017**, *139*, 4322−4325.
(65) Magra, K.; Domenichini, E.; Francés-Monerris, A.; Cebrián, C.; Beley, M.; Darari, M.; Pastore, M.; Monari, A.; Assfeld, X.; Haacke, S.; Gros, P. C. Impact of the fac/mer Isomerism on the Excited-State Dynamics of Pyridyl-carbene Fe(II) Complexes. *Inorg. Chem.* **2019**, *58*, 5069−5081.
(66) Winterling, E.; Ivlev, S.; Meggers, E. Chiral-at-Ruthenium Catalysts with Mixed Normal and Abnormal N-Heterocyclic Carbene Ligands. *Organometallics* **2021**, *40*, 1148−1155.
(67) van der Meer, M.; Glais, E.; Siewert, I.; Sarkar, B. Electrocatalytic Dihydrogen Production with a Robust Mesoionic Pyridylcarbene Cobalt Catalyst. *Angew. Chem., Int. Ed.* **2015**, *54*, 13792−13795.
(68) Bolje, A.; Hohloch, S.; Košmrlj, J.; Sarkar, B. Ru^{II}, Ir^{III} and Os^{II} mesoionic carbene complexes: efficient catalysts for transfer hydrogenation of selected functionalities. *Dalton Trans.* **2016**, *45*, 15983−15993.
(69) Juris, A.; Balzani, V.; Barigelletti, F.; Campagna, S.; Belser, P.; von Zelewsky, A. V. Ru(II) polypyridine complexes: photophysics, photochemistry, eletrochemistry, and chemiluminescence. *Coord. Chem. Rev.* **1988**, *84*, 85−277.
(70) Zhao, H. C.; Fu, B.-L.; Schweinfurth, D.; Harney, J. P.; Sarkar, B.; Tsai, M.-K.; Rochford, J. Tuning Oxyquinolate Non-Innocence at the Ruthenium Polypyridyl Core. *Eur. J. Inorg. Chem.* **2013**, *2013*, 4410−4420.
(71) Klein, J.; Stuckmann, A.; Sobottka, S.; Suntrup, L.; van der Meer, M.; Hommes, P.; Reissig, H.-U.; Sarkar, B. Ruthenium Complexes with Strongly Electron-Donating Terpyridine Ligands:

https://doi.org/10.1021/acsorginorgau.3c00005
ACS Org. Inorg. Au 2023, 3, 184−198

Effect of the Working Electrode on Electrochemical and Spectroelectrochemical Properties. *Chem. - Eur. J.* **2017**, *23*, 12314−12325.
(72) Nazeeruddin, M. K.; Zakeeruddin, S. M.; Kalyanasundaram, K. Enhanced intensities of the ligand-to-metal charge-transfer transitions in ruthenium(III) and osmium(III) complexes of substituted bipyridines. *J. Phys. Chem. A* **1993**, *97*, 9607−9612.
(73) Kumari, M.; Dey, K.; Bera, S. K.; Lahiri, G. K. Indazole-Derived Mono-/Diruthenium and Heterotrinuclear Complexes: Switchable Binding Mode, Electronic Form, and Anion Sensing Events. *Inorg. Chem.* **2022**, *61*, 16122−16140.
(74) Patra, S.; Sarkar, B.; Mobin, S. M.; Kaim, W.; Lahiri, G. K. Separating innocence and non-innocence of ligands and metals in complexes (L)Ru(acac)$_2^n$ (n = −1, 0, +1; L = *o*-iminoquinone or *o*-iminothioquinone). *Inorg. Chem.* **2003**, *42*, 6469−6473.
(75) Ghumaan, S.; Sarkar, B.; Patra, S.; Parimal, K.; van Slageren, J.; Fiedler, J.; Kaim, W.; Lahiri, G. K. 3,6-bis(2′-pyridyl)pyridazine (L) and its deprotonated form (L-H$^+$)$^-$ as ligands for {(acac)$_2$Ru^{n+}} or {(bpy)$_2$Ru^{m+}}: investigation of mixed valency in {(acac)$_2$Ru}$_2$(μ-L-H$^+$)]^0 and {(bpy)$_2$Ru}$_2$(μ-L-H$^+$)$^{4+}$ by spectroelectrochemistry and EPR. *Dalton Trans.* **2005**, 706−712.
(76) Motten, A. G.; Hanck, K.; DeArmound, M. ESR of the reduction products of [Fe(bpy)$_3$]$^{2+}$ and [Ru(bpy)$_3$]$^{2+}$. *Chem. Phys. Lett.* **1981**, *79*, 541−546.
(77) Ernst, S. D.; Kaim, W. Energy level tailoring in ruthenium(II) polyazine complexes based on calculated and experimental ligand properties. *Inorg. Chem.* **1989**, *28*, 1520−1528.
(78) Kaim, W.; Kasack, V. Stability rules for d5/d6 mixed-valent dimers. Effects from the donor/acceptor capability of the metal (ruthenium vs osmium) and from the occupancy of the mediating ligand orbital (LUMO vs HOMO). *Inorg. Chem.* **1990**, *29*, 4696−4699.
(79) Caspar, J. V.; Meyer, T. J. Photochemistry of Ru(bpy)$_3^{2+}$. Solvent effects. *J. Am. Chem. Soc.* **1983**, *105*, 5583−5590.
(80) Nakamaru, K. Solvent Effect on the Nonradiative Deactivation of the Excited State of Tris(2,2′-bipyridyl)ruthenium(II) Ion. *Bull. Chem. Soc. Jpn.* **1982**, *55*, 1639−1640.
(81) Tan, S. L.; Keith DeArmond, M.; Hanck, K. W. Electron transfer sequence and mechanism for bis bipyridine complexes of Ru(II). *J. Electroanal. Chem. Interfacial Electrochem.* **1984**, *181*, 187−197.
(82) Knoll, J. D.; Albani, B. A.; Durr, C. B.; Turro, C. Unusually efficient pyridine photodissociation from Ru(II) complexes with sterically bulky bidentate ancillary ligands. *J. Phys. Chem. A* **2014**, *118*, 10603−10610.
(83) Kojima, T.; Morimoto, T.; Sakamoto, T.; Miyazaki, S.; Fukuzumi, S. Ruthenium(II) pyridylamine complexes with diimine ligands showing reversible photochemical and thermal structural change. *Chem. - Eur. J.* **2008**, *14*, 8904−8915.
(84) Yuan, Y.-J.; Yu, Z.-T.; Chen, D.-Q.; Zou, Z.-G. Metal-complex chromophores for solar hydrogen generation. *Chem. Soc. Rev.* **2017**, *46*, 603−631.
(85) Cao, F.; Oskam, G.; Meyer, G. J.; Searson, P. C. Electron Transport in Porous Nanocrystalline TiO$_2$ Photoelectrochemical Cells. *J. Phys. Chem. A* **1996**, *100*, 17021−17027.
(86) Connelly, N. G.; Geiger, W. E. Chemical Redox Agents for Organometallic Chemistry. *Chem. Rev.* **1996**, *96*, 877−910.
(87) *The MERCK Index: An Encyclopedial of Chemical, Drugs and Biologicals*; Budavari, S., Ed.; Merck & Co.: Rahway, 1989.
(88) *APEX3*, v.5-2; 2015; Bruker AXS Inc.: Madison, Wisconsin, USA, 2015.
(89) SAINT+. *Data Integration Engine*, Version 8.27b; Bruker AXS Inc.: Madison, Wisconsin, USA, 2012.
(90) Sheldrick, G. M. *SHELXS-97 and SHELXL-97, Program for Crystal Structure Solution and Refinement*; University of Gottingen: Göttingen, Germany, 1997.
(91) Sheldrick, G. M. *Program for Empirical Absorption Correction*, SADABS Version 2008/1; University of Göttingen: Göttingen, Germany, 2008.
(92) Sheldrick, G. M. A short history of SHELX. *Acta Crystallogr., Sect. A: Found. Crystallogr.* **2008**, *64*, 112−122.
(93) Sheldrick, G. M. *Program for Chrystal Structure Solution and Refinement*, SHELXL Version 2014/7; University of Göttingen: Göttingen, Germany, 2014.
(94) Sheldrick, G. M. Crystal structure refinement with SHELXL. *Acta Crystallogr., Sect. C: Struct. Chem.* **2015**, *C71*, 3−8.
(95) Macrae, C. F.; Edgington, P. R.; McCabe, P.; Pidcock, E.; Shields, G. P.; Taylor, R.; Towler, M.; van de Streek, J. Mercury: visualization and analysis of crystal structures. *J. Appl. Crystallogr.* **2006**, *39*, 453−457.
(96) Krejčik, M.; Daněk, M.; Hartl, F. Simple construction of an infrared optically transparent thin-layer electrochemical cell. *J. Electroanal. Chem. Interfacial Electrochem.* **1991**, *317*, 179−187.
(97) Neese, F. The ORCA program system. *Wiley Interdiscip. Rev.: Comput. Mol. Sci.* **2012**, *2*, 73−78.
(98) Adamo, C.; Barone, V. Toward reliable density functional methods without adjustable parameters: The PBE0 model. *J. Chem. Phys.* **1999**, *110*, 6158−6170.
(99) Grimme, S. Accurate description of van der Waals complexes by density functional theory including empirical corrections. *J. Comput. Chem.* **2004**, *25*, 1463−1473.
(100) Grimme, S. Semiempirical GGA-type density functional constructed with a long-range dispersion correction. *J. Comput. Chem.* **2006**, *27*, 1787−1799.
(101) Grimme, S.; Antony, J.; Ehrlich, S.; Krieg, H. A consistent and accurate *ab initio* parametrization of density functional dispersion correction (DFT-D) for the 94 elements H-Pu. *J. Chem. Phys.* **2010**, *132*, No. 154104.
(102) Grimme, S.; Ehrlich, S.; Goerigk, L. Effect of the damping function in dispersion corrected density functional theory. *J. Comput. Chem.* **2011**, *32*, 1456−1465.
(103) Weigend, F.; Ahlrichs, R. Balanced basis sets of split valence, triple zeta valence and quadruple zeta valence quality for H to Rn: Design and assessment of accuracy. *Phys. Chem. Chem. Phys.* **2005**, *7*, 3297−3305.
(104) Whitten, J. L. Coulombic potential energy integrals and approximations. *J. Chem. Phys.* **1973**, *58*, 4496−4501.
(105) Vahtras, O.; Almlöf, J.; Feyereisen, M. W. Integral approximations for LCAO-SCF calculations. *Chem. Phys. Lett.* **1993**, *213*, 514−518.
(106) Neese, F.; Olbrich, G. Efficient use of the resolution of the identity approximation in time-dependent density functional calculations with hybrid density functionals. *Chem. Phys. Lett.* **2002**, *362*, 170−178.
(107) Neese, F. An improvement of the resolution of the identity approximation for the formation of the Coulomb matrix. *J. Comput. Chem.* **2003**, *24*, 1740−1747.
(108) Neese, F.; Wennmohs, F.; Hansen, A.; Becker, U. Efficient, approximate and parallel Hartree−Fock and hybrid DFT calculations. A 'chain-of-spheres' algorithm for the Hartree−Fock exchange. *Chem. Phys.* **2009**, *356*, 98−109.
(109) Izsák, R.; Neese, F. An overlap fitted chain of spheres exchange method. *J. Chem. Phys.* **2011**, *135*, No. 144105.
(110) Petrenko, T.; Kossmann, S.; Neese, F. Efficient time-dependent density functional theory approximations for hybrid density functionals: analytical gradients and parallelization. *J. Chem. Phys.* **2011**, *134*, No. 054116.
(111) Eichkorn, K.; Treutler, O.; Öhm, H.; Häser, M.; Ahlrichs, R. Auxiliary basis sets to approximate Coulomb potentials. *Chem. Phys. Lett.* **1995**, *242*, 652−660.
(112) Eichkorn, K.; Weigend, F.; Treutler, O.; Ahlrichs, R. Auxiliary basis sets for main row atoms and transition metals and their use to approximate Coulomb potentials. *Theor. Chem. Acc.* **1997**, *97*, 119−124.
(113) Barone, V.; Cossi, M. Quantum Calculation of Molecular Energies and Energy Gradients in Solution by a Conductor Solvent Model. *J. Phys. Chem. A* **1998**, *102*, 1995−2001.

https://doi.org/10.1021/acsorginorgau.3c00005
ACS Org. Inorg. Au 2023, 3, 184−198

(114) Mulliken, R. S. Electronic Population Analysis on LCAO–MO Molecular Wave Functions. I. *J. Chem. Phys.* **1955**, *23*, 1833–1840.
(115) Zhurko, G. A. Ivanovo, Russia Chemcraft-Graphical Program for Visualization of Quantum Chemistry Computations, 2023. Ver. 1.8. Available Online: http://www.chemcraftprog.com/.

https://doi.org/10.1021/acsorginorgau.3c00005
ACS Org. Inorg. Au 2023, 3, 184–198

3.3 Chromium(0) and Molybdenum(0) Complexes with a Pyridyl-Mesoionic Carbene Ligand: Structural, (Spectro)electrochemical, Photochemical and Theoretical Investigations

T. Bens,[†,§] P. Boden,[‡] P. Di Martino-Fumo,[‡] J. Beerhues,[†,§] U. Albold,[§] S. Sobottka,[§] N. I. Neuman,[§^] M. Gerhards,[‡*] B. Sarkar[†,§*]

[†]Lehrstuhl für Anorganische Koordinationschemie, Universität Stuttgart, Pfaffenwaldring 55, D-70569 Stuttgart, Germany, Email: biprajit.sarkar@iac.uni-stuttgart.de

[§]Institut für Chemie und Biochemie, Freie Universität Berlin, Fabeckstraße 34-36, 14195, Berlin, Germany.

[‡]Department of Chemistry and Research Center Optimas, TU Kaiserslautern, Erwin-Schrödinger-Straße, 67663 Kaiserslautern, Germany, Email: gerhards@chemie.uni-kl.de

[^]Instituto de Desarrollo Tecnológico para la Industria Química, INTEC, UNL-CONICET Paraje El Pozo, 3000 Santa Fe, Argentina.

This article was published and is reprinted with permission from ACS:

T. Bens, P. Boden, P. Di Martino-Fumo, J. Beerhues, U. Albold, S. Sobottka, N. I. Neuman, M. Gerhards, B. Sarkar, *Inorg. Chem.* **2020**, *59*, 20, 15504–15513.

DOI: 10.1021/acs.inorgchem.0c02537 (© 2020 American Chemical Society).

The **Supporting Information** is available free of charge at https://pubs.acs.org/doi/10.1021/acs.inorgchem.0c02537.

Autor contribution: The project was designed by Biprajit Sarkar. The complexes and ligands were synthesized and fully characterized by Tobias Bens. All (spectro)electrochemical measurements and theoretical calculation were performed by Tobias Bens (as a part of the master thesis). The EPR-SEC experiments were performed with the support of Nicolas I. Neuman and Sebastian Sobottka. The FTIR spectroscopy measurements were investigated by Pit Boden and Patrick Di Martino-Fumo. X-Ray diffraction analysis was carried out by Julia Beerhues and Uta Albold. The manuscript was written by Tobias Bens and Biprajit Sarkar.

Inorganic Chemistry

pubs.acs.org/IC Article

Chromium(0) and Molydenum(0) Complexes with a Pyridyl-Mesoionic Carbene Ligand: Structural, (Spectro)electrochemical, Photochemical, and Theoretical Investigations

Tobias Bens, Pit Boden, Patrick Di Martino-Fumo, Julia Beerhues, Uta Albold, Sebastian Sobottka, Nicolás I. Neuman, Markus Gerhards,* and Biprajit Sarkar*

Cite This: *Inorg. Chem.* 2020, 59, 15504−15513 Read Online

ACCESS | Metrics & More | Article Recommendations | Supporting Information

ABSTRACT: This work reports on the synthesis and in-depth electrochemical and photochemical characterization of two chromium(0) and molydenum(0) metal complexes with bidentate pyridyl-mesoionic carbene (MIC) ligands of the 1,2,3-triazol-5-ylidene type and carbonyl coligands. Metal complexes with MIC ligands have turned out to have very promising electrocatalytic and photochemical properties, but examples of MIC-containing complexes with early-transition-metal centers remain extremely rare. The electrochemistry of these new MIC complexes was studied by cyclic voltammetry and especially spectroelectrochemistry in the IR region consistent with a mainly metal-centered oxidation, which is fully reversible in the case of the chromium(0) complex. At the same time, the two reduction steps are predominantly ligand-centered according to the observed near-IR absorbance, with the first reduction step being reversible for both systems. The results of the electron paramagnetic resonance studies on the oxidized and reduced species confirm the IR spectroelectrochemistry experiments. The photochemical reactivity of the complexes with a series of organic ligands was investigated by time-resolved (step-scan) Fourier transform infrared (FTIR) spectroscopy. Interestingly, the photoreactions in pyridine and acetonitrile are fully reversible with a slow dark reverse reaction back to the educt species over minutes and even hours, depending on the metal center and reagent. This reversible behavior is in contrast to the expected loss of one or several CO ligands known from related homoleptic as well as heteroleptic $M(CO)_4L_2$ α-diimine transition-metal complexes.

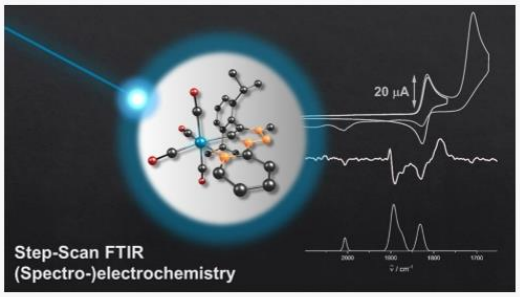

INTRODUCTION

Mesoionic carbenes (MICs) of the 1,2,3-triazol-5-ylidene type have established themselves as prominent ligands in organometallic chemistry.[1−6] While in the majority of cases these ligands have been used in homogeneous catalysis,[3−6] they have also found applications in small-molecule activation[7−11] and as parts of redox-active metal complexes.[12,13] Furthermore, such ligands have also been used in the field of photochemistry[14−23] and in redox-induced and redox-switchable catalysis.[24−28] Metal complexes of bidentate ligands containing one MIC and one pyridyl donor have displayed excellent photochemical[9,19,23] and electrocatalytic properties.[10] Most of the aforementioned metal complexes are predominantly based on late transition metals.[3−6] Examples of early transition metals with MIC ligands remain extremely rare.[29] As part of our continued interest in the transition-metal chemistry of bidentate pyridyl-MIC-type ligands, we have now turned our attention to the group 6 metals chromium and molybdenum. The carbonyl coligands on the Cr^0 and Mo^0 centers make them ideal platforms for a number of electrochemical and spectroscopic (including photochemical and photophysical) investigations.[30−33] In particular, the CO ligands are powerful markers for IR spectroscopy and can be very conveniently used for following excited-state dynamics and reactivity in these metal complexes. In this context, time-resolved step-scan Fourier transform infrared (FTIR) spectroscopy turned out to be an ideal tool to characterize the long-lived electronically excited states of transition-metal complexes on time scales of nanoseconds and microseconds.[34−39] At the same time, the step-scan technique has been successfully applied in the analysis of the photoinduced reactions[35,40,41] also involving transition metals.[42−44]

In the following, we present the synthesis and characterization of the chromium(0) and molydenum(0) complexes **1**

Received: August 25, 2020
Published: October 6, 2020

https://dx.doi.org/10.1021/acs.inorgchem.0c02537
Inorg. Chem. 2020, 59, 15504−15513

and **2** that contain the bidentate MIC-containing ligand **L** and additional CO coligands. The electronic structures were investigated by UV−vis−near-IR (NIR), IR, and electron paramagnetic resonance (EPR) spectroelectrochemical measurements for both complexes, in combination with density functional theory (DFT) calculations. Furthermore, the photochemical reactivity was studied by time-resolved FTIR spectroscopy to probe the dynamics and ligand-exchange reactions of these complexes in the excited state. The choice of ligand **L** for these investigations is interesting because **L** has certain similarities to the α-diimine ligands mentioned above. However, **L** possesses two different donors, and one of them is the strongly donating MIC, which is expected to have a profound influence on the properties of the resulting metal complexes. To the best of our knowledge, these are the first thorough investigations of transition-metal-bound radicals that are based on MIC ligands of the 1,2,3-triazol-5-ylidene type.

Additionally, these are also the first spectroscopic investigations using time-resolved FTIR spectroscopy on the light-induced ligand substitution reactions in transition-metal complexes containing MIC ligands.

RESULTS AND DISCUSSION

Synthesis and Characterization. The pyridyltriazolium salt [**HL1**]OTf was synthesized by using a five-step synthetic route in reasonable yield (see Scheme 1 and the Supporting Information). Despite the presence of an additional pyridyl N atom in **E6**, methylation of this compound with MeOTf was fairly selective.

Scheme 1. Synthetic Strategy for [HL1]OTf

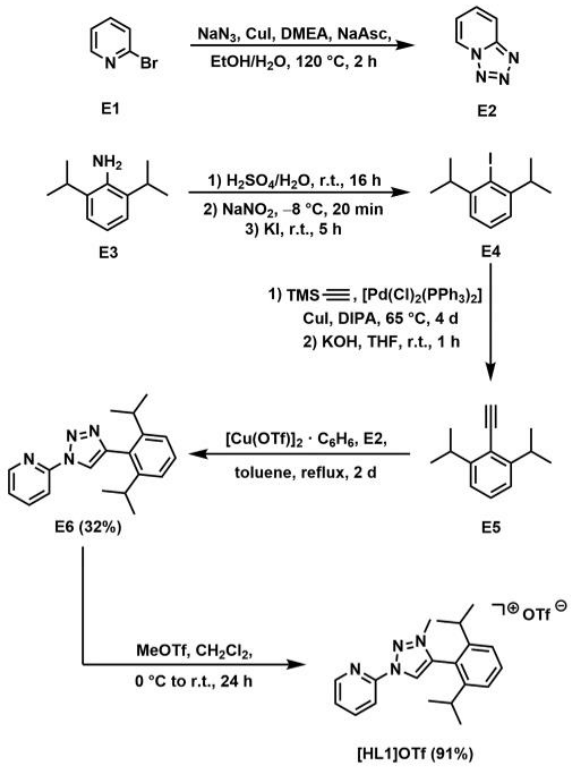

For the synthesis of complex **1**, $Cr(CO)_6$ was irradiated with UV light in tetrahydrofuran (THF; Scheme 2). The in situ formed solvato complex was further reacted with [**HL1**]OTf in the presence of NEt_3 as a base. Extractions and further chromatographic purification delivered complex **1** in good yield. A similar strategy was also used for the synthesis of complex **2**, except that in this case the prior formation of the norbornadiene complex from $Mo(CO)_6$ was necessary to get better product yield (Scheme 2). The identity and purity of the complexes were ascertained by NMR spectroscopy, elemental analysis, and electrospray ionization mass spectrometry.

We were able to obtain suitable single crystals for performing single-crystal X-ray diffraction studies. A look at the molecular structure in the crystal for both complexes (Figure 1) shows that the metal centers are coordinated in a distorted octahedral environment, with the distortion being imposed by the chelating nature of the **L1** ligand.

The Cr−C and Cr−N bond lengths to the MIC and pyridyl donors of **L1** are 2.065(2) and 2.147(2) Å. The corresponding Mo−C and Mo−N bond lengths in **2** are 2.202(1) and 2.275(1) Å. These differences in the bond lengths are a result of the different sizes of the two metal centers. The M−C bond lengths to the CO ligands that are trans to each other are longer than the M−C bond lengths to the CO ligands that are trans to **L1**. Accordingly, the C−O bond distances within the CO ligands that are trans to each other are shorter compared the same distances within the CO ligands that are trans to **L1** (Table S1). Both of these effects are likely related to the better trans influence of **L1** compared to that of the CO ligands. The C−C and C−N bond lengths within the **L1** ligand in both complexes **1** and **2** are all in the expected range.[3−6] The Dipp substituent on the 1,2,3-triazol-5-ylidene ligand in both **1** and **2** is twisted out-of-plane, with the dihedral angles between the two planes being 79.1(1)° and 79.5(1)°.

Electrochemistry and Spectroelectrochemistry. Both complexes **1** and **2** display oxidation steps at −0.17 and +0.08 V (Figure 2; all measurements were carried out in CH_3CN/0.1 M Bu_4NPF_6 and referenced against the FcH/FcH^+ couple).

These data show that both of these complexes are easy to oxidize, a fact that is a reflection of the low oxidation state of the metal centers combined with the strongly donating nature of the MIC-containing ligand.

The oxidation step for the chromium complex **1** is reversible, whereas that for the molybdenum complex **2** is irreversible. As reported previously,[45,46] we attribute this behavior to a more facile labilization of the M−CO bond upon oxidation for the molybdenum complex compared to the chromium complex. Notably, with the ligand **L1**, the oxidation step in complex **1** is reversible at ambient temperatures at normal scan rates (100 mV/s). For related α-diimine-containing $[Cr(CO)_4]$ complexes, usually lower temperatures, higher scan rates, or both are necessary to obtain reversibility.[47] We attribute the higher reversibility in our case to the presence of the strongly donating MIC unit in **L1**, which is likely able to compensate for the electron loss at the Cr center that is induced through oxidation.

Both complexes also display two reduction steps each (Figure 3). The first reduction steps, which are observed for **1** and **2** at −2.16 and −2.10 V, are reversible. The second reduction steps for these complexes appear at −2.79 and −2.68 V. This step is electrochemically and chemically irreversible for both complexes (Figure 3) because the second

https://dx.doi.org/10.1021/acs.inorgchem.0c02537
Inorg. Chem. 2020, 59, 15504−15513

Inorganic Chemistry pubs.acs.org/IC Article

Scheme 2. Synthetic Strategy for 1 and 2

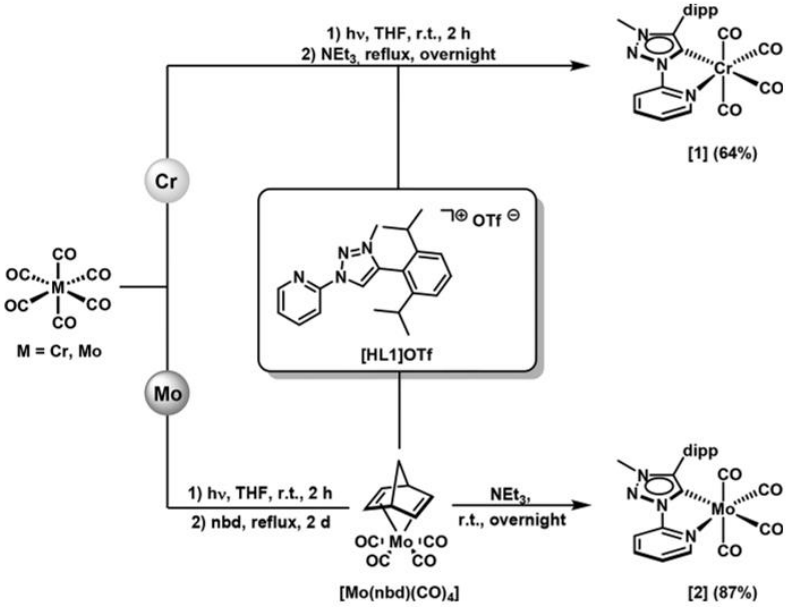

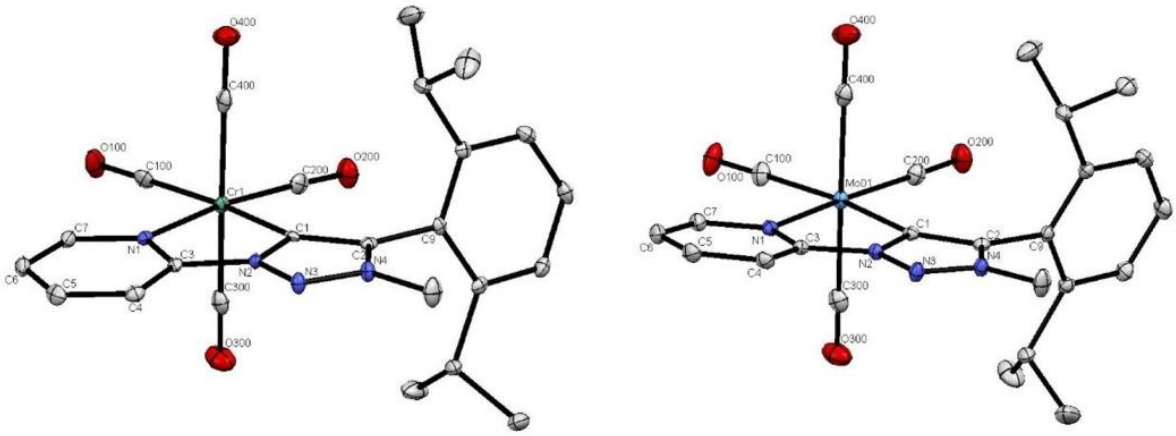

Figure 1. ORTEP representations of **1** (left) and **2** (right). H atoms are omitted for clarity. Ellipsoids are drawn with 50% probability.

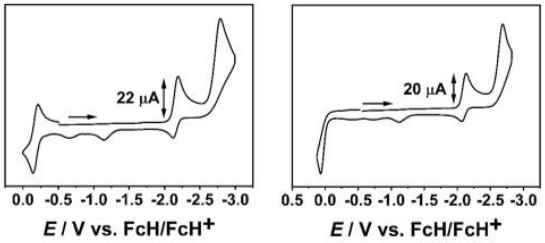

Figure 2. Cyclic voltammograms of **1** (left) and **2** (right) in CH_3CN/0.1 M Bu_4NPF_6 with a glassy carbon working electrode at a scan rate of 100 mV/s.

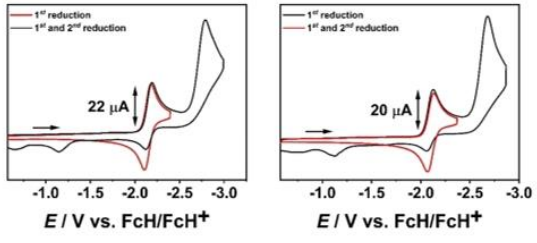

Figure 3. Cyclic voltammograms of **1** (left) and **2** (right) in CH_3CN/0.1 M Bu_4NPF_6 with a glassy carbon working electrode at a scan rate of 100 mV/s (red, first reduction; black, first and second reduction).

reduction step leads to the appearance of at least two reoxidation peaks that are shifted far to the positive side, indicating the irreversible nature of that reduction step.

As can be seen from above, the oxidation potentials for the two complexes differ substantially from each other, whereas the reduction potentials are fairly similar. These data are a first indication of a predominantly metal-centered oxidation and a

https://dx.doi.org/10.1021/acs.inorgchem.0c02537
Inorg. Chem. 2020, 59, 15504−15513

predominantly ligand-centered reduction. A more direct proof of these assignments comes from spectroelectrochemical studies and DFT calculations as discussed below.

The IR spectra of **1** and **2** in CH_3CN both display a four-band pattern in the region of 1830−2010 cm^{-1} typical for the stretching vibrations of CO ligands (Figures 4 and S19 and Tables S6 and S8), with the two middle bands being almost degenerate. This pattern is characteristic for group 6 $[M(CO)_4]$ complexes containing an additional bidentate ligand and is similar to what has been observed previously for such complexes with α-diimine ligands.[30−33] The oxidation of **1** to $\mathbf{1}^+$ leads to a strong shift of all of the CO bands to higher energies (Figure 4 and Table S6). For example, the band at 1998 cm^{-1} for **1** is shifted to 2089 cm^{-1} for $\mathbf{1}^+$, which is a change of 91 cm^{-1}. The other bands are also shifted accordingly to higher energies. Additionally, the bands at lower energies become more degenerate for $\mathbf{1}^+$, and the intensities of all the bands are more equal in the oxidized complex compared to the neutral form (Figure 4). The large shift (ca. 90 cm^{-1}) to higher energies of the CO bands is an indication of a metal-centered oxidation step. When the potential was returned to the starting potential after a full oxidation cycle was run, the spectrum of the starting complex was recovered quantitatively, thus displaying the reversibility of the oxidation step in **1**, also on the IR spectroelectrochemistry time scale (Figure S14). Even though the oxidation step of complex **2** is not reversible, the spectral shifts and intensities and the pattern observed in the IR spectrum of the oxidized species as well as a comparison of the spectrum with that of $\mathbf{1}^+$ indicate a metal-centered oxidation also for **2** (Figure S18 and Table S8).

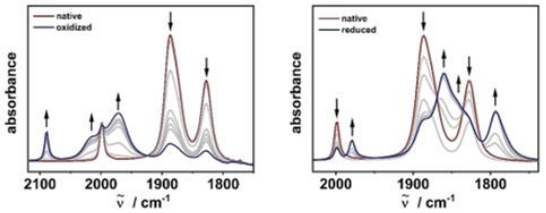

Figure 4. Changes in the IR spectra of **1** in CH_3CN/0.1 M Bu_4NPF_6 with a gold working electrode during the first oxidation (left) and first reduction (right).

In contrast to the oxidation step, the first reduction leads to a shift of all the CO bands to lower energies (Figures 4 and S19 and Tables S6 and S8). The extent of the band shifts is much smaller for the reduction step compared to the oxidation step. For example, the high energy band at 1998 cm^{-1} in **1** is only shifted to 1978 cm^{-1} in $\mathbf{1}^{\bullet-}$, which is just a difference of 20 cm^{-1}. A similar pattern is also observed for the conversion of **2** to $\mathbf{2}^{\bullet-}$. The small shift of the CO bands upon one-electron reduction is an indication of a predominantly **L1**-centered reduction step (see below). For both complexes **1** and **2**, running a complete first reduction and reoxidation back to the starting potential led to an almost quantitative regeneration of the starting spectrum, thus displaying the reversible nature of the first reduction step for both complexes (Figures S15 and S19).

The in situ generated one-electron-oxidized species $\mathbf{1}^+$ did not display any EPR signal in a fluid solution at ambient temperatures. In a frozen solution at −130 °C, $\mathbf{1}^+$ displays a signal with axial anisotropy with $g_{\parallel}$ = 1.980 and $g_{\perp}$ = 2.062, with Δ = 0.082. The simulated spectrum, including hyperfine coupling to the ^{53}Cr nucleus ($I = {}^3/_2$; natural abundance = 9.5%), fits nicely with the experimental spectrum (Figure 5). The absence of a signal in a fluid solution at room temperature and the substantial g anisotropy observed in a frozen solution indicate a predominantly metal-centered spin.

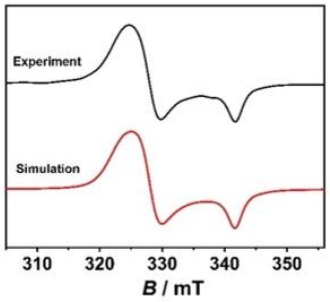

Figure 5. EPR spectrum of in situ generated $\mathbf{1}^+$ at −130 °C in CH_3CN/0.1 M Bu_4NPF_6.

The in situ generated reduced forms $\mathbf{1}^{\bullet-}$ and $\mathbf{2}^{\bullet-}$ display line-rich spectra in a fluid solution at ambient temperatures, centered at g = 2.003 and 2.004 (Figure 6). Both spectra could

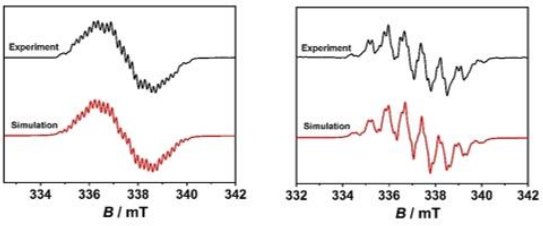

Figure 6. EPR spectra of $\mathbf{1}^{\bullet-}$ (left) and $\mathbf{2}^{\bullet-}$ (right) at room temperature in CH_3CN/0.1 M Bu_4NPF_6.

be simulated with good accuracy by considering a very small hyperfine coupling to the respective metal centers and predominant hyperfine couplings to four different ^{14}N nuclei and three or four different ^1H nuclei. These results suggest that the spin in the reduced complexes is predominantly localized on the MIC and pyridyl parts of the **L1** ligand (Tables S29 and S31).

Spin-density calculations (see below) support these results and also indicate spin densities on only three of the C atoms of the pyridyl rings. The EPR data on the oxidized and reduced complexes thus nicely complement the results from IR spectroelectrochemistry that were discussed above. To the best of our knowledge, this is the first thorough and unambiguous EPR spectroscopic characterization of a metal-bound MIC-containing radical.

Both complexes display two main absorbance bands in the visible region in their native state (Figures 7 and S22 and Tables S10 and S11). These bands have a predominantly metal-to-ligand charge-transfer (MLCT) character [a detailed assignment of the absorption bands observed in the UV−vis−NIR spectra will be made in the (TD-)DFT Calculations section]. The oxidation of complex **1** only leads to a decrease in the intensity of the bands in the visible region, with no other significant changes (Figure S21). In the case of **2**, a new

https://dx.doi.org/10.1021/acs.inorgchem.0c02537
Inorg. Chem. 2020, 59, 15504−15513

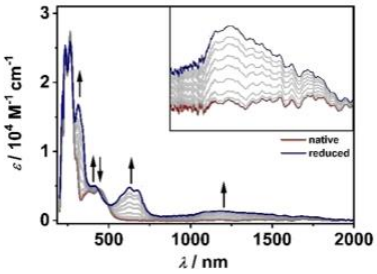

Figure 7. Changes in the UV−vis−NIR spectra of **2** in CH_3CN/0.1 M Bu_4NPF_6 during the first reduction with a gold working electrode (the inset shows the region from 800 to 2000 nm).

absorbance band is observed at about 325 nm upon oxidation, while all of the other bands decrease in intensity (Figure S23). The changes in the visible and NIR regions upon reduction in both complexes are, however, very prominent and interesting.

Both $\mathbf{1}^{\bullet-}$ and $\mathbf{2}^{\bullet-}$ display two low-energy bands in the visible region, as well as a relatively broad band in the NIR region (Figures 7 and S22 and Tables S10 and S11). Such low-energy bands in the visible and NIR regions are often an indication of a metal-bound ligand radical.[48] In view of the results from IR and EPR spectroscopy on the reduced complexes, such an assignment of these long-wavelength bands seems reasonable. A thorough discussion of these assignments will be presented in the (TD-)DFT Calculations section.

Time-Resolved FTIR Spectroscopy. The photochemical reactivity of **1** and **2** with a series of potential organic ligands, namely, CH_3CN, pyridine, 2,2′-bipyridine, and CH_2Cl_2, was analyzed by time-resolved FTIR spectroscopy.

At first, step-scan FTIR investigations were performed on **2** in a CH_3CN solution, where the sample was excited with a 355 nm laser pulse. The negative bleach bands in the step-scan difference spectrum correlate with the educt vibrations and result from a decrease of the educt concentration. The positive bands are assigned to the photoproduct, which is formed upon excitation. The educt vibration at 1831 cm^{-1} is red-shifted to 1785 cm^{-1} in the photoproduct, whereas the initial band at 1894 cm^{-1} is blue-shifted to 1902 cm^{-1}.

The transition observed at 2006 cm^{-1} for the educt is not observed at all upon excitation because only the corresponding bleach without any positive feature is observed (Figure 8).

The pattern and intensities of the step-scan difference spectrum do not change significantly over the entire time range of the experiment (approximately 500 μs after laser excitation), indicating the formation of a long-lived photoproduct (Figure S47). The presented spectra were averaged over 200 μs to obtain smooth spectra with a very good signal-to-noise ratio.

The persistence of the step-scan spectrum over the complete time range of almost 500 μs prompted us to follow the light-induced reaction pathways over longer time scales up to minutes. For this purpose, the sample was irradiated over 5 min at a repetition rate of 100 Hz, which leads to an almost complete disappearance of the educt CO absorption bands. Nevertheless, the remaining weak educt features show that **2** is photochemically quite stable and only reacts under harsh conditions. Interestingly, the new bands observed upon 5 min of irradiation agree perfectly with the positive features seen in the step-scan difference spectrum, so that the same photoproduct is observed independently of the experiment (Figure 9). After the period of irradiation (5 min), the reaction was followed without further UV excitation to analyze potential dark reactions after formation of the mentioned photoproduct. Surprisingly, a slow dark reverse reaction was observed, with complete reformation of the educt after about 30 min and an IR spectrum that is identical with the educt spectrum.

A second period of irradiation (5 min) again leads to the formation of the same changes in the IR spectrum, which underlines the reversibility of the reaction. Hence, the observations definitely do not agree with the mechanism reported for the related homoleptic complex $W(CO)_6$, which was studied by transient IR spectroscopy by Schultz and Krav-Ami.[49] The expected loss of one or several CO ligands, known from homoleptic $M(CO)_6$[50,51] and the related $M(CO)_4L_2$ α-diimine[32,52−54] transition-metal complexes, is not observed here and rather corresponds to cleavage of a coordinative bond of the bidentate MIC ligand to the Mo center and occupation of the free coordination site by a CH_3CN molecule. It is suggested that coordination of the pyridyl moiety of the MIC ligand to the metal center breaks up because the carbene

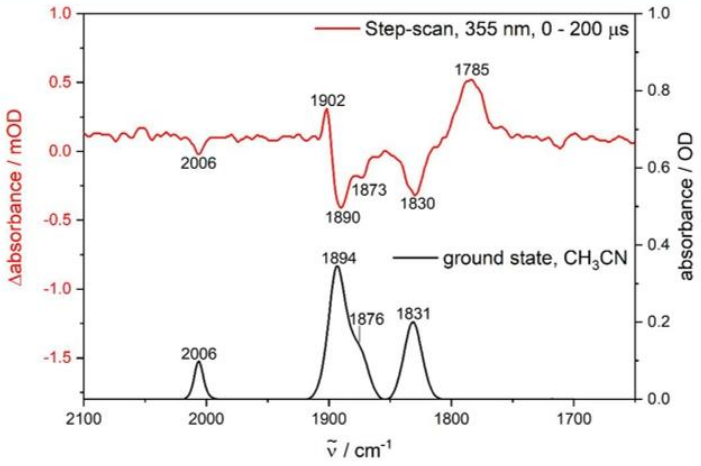

Figure 8. Ground-state FTIR and step-scan difference spectra (λ_{ex} = 355 nm, 0−200 μs) of **2** in CH_3CN.

https://dx.doi.org/10.1021/acs.inorgchem.0c02537
Inorg. Chem. 2020, 59, 15504−15513

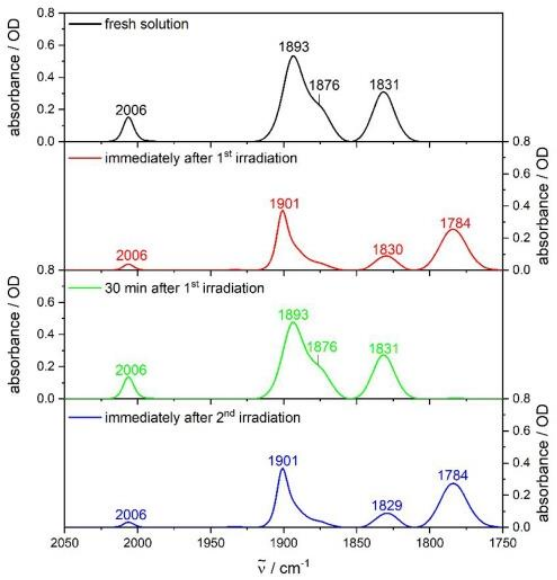

Figure 9. FTIR spectrum of a fresh solution of **2** in CH_3CN (black), immediately after the first irradiation (red), at 30 min in the dark after the first irradiation (green), and immediately after the second irradiation (blue).

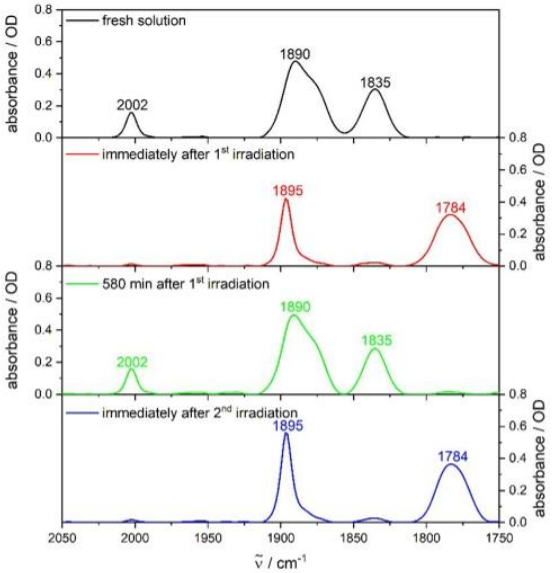

Figure 10. FTIR spectrum of a fresh solution of **2** in pyridine (black), immediately after the first irradiation (red), at 580 min in the dark after the first irradiation (green), and immediately after the second irradiation (blue).

would be protonated to the triazolium salt, which would definitely inhibit the observed reverse reaction. At the same time, dimerization, as described in the literature for the related species $[M(bpy)(CO)_3(Cl)]$ (M = Mn,[55] Re[56]), cannot be completely excluded. A large series of different potential photoproducts, including aggregates with the solvent, CO-bridged dimers, and dimers with metal−metal bonds as well as intermediate binding of free CO ligands by solvent molecules, were considered in the quantum-chemical calculations but did not lead to a good description of the measured IR spectrum.

The chromium complex **1** showed similar spectra, with the only difference being that the reactivity is lower and that one additional weak CO absorption band appears at 1928 cm^{-1} upon irradiation (Figure S48). This feature might result from the formation of a second isomer to a small extent. In addition, it should be mentioned that the dark reverse reaction is completed already after about 15 min and is thus twice as fast as that in the case of **2**, so that the metal center has an influence on the reaction dynamics. The step-scan data are analogous to the results obtained for **1** (Figures S49 and S50).

After the studies in CH_3CN, the better N-donating ligand pyridine was considered, where it should be mentioned that **1** and **2** are both stable in a pyridine solution in the dark. The full conversion of the educt species to the respective photoproduct is completed for both complexes after 5 min of irradiation (Figures 10 and S51).

The observation that almost no educt is left after this period of irradiation is explained by the better σ donation of pyridine compared to CH_3CN. Interestingly, the measured IR spectra are all analogous to the observations in CH_3CN, so that the reaction dynamics may be identical. The reverse reactions from the photoproducts back to the educts are completed after about 35 min for **1** and 10 h for **2**, so they are much slower compared to CH_3CN. This demonstrates that stable photoproducts are formed in a pyridine solution upon UV irradiation, in particular for the molybdenum(0) species.

The interesting photochemical reactivity toward pyridine incentivized us to analyze the reactivity under the presence of the bidentate ligand 2,2′-bipyridine, using CH_2Cl_2 as the solvent. For a solution of **2** saturated with 2,2′-bipyridine, a dark reaction is already observed in the first FTIR spectrum recorded immediately after preparation of the reaction mixture, which corresponds to a few tenths of seconds.

Three new weak CO bands are observed between 1925 and 2000 cm^{-1}, which do, however, not increase over time neither in the dark nor upon light excitation (Figure S52). The bleaching of the educt bands is assigned to a photochemical reaction with the solvent. Hence, the reaction with 2,2′-bipyridine is definitely incomplete with a low turnover. The observation of three CO bands might result from a loss of one CO ligand, lifting of one coordinative bond of the MIC ligand to the metal center, and coordination of the bidentate 2,2′-bipyridine ligand. However, a superimposition of additional product vibrations by the educt peaks and/or the formation of different isomers (three new peaks) cannot be excluded.

Because investigations with 2,2′-bipyridine in a CH_2Cl_2 solution gave first indications for a reaction with solvent molecules, we performed step-scan measurements for **1** and **2** in a CH_2Cl_2 solution. The obtained step-scan difference spectra are very similar to the results in CH_3CN, with the lowest-energy CO vibration being red-shifted by about 40 cm^{-1}, the energetically highest educt band showing only a bleach band without any positive peak, and the third CO motion being blue-shifted by approximately 20 cm^{-1} in the photoproduct (Figures S53−S56). This indicates that the reaction mechanism under the presence of CH_2Cl_2 may be analogous to the suggested dynamics in a CH_3CN solution with cleavage of a coordinative bond of the bidentate MIC ligand to the metal and occupation of the free coordination site

https://dx.doi.org/10.1021/acs.inorgchem.0c02537
Inorg. Chem. 2020, 59, 15504−15513

by a solvent molecule. Again, the features and intensities of the difference spectrum do not change significantly over the whole step-scan experiment, so that investigations were performed on longer times scales for **2**.

An irradiation over 5 min leads to a significant decrease of the educt bands and the appearance of a new CO vibration at about 1930 cm^{-1}. Different CO bands are observed temporarily around 1925 and 1980 cm^{-1} over the next 7 h after irradiation, indicating the formation of different intermediates with a series of coordination motifs (Figure S57).

Time-Dependent [(TD-)DFT] Calculations. DFT calculations at the B3LYP/RIJCOSX/D3/def2-TZVP level of theory were carried out on **1** and **2**, as well as on their oxidized and reduced forms. The calculated bond lengths (Tables S17 and S25) from the optimized structures of both complexes are in good agreement with the experimental bond lengths obtained from single-crystal X-ray diffraction data.

The highest occupied molecular orbital (HOMO) is largely localized on the central metal atom and the two equatorial CO ligands for **1** and **2**, whereas the lowest occupied molecular orbitals (LUMOs) in both the complexes are almost exclusively localized on the chelating pyridyl-MIC ligand **L1** (Tables S12 and S21 and Figures 11 and S25).

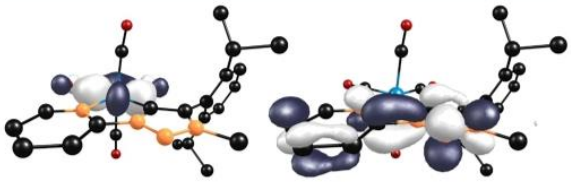

Figure 11. HOMO (left) and LUMO (right) of complex **2** (isovalue = 0.052).

Because both the first oxidation and first reduction steps of **1** are reversible on the electrochemical and spectroelectrochemical time scales, we briefly comment here on the calculated structural parameters of $\mathbf{1}^{+}$ and $\mathbf{1}^{\bullet-}$. In comparison to **1**, all of the calculated Cr−CO bond distances in $\mathbf{1}^{+}$ are strongly elongated, whereas the changes in these bond distances in $\mathbf{1}^{\bullet-}$ are only marginal (Table S17). Accordingly, the C−O bond distances in $\mathbf{1}^{+}$ are much shorter compared to those in **1**, and those in $\mathbf{1}^{\bullet-}$ display only marginal changes compared to those in **1**. The changes in the calculated bond lengths within the **L1** ligand in the three redox forms provide some further interesting trends. In **1** and $\mathbf{1}^{+}$, the changes in the bond distances within **L1** are marginal. However, when the same distances are compared between **1** and $\mathbf{1}^{\bullet-}$, some systematic changes are apparent. Within the 1,2,3-triazol-5-ylidene part of **L1**, the C1−C2 bond is shortened in $\mathbf{1}^{\bullet-}$ compared to **1**, whereas all of the other four bonds are elongated in the reduced complex in comparison to the neutral one. These observations fit nicely with the bonding/antibonding interactions between the atoms, as seen in the α-HOMO of $\mathbf{1}^{\bullet-}$ (Figure S28).

The C3−N2 bond that connects the pyridyl and MIC units in **L1** is significantly shorter in $\mathbf{1}^{\bullet-}$ than in **1**. Within the pyridyl ring, the most significant changes are in the C3−N1 and C3−C4 bond distances, both of which become longer upon moving from **1** to $\mathbf{1}^{\bullet-}$. With these optimized structures, we calculated the IR, EPR, and UV−vis−NIR spectroscopic features for the various redox forms of both complexes. In the following, we will restrict the discussion on the ground-state spectroscopic properties to the chromium complex **1** because the properties of the molybdenum complex **2** are very similar to those of **1**.

The calculated IR spectrum of **1** nicely reproduces the experimentally observed four-band pattern in the CO region (Figures 4 and 12). The calculated absolute values of the CO stretching frequencies are, however, shifted to higher energies compared to the experimentally observed ones, which can be explained by the applied harmonic approximation (Figure S13 and Table S5). Additionally, the shift of the CO bands for the reduced form of **1** in comparison to the native form is also nicely reproduced by the calculations (Figure 12 and Table S7). The calculated spectrum of $\mathbf{1}^{+}$ (Figure S16) differs significantly from the experimental spectrum. The reasons for this discrepancy are not very clear at this moment and may result from ion pairing. Further high-level quantum-chemical calculations will be required to clarify this point.

TD-DFT calculations on **1** show that the experimentally observed absorption band at 485 nm (see above) is a mixture of transitions of HOMO−2 → LUMO (23%) and HOMO−1 → LUMO (71%) (Figures S25 and S30 and Table S13). This band can thus be assigned to a mixture of d(Cr) → π^*(**L1**) MLCT and CO → **L1** ligand-to-ligand charge-transfer (LLCT) transitions. The other prominent band in the visible region at 394 nm arises from transition HOMO−2 → LUMO+1. This band can thus be assigned to predominantly d(Cr) → π^*(pyridyl) MLCT and CO → pyridyl LLCT transitions (Figure S30 and Table S13). As discussed above, upon oxidation of **1** to $\mathbf{1}^{+}$, the original bands of **1** basically decrease in intensity, with no new prominent features appearing. Thus, the bands of $\mathbf{1}^{+}$ will not be discussed further

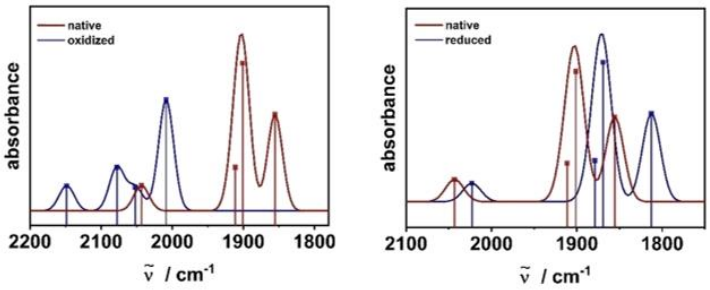

Figure 12. Calculated IR spectra of **1**, $\mathbf{1}^{+}$ (left), and $\mathbf{1}^{\bullet-}$ (right) in CH_3CN (B3LYP/RIJCOSX/D3 def2-TZVP).

https://dx.doi.org/10.1021/acs.inorgchem.0c02537
Inorg. Chem. 2020, 59, 15504−15513

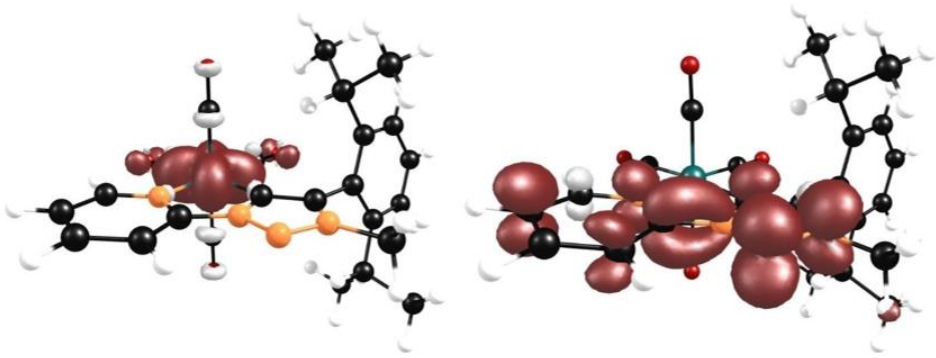

Figure 13. Spin-density plots of complex 1^+ (left) and 1^- (right) (isovalue = 0.003).

here. The reduced species $1^{\bullet-}$, on the other hand, displays multiple prominent bands in the low-energy visible and NIR regions. The origin of all of these bands is in the α-HOMO of $1^{\bullet-}$, which is delocalized over the ligand **L1** (Table S15 and Figure S28). Thus, for the reduced species, the transitions in the lower-energy visible and NIR regions can all be assigned to ligand-centered transitions. In particular, the broad NIR band centered at around 1180 nm can be assigned to a α-HOMO → α-LUMO transition, which is an intraligand-charge-transfer-type transition from the MIC to pyridyl part of **L1**. Additionally, spin-density distributions were calculated for 1^+ and $1^{\bullet-}$. In keeping with the results from EPR spectroscopy, for 1^+, the spin density is almost exclusively centered on chromium, and for $1^{\bullet-}$, the spin density is almost exclusively centered on the **L1** ligand (Figure 13 and Table S28).

■ CONCLUSIONS

In summary, we have presented here the synthesis and characterization of the first examples of chromium(0) and molydenum(0) complexes with a MIC-containing ligand of the 1,2,3-triazol-5-ylidene type (together with an additional pyridyl donor).

A combination of IR, EPR, and UV−vis−NIR spectroelectrochemical measurements shows that the oxidation step is metal-centered and completely reversible for the chromium(0) complex.[45,46] This result is a confirmation that the MIC ligands can support reversible redox processes at metal centers by compensating for the electron loss through their strong donating power. The first reduction step for both complexes is reversible for both complexes and almost exclusively centered on the pyridyl-MIC ligand. This is also the first report on a thorough characterization of a transition-metal-bound MIC radical. DFT and TD-DFT calculations were performed to further understand and support the aforementioned spectroscopic data.

The photochemical reactivity under the presence of different organic ligands was investigated by time-resolved (step-scan) FTIR spectroscopy, with the formation of metastable photoproducts reacting back to the educt species in slow reverse reactions. The reaction mechanism will be further elucidated by high-level quantum-chemical calculations, but the presented results already show that the irreversible loss of a CO ligand and occupation of a free coordination site by a solvent molecule, which are typically observed for homoleptic $M(CO)_6$ and heteroleptic $M(CO)_4L_2$ transition-metal complexes, are definitely not observed for the MIC-containing systems presented in this work because of the unexpected reversibility.

■ ASSOCIATED CONTENT

Supporting Information

The Supporting Information is available free of charge at https://pubs.acs.org/doi/10.1021/acs.inorgchem.0c02537.

Experimental section, NMR spectra, electrochemistry measurements, photophysical measurements, crystallographic details and molecular structures, and DFT (PDF)

Accession Codes

CCDC 2023753 and 2023754 contain the supplementary crystallographic data for this paper. These data can be obtained free of charge via www.ccdc.cam.ac.uk/data_request/cif, or by emailing data_request@ccdc.cam.ac.uk, or by contacting The Cambridge Crystallographic Data Centre, 12 Union Road, Cambridge CB2 1EZ, UK; fax: +44 1223 336033.

■ AUTHOR INFORMATION

Corresponding Authors

Markus Gerhards − *Department of Chemistry and Research Center Optimas, Technische Universität Kaiserslautern, 67663 Kaiserslautern, Germany;* orcid.org/0000-0002-8748-2940; Email: gerhards@chemie.uni-kl.de

Biprajit Sarkar − *Lehrstuhl für Anorganische Koordinationschemie, Universität Stuttgart, D-70569 Stuttgart, Germany; Institut für Chemie und Biochemie, Freie Universität Berlin, 14195 Berlin, Germany;* orcid.org/0000-0003-4887-7277; Email: biprajit.sarkar@iac.uni-stuttgart.de

Authors

Tobias Bens − *Lehrstuhl für Anorganische Koordinationschemie, Universität Stuttgart, D-70569 Stuttgart, Germany; Institut für Chemie und Biochemie, Freie Universität Berlin, 14195 Berlin, Germany*

Pit Boden − *Department of Chemistry and Research Center Optimas, Technische Universität Kaiserslautern, 67663 Kaiserslautern, Germany*

Patrick Di Martino-Fumo − *Department of Chemistry and Research Center Optimas, Technische Universität Kaiserslautern, 67663 Kaiserslautern, Germany*

Julia Beerhues − *Lehrstuhl für Anorganische Koordinationschemie, Universität Stuttgart, D-70569 Stuttgart, Germany; Institut für Chemie und Biochemie, Freie Universität Berlin, 14195 Berlin, Germany*

https://dx.doi.org/10.1021/acs.inorgchem.0c02537
Inorg. Chem. 2020, 59, 15504−15513

Uta Albold − *Institut für Chemie und Biochemie, Freie Universität Berlin, 14195 Berlin, Germany*
Sebastian Sobottka − *Institut für Chemie und Biochemie, Freie Universität Berlin, 14195 Berlin, Germany*
Nicolás I. Neuman − *Institut für Chemie und Biochemie, Freie Universität Berlin, 14195 Berlin, Germany; Instituto de Desarrollo Tecnológico para la Industria Química, INTEC, UNL-CONICET, 3000 Santa Fe, Argentina;* orcid.org/0000-0003-3368-0228

Complete contact information is available at: https://pubs.acs.org/10.1021/acs.inorgchem.0c02537

Notes

The authors declare no competing financial interest.

■ ACKNOWLEDGMENTS

The high-performance computing facilities at ZEDAT of Freie Universität Berlin are acknowledged for access to computing resources. The core facility (BioSupraMol) is gratefully acknowledged. The authors are grateful to the DFG Priority Program SPP 2102 "Light-controlled reactivity of metal complexes" (SA 1840/7-1 and GE 961/10-1) for financial support. N.I.N. is grateful to the Alexander von Humboldt Foundation for a postdoctoral fellowship.

■ DEDICATION

Dedicated to Prof. Christoph Janiak on the occasion of his 60th birthday.

■ REFERENCES

(1) Guisado-Barrios, G.; Bouffard, J.; Donnadieu, B.; Bertrand, G. Crystalline 1H-1,2,3-Triazol-5-ylidenes: New Stable Mesoionic Carbenes (MICs). *Angew. Chem., Int. Ed.* **2010**, *49*, 4759−4762.
(2) Mathew, P.; Neels, A.; Albrecht, M. 1,2,3-Triazolylidenes as Versatile Abnormal Carbene Ligands for Late Transition Metals. *J. Am. Chem. Soc.* **2008**, *130*, 13534−13535.
(3) Crowley, J. D.; Lee, A.-L.; Kilpin, K. J. 1,3,4-Trisubtituted-1,2,3-Triazol-5-ylidene 'Click' Carbene Ligands: Synthesis, Catalysis and Self-Assembly. *Aust. J. Chem.* **2011**, *64*, 1118−1132.
(4) Guisado-Barrios, G.; Soleilhavoup, M.; Bertrand, G. 1 H-1,2,3-Triazol-5-ylidenes: Readily Available Mesoionic Carbenes. *Acc. Chem. Res.* **2018**, *51*, 3236−3244.
(5) Schweinfurth, D.; Hettmanczyk, L.; Suntrup, L.; Sarkar, B. Metal Complexes of Click-Derived Triazoles and Mesoionic Carbenes: Electron Transfer, Photochemistry, Magnetic Bistability, and Catalysis. *Z. Anorg. Allg. Chem.* **2017**, *643*, 554−584.
(6) Vivancos, Á.; Segarra, C.; Albrecht, M. Mesoionic and Related Less Heteroatom-Stabilized N-Heterocyclic Carbene Complexes: Synthesis, Catalysis, and Other Applications. *Chem. Rev.* **2018**, *118*, 9493−9586.
(7) Corbucci, I.; Petronilho, A.; Müller-Bunz, H.; Rocchigiani, L.; Albrecht, M.; Macchioni, A. Substantial Improvement of Pyridine-Carbene Iridium Water Oxidation Catalysts by a Simple Methyl-to-Octyl Substitution. *ACS Catal.* **2015**, *5*, 2714−2718.
(8) Kleinhans, G.; Guisado-Barrios, G.; Liles, D. C.; Bertrand, G.; Bezuidenhout, D. I. A rhodium(I)-oxygen adduct as a selective catalyst for one-pot sequential alkyne dimerization-hydrothiolation tandem reactions. *Chem. Commun.* **2016**, *52*, 3504−3507.
(9) Suntrup, L.; Stein, F.; Klein, J.; Wilting, A.; Parlane, F. G. L.; Brown, C. M.; Fiedler, J.; Berlinguette, C. P.; Siewert, I.; Sarkar, B. Rhenium Complexes of Pyridyl-Mesoionic Carbenes: Photochemical Properties and Electrocatalytic CO_2 Reduction. *Inorg. Chem.* **2020**, *59*, 4215−4227.
(10) van der Meer, M.; Glais, E.; Siewert, I.; Sarkar, B. Electrocatalytic Dihydrogen Production with a Robust Mesoionic Pyridylcarbene Cobalt Catalyst. *Angew. Chem., Int. Ed.* **2015**, *54*, 13792−13795.
(11) Woods, J. A.; Lalrempuia, R.; Petronilho, A.; McDaniel, N. D.; Müller-Bunz, H.; Albrecht, M.; Bernhard, S. Carbene iridium complexes for efficient water oxidation: scope and mechanistic insights. *Energy Environ. Sci.* **2014**, *7*, 2316−2328.
(12) Maity, R.; van der Meer, M.; Sarkar, B. Redox-active multinuclear Pd(II) complexes with bis- and tris-mesoionic carbenes. *Dalton Trans.* **2015**, *44*, 46−49.
(13) Suntrup, L.; Klenk, S.; Klein, J.; Sobottka, S.; Sarkar, B. Gauging Donor/Acceptor Properties and Redox Stability of Chelating Click-Derived Triazoles and Triazolylidenes: A Case Study with Rhenium-(I) Complexes. *Inorg. Chem.* **2017**, *56*, 5771−5783.
(14) Baschieri, A.; Monti, F.; Matteucci, E.; Mazzanti, A.; Barbieri, A.; Armaroli, N.; Sambri, L. A Mesoionic Carbene as Neutral Ligand for Phosphorescent Cationic Ir(III) Complexes. *Inorg. Chem.* **2016**, *55*, 7912−7919.
(15) Brown, D. G.; Sanguantrakun, N.; Schulze, B.; Schubert, U. S.; Berlinguette, C. P. Bis(tridentate) Ruthenium-Terpyridine Complexes Featuring Microsecond Excited-State Lifetimes. *J. Am. Chem. Soc.* **2012**, *134*, 12354−12357.
(16) Chábera, P.; Liu, Y.; Prakash, O.; Thyrhaug, E.; Nahhas, A. E.; Honarfar, A.; Essén, S.; Fredin, L. A.; Harlang, T. C. B.; Kjær, K. S.; et al. A low-spin Fe(iii) complex with 100-ps ligand-to-metal charge transfer photoluminescence. *Nature* **2017**, *543*, 695−699.
(17) Hettmanczyk, L.; Spall, S. J. P.; Klenk, S.; van der Meer, M.; Hohloch, S.; Weinstein, J. A.; Sarkar, B. Structural, Electrochemical, and Photochemical Properties of Mono- and Digold(I) Complexes Containing Mesoionic Carbenes. *Eur. J. Inorg. Chem.* **2017**, *2017*, 2112−2121.
(18) Kleinhans, G.; Chan, A. K.-W.; Leung, M.-Y.; Liles, D. C.; Fernandes, M. A.; Yam, V. W.-W.; Fernández, I.; Bezuidenhout, D. I. Synthesis and Photophysical Properties of T-Shaped Coinage-Metal Complexes. *Chem. - Eur. J.* **2020**, *26*, 6993−6998.
(19) Leigh, V.; Ghattas, W.; Lalrempuia, R.; Müller-Bunz, H.; Pryce, M. T.; Albrecht, M. Synthesis, Photo-, and Electrochemistry of Ruthenium Bis(bipyridine) Complexes Comprising a N-heterocyclic Carbene Ligand. *Inorg. Chem.* **2013**, *52*, 5395−5402.
(20) Matteucci, E.; Monti, F.; Mazzoni, R.; Baschieri, A.; Bizzarri, C.; Sambri, L. Click-Derived Triazolylidenes as Chelating Ligands: Achievement of a Neutral and Luminescent Iridium(III)-Triazolide Complex. *Inorg. Chem.* **2018**, *57*, 11673−11686.
(21) Sarkar, B.; Suntrup, L. Illuminating Iron: Mesoionic Carbenes as Privileged Ligands in Photochemistry. *Angew. Chem., Int. Ed.* **2017**, *56*, 8938−8940.
(22) Soellner, J.; Tenne, M.; Wagenblast, G.; Strassner, T. Phosphorescent Platinum(II) Complexes with Mesoionic 1H-1,2,3-Triazolylidene Ligands. *Chem. - Eur. J.* **2016**, *22*, 9914−9918.
(23) Suntrup, L.; Stein, F.; Hermann, G.; Kleoff, M.; Kuss-Petermann, M.; Klein, J.; Wenger, O. S.; Tremblay, J. C.; Sarkar, B. Influence of Mesoionic Carbenes on Electro- and Photoactive Ru and Os Complexes: A Combined (Spectro-)Electrochemical, Photochemical, and Computational Study. *Inorg. Chem.* **2018**, *57*, 13973−13984.
(24) Hettmanczyk, L.; Manck, S.; Hoyer, C.; Hohloch, S.; Sarkar, B. Heterobimetallic complexes with redox-active mesoionic carbenes as metalloligands: electrochemical properties, electronic structures and catalysis. *Chem. Commun.* **2015**, *51*, 10949−10952.
(25) Hettmanczyk, L.; Suntrup, L.; Klenk, S.; Hoyer, C.; Sarkar, B. Heteromultimetallic Complexes with Redox-Active Mesoionic Carbenes: Control of Donor Properties and Redox-Induced Catalysis. *Chem. - Eur. J.* **2017**, *23*, 576−585.
(26) Klenk, S.; Rupf, S.; Suntrup, L.; van der Meer, M.; Sarkar, B. The Power of Ferrocene, Mesoionic Carbenes, and Gold: Redox-Switchable Catalysis. *Organometallics* **2017**, *36*, 2026−2035.
(27) Vanicek, S.; Beerhues, J.; Bens, T.; Levchenko, V.; Wurst, K.; Bildstein, B.; Tilset, M.; Sarkar, B. Oxidative Access via Aqua Regia to an Electrophilic, Mesoionic Dicobaltoceniumyltriazolylidene Gold-(III) Catalyst. *Organometallics* **2019**, *38*, 4383−4386.

https://dx.doi.org/10.1021/acs.inorgchem.0c02537
Inorg. Chem. 2020, 59, 15504−15513

(28) Vanicek, S.; Podewitz, M.; Stubbe, J.; Schulze, D.; Kopacka, H.; Wurst, K.; Müller, T.; Lippmann, P.; Haslinger, S.; Schottenberger, H.; et al. Highly Electrophilic, Catalytically Active and Redox-Responsive Cobaltoceniumyl and Ferrocenyl Triazolylidene Coinage Metal Complexes. *Chem. - Eur. J.* **2018**, *24*, 3742−3753.
(29) Baltrun, M.; Watt, F. A.; Schoch, R.; Wölper, C.; Neuba, A. G.; Hohloch, S. A new bis-phenolate mesoionic carbene ligand for early transition metal chemistry. *Dalton Trans.* **2019**, *48*, 14611−14625.
(30) Vichova, J.; Hartl, F.; Vlček, A., Jr. Wavelength-Dependent Photosubstitution and Excited-State Dynamics of $[Cr(CO)_4(2,2'$-bipyridine)]: A Quantum Yield and Picosecond Absorption Atudy. *J. Am. Chem. Soc.* **1992**, *114*, 10903−10910.
(31) Stufkens, D. J. Spectroscopy, Photophysics and Photochemistry of Zerovalent Transition Metal α-Diimine Complexes. *Coord. Chem. Rev.* **1990**, *104*, 39−112.
(32) Vlček, A., Jr. Highlights of spectroscopy, photochemistry and electrochemistry of $[M(CO)_4(\alpha$-diimine)] complexes, M = Cr, Mo, W. *Coord. Chem. Rev.* **2002**, *230*, 225−242.
(33) Tory, J.; Setterfield-Price, B.; Dryfe, R. A. W.; Hartl, F. $[M(CO)_4$ (2,2′-bipyridine)] (M = Cr, Mo, W) Complexes as Efficient Catalysts for Electrochemical Reduction of CO_2 at a Gold Electrode. *ChemElectroChem* **2015**, *2*, 213−217.
(34) Schoonover, J. R.; Strouse, G. F.; Omberg, K. M.; Dyer, R. B. Time-Resolved, Step-Scan FTIR Spectroscopy of Excited States of Transition Metal Complexes. *Comments Inorg. Chem.* **1996**, *18*, 165−188.
(35) Skopintsev, P.; Ehrenberg, D.; Weinert, T.; James, D.; Kar, R. K.; Johnson, P. J. M.; Ozerov, D.; Furrer, A.; Martiel, I.; Dworkowski, F.; et al. Femtosecond-to-millisecond structural changes in a light-driven sodium pump. *Nature* **2020**, *583*, 314−318.
(36) Smith, G. D.; Hutson, M. S.; Lu, Y.; Tierney, M. T.; Grinstaff, M. W.; Palmer, R. A. Step-Scan FT-IR Time-Resolved Spectroscopy in the Solid State. *Appl. Spectrosc.* **2001**, *55*, 637−641.
(37) Treiling, S.; Wang, C.; Förster, C.; Reichenauer, F.; Kalmbach, J.; Boden, P.; Harris, J. P.; Carrella, L. M.; Rentschler, E.; Resch-Genger, U.; et al. Luminescence and Light-Driven Energy and Electron Transfer from an Exceptionally Long-Lived Excited State of a Non-Innocent Chromium(III) Complex. *Angew. Chem., Int. Ed.* **2019**, *58*, 18075−18085.
(38) Wagner, H. E.; Di Martino-Fumo, P.; Boden, P.; Zimmer, M.; Klopper, W.; Breher, F.; Gerhards, M. Structural Characterization and Lifetimes of Triple-Stranded Helical Coinage Metal Complexes: Synthesis, Spectroscopy and Quantum Chemical Calculations. *Chem. - Eur. J.* **2020**, *26*, 10743−10751.
(39) Zimmer, M.; Rupp, F.; Singer, P.; Walz, F.; Breher, F.; Klopper, W.; Diller, R.; Gerhards, M. Time-resolved IR spectroscopy of a trinuclear palladium complex in solution. *Phys. Chem. Chem. Phys.* **2015**, *17*, 14138−14144.
(40) Harris, A.; Saita, M.; Resler, T.; Hughes-Visentin, A.; Maia, R.; Pranga-Sellnau, F.; Bondar, A.-N.; Heberle, J.; Brown, L. S. Molecular details of the unique mechanism of chloride transport by a cyanobacterial rhodopsin. *Phys. Chem. Chem. Phys.* **2018**, *20*, 3184−3199.
(41) Schroeder, L.; Oldemeyer, S.; Kottke, T. Time-Resolved Infrared Spectroscopy on Plant Cryptochrome-Relevance of Proton Transfer and ATP Binding for Signaling. *J. Phys. Chem. A* **2018**, *122*, 140−147.
(42) Schultz, H. R.; Krav-Ami, S. When the ligands go marching in: a step-scan Fourier transform infrared spectroscopic study of ligand attack at the transient species $W(CO)_5$(CyH). *J. Chem. Soc., Dalton Trans.* **1999**, 115−117.
(43) Moore, B. D.; Poliakoff, M.; Simpson, M. B.; Turner, J. J. Fast Time-Resolved FTIR Detection of Short-Lived Photochemical Transient Species in Solution: A Direct Comparison with IR Laser Spectroscopy. *J. Phys. Chem.* **1985**, *89*, 850−853.
(44) Torres-Alacan, J.; Vöhringer, P. Photolysis of a High-Spin Azidoiron(III) Complex Studied by Time-Resolved Fourier-Transform Infrared Spectroscopy. *Chem. - Eur. J.* **2017**, *23*, 6746−6751.
(45) Bohnenberger, J.; Feuerstein, W.; Himmel, D.; Daub, M.; Breher, F.; Krossing, I. Stable salts of the hexacarbonyl chromium(I) cation and its pentacarbonyl-nitrosyl chromium(I) analogue. *Nat. Commun.* **2019**, *10*, 624.
(46) Bohnenberger, J.; Schmitt, M.; Feuerstein, W.; Krummenacher, I.; Butschke, B.; Czajka, J.; Malinowski, P. J.; Breher, F.; Krossing, I. Completing the triad: synthesis and full characterization of homoleptic and heteroleptic carbonyl and nitrosyl complexes of the group VI metals. *Chem. Sci.* **2020**, *11*, 3592−3603.
(47) Vlček, A., Jr.; Baumann, F.; Kaim, W.; Grevels, F.-W.; Hartl, F. Electron distribution in the Cr(CO4(bpy)$^{\bullet-}$ (bpy = 2,2′-bipyridine) radical anion as reveal by EPR spectroscopy and IR spectroelectrochemistry of ^{13}C-enriched species. *J. Chem. Soc., Dalton Trans.* **1998**, 215−220.
(48) Kaim, W. Concepts for metal complex chromophores absorbing in the near infrared. *Coord. Chem. Rev.* **2011**, *255*, 2503−2513.
(49) Schultz, H. R.; Krav-Ami, S. When the ligand go marching in: a step-scan Fourier transform infrared spectroscopic study of ligand attack at the transient species $W(CO)_5$(CyH). *J. Chem. Soc., Dalton Trans.* **1999**, 115−117.
(50) Schaffner, K.; Grevels, F.-W. Infrared Spectroscopy of Excited States and Transient in Photochemistry. *J. Mol. Struct.* **1988**, *173*, 51−65.
(51) Greetham, G. M.; Sole, D.; Clark, I. P.; Parker, A. W.; Pollard, M. R.; Towrie, M. Time-resolved multiple probe spectroscopy. *Rev. Sci. Instrum.* **2012**, *83*, 103107.
(52) Manuta, D. M.; Lees, A. J. Emission and Photochemistry of $M(CO)_4$(diimine) (M = Cr, Mo, W) Complexes in Room-Temperature Solution. *Inorg. Chem.* **1986**, *25*, 1354−1359.
(53) Moore, K. J.; Petersen, J. D. Synthesis, Characterization and Photochemistry of some Monometallic and Bimetallic 2,2′-Bipyrimidine Complexes of Chromum and Tungsten Carbonyls. *Polyhedron* **1983**, *2*, 279−284.
(54) Kianfar, E.; Kaiser, M.; Knör, G. Synthesis, characterization and photoreactivity of rhenium and molybdenum carbonyl complexes with iminopyridine ligands. *J. Organomet. Chem.* **2015**, *799*−*800*, 13−18.
(55) Hartl, F.; Rossenaar, B. D.; Stor, G. J.; Stufkens, D. J. Role of an electrontransfer chain reaction in the unusual photochemical formation of fivecoordinated anions $[Mn(CO)_3$(diimine)]$^-$ from fac$[Mn(X)(CO)_3$(diimine)] (X = halide) at low temperatures. *Red. Trav. Chim. Pays-Bas* **1995**, *114*, 565−570.
(56) Lang, P.; Giereth, R.; Tschierlei, S.; Schwalbe, M. Unexpected wavelength dependency of the photocatalytic CO_2 reduction performance of the well-known (bpy)$Re(CO)_3Cl$ complex. *Chem. Commun.* **2019**, *55*, 600−603.

https://dx.doi.org/10.1021/acs.inorgchem.0c02537
Inorg. Chem. 2020, 59, 15504−15513

3.4 The Best of Both Worlds: Combining the Power of MICs and WCAs to generate Stable and Crystalline Cr^{I}-tetracarbonyl Complexes with π −Accepting Ligands

T. Bens,† R. R. M. Walter,† J. Beerhues,†,^ M. Schmitt,‡ Prof. Dr. I. Krossing,‡, Prof. Dr. B. Sarkar†,*

†Institut für Anorganische Chemie, Universität Stuttgart, Pfaffenwaldring 55, D-70569 Stuttgart, Germany, Email: biprajit.sarkar@iac.uni-stuttgart.de

^Current Address: Institute of Chemical Research of Catalonia (ICIQ), Barcelona Institute of Science and Technology (BIST), Av. Països Catalans 16, 43007 Tarragona, Spain.

‡Institut für Anorganische und Analytische Chemie und Freiburger Materialforschungszentrum (FMF), Universität Freiburg, Albertstr. 21, 79104 Freiburg, Germany; Email: krossing@uni-freiburg.de

This article was published and is reprinted with permission from WILEY-VCH:

T. Bens, R. R. M. Walter, J. Beerhues, M. Schmitt, I. Krossing, B. Sarkar, *Chem. Eur. J.* **2023**, *29*, e202301205.

DOI: 10.1002/chem.202301205 (© WILEY-VCH Verlag GmbH & Co. KGaA, Weinheim).

The **Supporting Information** is available free of charge at https://chemistry-europe.onlinelibrary.wiley.com/doi/full/10.1002/chem.202301205.

Autor contribution: The project was designed by Biprajit Sarkar. The presented complexes were synthesized and fully characterized by Tobias Bens. All (spectro)electrochemical measurements and theoretical calculation were performed by Tobias Bens. However, the [Cr(**C–C**)] complex was synthesized as a part of the master thesis. The weak coordinating anion (WCA = $[Al(OR^F)_4]^-$ with $R^F = C(CF_3)_3$) was provided by Manuel Schmitt. X-Ray diffraction analysis was carried out by Robert R. M. Walter and Julia Beerhues. The manuscript was written by Tobias Bens and Biprajit Sarkar.

Check for updates

Chemistry–A European Journal

Research Article
doi.org/10.1002/chem.202301205

Chemistry Europe
European Chemical Societies Publishing

www.chemeurj.org

The Best of Both Worlds: Combining the Power of MICs and WCAs To Generate Stable and Crystalline Cr^{I}-Tetracarbonyl Complexes with π-Accepting Ligands

Tobias Bens,[a] Robert R. M. Walter,[a] Julia Beerhues,[a, b] Manuel Schmitt,[c] Ingo Krossing,[c] and Biprajit Sarkar*[a]

Abstract: Here we present stable and crystalline chromium(I) tetracarbonyl complexes with pyridyl-MIC (MIC = mesoionic carbene) ligands and weakly coordinating anions (WCA = $[Al(OR^F)_4]^-$, $R^F = C(CF_3)_3$ and $BAr^F = [B(Ar^F)_4]^-$, $Ar^F = 3,5\text{-}(CF_3)_2C_6H_3$). The complexes were fully characterized via crystallographic, spectroscopic and theoretical methods. The influence of counter anions on the IR and EPR spectroscopic properties of the Cr^{I} complexes was investigated, and the electronic innocence versus non-innocence of WCAs was probed. These are the first examples of stable and crystalline $[Cr(CO)_4]^+$ complexes with a chelating π–accepting ligand, and the data presented here are of relevance for both the photochemical and the electrochemical properties of these classes of compounds.

Introduction

Group 6 tetracarbonyl complexes of the type $[M(CO)_4(L)]$ (M = Cr, Mo, W; L = chelating π–accepting ligands)[1–11] have received increasing attention due to their intriguing physical and chemical properties.[7,12] They are attractive candidates for electrochemical and photophysical bond activation, which makes them suitable compounds for electrochemical CO_2 reduction[4,6–8,10] and photoredox catalysis.[9]

In the last 50 years, great efforts have been made to study the photophysical/photochemical[2,3,11,13,14] and electrochemical[1,4,6,8,10,11,15,16–20] properties of such systems. Photoexcitation of carbonyl complexes of zero-valent group 6 metals with chelating π–accepting ligands can sometimes lead to emissive states,[21,22] but CO dissociation is often the main consequence of light excitation in these molecules.[1,3,22,23,24] The MLCT excited states are indirectly linked to the oxidized and the reduced forms of the ground state of such molecules. Thus, the photochemistry and the redox chemistry of these systems are often studied hand in hand. In this context, it was observed early on in the research of such compounds that the oxidation step of $[M(CO_4)L)]$ with π–accepting ligands, as investigated by cyclic voltammetry, is often irreversible.[11,16,18–20] Only in very few cases a reversible oxidation has been observed, albeit only at low temperatures.[25] This irreversibility is due to the kinetic lability and uncompensated electron deficiency of the central metal atom, resulting in decreased π–backdonation from the metal center to the CO ligand and consequently weakening of the M–CO bond.[16–20] Thus, attempts to isolate, crystallize and thoroughly characterize such oxidized species with π–accepting chelating ligands have never been successful.

Some of us have recently shown that pyridyl-mesoionic carbene (MIC) chelating ligands (Scheme 1) are a privileged class of ligands that retain a similar π–accepting property to 2,2′-bipyridine (bpy), while at the same time incorporating the excellent σ–donor properties of a MIC.[26] Investigations with Re^{I} compounds as well as with group 6 compounds[1–3] clearly demonstrated both the good π–accepting and σ–donor properties of this ligand class.[27]

Recently, Krossing and co-workers developed a synthetic strategy to access the homoleptic 17 VE $[M(CO)_6]^+$ (M = Cr, Mo, W) complexes with weakly coordinating anions ($WCA^- = [Al(OR^F)_4]^-$ with $R^F = C(CF_3)_3$) to overcome CO dissociation, substitution and dimerization of the so-called (super-)electrophiles.[28] In the following, we show that by combining WCA or BAr^F (= tetrakis(3,5-bis(trifluoromethyl)-phenyl)borate) with our pyridyl-MIC ligands (C–C = pyridyl-4-triazolylidene[26] and C-N = pyridyl-1-triazolylidene)[1] it is possible to isolate cationic $[Cr(CO)_4$(pyridyl-MIC)](WCA) complexes with

[a] T. Bens, R. R. M. Walter, Dr. J. Beerhues, Prof. Dr. B. Sarkar
Institut für Anorganische Chemie
Universität Stuttgart
Pfaffenwaldring 55, 70569 Stuttgart (Germany)
E-mail: biprajit.sarkar@iac.uni-stuttgart.de
Homepage: http://www.iac.uni-stuttgart.de/en/research/aksarkar/

[b] Dr. J. Beerhues
Current Address: Institute of Chemical Research of Catalonia (ICIQ)
Barcelona Institute of Science and Technology (BIST)
Av. Paisos Catalans 16, 43007 Tarragona (Spain)

[c] M. Schmitt, Prof. Dr. I. Krossing
Institut für Anorganische und Freiburger Materialforschungszentrum (FMF)
Universität Freiburg
Albertstr. 21, 79104 Freiburg (Germany)

Supporting information for this article is available on the WWW under https://doi.org/10.1002/chem.202301205

This manuscript is part of a special collection on 3rd International Conference on Organometallics and Catalysis (ICOC-2023).

Chemistry–A European Journal | Research Article
doi.org/10.1002/chem.202301205
Chemistry Europe
European Chemical Societies Publishing

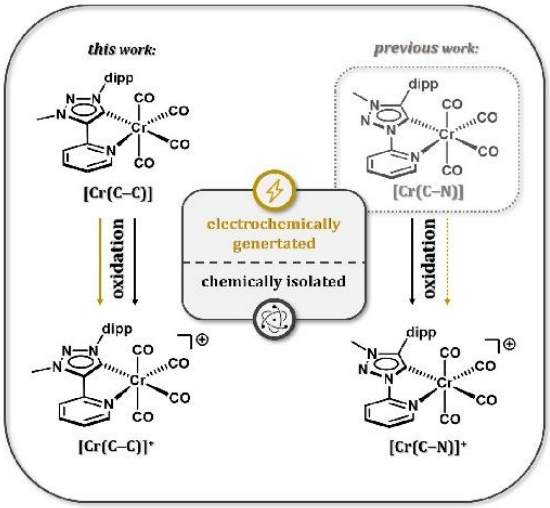

Scheme 1. Chemical (black) and electrochemical (yellow) oxidation of [Cr-(C–C)] and [Cr(C–N)]. The neutral complex [Cr(C–N)] (top, right) was reported previously.[1]

π–accepting ligands, similar to those of bpy, as stable and crystalline material (Scheme 1).[26]

Results and Discussions

The 18 VE complex [Cr(C–C)] was synthesized according to a previously described protocol in our group with irradiation of $[Cr(CO)_6]$ for 2 h in THF and subsequent addition of the corresponding triazolium salt $[H(C–C)]BF_4$ in the presence of a base (NEt_3). Crystallization from a concentrated solution of [Cr(C–C)] in CH_2Cl_2 and *n*-hexane, yielded 64% red crystals suitable for X-ray diffraction (Figure 1). All metal-ligand as well as intra-ligand bond lengths are in the expected range and fit nicely with the previously reported pyridyl-MIC [Cr(C–N)] complex (Table 1, Tables S1 and S2 in Supporting Information).[1]

The cyclic voltammogram of [Cr(C–C)] versus FcH/FcH$^+$ at ambient temperatures shows a reversible oxidation at −0.21 V and a reversible reduction at −2.26 V (Figure 2), followed by an irreversible second reduction at −2.80 V. These data are similar but slightly cathodically shifted compared to what was previously reported for [Cr(C–N)] (Table S4).

As the oxidation potential of Ag^+ in CH_2Cl_2 is +0.65 V versus FcH/FcH$^+$,[29] silver salts should in principle be able to oxidize both [Cr(C–C)] (−0.21 V) and [Cr(C-N)] (+0.17 V) complexes. However, the addition of $AgPF_6$ to [Cr(C–C)] or [Cr(C-N)] in non-coordinating CH_2Cl_2 resulted in an immediate gas evolution, even at lower temperatures of −40 °C. This observation is most likely related to the release of CO gas from the complexes on using the aforementioned silver salt, potentially

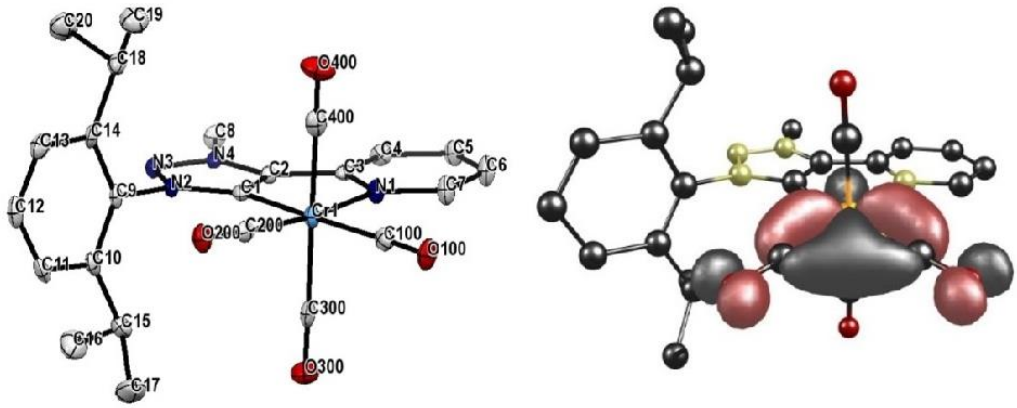

Figure 1. ORTEP representation (left) and HOMO orbital (right, iso value = 0.052, B3LYP/D3/def2-TZVP) of [Cr(C–C)] (hydrogen atoms are omitted for clarity). Ellipsoids are drawn with 50% probability.

Table 1. Selected bond lengths of [Cr(C–C)] and [Cr(C–N)] in Å.

	[Cr(C–C)]	[Cr(C–C)](BAr^F)	[Cr(C–N)][1]	[Cr(C–N)](WCA)
Cr-C1	2.049(3)	2.040(7)	2.065(2)	2.063(7)
Cr-N1	2.163(3)	2.139(6)	2.147(2)	2.118(6)
Cr-C100	1.851(3)	1.930(9)	1.855(2)	1.951(8)
Cr-C200	1.827(4)	1.925(1)	1.847(2)	1.915(9)
Cr-C300	1.906(4)	1.877(9)	1.894(2)	1.930(8)
Cr-C400	1.895(4)	1.906(1)	1.903(2)	1.898(9)

Chemistry–A European Journal
Research Article
doi.org/10.1002/chem.202301205
Chemistry Europe
European Chemical Societies Publishing

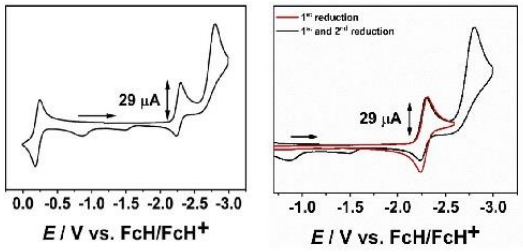

Figure 2. Cyclic voltammograms of [Cr(C–C)] in CH_3CN and 0.1 M Bu_4NPF_6 with a scan rate of 100 mV s^{-1}.

with concomitant coordination of $[PF_6]^-$. Therefore, we changed our strategy for the isolation of $[Cr(C–C)]^+$ and $[Cr(C–N)]^+$ using a synthetic protocol involving oxidizing agents based on WCAs (Ag[WCA][30] and Fc[BAr^F][31]).

Under exclusion of light, the chromium carbonyl complexes were dissolved in CH_2Cl_2 and the corresponding oxidizing agent was added at room temperature, resulting in an immediate color change from red to yellow. After three hours, the reaction mixture was filtered and layered with *n*-hexane at −40 °C, which ultimately yielded 87% crystalline material of [Cr(C–C)](BAr^F) and 89% of [Cr(C-N)](WCA) suitable for single-crystal X-ray diffraction (Figure 3).

A comparison of the bond lengths for the neutral and oxidized complexes shows some interesting trends. The intra-ligand bond lengths within the pyridyl-MIC ligands change only slightly on moving from the neutral to the oxidized complexes. On the contrary, the metal-ligand bond distances are strongly affected on oxidation (Table 1, Tables S1 and S2). Substantial bond elongation is observed for the Cr–CO bonds in the oxidized complexes in the equatorial plane. These results agree with the fact that the HOMO of the neutral complexes is composed of a *d*-orbital that is in the equatorial plane and the π−type orbitals from the two CO ligands in that plane (Figure 1, right). Removal of electron density from that orbital will have the strongest effects on the metal ligand bond lengths that are in the equatorial plane. In keeping with the elongated Cr–CO bond distances in the equatorial plane, the corresponding CO bond lengths in that plane decrease. For [Cr(C–C)](BAr^F) weak cation-anion interactions are observed between a C–F group of BAr^F and an axial CO ligand (Figure S6). The C400-F and O400-F distances are 2.951 and 2.783 Å respectively, and are smaller than the sum of the van der Waals radii of the respective atoms. No such interactions were detected for the complex [Cr-(C–N)](WCA).

In contrast to the Cr–CO bond distances, the Cr–C1 and Cr–N1 bonds to the pyridyl-MIC ligand become stronger upon oxidation. This fact is likely related to the excellent σ−donor properties of the pyridyl-MIC ligands. All these data clearly support a predominantly chromium centered oxidation in these complexes.

IR-spectroelectrochemistry (SEC) on the complex was performed in the presence of Bu_4NPF_6 as a supporting electrolyte, (Figure 4 and Figure S11) and the results are in good agreement with our theoretical B3LYP/D3/def2-TZVP calculations (Figure S10 and S12). The average shift of around 130 cm^{-1} for the CO stretching frequencies (Table 2) upon one-electron oxidation fits nicely with a Cr-centered oxidation in this complex.

Apart from the large shift of the CO bands upon one-electron oxidation, the IR data also display an effect of the counter anion on the position of the bands. Thus, the CO bands with a WCA display a slight blue shift compared to the ones with $[PF_6]^-$ as anion (see section 5.2 and 5.3 of Supporting Information).

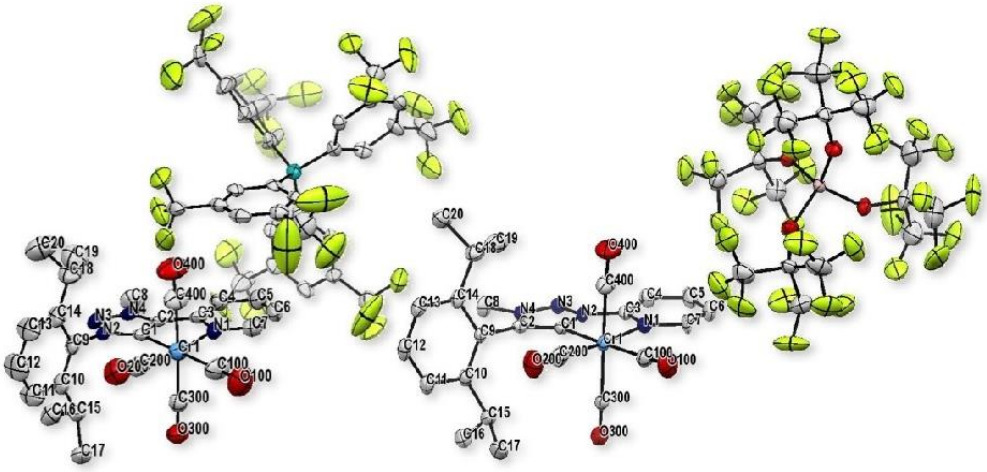

Figure 3. ORTEP representation of [Cr(C–C)](BAr^F) (left) and [Cr(C-N)](WCA) (right). Hydrogen atoms are omitted for clarity. Ellipsoids were drawn with 50% probability.

Chemistry–A European Journal | Research Article doi.org/10.1002/chem.202301205 | Chemistry Europe European Chemical Societies Publishing

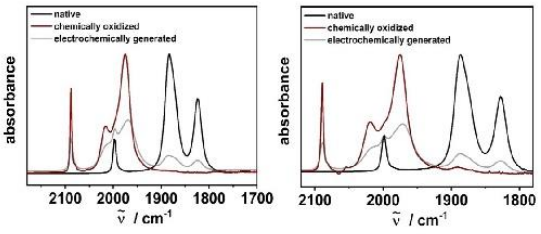

Figure 4. Left: [Cr(C–C)] (black), electrochemically generated $[Cr(C–C)]^+$ (grey) in CH_3CN/0.1 M Bu_4NPF_6 (Au WE) and $[Cr(C–C)](BAr^F)$ in CH_2Cl_2 (red). Right: [Cr(C–N)] (black), electrochemically generated (Au WE) $[Cr(C–N)]^+$ (grey) in CH_3CN/0.1 M Bu_4NPF_6 and [Cr(C–N)](WCA) in CH_2Cl_2 (red). The Y-axis is not normalized.

Further insights into the electronic structures of the native and the oxidized complexes were obtained via UV/vis/NIR-SEC in combination with TD-DFT calculations at B3LYP/D3/def2-TZVP level. Even though results from TD-DFT calculations may not always be very accurate, they can be used to get a first insight into such transitions. Both complexes show bands between 300–500 nm (see Supporting Information, section 7). These transitions occur from the HOMO-1 and HOMO-2 orbitals, which have contributions from both Cr and CO, to orbitals that are predominantly centered on the pyridyl-MIC ligands. Such transitions can thus be assigned as MLCT with a small LLCT contribution. These results are in good agreement with previous reports on $[Cr(bpy)(CO)_4]$.[14] Depopulation of the metal centered $Cr(d_{xz})$ orbitals lead to weakening of the Cr–C bond and consequently rapid photodissociation from the ^{1}MLCT.[23] In the oxidized form, the MLCTs are slightly blue-shifted and show a strong contribution from the pyridyl-MIC ligand instead of CO ligands. These results indirectly indicate that the electron-deficiency of the oxidized metal-center, which results in a decreased π–backdonation, is compensated by the strongly σ–donating pyridyl-MIC ligands.

To gain a detailed insight into the electronic structure, the one-electron oxidized 17 VE complexes were further investigated by EPR-spectroscopy and compared with the electrochemically generated species (Figure 5). The slightly stronger interaction of the $[BArF]^-$ anion with the cationic metal complex

Table 2. CO stretching frequencies of [Cr(C–C)], [Cr(C–N)], [Cr(C–C)](BAr^F) and Cr(C–N)](WCA) in CH_2Cl_2.

	$\tilde{\nu}$(CO)/cm^{-1}				$\tilde{\nu}_{average}$(CO)/cm^{-1}
[Cr(C–C)]	1998	1882	1873 (sh)	1822	1894
[Cr(C–N)][1]	1998	1890	1878 (sh)	1830	1899
[Cr(C–C)](BAr^F)	2087	2015	1992 (sh)	1975	2017
[Cr(C–N)](WCA)	2089	2019	1995 (sh)	1975	2020

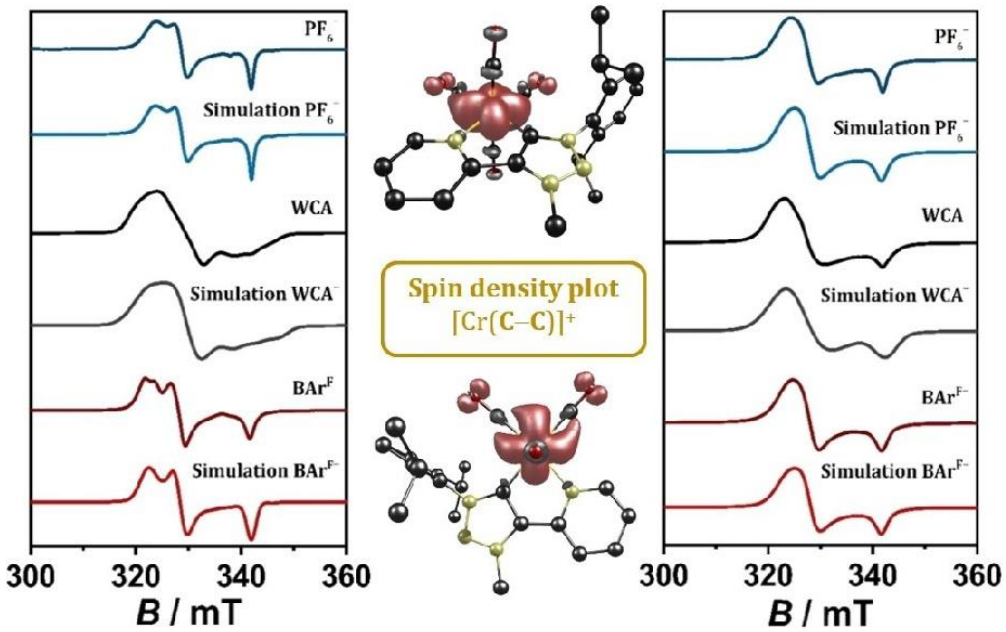

Figure 5. Left: EPR spectra of [Cr(C–C)](X). Right: EPR spectra of [Cr(C–N)](X). Electrochemically generated in 0.1 M NBu_4PF_6/CH_3CN at −175 °C (blue: PF_6^-, light blue: simulation) and chemically oxidized (X=WCA^-, BAr^{F-}) in CH_2Cl_2 at −175 °C (black: WCA^-, grey: simulation; dark red: BAr^{F-}, red: simulation). Center: Calculated spin density plot of $[Cr(C–C)]^+$ (B3LYP/D3/def2-TZVP, iso value = 0.033).

Chemistry–A European Journal | Research Article
doi.org/10.1002/chem.202301205
Chemistry Europe
European Chemical Societies Publishing

in the crystals triggered our interest to further investigate the influence of the counterion on properties of the oxidized $[Cr(CO)_4(pyridyl\text{-}MIC)]^+$ framework.

[Cr(C–C)](X) with more interacting anions X = PF_6^-, BAr^{F-}[1] show rhombic EPR signals at g_x =2.09, g_y =2.06 and g_z =1.98 with a *g*-anisotropy, Δg of up to 0.08, typical for predominantly metal-centered electron spins, and a partially resolved hyperfine coupling to the ^{53}Cr nucleus (I = 3/2, natural abundance: 9.55%). In addition, spin density calculation on the oxidized complex display about 99% spin on the chromium center (Figure 5 and Table S14).

Replacing the counterion in $[Cr(C–C)]^+$ from $[PF_6]^-$ and $[BAr^F]^-$ with $[WCA]^-$ results in a pseudo-axial EPR spectrum with hyperfine-coupling to the pyridyl-*N*. (Table S15 and Figure 5, left). The effect can also be noticed in [Cr(C-N)](WCA). The axial signal shows *g*-values of $g_\perp$ =2.08 and $g_{||}$ =1.98 with an unresolved pyridyl-*N* hyperfine coupling, caused by the strong anisotropic line broadening. In contrast, the EPR spectra with $[PF_6]^-$ and $[BAr^F]^-$ counterion show no hyperfine coupling to the pyridyl-*N*. Instead a dominant metal-centered spin with *g*-values of $g_\perp$ =2.08 and $g_{||}$ =1.98 for [Cr(C–N)](PF_6), and $g_\perp$ =2.06 and $g_{||}$ =1.98 for [Cr(C-N)](BAr^F), respectively, are observed (Table S**16**). The data are in good agreement with the previously reported spin density calculation for $[Cr(C\text{-}N)]^+$ indicating a predominantly chromium-centered spin of > 99%.[1]

The "level of innocence" of so-called weakly coordinating anions, such as $[PF_6]^-$ and $[BAr^F]^-$, compared to the well-established $[Al(OR^F)_4]^-$ (R^F = $C(CF_3)_3$) has been intensively studied[32] and classical WCAs are often not as "innocent" as perceived. This effect is indeed present here: It is reasonable to assume, that the cation-anion interactions for $[PF_6]^-$ and $[BAr^F]^-$ are stronger compared to their WCA counterparts. PF_6^- is a small anion and the partial negative charges on the F-atoms are high which will increase the propensity of H···F and C···F interactions with the ligand. The ability of $[BAr^F]^-$ to undergo such interactions will be much smaller compared to the hexafluorophosphate anion. However, $[BAr^F]^-$ can undergo additional π··· π interactions. Neither of these interactions are very likely with WCA. Thus, $[PF_6]^-$ and $[BAr^F]^-$ reduce the electron deficiency of the $[Cr(CO)_4(pyridyl\text{-}MIC)]^+$ fragment, while $[WCA]^-$ remains "innocent" and truly non-interacting also in an electronic sense.

Consequently, the pyridyl-MIC ligands show stronger contributions to compensate for the electron deficiency, as evident from the EPR spectra of [Cr(C–C)](WCA) and [Cr(C-N)](WCA). The stronger hyperfine coupling of pyridyl-*N* (100 MHz) in [Cr(C–C)](WCA), if compared to the hyperfine coupling of 30 Hz in [Cr(C–N)](WCA), underlines the strong influence of the two constitutional isomers and is in good agreement with the overall σ–donor strengths.

Conclusions

In summary, we present the first isolated, crystalline and crystallographically characterized chromium $[Cr(CO)_4]^+$ complexes with pyridyl-MIC ligands that are not only strong σ–donors, but also strong π–acceptors. The chemically oxidized complexes were investigated by IR- and EPR-spectroscopy and compared with their electrochemically-generated analogues, supported by theoretical calculations. The combination of TD-DFT with our (spectro–)electrochemical measurements reveals the unique properties of the pyridyl-MIC ligands upon oxidation of the chromium metal-center. The strong σ–donor properties of the MIC ligand can compensate for the electron deficiency of $[Cr(CO)_4]^+$, which usually undergoes CO dissociation due to the reduced π–backbonding to the CO ligands, while largely retaining its MLCT character.

While the use of the pyridyl-MIC ligands alone is enough for the in situ generation and characterization of the 17 VE cationic Cr-carbonyl complex, its isolation in the pure form and crystallization needs the additional help from WCAs. Intriguingly, the fine-tuning of the electronic structure is not determined exclusively by the two ligand isomers, but also to a limited extent by the Lewis acid-base interactions with the counterions. The "classical" WCAs produce stronger ionic interactions compared to the $[Al(OR^F)_4]^-$ (R^F = $C(CF_3)_3$) type WCA, which have a direct influence on the contribution of the pyridyl-MIC moieties to their electronic structure. These results are of fundamental interest for the understanding of the electrochemical, photochemical and in general geometric/electronic structures of group 6 carbonyl complexes, as the isolation of kinetically labile complexes is no longer limited by purely electron-donating ligands,[33] but can also be achieved with ligands that are good π–acceptors.

Experimental Section

General procedures, materials and instrumentation

***Caution**! Compounds containing azides are potentially explosive. Although we never experienced any problems during synthesis or analysis, all compounds should be synthesized only in small quantities and handled with great care!* Unless otherwise noted, all reactions were carried out using standard Schlenk-line-techniques under an inert atmosphere of argon (Linde Argon 4.8, purity 99.998%) or in a glovebox (Glovebox Systemtechnik, GS095218). Commercially available chemicals were used without further purification. The solvents used for metal complex synthesis and catalysis were available from MBRAUN MB-SPS-800 solvent System and degassed by standard techniques prior to use. The identity and purity of compounds were established via ^1H and ^{13}C NMR spectroscopy, elemental analysis and mass spectrometry. Solvents for cyclic voltammetry and UV/vis- and EPR-spectroelectrochemical measurements were dried and distilled under argon and degassed by common techniques prior to use. Column chromatography was performed over silica 60 M (0.04–0.063 mm). ^1H and $^{13}C\{^1H\}$ NMR spectra were recorded on a JOEL ECZ 400R spectrometer at 19–22 °C. Chemical shifts are reported in ppm referenced to the residual solvent peaks.[34] The following abbreviations are used to represent the multiplicity of the signals: s (singlet), d (doublet), t (triplet), q (quartet), p (pentet), sept (septet). Mass spectrometry was performed on an Agilent 6210 ESI-TOF. Elemental analyses were performed with an Elementar Micro Cube elemental analyser.

Chemistry–A European Journal | Research Article doi.org/10.1002/chem.202301205 | Chemistry Europe European Chemical Societies Publishing

X-ray Diffraction: X-ray data were collected on a BRUKER Smart AXS, BRUKER D8 Venture or Bruker Kappa Apex2duo system. Data were collected at 100(2) or 140(2) K, respectively, using graphite-monochromatic MoK_α radiation (λ_α =0.71073 Å) or CuK_α radiation (λ_α =1.54178 Å), respectively. The strategy for the data collection was evaluated by using the APEX2 or Smart software. The data were collected by standard "ω scan techniques" or "$\omega - \varphi$ scan techniques" and were scaled and reduced using APEX2, SAINT+, and SADABS software. The structures were solved by direct methods using SHELXL-97 or intrinsic phasing using SHELXL-2014/7 and refined by full matrix least-squares with SHELXL-2014/7, refining on F^2. Non-hydrogen atoms were refined anisotropically. If it is noted, bond length and angles were measured with Mercury, version 3.8.[35]

Deposition Number(s) 2075622 (for [Cr(C–C)]), 2216773 (for [Cr(C–C)](BAr^F)) and 2173735 (for [Cr(C–N)](WCA)) contain(s) the supplementary crystallographic data for this paper. These data are provided free of charge by the joint Cambridge Crystallographic Data Centre and Fachinformationszentrum Karlsruhe Access Structures service.

Electrochemistry: Cyclic voltammograms were recorded with a PalmSens4 potentiostat or PAR VersaStat (Ametek), respectively, with a conventional three-electrode configuration consisting of a glassy carbon working electrode, a platinum auxiliary electrode, and a coiled silver wire as a pseudo reference electrode. The (decamethyl)ferrocene/(decamethyl)ferrocenium couple was used as internal reference. All measurements were performed at room temperature with a scan rate between 25 and 1000 mVs^{-1}. The experiments were carried out in absolute Acetonitrile containing 0.1 M Bu_4NPF_6 (Sigma Aldrich, ≥99.0 %, electrochemical grade) as the supporting electrolyte.

Spectroelectrochemistry: UV/vis spectra were recorded with a J&M TIDAS spectrometer or an Avantes spectrometer consisting of a light source (AvaLight-DH–S-Bal), a UV/Vis detector (AvaSpec-ULS2048), and an NIR detector (AvaSpec-NIR256-TEC). UV/vis-spectroelectrochemical measurements were carried out in an optically transparent thin-layer electrochemical (OTTLE)[36] cell (CaF_2 windows) with a gold-mesh working electrode, a platinum-mesh counter electrode, and a silver-foil pseudo reference. EPR spectra at the X-band frequency (ca. 9.5 GHz) were obtained with a Magnettech MS-5000 benchtop EPR spectrometer equipped with a rectangular TE 102 cavity and a TC HO4 temperature controller. The measurements were carried out in synthetic quartz glass tubes. For EPR spectroelectrochemistry, a three-electrode setup was employed using two Teflon-coated platinum wires (0.005 in. bare and 0.008 in. coated) as the working and counter electrodes and a Teflon-coated silver wire (0.005 in. bare and 0.007 in coated) as the pseudo reference electrode. The low temperature EPR-spectra were performed at −175 °C. The experiments were carried out in absolute Acetonitrile containing 0.1 M Bu_4NPF_6 as the supporting electrolyte. The same solvents as for the CV measurements were used for each compound. All EPR spectra recorder under chemical oxidation conditions were carried out in dry CH_2Cl_2.

Calculations: The program package ORCA 4.1. was used for all DFT calculations.[37] Starting from the molecular structure obtained from X-ray diffraction geometry optimizations were carried out using the B3LYP[38,39] functional and no symmetry restrictions were imposed during the optimization. All calculations were performed with empirical Van der Waals correction (D3).[40] The restricted and unrestricted DFT methods were employed for closed and open shell molecules respectively unless stated otherwise. Convergence criteria were set to default for geometry-optimization (OPT), and tight for SCF calculations (TIGHTSCF). Triple-ζ-valence basis sets (def2-TZVP)[41] were employed for all atoms. Calculations were performed using resolution of the identity approximation[42] with matching auxiliary basis sets[43] for geometry optimizations and numerical frequency calculations and the RIJCOSX (combination of the resolution of the identity and chain of spheres algorithms) approximation for single point calculations using the B3LYP functional.[38,39] Low-lying excitation energies were calculated with time-dependent DFT (TD-DFT). Solvent effects were taken into account with the conductor-like polarizable continuum model, CPCM.[44] Spin densities were calculated according to the Mulliken population analysis.[45] The absence of imaginary frequency Spin densities, molecular orbitals and difference densities were visualized with the modified Chemcraft 1.8 program.[46] All molecular orbitals are illustrated with an iso value of 0.052. All calculated TD-DFT spectra are Gaussian broadened with a band width of 25 nm at half height.

Synthesis of [Cr(C–C)]: A suspension of [$Cr(CO)_6$] (11.7 mg, 0.053 mmol) in 6 mL THF was stirred for 2 h under UV light. The CO overpressure was released at least 3 times during this period. To the yellow solution [H(C–C)]BF_4[47] (21.7 mg, 0.053 mmol) and an excess of NEt_3 (0.6 mL) were added. The mixture was refluxed with an equipped reflux condenser and a gas bubbler overnight. After cooling to room temperature, the solvent was evaporated, and the residue was dissolved in 20 mL CH_2Cl_2 and extracted three times with 20 mL H_2O. The organic phases were collected and dried over Na_2SO_4. The solvent was reduced, and the crude product was purified by column chromatography (SiO_2, 100 % CH_2Cl_2). Analytically pure product was isolated after recrystallization from CH_2Cl_2 and *n*-hexane yielding red crystals (16.4 mg, 64 %).

^{1}H NMR (401 MHz, CD_3CN) δ = 9.12 ppm (dt, J=5.5, 1.1 Hz, 1H), 7.98–7.90 ppm (m, 2H), 7.59–7.54 ppm (m, 1H), 7.41 ppm (d, ^3J= 7.8 Hz, 2H), 7.31–7.26 ppm (m, 1H), 4.42 ppm (s, 3H, CH_3), 2.67 ppm (hept, ^3J=6.6 Hz, 2H, R_3CH), 1.30 ppm (d, ^3J=6.8 Hz, 6H, CH_3), 1.10 ppm (d, ^3J=6.8 Hz, 6H, CH_3); HRMS (ESI): m/z calcd for $C_{24}H_{24}CrN_4O_4^+$: 484.1203 [*Cr(C–C)*]$^+$; found: 484.1230; IR (CH_2Cl_2) $\tilde{\nu}$ = 1998 (m) cm^{-1}, 1890 (s) cm^{-1}, 1873 (sh) cm^{-1}, 1822 (s) cm^{-1} (C≡O); ^{13}C NMR (176 MHz, CD_2Cl_2) δ = 231.76 ppm, 229.13 ppm, 218.03 ppm, 204.28 ppm, 156.07 ppm, 151.01 ppm, 146.41 ppm, 144.36 ppm, 137.17 ppm, 136.02 ppm, 131.30 ppm, 124.27 ppm, 123.26 ppm, 119.56 ppm, 39.01 ppm, 29.15 ppm, 25.79 ppm, 22.81 ppm; elemental analysis calcd (%) for $C_{24}H_{24}CrN_4O_4$: C 59.50, H 4.99, N 11.56; found: C 59.16, H 5.11, N 11.16.

Synthesis of [Cr(C–C)](BAr^F): In a synthetic glovebox, **[Cr(C–C)]** (20.1 mg, 0.042 mmol) was dissolved in CH_2Cl_2 and ferrocenium-tetrakis(3,5-bis(trifluoromethyl)phenyl)borate (44.1 mg, 0.042 mmol) was added. The red mixture changed immediately to yellow and was stirred for additional three hours at room temperature under the exclusion of light. The resulting yellow mixture was filtered through a syringe filter, overlaid with *n*-hexane, and placed in the freezer at −40 °C for two weeks yielding 50 mg (89 %, 0.037 mmol) of crystalline [Cr(C–C)](BAr^F) suitable for X-ray diffraction analysis. In the case of remaining ferrocenium-tetrakis(3,5-bis(trifluoromethyl) phenyl)borate, the yellow solution was decanted, overlaid with additional *n*-hexane and again placed in the −40 °C freezer.

^{19}F NMR (235 MHz, CD_2Cl_2) δ = 62.80 ppm (BArF); HRMS (ESI): m/z calcd for $C_{24}H_{24}CrN_4O_4^+$: 484.1203; found [*Cr(C–C)*]$^+$: 484.1238; IR (CH_2Cl_2) $\tilde{\nu}$ = 2088 (m) cm^{-1}, 2016 (s) cm^{-1}, 1991 (sh) cm^{-1}, 1975 (s) cm^{-1} (C≡O).

Synthesis of [Cr(C–N)](WCA): In a synthetic glovebox, [Cr(C–N)][1] (25.2 mg, 0.052 mmol) was dissolved in CH_2Cl_2 and [$Ag(Al(OC(CF_3)_3)_4$][15] (WCA = [$Al(OC(CF_3)_3)_4^-$]) (58.7 mg, 0.055 mmol) was added. The dark red mixture changed immediately to orange and was stirred for additional three hours at room temperature under the exclusion of light. The resulting orange mixture was

Chemistry–A European Journal | Research Article doi.org/10.1002/chem.202301205 | Chemistry Europe European Chemical Societies Publishing

filtered through a syringe filter, overlaid with *n*-hexane, and placed in the freezer at −40 °C for two weeks yielding 69 mg (87 %, 0.048 mmol) of crystalline [Cr(C–N)](WCA) suitable for X-ray diffraction analysis. In the case of remaining $[Ag(Al(OC(CF_3)_3)_4]$, the orange solution was filtered again through a syringe filter and overlaid with additional *n*-hexane or the orange solid is again dissolved and filtered through a syringe filter, too.

^{19}F NMR (235 MHz, CD_2Cl_2) $\delta = 75.67$ ppm ($Al(OC(CF_3)_3)_4$); HRMS (ESI): *m/z* calcd for $C_{24}H_{24}CrN_4O_4^+$: 484.1203 [*Cr(C–C)*]$^+$; found: 484.1234; IR (CH_2Cl_2) $\tilde{\nu} = 2089$ (m) cm^{-1}, 2018 (s) cm^{-1}, 1996 (sh) cm^{-1}, 1975 (s) cm^{-1} (C≡O).

Supporting Information

Cyclic voltammetry, ^1H and ^{19}F NMR spectroscopy, IR-, UV/vis/NIR- and EPR-spectroelectrochemistry, single X-ray diffraction data, synthesis, (TD)DFT calculations.

Acknowledgements

We further thank B. Förtsch for elemental analyses and Dr. W. Frey (Institut für Organische Chemie) for collecting the X-ray data sets and the support by the state of Baden-Württemberg through bwHPC and the German Research Foundation (DFG) through grant no INST 40/575-1 FUGG (JUSTUS 2 cluster). We kindly acknowledge the German Science Foundation (DFG, Priority Program SPP 2102 "Light-controlled reactivity of metal complexes", SA 1840/7-1 and SA 1840/7-2) for financial support. Open Access funding enabled and organized by Projekt DEAL.

Conflict of Interests

The authors declare no conflict of interest.

Data Availability Statement

The data that support the findings of this study are available in the Supporting Information of this article.

Keywords: carbonyl ligands · chromium(I) · mesoionic carbenes · (spectro)electrochemistry · weakly coordinating anions

[1] T. Bens, P. Boden, P. Di Martino-Fumo, J. Beerhues, U. Albold, S. Sobottka, N. I. Neuman, M. Gerhards, B. Sarkar, *Inorg. Chem.* **2020**, *59*, 15504–15513.
[2] P. Boden, P. Di Martino-Fumo, T. Bens, S. Steiger, U. Albold, G. Niedner-Schatteburg, M. Gerhards, B. Sarkar, *Chem. Eur. J.* **2021**, *27*, 12959–12964.
[3] P. J. Boden, P. Di Martino-Fumo, T. Bens, S. T. Steiger, D. Marhöfer, G. Niedner-Schatteburg, B. Sarkar, *Chem. Eur. J.* **2022**, *28*, e202201038.
[4] M. L. Clark, K. A. Grice, C. E. Moore, A. L. Rheingold, C. P. Kubiak, *Chem. Sci.* **2014**, *5*, 1894–1900.
[5] I. R. Farrell, P. Matousek, A. Vlček, *J. Am. Chem. Soc.* **1999**, *121*, 5296–5301.
[6] F. Franco, C. Cometto, F. Sordello, C. Minero, L. Nencini, J. Fiedler, R. Gobetto, C. Nervi, *ChemElectroChem* **2015**, *2*, 1372–1379.
[7] M. Isegawa, *Chem. Phys.* **2023**, *565*, 111758.
[8] D. Sieh, D. C. Lacy, J. C. Peters, C. P. Kubiak, *Chem. Eur. J.* **2015**, *21*, 8497–8503.
[9] M. Tang, L. Cameron, E. M. Poland, L.-J. Yu, S. A. Moggach, R. O. Fuller, H. Huang, J. Sun, S. C. Thickett, M. Massi, M. L. Coote, C. C. Ho, A. C. Bissember, *Inorg. Chem.* **2022**, *61*, 1888–1898.
[10] J. Tory, B. Setterfield-Price, R. A. W. Dryfe, F. Hartl, *ChemElectroChem* **2015**, *2*, 213–217.
[11] A. Vlček Jr., *Coord. Chem. Rev.* **2002**, *230*, 225–242.
[12] a) T. Scherpf, C. R. Carr, L. J. Donnelly, Z. S. Dubrawski, B. S. Gelfand, W. E. Piers, *Inorg. Chem.* **2022**, *61*, 13644–13656; b) J. Agarwal, T. W. Shaw, C. J. Stanton, G. F. Majetich, A. B. Bocarsly, H. F. Schaefer, *Angew. Chem. Int. Ed. Engl.* **2014**, *53*, 5152–5155; c) E. E. Benson, C. P. Kubiak, *Chem. Commun.* **2012**, *48*, 7374–7376; d) V. Blasczak, M. McKinnon, L. Suntrup, N. A. Aminudin, B. Reed, S. Groysman, M. Z. Ertem, D. C. Grills, J. Rochford, *Inorg. Chem.* **2022**, *61*, 15784–15800; e) M. Bourrez, F. Molton, S. Chardon-Noblat, A. Deronzier, *Angew. Chem. Int. Ed. Engl.* **2011**, *50*, 9903–9906; f) F. Franco, M. F. Pinto, B. Royo, J. Lloret-Fillol, *Angew. Chem. Int. Ed. Engl.* **2018**, *57*, 4603–4606; g) K. A. Grice, N. X. Gu, M. D. Sampson, C. P. Kubiak, *Dalton Trans.* **2013**, *42*, 8498–8503; h) J. Hawecker, J.-M. Lehn, R. Ziessel, *J. Chem. Soc. Chem. Commun.* **1984**, 328–330; i) J. A. Keith, K. A. Grice, C. P. Kubiak, E. A. Carter, *J. Am. Chem. Soc.* **2013**, *135*, 15823–15829; j) C. W. Machan, M. D. Sampson, S. A. Chabolla, T. Dang, C. P. Kubiak, *Organometallics* **2014**, *33*, 4550–4559; k) J. F. Martinez, N. T. La Porte, S. Chaudhuri, A. Sinopoli, Y. J. Bae, M. Sohail, V. S. Batista, M. R. Wasielewski, *J. Phys. Chem. C* **2019**, *123*, 10178–10190; l) T. Scherpf, C. Carr, L. Donnelley, Z. Dubrawski, W. Piers, B. Gelfand, *ChemRxiv.* **2022**; m) H. Shirley, T. M. Sexton, N. P. Liyanage, C. Z. Palmer, L. E. McNamara, N. I. Hammer, G. S. Tschumper, J. H. Delcamp, *Eur. J. Inorg. Chem.* **2020**, *2020*, 1844–1851; n) J. M. Smieja, M. D. Sampson, K. A. Grice, E. E. Benson, J. D. Froehlich, C. P. Kubiak, *Inorg. Chem.* **2013**, *52*, 2484–2491; o) B. P. Sullivan, C. M. Bolinger, D. Conrad, W. J. Vining, T. J. Meyer, *J. Chem. Soc. Chem. Commun.* **1985**, 1414–1416; p) L. Suntrup, F. Stein, J. Klein, A. Wilting, F. G. L. Parlane, C. M. Brown, J. Fiedler, C. P. Berlinguette, I. Siewert, B. Sarkar, *Inorg. Chem.* **2020**, *59*, 4215–4227.
[13] a) P. Datta, D. Sardar, A. P. Mukhopadhyay, E. López-Torres, C. J. Pastor, C. Sinha, *J. Organomet. Chem.* **2011**, *696*, 488–495; b) D. M. Manuta, A. J. Lees, *Inorg. Chem.* **1986**, *25*, 1354–1359; c) S. Zális, I. R. Farrell, A. Vlcek, *J. Am. Chem. Soc.* **2003**, *125*, 4580–4592.
[14] F. Ma, M. Jarenmark, S. Hedström, P. Persson, E. Nordlander, A. Yartsev, *RSC Adv.* **2016**, *6*, 20507–20515.
[15] a) A. M. Bond, R. Colton, J. E. Kevekordes, P. Panagiotidou, *Inorg. Chem.* **1987**, *1987*, 1430–1435; b) S. Ernst, W. Kaim, *Inorg. Chim. Acta* **1986**, *114*, 123–125.
[16] A. M. Bond, R. Colton, J. E. Kevekordes, P. Panagiotidou, *Inorg. Chem.* **1987**, *26*, 1430–1435.
[17] S. Ernst, W. Kaim, *J. Am. Chem. Soc.* **1986**, *108*, 3578–3586.
[18] I. R. Farrell, F. Hartl, S. Záliš, M. Wanner, W. Kaim, A. Vlček, *Inorg. Chim. Acta* **2001**, *318*, 143–151.
[19] J. Hanzlík, L. Pospíšil, A. A. Vlček, M. Krejčík, *J. Electroanal. Chem.* **1992**, *331*, 831–844.
[20] R. Johnson, H. Madhani, J. P. Bullock, *Inorg. Chim. Acta* **2007**, *360*, 3414–3423.
[21] a) I. R. Farrell, J. van Slageren, S. Záliš, A. Vlček, *Inorg. Chim. Acta* **2001**, *315*, 44–52; b) K. A. Rawlins, A. J. Lees, *Inorg. Chem.* **1989**, *28*, 2154–2160; c) P. C. Servaas, H. K. van Dijk, T. L. Snoeck, D. J. Stufkens, A. Oskam, *Inorg. Chem.* **1985**, *24*, 4494–4498; d) D. J. Stufkens, *Coord. Chem. Rev.* **1990**, *104*, 39–112.
[22] D. M. Manuta, A. J. Lees, *Inorg. Chem.* **1986**, *25*, 1354–1359.
[23] R. W. Balk, T. Snoeck, D. J. Stufkens, A. Oskam, *Inorg. Chem.* **1980**, *19*, 3015–3021.
[24] a) R. S. Panesar, N. Dunwoody, A. J. Lees, *Inorg. Chem.* **1998**, *37*, 1648–1650; b) S. Wieland, K. B. Reddy, R. van Eldik, *Organometallics* **1990**, *9*, 1802–1806.
[25] D. Miholová, B. Gaš, S. Záliš, J. Klíma, A. A. Vlček, *J. Organomet. Chem.* **1987**, *330*, 75–84.
[26] L. Suntrup, S. Klenk, J. Klein, S. Sobottka, B. Sarkar, *Inorg. Chem.* **2017**, *56*, 5771–5783.
[27] a) G. Guisado-Barrios, M. Soleilhavoup, G. Bertrand, *Acc. Chem. Res.* **2018**, *51*, 3236–3244; b) R. Maity, B. Sarkar, *JACS Au* **2022**, *2*, 22–57; c) K. O. Marichev, S. A. Patil, A. Bugarin, *Tetrahedron* **2018**, *74*, 2523–

Chemistry–A European Journal | Research Article doi.org/10.1002/chem.202301205 | Chemistry Europe European Chemical Societies Publishing

2546; d) Á. Vivancos, C. Segarra, M. Albrecht, *Chem. Rev.* **2018**, *118*, 9493–9586.
[28] a) J. Bohnenberger, W. Feuerstein, D. Himmel, M. Daub, F. Breher, I. Krossing, *Nat. Commun.* **2019**, *10*, 1–8; b) J. Bohnenberger, D. Kratzert, S. M. N. V. T. Gorantla, S. Pan, G. Frenking, I. Krossing, *Chem. Eur. J.* **2020**, *26*, 17203–17211; c) J. Bohnenberger, I. Krossing, *Angew. Chem. Int. Ed. Engl.* **2020**, *59*, 5581–5585; d) J. Bohnenberger, M. Schmitt, W. Feuerstein, I. Krummenacher, B. Butschke, J. Czajka, P. J. Malinowski, F. Breher, I. Krossing, *Chem. Sci.* **2020**, *11*, 3592–3603; e) J. M. Rall, M. Schorpp, M. Keilwerth, M. Mayländer, C. Friedmann, M. Daub, S. Richert, K. Meyer, I. Krossing, *Angew. Chem. Int. Ed. Engl.* **2022**, *61*, e202204080; f) M. Schmitt, M. Mayländer, J. Goost, S. Richert, I. Krossing, *Angew. Chem. Int. Ed. Engl.* **2021**, *60*, 14800–14805; g) W. Unkrig, M. Schmitt, D. Kratzert, D. Himmel, I. Krossing, *Nat. Chem.* **2020**, *12*, 647–653.
[29] N. G. Connelly, W. E. Geiger, *Chem. Rev.* **1996**, *96*, 877–910.
[30] I. Krossing, *Chem. Eur. J.* **2001**, *7*, 490–502.
[31] L. E. Bowen, M. F. Haddow, A. G. Orpen, D. F. Wass, *Dalton Trans.* **2007**, 1160–1168.
[32] I. M. Riddlestone, A. Kraft, J. Schaefer, I. Krossing, *Angew. Chem. Int. Ed. Engl.* **2018**, *57*, 13982–14024.
[33] A. J. Rucklidge, D. S. McGuinness, R. P. Tooze, A. M. Z. Slawin, J. D. A. Pelletier, M. J. Hanton, P. B. Webb, *Organometallics* **2007**, *26*, 2782–2787.
[34] S. Budavari (Ed.) *The MERCK Index. An Encyclopedia of Chemical, Drugs and Biologicals*, Merck & Co, Rahway, **1989**.
[35] a) APEX3. v2015.5-2, Bruker AXS Inc, Madison, Wisconsin (USA), **2015**; b) G. M. Sheldrick, SHELXS-97 and SHELXL-97, Program for Crystal Structure Solution and Refinement, University of Gottingen, Göttingen (Germany), **1997**; c) G. M. Sheldrick, Program for Empirical Absorption Correction. SADABS Version 2008/1, University of Göttingen, Göttingen (Germany), **2008**; d) G. M. Sheldrick, Program for Crystal Structure Solution and Refinement. SHELXL Version 2014/7, University of Göttingen, Göttingen (Germany), **2014**; e) C. F. Macrae, P. R. Edgington, P. McCabe, E. Pidcock, G. P. Shields, R. Taylor, M. Towler, J. van de Streek, *J. Appl. Crystallogr.* **2006**, *39*, 453–457; f) SAINT+, Data Integration Engine. Version 8.27b ©, Bruker AXS Inc., Madison, Wisconsin (USA), 1997–2012; g) G. M. Sheldrick, *Acta Crystallogr.* **2008**, *A64*, 112–122; h) G. M. Sheldrick, *Acta Crystallogr.* **2015**, *C71*, 3–8.
[36] a) J. Klein, A. Stuckmann, S. Sobottka, L. Suntrup, M. van der Meer, P. Hommes, H.-U. Reissig, B. Sarkar, *Chem. Eur. J.* **2017**, *23*, 12314–12325; b) M. Krejčik, M. Daněk, F. Hartl, *J. Electroanal. Chem. Interfacial Electrochem.* **1991**, *317*, 179–187.
[37] F. Neese, *WIREs Comput. Mol. Sci.* **2012**, *2*, 73–78.
[38] A. D. Becke, *J. Chem. Phys.* **1993**, *98*, 5648–5652.
[39] C. Lee, W. Yang, R. G. Parr, *Phys. Rev. B* **1988**, *37*, 785–789.
[40] a) S. Grimme, *J. Comput. Chem.* **2004**, *25*, 1463–1473; b) S. Grimme, *J. Comput. Chem.* **2006**, *27*, 1787–1799; c) S. Grimme, J. Antony, S. Ehrlich, H. Krieg, *J. Chem. Phys.* **2010**, *132*, 154104; d) S. Grimme, S. Ehrlich, L. Goerigk, *J. Comput. Chem.* **2011**, *32*, 1456–1465.
[41] F. Weigend, R. Ahlrichs, *Phys. Chem. Chem. Phys.* **2005**, *7*, 3297–3305.
[42] a) R. Izsák, F. Neese, *J. Chem. Phys.* **2011**, *135*, 144105–1-144105-11; b) F. Neese, *J. Comput. Chem.* **2003**, *24*, 1740–1747; c) F. Neese, G. Olbrich, *Chem. Phys. Lett.* **2002**, *362*, 170–178; d) F. Neese, F. Wennmohs, A. Hansen, U. Becker, *Chem. Phys.* **2009**, *356*, 98–109; e) T. Petrenko, S. Kossmann, F. Neese, *J. Chem. Phys.* **2011**, *134*, 054116–1-054116-14; f) O. Vahtras, J. Almlöf, M. W. Feyereisen, *Chem. Phys. Lett.* **1993**, *213*, 514–518; g) J. L. Whitten, *J. Chem. Phys.* **1973**, *58*, 4496–4501.
[43] a) K. Eichkorn, O. Treutler, H. Öhm, M. Häser, R. Ahlrichs, *Chem. Phys. Lett.* **1995**, *242*, 652–660; b) K. Eichkorn, F. Weigend, O. Treutler, R. Ahlrichs, *Theor. Chem. Acc.* **1997**, *97*, 119–124.
[44] V. Barone, M. Cossi, *J. Phys. Chem. A* **1998**, *102*, 1995–2001.
[45] R. S. Mulliken, *J. Chem. Phys.* **1955**, *23*, 1833–1840.
[46] G. A. Zhurko, Chemcraft-Graphical Program for Visualization of Quantum Chemistry Computations. Ver. 1.8., http://www.chemcraftprog.com/, Ivanovo (Russia), **2023**.
[47] T. Bens, J. A. Kübler, R. R. M. Walter, J. Beerhues, O. S. Wenger, B. Sarkar, *ACS Org. Inorg. Au* **2023**, https://doi.org/10.1021/acsorginorgau.3c00005.

Manuscript received: April 17, 2023
Accepted manuscript online: May 22, 2023
Version of record online: July 17, 2023

3.5 A Different Perspective in Tuning the Photophysical and Photochemical Properties: The Influence of Constitutional Isomers in Group 6 Carbonyl Complexes with Pyridyl-Mesoionic Carbenes

Tobias Bens,[†,§,#] Daniel Marhöfer,[‡,#] Pit Boden,[‡] Sophie T. Steiger,[‡] Lisa Suntrup,[§] Gereon Niedner-Schatteburg,[‡] Biprajit Sarkar[†,§,*]

[†]Institut für Anorganische Chemie, Universität Stuttgart, Pfaffenwaldring 55, D-70569 Stuttgart, Germany, Email: biprajit.sarkar@iac.uni-stuttgart.de
[§]Institut für Chemie und Biochemie, Freie Universität Berlin, Fabeckstraße 34-36, 14195, Berlin, Germany.
[‡]Department of Chemistry and Research Center Optimas, TU Kaiserslautern, Erwin-Schrödinger-Straße, 67663 Kaiserslautern, Germany.
[#]The authors contributed equally

This article was published and is reprinted with permission from ACS:
T. Bens, D. Marhöfer, P. Boden, S. T. Steiger, L. Suntrup, G. Niedner-Schatteburg, B. Sarkar, *Inorg. Chem.* **2023**, *62*, 39, 16182-16195.
DOI: 10.1021/acs.inorgchem.3c02478 (© 2023 American Chemical Society).

The **Supporting Information** is available free of charge at https://pubs.acs.org/doi/10.1021/acs.inorgchem.3c02478.

Autor contribution: The project was designed by Biprajit Sarkar. The presented complexes were synthesized and fully characterized by Tobias Bens (as a part of the master thesis). All photophysical and photochemical measurements were investigated by Daniel Marhöfer, Pit Boden and Sophie T. Steiger. The theoretical calculations were performed by Daniel Marhöfer. X-Ray diffraction analysis was carried out by Lisa Suntrup. The manuscript was written by Tobias Bens and Biprajit Sarkar.

Inorganic Chemistry

pubs.acs.org/IC Article

A Different Perspective on Tuning the Photophysical and Photochemical Properties: The Influence of Constitutional Isomers in Group 6 Carbonyl Complexes with Pyridyl-Mesoionic Carbenes

Tobias Bens, Daniel Marhöfer, Pit Boden, Sophie T. Steiger, Lisa Suntrup, Gereon Niedner-Schatteburg, and Biprajit Sarkar*

Cite This: *Inorg. Chem.* 2023, 62, 16182−16195 Read Online

ACCESS | Metrics & More | Article Recommendations | Supporting Information

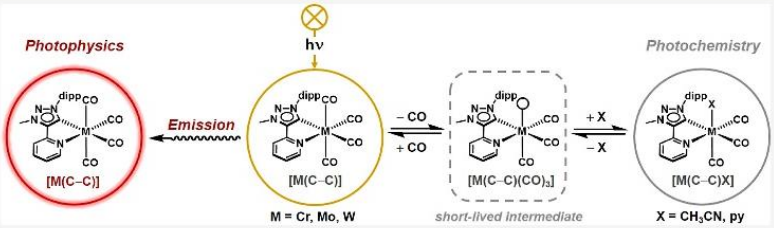

ABSTRACT: Exploring novel and existing design principles to tune the photochemical and photophysical properties of transition-metal complexes is an important goal in contemporary research. Here, we highlight the influence of constitutional isomers of pyridyl-1,2,3-triazolylidene mesoionic carbene (MIC) ligands on the photophysical and photochemical properties of the corresponding tetracarbonyl group 6 metal complexes (M = Cr, Mo, W). All new complexes [M(**C**−**C**)] presented herein incorporate a **C**−**C** linked pyridyl-MIC ligand and were fully characterized by X-ray diffraction analysis, elemental analysis, and ^{1}H NMR and IR spectroscopy. Detailed photophysical investigations reveal a single emission in the VIS region, which extends into the NIR with lifetimes of up to 3.5 μs in the solid state at lower temperatures. The quantum yields were determined for all three complexes, and, in particular, the W^0 complex shows an unusually high quantum yield of 29% compared to the values of 0.02% obtained for the [M(**C**−**N**)] isomers investigated in earlier works. Beyond this, the investigated W^0 complex also exhibits an emission at 717 nm in a fluid solution. The combination of luminescence and FTIR-step scan spectroscopy with theoretical calculations reveals an emissive ^{3}MLCT state. Irradiation of the presented complexes leads to a clean cleavage of one axial CO ligand. A metastable 16 VE species with a vacant axial coordination site was detected in the solid state at low temperatures. In solution, the respective solvato complexes are formed. A dark reverse reaction is observed, as previously described for the [M(**C**−**N**)] analogues. The increased electron density induced by the **C**−**C** linked pyridyl-MIC ligand leads to an increased kinetic rate constant for the reformation of the starting species and is also reflected in the lower photodissociation quantum yields.

INTRODUCTION

Since the discovery of [Ru(bpy)$_3$]$^{2+}$ (bpy = 2,2′-bipyridine),[1] the field of photochemistry has been undisputedly dominated by octahedral transition-metal complexes of the fourth and fifth periods, such as ruthenium,[2] osmium,[3,4] iridium,[5−7] and rhenium,[8−10] due to their high stability and long-lived excited states. In recent years, earth-abundant 3d metal complexes have been intensively investigated to replace the expensive and rare 4d and 5d transition metals.[11−15] The incorporation of strongly σ-donating and π-accepting ligands is a common strategy to increase the naturally weak ligand field splitting in transition metals of the third period,[15] while structurally rigid and highly symmetrical chelating ligands are implemented to optimize the metal−ligand overlap and to minimize the excited-state distortion by an enlarged π-conjugation.[12] The influence of constitutional isomers has received less attention in this context. However, the continuous efforts to enhance the excited-state lifetime have motivated several groups to explore alternative strategies beyond classical ligand optimization.[16−18]

After more than 40 years, since the first discovery of luminescent Cr^0, Mo^0, and W^0 complexes, the isoelectronic and isostructural group 6 metal complexes have experienced a renaissance in photochemistry.[19,20] In 2013, Gray and co-workers reported highly emissive homoleptic W^0 isocyanide

Received: July 20, 2023
Published: September 18, 2023

https://doi.org/10.1021/acs.inorgchem.3c02478
Inorg. Chem. 2023, 62, 16182−16195

Inorganic Chemistry pubs.acs.org/IC Article

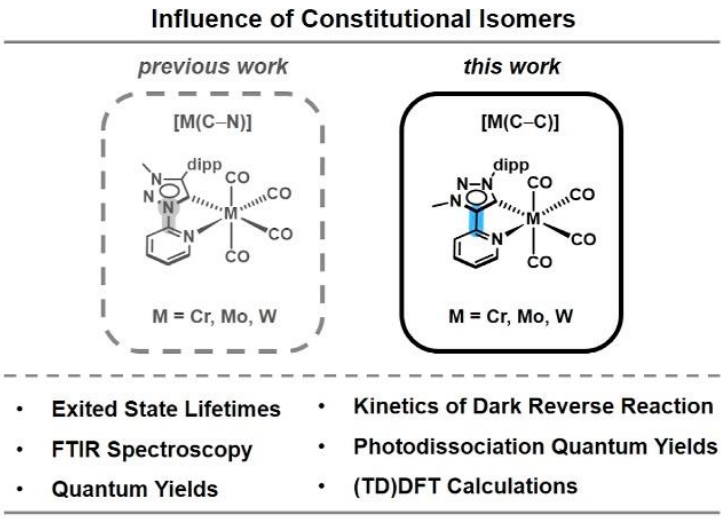

Figure 1. Comparison of the previously reported complexes (gray, **C–N**)[28,47] and the complexes presented in this work (black, **C–C**)[77] (M = Cr, Mo, W) with the incorporated pyridyl-1,2,3-triazolylidene constitutional isomers.

complexes with lifetimes of up to 73 ns.[21] The lifetimes could be further increased by the modulation of the aromatic ligand backbone, leading to outstanding lifetimes in the microsecond range (up to 3.83 μs) and luminescence quantum yields of Φ = 0.41−0.78 in toluene at 25 °C. The homoleptic W^0 complexes represent one of the strongest photoreductants reported so far.[22−24] In contrast, complexes of the 3d and 4d metals (=Cr, Mo) are more labile toward substitution. Wenger and co-workers introduced chelating diisocyanide ligands with sterically demanding substituents, which drastically increased the photostability of the complexes and led to lifetimes of up to 2.37 μs and quantum yields as high as 0.2 at room temperature.[25−27]

Luminescence studies of group 6 carbonyl complexes have been performed either in the solid state or in the glass matrix.[28−31] Only a few carbonyl complexes show luminescence at room temperature. Of particular interest are tetracarbonyl complexes with polypyridine ligands of the type [M(**L–L**)] (M = Cr, Mo, W) since they show dual emission in fluid solution.[29,31−36]

The two emissions originate from two close-lying low energy (LE) and high energy (HE) metal-to-ligand charge transfer (MLCT) states from the central metal atom to the incorporated ligand and the CO ligands, as indicated by the excitation energy dependence and resonance Raman spectroscopy.[31] Emission lifetimes of up to 380 ns at room temperature have been observed, which are in a similar range as reported for monosubstituted pyridine tungsten pentacarbonyl complexes.[37]

The emission spectroscopy pattern shows an interesting dependence on the coordinated ligand in [M(**L–L**)] (M = W; **L–L** = pyridine-2-carbaldehyde, 1,4-diaza-butadiene),[31,35] as the LE band is completely absent at room temperature, which is attributed to the increased delocalization of the metal–ligand moiety, resulting in an accelerated nonradiative decay between the excited state and the ground state.[37]

The excited-state lifetimes in group 6 tetracarbonyl complexes are strongly dependent on the excitation wavelength, as the excitation with near UV light enables the population of the HE ^{1}MLCT state, leading to irreversible CO dissociation.[33,38−46] Recently, some of us reported an unusual reversible binding of CO in a dark reverse reaction, which is in contrast to previous observations made for group 6 carbonyl complexes.[47]

The investigated MICs of the 1,2,3-triazolylidene type are privileged ligands in the field of photochemistry.[16,28,48−63] The strongly σ-donating ligands show promising excited-state properties for the generation of emissive transition-metal complexes, such as Fe(II/III),[16,64] Cu(I),[49,52] Ru(II),[60,65−69] Pd(II),[62] Re(I),[61] Os(II),[60] Ir(III),[54,70−73] Pt(II)/Pt-(IV),[56,59,74,75] and Au(I).[49,51,76]

The pyridyl-1,2,3-triazolylidene mesoionic carbene (py-MIC) tetracarbonyl complexes [M(py-MIC)] (M = Cr, Mo, W) investigated by us show photodissociation quantum yields of up to 46% in CH_3CN. FTIR spectroscopy at low temperatures revealed a metastable reactive intermediate with an axial vacant coordination site after the selective cleavage of an axial CO ligand (Figure 1).[47] The resulting solvato complexes [M(py-MIC)$(CO)_3X_{ax}$] (X = CH_3CN, py) are stable for several hours under ambient conditions, providing new perspectives in the field of (photo)switchable transition-metal complexes.[48] Furthermore, emission with lifetimes of up to 600 ns have been observed in the solid state at room temperature.[28]

The light-dependent duality between excited-state lifetimes and photoinduced CO cleavage inspired us to present a new series of py-MIC containing group 6 tetracarbonyl complexes.

We present here an alternative ligand design concept to modulate the photophysical and photochemical properties of octahedral group 6 tetracarbonyl complexes, which has not gained much attention in terms of photochemistry—the influence of constitutional isomers. The exchange of the pyridyl-1-triazolylidene ligand (**C–N**) with the pyridyl-4-triazolylidene ligand (**C–C**) in the tetracarbonyl complexes [M(**C–X**)] (M = Cr, Mo, W; **X** = C or N) (Figure 1) drastically influences the photophysical properties such as excited-state lifetimes and quantum yields depending on the temperature. Photodissociation quantum yields were determined, and the kinetics of the dark reverse reaction were investigated based on the IR spectra evolution over time,

https://doi.org/10.1021/acs.inorgchem.3c02478
Inorg. Chem. 2023, 62, 16182−16195

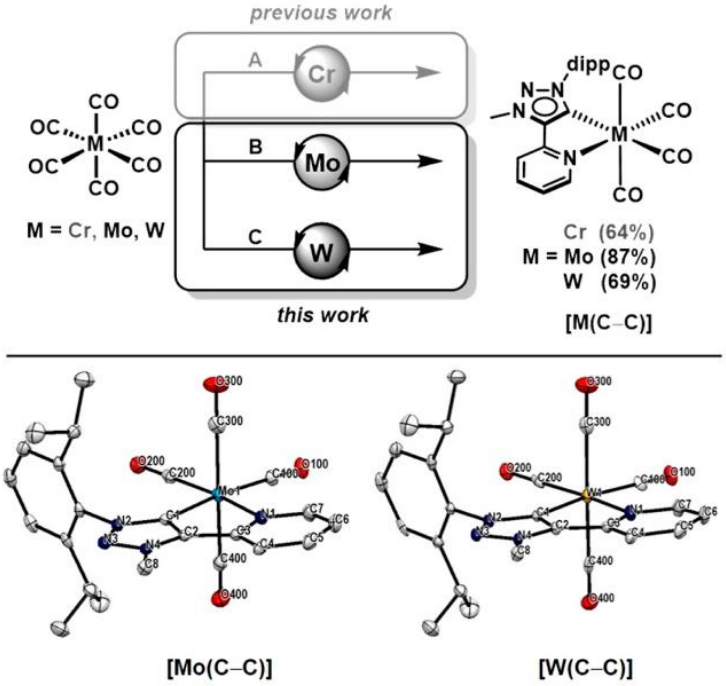

Figure 2. Synthetic strategy (top) of the investigated [M(**C**−**C**)] (M = Cr, Mo, W) complexes and ORTEP representation of [Mo(**C**−**C**)] (bottom left) and [W(**C**−**C**)] (bottom right) (hydrogen atoms are omitted for clarity). Ellipsoids are drawn with a 50% probability. (A) (1) *hν*, THF, RT., 2 h; (2) [H(**C**−**C**)]BF_4, NEt_3, reflux, overnight;[77] (B) (1) *hν*, THF, RT, 2 h; (2) norbornadiene, reflux, 2 d; (3) [H(**C**−**C**)]BF_4, NEt_3, RT, overnight; (C) (1) *hν*, CH_3CN, RT, 2 h; (2) [H(**C**−**C**)]BF_4, NEt_3, reflux, overnight.

Table 1. Selected Bond Lengths for [M(C−C)] and [M(C−N)] (M = Cr, Mo, W) in Å; Atomic Labels Are as in Figure 2

	[Cr(C−C)][77]	[Mo(C−C)]	[W(C−C)]	[Cr(C−N)][48]	[Mo(C−N)][48]	[W(C−N)][28]
M−C1	2.049(3)	2.186(2)	2.173(4)	2.065(2)	2.202(1)	2.186(3)
M−N1	2.163(3)	2.309(2)	2.286(4)	2.147(2)	2.275(1)	2.259(2)
M−C100	1.851(3)	1.997(2)	1.994(5)	1.855(2)	1.997(2)	1.990(3)
M−C200	1.827(4)	1.948(2)	1.956(5)	1.847(2)	1.973(1)	1.974(3)
M−C300	1.906(4)	2.045(2)	2.038(5)	1.894(2)	2.051(2)	2.039(3)
M−C400	1.895(4)	2.054(2)	2.042(5)	1.903(2)	2.040(2)	2.028(3)

facilitating an in-depth comparison with the previously reported [M(**C**−**N**)] complexes. Additionally, FTIR spectroscopy in combination with theoretical calculations provides detailed insights into the mechanism of the CO cleavage and the involved emissive states.

■ RESULTS AND DISCUSSION

Synthesis and Characterization. The synthesis of [Cr(**C**−**C**)],[77] [Mo(**C**−**C**)], and [W(**C**−**C**)] was performed according to the previously reported protocol for bidentate pyridyl-MIC group 6 carbonyl complexes (Figure 2).[28,48] The light-induced activation of $[M(CO)_6]$ (M = Cr, Mo, W) in THF or CH_3CN and subsequent addition of [H(**C**−**C**)]BF_4 in the presence of a base lead to the respective Cr^0 and W^0 complexes.

In order to obtain [Mo(**C**−**C**)], $[Mo(nbd)(CO)_4]$ (nbd = norbornadiene) was synthesized and further reacted with [H(**C**−**C**)]BF_4 in the presence of a base at ambient temperatures to generate *in situ* the pyridyl-MIC. Extraction and purification *via* column chromatography resulted in the isolation of the [M(**C**−**C**)] (M = Cr, Mo, W) complexes in good yields. Addition of *n*-hexane or *n*-pentane to a concentrated solution of the respective complexes in CH_2Cl_2 yields single crystals suitable for X-ray diffraction analysis.

In the series of [M(**C**−**C**)] (M = Cr, Mo, W), the M−C1 and M−N1 bond lengths increase in the order Cr < W < Mo, in analogy to the previously reported [M(**C**−**N**)][28,48] complexes (Table 1). The comparison of the [M(**C**−**C**)] complexes with the [M(**C**−**N**)] analogues shows an interesting trend. The M−C1 bond lengths are shorter than those of their [M(**C**−**N**)] counterparts, indicating an enhanced metal−carbene bond interaction, while the M−N1 bonds in [M(**C**−**C**)] are elongated as a consequence of the weaker *π*-backbonding from the metal center to the more electron-rich **C**−**C** ligand. This effect is particularly evident in the trans-positioned M−C200 bond distances (Table 1). The increased electron density at the metal center of [M(**C**−**C**)] leads to an increased *π*-backbonding from the metal center to the CO ligands, which results in a shorter metal−carbon bond and in the elongation of the C−O bond distances (Table S1).[28,48]

Photophysical/Photochemical Properties and DFT Calculations. The UV/vis absorption spectra of [M(**C**−**C**)] in solution exhibit two low energy bands in the range of 325−550 nm, which are slightly blue-shifted with respect to the

https://doi.org/10.1021/acs.inorgchem.3c02478
Inorg. Chem. 2023, 62, 16182−16195

[M(C−N)] analogues. Increasing the solvent polarity leads to a blue shift of the absorption maxima of the low energy bands by up to 17 nm (Section S4). The solvatochromic shift indicates an MLCT character of the electronic transition, and it is further supported by TD-DFT calculations (see Supporting Information, Section S7.2).

[Cr(C−C)] shows the lowest energy absorption, while the absorption bands in [W(C−C)] and [Mo(C−C)] occur at higher energies, independent of the solvent. The same trend in this regard was observed in the UV/vis absorption spectra in a KBr matrix (Figure 3).

The Cr^0 complex shows an onset at 633 nm, similar to that of the W^0 complex at 631 nm. In contrast to the Cr and W cases, which allow for unambiguous straight line fits of their rising slopes, the 620 nm excitation spectrum of [Mo(C−C)] clearly reveals a two-slope rise, which may be fitted accordingly (see Supporting Information, Figure S9) and thereby provides some evidence of two excitation thresholds at 529 and 507 nm, which may relate to two electronic states, which are separated roughly by 10 kJ/mol or 0.1 eV. In the case of [W(C−C)], an emission with a maximum at λ_{ex} = 662 nm was detected in the solid state, while [Mo(C−C)] and [Cr(C−C)] show no or only weak luminescence at room temperature (Figure 4). However, lowering the temperatures down to 5 K leads to an intense luminescence in the region of 520−850 nm. The emission maxima follow the order of $\lambda_{max}^{Cr} > \lambda_{max}^{W} > \lambda_{max}^{Mo}$ and are blue-shifted compared to their [M(C−N)] analogues[28,48] (Table 2).

The integrated emission intensities for Mo^0 and W^0 exhibit a linear dependence upon cooling from 290 to 5 K and increase 5 times. In contrast, the emission of the Cr^0 complex increases rapidly upon cooling to 90 K. However, at lower temperatures, no significant changes in the emission intensity are observed (Figures 4 and S21).

The increased luminescence is likely a consequence of inhibited nonradiative deactivation pathways (*e.g.*, vibrational cooling), presumably originating from an enhanced rigidity in the solid state at lower temperatures.

The observed temperature dependence become particularly prominent in view of the luminescence lifetimes in [M(C−C)] and its [M(C−N)][28] counterparts (Table 2). At room temperature, a luminescence lifetime of 7 ns (94% contribution) was determined for [Mo(C−C)] by time-correlated single photon counting (TCSPC), similar to those observed for [Mo(C−N)] with 10 ns. Upon cooling, [Mo(C−C)] exhibits an excited-state lifetime of 3500 ns (95% contribution), nearly 22 times higher than that observed for the previously reported [Mo(C−N)] complex.[15] The temperature-dependent increase and the prolonged excited-state lifetimes are strong evidence for a triplet state with a visible emission (Table S3 and Figure S24).

The [W(C−C)] complex follows the same trend with luminescence lifetimes of 3000 ns (86% contribution) at 5 K. However, the excited-state lifetime at room temperature is significantly higher compared to its [W(C−N)][28] counterpart. The W^0 complex exhibits a luminescence lifetime of 50 ns (70% contribution), 25 times higher than that observed for [W(C−N)] (Table S4 and Figure S25).

The residual, minor component of 30% might result from heterogeneous microenvironments, a second isomer, or a long-lived [W(C−C)$(CO)_3$] photoproduct, which is generated after CO elimination. Furthermore, the quantum yields of [Mo(C−C)] in the solid state are 5×10^{-4} at room temperature and in good agreement with earlier reported polypyridine group 6 carbonyl complexes.[29,78]

To our surprise, the higher homologue [W(C−C)] exhibits very high quantum yields of 29% in the solid state at room

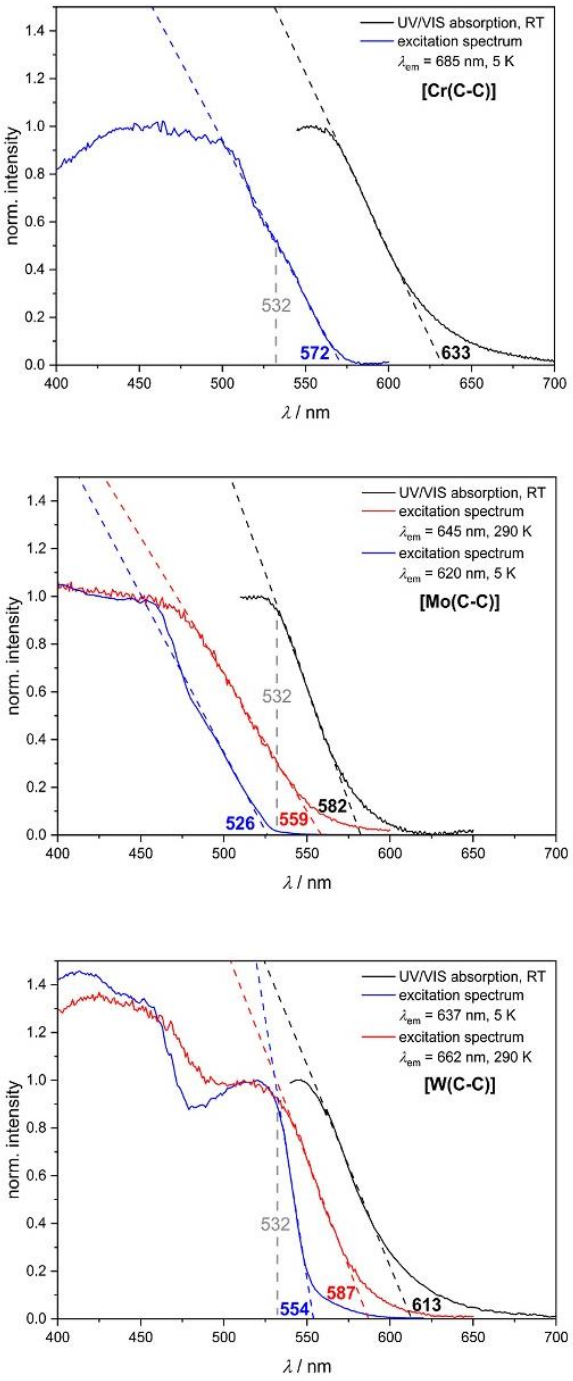

Figure 3. UV/vis absorption spectra at 290 K (black, powder of the complex diluted with KBr) and excitation spectra at 5 and 290 K (blue and red, respectively) of [Cr(C−C)] (top), [Mo(C−C)] (middle), and [W(C−C)] (bottom), taken from KBr pellets. The absorption onsets were determined tangentially.

https://doi.org/10.1021/acs.inorgchem.3c02478
Inorg. Chem. 2023, 62, 16182−16195

Inorganic Chemistry pubs.acs.org/IC Article

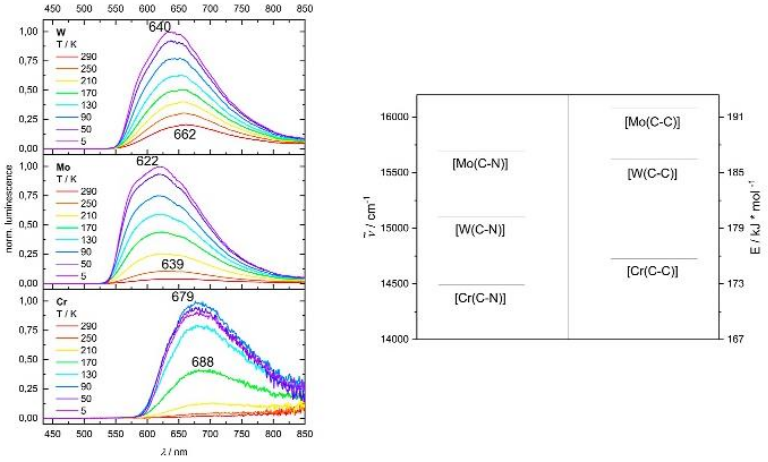

Figure 4. Left: temperature-dependent luminescence spectra of [W(**C**−**C**)], [Mo(**C**−**C**)], and [Cr(**C**−**C**)] in the solid state (KBr matrix) at temperatures of 5−290 K (at λ_{ex} = 420 nm). Right: emission energy diagram of [M(**C**−**C**)] and [M(**C**−**N**)] (M = Cr, Mo, W).

Table 2. Emission Maxima (λ_{max}), Luminescence Quantum Yields (Φ), and Averaged Excited-State Lifetimes (τ_{av}) of [M(C−C)] and [M(C−N)][28] (M = Cr, Mo, W) in the Solid State (KBr Pellet) at 290 and <20 K

complex	λ_{max}/nm		Φ (VIS)[a]	τ_{av}(TSCPC)[b]/ns		τ (step-scan)[b]/ns	
	290 K	<20 K	290 K	290 K	<20 K	290 K	<20 K
[Cr(**C**−**C**)]	N/A	685	N/A	N/A	N/A	620 ± 10	930 ± 10
[Mo(**C**−**C**)]	645	619	5.0×10^{-4}	7 ± 1	3500 ± 350	350 ± 10	720 ± 40
[W(**C**−**C**)]	662	637	0.29	50 ± 5	3000 ± 300	300 ± 10	1720 ± 60
[Cr(**C**−**N**)][28]	≈695	690	N/A	N/A	N/A	380 ± 10	135 ± 2
[Mo(**C**−**N**)][28]	666	637	1.1×10^{-4}	10 ± 1	160 ± 16	600 ± 10	150 ± 10
[W(**C**−**N**)][28]	673	662	1.7×10^{-4}	2.2 ± 0.2	290 ± 29	370 ± 10	116 ± 5

[a]The error bars for the photoluminescence quantum yields are estimated to ±25% according to the literature. [b]The error bars for the time constants are estimated to ±10%.

temperature. To the best of our knowledge, these are the highest quantum yields reported for W^0 carbonyl complexes so far. Intrigued by these results, we recorded emission spectra in deaerated butyronitrile (PrCN). In the series of [M(**C**−**C**)] and [M(**C**−**N**)], only [W(**C**−**C**)] exhibits an emission at $\lambda_{em}^{420\ nm}$ = 717 nm with luminescence lifetimes of up to 28 ns at room temperature (Figure 5). Lowering the temperature to 20 K leads to the formation of a clear PrCN glass. The emission spectra show an increase of the emission intensity of about 2 times. The bathochromic shifts in the series of [M(**C**−**C**)] follow the trend $\lambda_{em}^{DMSO} < \lambda_{em}^{CH_3CN} < \lambda_{em}^{CH_2Cl_2}$ (see Supporting Information, Section S4), indicating an MLCT character for the emission. The MLCT character is further supported by the rigidochromism[79−81] observed upon lowering the temperature from 290 to 5 K, as a blue shift of ≈25 nm in the emission maxima is present (Figure 4).

To further investigate the nature of the excited states, time-resolved step-scan FTIR spectroscopy was performed. The ground-state FTIR spectra of all three complexes are well-described by the calculated vibrational spectra of the S_0 ground state (Figures 6 and S38−S46). Step-scan difference spectra in the solid state were recorded after excitation at 20 and 290 K (λ_{ex} = 355 nm), respectively (see Supporting Information, Section S6.1). The obtained excited-state vibrational spectra are obtained by correction for small contributions from the ground-state bleach (see Supporting Information, Figures S69−S71).

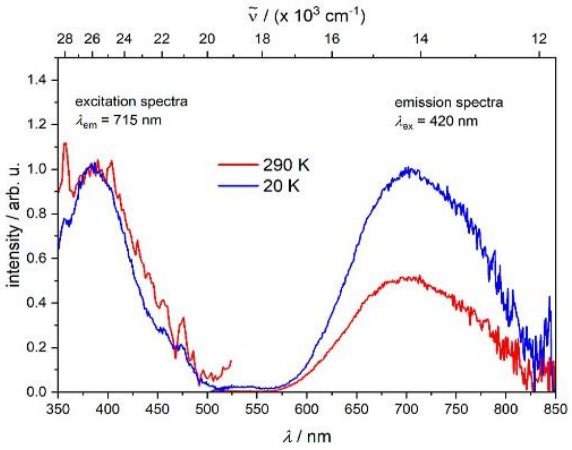

Figure 5. Measured excitation and emission spectra of [W(**C**−**C**)] at 290 K (red) and 20 K (blue) in PrCN solution, λ_{ex} = 420 nm.

The ground- and excited-state spectra display similar vibrational bands, which are in good accordance with the theoretically calculated CO stretching frequencies. Only within the first 500 ns after laser excitation, a weak additional band at 1977 cm^{-1} is detected in the averaged excited-state spectra at 10 K for [Mo(**C**−**C**)] and [W(**C**−**C**)], which is also observed at 290 K in the case of [W(**C**−**C**)] (Figure 6). According to

https://doi.org/10.1021/acs.inorgchem.3c02478
Inorg. Chem. 2023, 62, 16182−16195

Inorganic Chemistry pubs.acs.org/IC Article

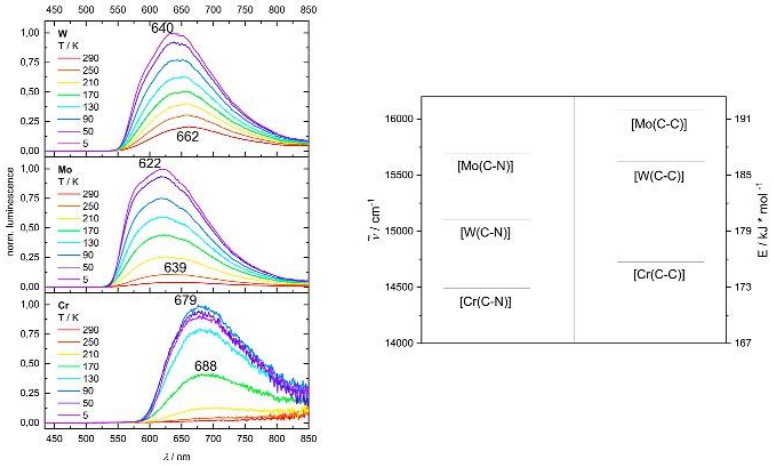

Figure 4. Left: temperature-dependent luminescence spectra of [W(**C**−**C**)], [Mo(**C**−**C**)], and [Cr(**C**−**C**)] in the solid state (KBr matrix) at temperatures of 5−290 K (at λ_{ex} = 420 nm). Right: emission energy diagram of [M(**C**−**C**)] and [M(**C**−**N**)] (M = Cr, Mo, W).

Table 2. Emission Maxima (λ_{max}), Luminescence Quantum Yields (Φ), and Averaged Excited-State Lifetimes (τ_{av}) of [M(C−C)] and [M(C−N)][28] (M = Cr, Mo, W) in the Solid State (KBr Pellet) at 290 and <20 K

complex	λ_{max}/nm		Φ (VIS)[a]	τ_{av}(TSCPC)[b]/ns		τ (step-scan)[b]/ns	
	290 K	<20 K	290 K	290 K	<20 K	290 K	<20 K
[Cr(**C**−**C**)]	N/A	685	N/A	N/A	N/A	620 ± 10	930 ± 10
[Mo(**C**−**C**)]	645	619	5.0×10^{-4}	7 ± 1	3500 ± 350	350 ± 10	720 ± 40
[W(**C**−**C**)]	662	637	0.29	50 ± 5	3000 ± 300	300 ± 10	1720 ± 60
[Cr(**C**−**N**)][28]	≈695	690	N/A	N/A	N/A	380 ± 10	135 ± 2
[Mo(**C**−**N**)][28]	666	637	1.1×10^{-4}	10 ± 1	160 ± 16	600 ± 10	150 ± 10
[W(**C**−**N**)][28]	673	662	1.7×10^{-4}	2.2 ± 0.2	290 ± 29	370 ± 10	116 ± 5

[a]The error bars for the photoluminescence quantum yields are estimated to ±25% according to the literature. [b]The error bars for the time constants are estimated to ±10%.

temperature. To the best of our knowledge, these are the highest quantum yields reported for W^0 carbonyl complexes so far. Intrigued by these results, we recorded emission spectra in deaerated butyronitrile (PrCN). In the series of [M(**C**−**C**)] and [M(**C**−**N**)], only [W(**C**−**C**)] exhibits an emission at $\lambda_{em}^{420\ nm}$ = 717 nm with luminescence lifetimes of up to 28 ns at room temperature (Figure 5). Lowering the temperature to 20 K leads to the formation of a clear PrCN glass. The emission spectra show an increase of the emission intensity of about 2 times. The bathochromic shifts in the series of [M(**C**−**C**)] follow the trend $\lambda_{em}^{DMSO} < \lambda_{em}^{CH_3CN} < \lambda_{em}^{CH_2Cl_2}$ (see Supporting Information, Section S4), indicating an MLCT character for the emission. The MLCT character is further supported by the rigidochromism[79−81] observed upon lowering the temperature from 290 to 5 K, as a blue shift of ≈25 nm in the emission maxima is present (Figure 4).

To further investigate the nature of the excited states, time-resolved step-scan FTIR spectroscopy was performed. The ground-state FTIR spectra of all three complexes are well-described by the calculated vibrational spectra of the S_0 ground state (Figures 6 and S38−S46). Step-scan difference spectra in the solid state were recorded after excitation at 20 and 290 K (λ_{ex} = 355 nm), respectively (see Supporting Information, Section S6.1). The obtained excited-state vibrational spectra are obtained by correction for small contributions from the ground-state bleach (see Supporting Information, Figures S69−S71).

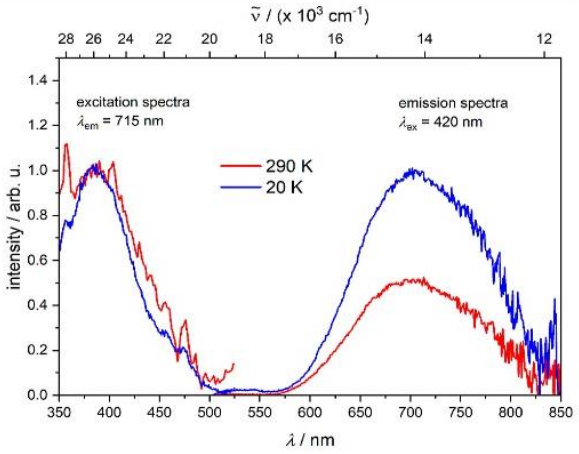

Figure 5. Measured excitation and emission spectra of [W(**C**−**C**)] at 290 K (red) and 20 K (blue) in PrCN solution, λ_{ex} = 420 nm.

The ground- and excited-state spectra display similar vibrational bands, which are in good accordance with the theoretically calculated CO stretching frequencies. Only within the first 500 ns after laser excitation, a weak additional band at 1977 cm^{-1} is detected in the averaged excited-state spectra at 10 K for [Mo(**C**−**C**)] and [W(**C**−**C**)], which is also observed at 290 K in the case of [W(**C**−**C**)] (Figure 6). According to

https://doi.org/10.1021/acs.inorgchem.3c02478
Inorg. Chem. 2023, 62, 16182−16195

Inorganic Chemistry pubs.acs.org/IC Article

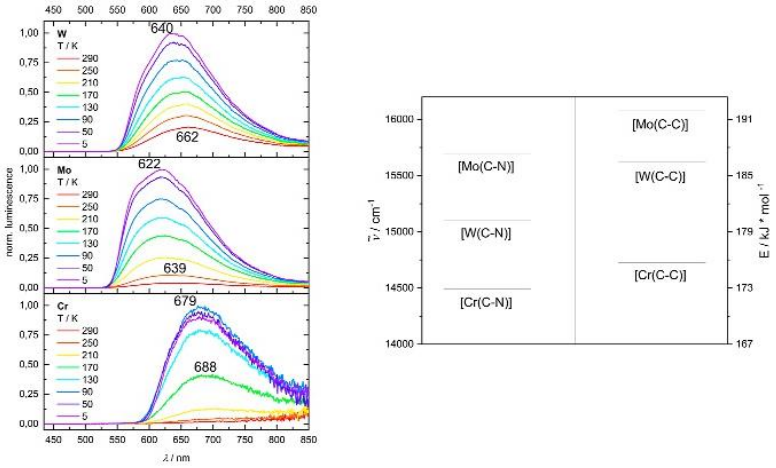

Figure 4. Left: temperature-dependent luminescence spectra of [W(**C**−**C**)], [Mo(**C**−**C**)], and [Cr(**C**−**C**)] in the solid state (KBr matrix) at temperatures of 5−290 K (at λ_{ex} = 420 nm). Right: emission energy diagram of [M(**C**−**C**)] and [M(**C**−**N**)] (M = Cr, Mo, W).

Table 2. Emission Maxima (λ_{max}), Luminescence Quantum Yields (Φ), and Averaged Excited-State Lifetimes (τ_{av}) of [M(C−C)] and [M(C−N)][28] (M = Cr, Mo, W) in the Solid State (KBr Pellet) at 290 and <20 K

complex	λ_{max}/nm		Φ (VIS)[a]	τ_{av}(TSCPC)[b]/ns		τ (step-scan)[b]/ns	
	290 K	<20 K	290 K	290 K	<20 K	290 K	<20 K
[Cr(**C**−**C**)]	N/A	685	N/A	N/A	N/A	620 ± 10	930 ± 10
[Mo(**C**−**C**)]	645	619	5.0×10^{-4}	7 ± 1	3500 ± 350	350 ± 10	720 ± 40
[W(**C**−**C**)]	662	637	0.29	50 ± 5	3000 ± 300	300 ± 10	1720 ± 60
[Cr(**C**−**N**)][28]	≈695	690	N/A	N/A	N/A	380 ± 10	135 ± 2
[Mo(**C**−**N**)][28]	666	637	1.1×10^{-4}	10 ± 1	160 ± 16	600 ± 10	150 ± 10
[W(**C**−**N**)][28]	673	662	1.7×10^{-4}	2.2 ± 0.2	290 ± 29	370 ± 10	116 ± 5

[a]The error bars for the photoluminescence quantum yields are estimated to ±25% according to the literature. [b]The error bars for the time constants are estimated to ±10%.

temperature. To the best of our knowledge, these are the highest quantum yields reported for W^0 carbonyl complexes so far. Intrigued by these results, we recorded emission spectra in deaerated butyronitrile (PrCN). In the series of [M(**C**−**C**)] and [M(**C**−**N**)], only [W(**C**−**C**)] exhibits an emission at $\lambda_{em}^{420\ nm}$ = 717 nm with luminescence lifetimes of up to 28 ns at room temperature (Figure 5). Lowering the temperature to 20 K leads to the formation of a clear PrCN glass. The emission spectra show an increase of the emission intensity of about 2 times. The bathochromic shifts in the series of [M(**C**−**C**)] follow the trend $\lambda_{em}^{DMSO} < \lambda_{em}^{CH_3CN} < \lambda_{em}^{CH_2Cl_2}$ (see Supporting Information, Section S4), indicating an MLCT character for the emission. The MLCT character is further supported by the rigidochromism[79−81] observed upon lowering the temperature from 290 to 5 K, as a blue shift of ≈25 nm in the emission maxima is present (Figure 4).

To further investigate the nature of the excited states, time-resolved step-scan FTIR spectroscopy was performed. The ground-state FTIR spectra of all three complexes are well-described by the calculated vibrational spectra of the S_0 ground state (Figures 6 and S38−S46). Step-scan difference spectra in the solid state were recorded after excitation at 20 and 290 K (λ_{ex} = 355 nm), respectively (see Supporting Information, Section S6.1). The obtained excited-state vibrational spectra are obtained by correction for small contributions from the ground-state bleach (see Supporting Information, Figures S69−S71).

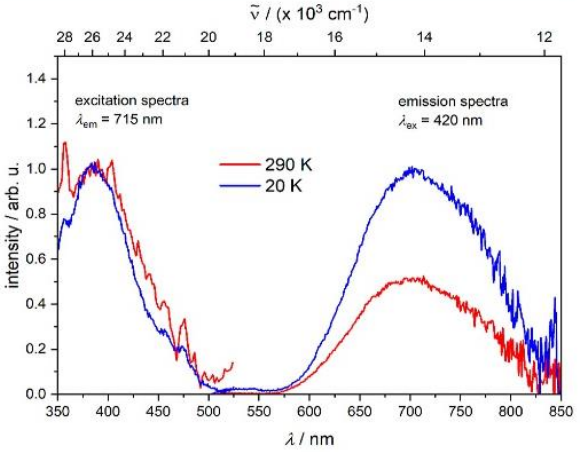

Figure 5. Measured excitation and emission spectra of [W(**C**−**C**)] at 290 K (red) and 20 K (blue) in PrCN solution, λ_{ex} = 420 nm.

The ground- and excited-state spectra display similar vibrational bands, which are in good accordance with the theoretically calculated CO stretching frequencies. Only within the first 500 ns after laser excitation, a weak additional band at 1977 cm^{-1} is detected in the averaged excited-state spectra at 10 K for [Mo(**C**−**C**)] and [W(**C**−**C**)], which is also observed at 290 K in the case of [W(**C**−**C**)] (Figure 6). According to

https://doi.org/10.1021/acs.inorgchem.3c02478
Inorg. Chem. 2023, 62, 16182−16195

The generated photoproducts in [M(C−C)] are stable for up to 9 h in pyridine (Figure 8 and Supporting Information, Section S6.1) but significantly short-lived compared to its [M(C−N)][47] analogues. Accordingly, the kinetics of the dark reversible CO binding and the photodissociation quantum yields in [M(C−C)] were investigated to gain in-depth information on the photoinduced reactivity (Table 4).

Table 4. Selected First-Order Reaction Rate Constants of the Dark Reverse Reaction for [M(C−C)] (M = Cr, Mo, or W) in CH_3CN after Irradiation at λ_{ex} = 355 nm

	k/s^{-1}		
c/mM	[Cr(C−C)]	[Mo(C−C)]	[W(C−C)]
3	0.05 ± 0.01	(1.8 ± 0.04) × 10^{-3}	(1.2 ± 0.03) × 10^{-3}
6	0.06 ± 0.01	(2.1 ± 0.05) × 10^{-3}	(1.4 ± 0.03) × 10^{-3}
c/mM	[Cr(C−N)][47]	[Mo(C−N)][47]	[W(C−N)][47]
3	0.025 ± 0.006	(1.7 ± 0.04) × 10^{-3}	(1.4 ± 0.04) × 10^{-3}
6	0.023 ± 0.006	(1.9 ± 0.04) × 10^{-3}	(1.7 ± 0.04) × 10^{-3}

The dark reaction was monitored by the well-separated frequencies between 1778 and 1773 cm^{-1} after irradiation at 355 and 490 nm in CH_3CN, respectively. The decay of the photoproduct could be assigned to first-order kinetics for all three complexes, with deviations at longer time scales (Figures 9 and S31).

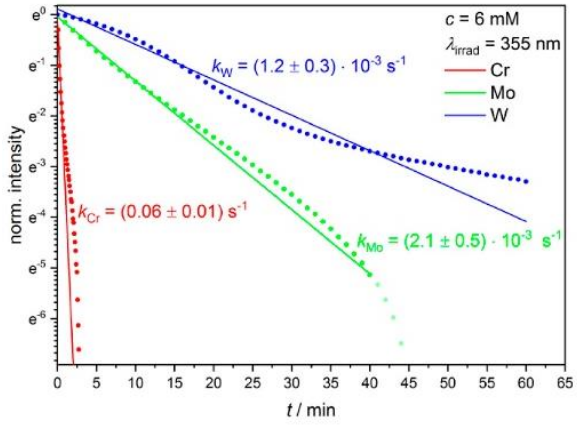

Figure 9. Recorded kinetics plots and first-order fits of the dark reverse reaction of [M(C−C)] (M = Cr, Mo, W) in CH_3CN (c = 6 mM), after exposure to λ_{ex} = 355 nm, which defines t = 0 in the plot.

The first-order kinetics are probably a consequence of initial thermal dissociation of the solvent molecule, which might be the rate-limiting step (Figure 10).

The obtained first-order rate constants (Table 4) are independent of the concentration and follow the trend of $k_{Cr} \gg k_{Mo} \approx k_W$. The influence of constitutional isomers, C−C versus C−N, is particularly evident in the Cr^0 complexes. The rate constant of the dark reverse reaction in [Cr(C−C)] is two times higher compared to its [Cr(C−N)] counterpart and could be a direct consequence of the increased electron density in the 16 VE [Cr(C−C)$(CO)_3$] species, as indicated by the enhanced CO binding rate constant.

Changing the excitation energies does not significantly affect the kinetic rate constant in [Cr(C−C)], revealing a minor influence on the excitation energies (Table 5).

In contrast, changing the photoexcitation energies from 420 to 355 nm in [Mo(C−C)] and [W(C−C)] increases the rate constants of the dark reverse reaction by a factor of 2, indicating at least two competing pathways for the reversible CO binding at the higher excitation energy.

For the determination of the photodissociation quantum yields (Φ_{diss}), irradiation times were kept short to minimize the influence of the dark reverse reaction on the obtained quantum yields. Within the [M(C−C)] series, the Cr^0 complex shows the highest photodissociation quantum yield of 34% at 355 nm, followed by the Mo^0 complex of 11% and the W^0 complex of 0.6% (Table 5).

The difference in photoreactivity is in good accordance with the magnitude of the ligand field splitting, modulating the shape of the affected d-orbitals. The more diffuse 5d and to a lesser extent 4d orbitals facilitate a significant increase in the π-backbonding compared to 3d orbitals. Hence, photodissociation quantum yields at 355 nm correlate with the M−CO stabilization, as reported earlier in Cr^0, Mo^0, and W^0 complexes with bipyridine ligands.[37]

Lowering the excitation energy to 490 nm leads to a decrease in the photodissociation quantum yields, while higher excitation energies facilitate the population of other reactive excited states. Consequently, higher photodissociation quantum yields are observed during the excitation at 266 nm.

Indeed, the photodissociation quantum yield in the W^0 complex increases drastically upon changing the excitation energy from 355 to 266 nm, while the photoreactivity in [Mo(C−C)] remains unaffected. In the case of [Cr(C−C)], the photodissociation quantum yield even decreases, which is most likely a consequence of the population of other photoreactive excited states.

Comparison between the [M(C−C)] and [M(C−N)] complexes shows that the incorporation of the more electron-donating C−C ligand leads to an overall decrease of the photodissociation quantum yields.[77] The enhanced π-backbonding to the CO ligands results in a stronger M−CO bond, disfavoring CO dissociation, and consequently an overall decrease of the photodissociation quantum yields.

CONCLUSIONS

The photophysical and photochemical properties of a new series of group 6 tetracarbonyl complexes with a C−C linked pyridyl-MIC ligand were investigated and compared with those of their analogous complexes bearing the constitutional isomer of the C−N type. All [M(C−C)] (M = Cr, Mo, W) complexes exhibit luminescence in the visible region in the solid state with lifetimes of up to 3.5 μs at cryo temperatures. The W^0 complex shows a remarkable quantum yield of 29% at room temperature in the solid state and emission in a fluid solution at 717 nm. Step-scan FTIR spectra in a KBr matrix and their quantum chemical modeling reveal a ^{3}MLCT character of the emissive excited state.

In addition, FTIR spectra at lower temperatures give evidence of the formation of a metastable 16 VE [M(C−C)$(CO)_3$] intermediate with a vacant axial coordination site upon UV/vis irradiation.

Photodissociation quantum yields of up to 34% are observed for the Cr^0 complex in CH_3CN. However, the photoreactivity in [M(C−C)] strongly depends on the excitation energy.

In solution, a clean conversion to the photoproduct with an axial coordinated solvent molecule is observed for all present complexes, as shown by time-resolved FTIR spectroscopy in

https://doi.org/10.1021/acs.inorgchem.3c02478
Inorg. Chem. 2023, 62, 16182−16195

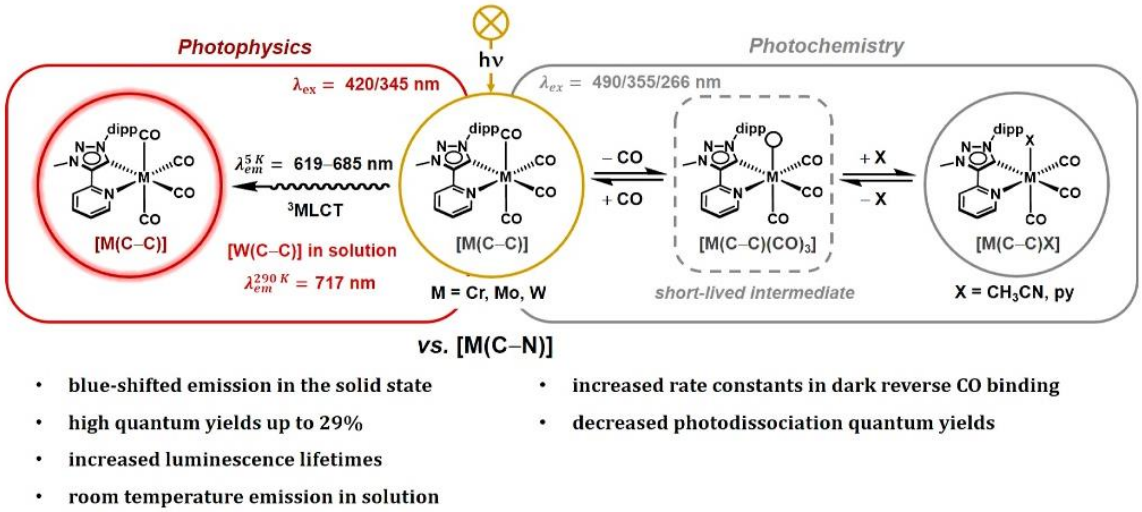

Figure 10. Illustrative summary of the photophysical and photochemical properties of [M(**C**–**C**)] (M = Cr, Mo, W) compared to its [M(**C**–**N**)][28,47] counterpart.

Table 5. Photodissociation Quantum Yields of [M(C–C)] (M = Cr, Mo, W) in CH_3CN (λ_{ex} = 490, 355, and 266 nm)[a]

	Φ_{diss}/%					
λ_{ex}/nm	[Cr(**C**–**C**)]	[Mo(**C**–**C**)]	[W(**C**–**C**)]	[Cr(**C**–**N**)][47]	[Mo(**C**–**N**)][47]	[W(**C**–**N**)][47]
490	5.6	2.6	0.3			
355	34	11	0.6	43	15	5
266	25	12	24	46	44	10

[a]The error bars for the photodissociation quantum yields are estimated to ±25%.

combination with theoretical calculations. Leaving the photoproducts in the dark leads to an almost complete recovery of the initial IR spectra, providing great opportunities for (photo)switchable transition-metal complexes. Accordingly, the kinetics of the reverse dark reaction have been investigated and the kinetic rate constants for the reversible CO binding were determined, following the order of Cr ≫ Mo ≈ W.

The more electron-donating **C**–**C** linked pyridyl-MIC ligand reveals a blue shift of the emission in [M(**C**–**C**)] as compared to its [M(**C**–**N**)] counterparts and increased excited-state lifetimes, in particular at lower temperatures. Furthermore, the increased electron density at the metal center results in lower photodissociation quantum yields, which is a consequence of the stronger π-backbonding from the metal center to the CO ligands. The change in the electronic properties is also evident in the kinetic rates of dark reversible CO binding. While the kinetic rates in the Mo^0 and W^0 complexes only slightly increase, the kinetic rate constant in Cr^0 is twice as high as in the previously reported [Cr(**C**–**N**)] analogue. The data presented here represent the first comprehensive study on the influence of constitutional isomers of bidentate ligands in tetracarbonyl group 6 complexes. The study provides a rare perspective on how to tune the photophysical and photochemical properties of transition-metal-based complexes based on constitutional isomers of ligands.

EXPERIMENTAL SECTION

General Procedures, Materials, and Instrumentation. Caution! Compounds containing azides are potentially explosive. Although we never experienced any problems during synthesis or analysis, all compounds should be synthesized only in small quantities and handled with great care!

Unless otherwise noted, all reactions were carried out using standard Schlenk-line techniques under an inert atmosphere of argon (Linde Argon 4.8, purity 99.998%). All reactions, which require heating, were performed with an oil bath.

Commercially available chemicals were used without further purification. The solvents used for metal complex synthesis and catalysis were available from the MBRAUN MB-SPS-800 solvent System and degassed by standard techniques prior to use. The identity and purity of compounds were established *via* ^{1}H and ^{13}C NMR spectroscopy, elemental analysis, and mass spectrometry. ^{1}H and ^{13}C{^{1}H} NMR spectra were recorded on a Bruker Avance 250/400/500 spectrometer at 19–22 °C. Chemical shifts are reported in ppm referenced to the residual solvent peaks.[84] The following abbreviations are used to represent the multiplicity of the signals: s (singlet), d (doublet), t (triplet), q (quartet), p (pentet), and sept (septet). Mass spectrometry was performed on an Agilent 6210 ESI-TOF. Elemental analyses were performed with an Elementar Micro Cube elemental analyzer.

X-ray Diffraction. X-ray data were collected on a BRUKER Smart AXS, BRUKER D8 Venture or Bruker Kappa Apex2duo system. Data were collected at 100(2) or 140(2) K using graphite-monochromatic Mo K_α radiation (λ_α = 0.71073 Å). The strategy for data collection was evaluated using the APEX2 or Smart software. The data were collected by standard "ω scan techniques" or "$\omega - \varphi$ scan techniques" and were scaled and reduced using APEX2, SAINT+, and SADABS software. The structures were solved by direct methods using SHELXL-97 or intrinsic phasing using SHELXL-2014/7 and refined by full matrix least-squares with SHELXL-2014/7, refining on F^2. Non-hydrogen atoms were refined anisotropically. If it is noted, bond length and angles were measured with Mercury, version 3.8.[85−92]

Synthesis and Characterization. *Synthesis of [Mo(C–C)].* [$Mo(CO)_4$(nbd)] (11.0 mg, 0.037 mmol) and [H(**C**–**C**)]BF_4

https://doi.org/10.1021/acs.inorgchem.3c02478
Inorg. Chem. 2023, 62, 16182−16195

(15.0 mg, 0.037 mmol) were dissolved in 6 mL of THF. Excess of NEt_3 (0.6 mL) was added, and the reaction mixture was stirred overnight. The solvent was evaporated, and the residue was dissolved in 20 mL of CH_2Cl_2 and extracted three times with 20 mL of H_2O. The organic phases were collected and dried over Na_2SO_4. The solvent was reduced, and the crude product was purified by column chromatography (SiO_2, 1:10, *n*-pentane/CH_2Cl_2). An analytically pure product was isolated after recrystallization from CH_2Cl_2 and *n*-pentane yielding orange crystals (16.9 mg, 87%).

^{1}H NMR (400 MHz, acetone-d_6) δ (ppm) = 9.11 (ddd, J = 5.4, 1.5, 0.9 Hz, 1H), 8.31−8.25 (m, 1H), 8.14−8.09 (m, 1H), 7.56 (t, J = 7.8 Hz, 1H), 7.48−7.44 (m, 1H), 7.41 (d, J = 7.8 Hz, 2H), 4.79 (s, 3H), 2.62 (hept, J = 6.8 Hz, 2H), 1.30 (d, J = 6.8 Hz, 6H), 1.11 (d, J = 6.9 Hz, 6H); **^{13}C NMR** (176 MHz, CD_2Cl_2) δ (ppm) = 224.92, 221.56, 207.62, 197.30, 155.87, 150.47, 146.10, 145.45, 137.73, 136.19, 131.30, 124.32, 123.80, 120.23, 39.44, 29.15, 25.60, 22.89; **MS (ESI)**: m/z found: 530.0848, calcd: 530.0848 [$C_{24}H_{24}MoN_4O_4^+$], 321.2102, calcd: 321.2074 [$C_{20}H_{25}N_4^+$]; **IR** ($\tilde{\nu}$(CO), CH_2Cl_2) = 2004 cm^{-1} (s), 1894 cm^{-1} (s), 1876 cm^{-1} (sh), 1830 cm^{-1} (s); **Anal. Calcd for $C_{24}H_{24}MoN_4O_4$**: C, 54.55; H, 4.58; N, 10.60. **Found**: C, 54.71; H, 4.73; N, 10.25.

*Synthesis of [W(**C−C**)].* A suspension of [W(CO)$_6$] (52.0 mg, 0.147 mmol) in 20 mL of CH_3CN was stirred for 2 h under UV light. The CO overpressure was released at least 3 times during this period. [H(**C−C**)]BF_4 (60 mg, 0.147 mmol) and an excess of NEt_3 (1.0 mL) were added. The mixture was refluxed with an equipped reflux condenser and a gas bubbler for 3 days. After the mixture cooled to room temperature, the solvent was evaporated and the remaining residue was dissolved in CH_2Cl_2 and extracted two times with H_2O. The organic phases were collected and dried over Na_2SO_4. The solvent was removed, and the crude product was purified by column chromatography (SiO_2, 1:10, *n*-pentane/CH_2Cl_2). An analytically pure product was isolated after recrystallization from CH_2Cl_2 and *n*-pentane yielding orange crystals (62 mg, 69%).

^{1}H NMR (250 MHz, $CDCl_3$) δ (ppm) = 9.00 (ddd, J = 5.5, 1.6, 0.8 Hz, 1H), 8.18 (dt, J = 8.3, 1.0 Hz, 1H), 8.00 (ddd, J = 8.3, 7.5, 1.7 Hz, 1H), 7.60−7.49 (m, 1H), 7.39−7.30 (m, 3H), 3.90 (s, 3H), 2.63 (hept, J = 6.7 Hz, 2H), 1.30 (d, J = 6.7 Hz, 6H), 1.14 (d, J = 6.9 Hz, 6H); **^{13}C NMR** (176 MHz, CD_2Cl_2) δ (ppm) = 216.74, 215.45, 201.87, 195.16, 156.41, 151.11, 148.31, 146.12, 137.69, 135.83, 131.44, 124.52, 124.38, 120.54, 39.42, 29.29, 25.60, 22.88; **MS (ESI)**: m/z found: 616.1303, calcd: 616.1307 [$C_{24}H_{24}WN_4O_4^+$], 639.1189, calcd: [$C_{24}H_{24}WN_4O_4Na^+$], 655.0928, calcd: 655.0938 [$C_{24}H_{24}WN_4O_4K^+$], 611.1965, calcd: 611.1250 [$C_{23}H_{24}N_4NaO_3W^+$], 321.2076, calcd: 321.2079 [$C_{20}H_{25}N_4^+$]; **IR** ($\tilde{\nu}$(CO), CH_2Cl_2) = 1998 cm^{-1} (s), 1882 cm^{-1} (s), 1870 cm^{-1} (sh), 1826 cm^{-1} (s); **Anal. Calcd for $C_{24}H_{24}WN_4O_4$**: C, 46.77; H, 3.93; N, 9.09. **Found**: C, 46.31; H, 3.95; N, 8.99.

Sample Preparation. Preparation of KBr pellets: the isolated compound (0.80−1.77 mg, depending on the compound and experiment) and dry KBr (180−300 mg, depending on the experiment, purchased from Merck and stored in a compartment dryer at 70 °C) were ground to a homogeneous mixture. The mixture was sintered inside an evacuable pellet die (Ø = 13 mm) at a pressure of 7.5 kbar for at least 3 min. Preparation of solutions under an inert-gas atmosphere: All solvents used were purchased of Uvasol grade (if available). Degassed solvent was prepared freshly by the commonly used Pump-Freeze procedure on the same day as the experiment. The isolated compound was dissolved in the degassed solvent to a solution of $c = 2 \times 10^{-5}$ M. The solutions were transferred to a (inert-gas) cuvette under a gentle stream of Ar gas.

Quantum Chemical Calculations (DFT). The crystal structures of the respective complexes were used as a starting geometry for the geometry optimization. The Berny algorithm implemented in Gaussian 09 was used in combination with energies and gradients calculated by Turbomole 7.4. All calculations were performed by using the hybrid functional B3LYP and the dev2-TZVP basis set for all atoms. Electronic core potentials were used for Mo and W. The electrostatic interactions with the solvent or KBr matrix were modeled by the COSMO. The vibrational frequencies were scaled by a factor of 0.99 (KBr matrix) or 0.975 (solvents). A Gaussian convolution with full width at half-maximum of 4 cm^{-1} was applied to generate the calculated IR spectra presented. The absorbance spectra were generated using the linear excitations derived from TD-DFT calculations on the geometrically optimized ground states corrected for solvent effects using COSMO. The presented spectra are generated with the full width at half-maximum set to 1500 cm^{-1}. For the computation of all intermediates and photoproducts, the optimized geometry of the starting complex was modified by removing a CO ligand or by replacing it with a solvent molecule. Another geometry optimization was performed thereafter using the same method as described above.

Absorption and Luminescence Spectroscopy. UV/vis Absorption. The absorption experiments were all performed using a Lambda 900 UV/vis spectrometer manufactured by PerkinElmer. The measurements in solution were carried out in different solvents (CH_3CN, CH_2Cl_2, DMSO, and PrCN) in a quartz cell cuvette of path length 1 cm. The spectra were recorded relative to those of the pure solvent. The solid-state reflectance spectra were recorded on the same spectrometer with a Praying Mantis diffuse reflectance accessory by Harrick installed inside the sample chamber.

Luminescence Spectroscopy. (Temperature-dependent) static luminescence spectra were recorded on a Horiba Jobin Yvon Fluorolog 3−22 τ. Excitation light was generated by a 450 W xenon short arc lamp and emission light detected by a R928 P photomultiplier detector (240 nm < λ_{em} < 850 nm). Double grating monochromators with 1200 grooves/mm and a 300 nm/500 nm blaze in the excitation and emission path were used to select/screen the desired wavelengths. The monochromators were calibrated to the 467 nm peak of the xenon lamp for the excitation pathway or to the Raman band of water for the emission pathway, respectively. The recorded spectra were corrected with a correction function that compensates for the varying detector sensitivities at different wavelengths. In order to avoid higher-order excitation light to be detected, long-pass filters were utilized taking the position of the emission peaks into account. Temperature-dependent measurements were carried out in a temperature range between 5 or 10 and 290 K with the sample being placed inside a closed-cycle helium cryostat equipped with either a pellet holder (ColdEdge, 101J cryocooler) or a cryo-cuvette holder (ARS Model DE-202A).

Time-Correlated Single Photon Counting. To obtain the luminescence lifetimes, a Horiba DeltaFlex spectrometer was used to count the single photons emitted by the sample with a picosecond photon counting detector module, including a fast-rise photomultiplier with an integral GHz timing preamplifier, a constant fraction discriminator, and a regulated high-voltage power supply. The sample was therefore excited by a pulsed NanoLED 345 (peak wavelength: 345 nm; pulse width: 1.3 ns). The scattered excitation light was suppressed by a long-pass filter (cut-on wavelength 540 nm for [Mo(**C−C**)] and 600 nm for [W(**C−C**)]) in the emission pathway. The measured decay data were fitted with monoexponential or biexponential fits using ORIGIN. Temperature-dependent measurements were performed with the ColdEdge 101J cryocooler described in the previous section.

Fluorescence Quantum Yields. Determination of luminescence quantum yields was performed as reported in previous publications.[28] Absolute UV/vis photoluminescence quantum yields of solid samples (KBr pellets) were measured in analogy to the procedures described by Wrighton *et al.* and latter Liu *et al.*, who measured fluorescence quantum yields with a conventional fluorescence spectrometer.[93,94] All spectra were recorded at room temperature on the Horiba Jobin Yvon Fluorolog 3−22 τ spectrometer described above, with the KBr pellets being mounted in a solid-state sample holder. The pellets were prepared as described above. The absorption of the complex was measured by considering the difference in area between the excitation light (λ_{ex} = 380 nm) scattered by a neat KBr pellet (J_0) and a pellet containing the complex (J).

For the luminescence, the area J_f under the emission curve was considered. The photoluminescence quantum yield ϕ was then calculated according to the following formula

https://doi.org/10.1021/acs.inorgchem.3c02478
Inorg. Chem. 2023, 62, 16182−16195

$$\Phi_{VIS} = \frac{J_f}{J_0 - J}$$

The error bars for the photoluminescence quantum yields are estimated to ±25% for the applied procedures according to literature.[4]

Time-Resolved FTIR Spectroscopy. All FTIR measurements were performed on a Bruker Vertex 80v. Signal detection and processing were performed by a mercury cadmium telluride detector (Kolmar Tech., Model KV100-1-B-7/190) connected to a preamplifier and a 14-bit transient recorder board (Spectrum Germany, Model M3I4142, 400 MS/s). Time-resolved rapid-scan FTIR was used to monitor the CO-cleavage/substitution reactions and the back-reaction. Excitation was induced by a pulsed Nd/YAG laser (Innolas SpitLight Evo I) with pulse energies between 1.0 and 5.0 mJ at a 100 Hz repetition rate and a bandwidth of around 7 ns, either by using an harmonic frequency directly or by introduction of a dye laser setup (Sirah Precision Scan, Pumpwellenlänge 355 nm, Coumarin 307 in methanol). Both during and after the irradiation period of 60 s, the FTIR experiment was repeated in well-defined time intervals. A sealed specac Omnicell cuvette with CaF_2 windows with an optical path length of 200 μm was used to hold the sample during this type of experiment. An IR long-pass filter (cutoff frequency of 2200 cm^{-1}) was used for all time-resolved measurements. Step-scan measurements were performed using an ARS cryostat, that is described in the previous sections. A Stanford research systems DG535 delay generator was used to time the experiment as well as to trigger the excitation laser. The measurement was initiated about 1.3 μs before the Nd/YAG laser pulse reached the sample. This time was set as the zero point for the experiment. The time resolution was set to 20 or 50 ns, respectively, depending on the expected lifetimes.

■ ASSOCIATED CONTENT

Supporting Information

The Supporting Information is available free of charge at https://pubs.acs.org/doi/10.1021/acs.inorgchem.3c02478.

Additional experimental details, ^1H and ^{13}C NMR spectra for all compounds, crystallographic details, photophysical measurements, time-resolved IR spectra, and density functional theory (PDF)

Accession Codes

CCDC 2075627 and 2075631 contain the supplementary crystallographic data for this paper. These data can be obtained free of charge via www.ccdc.cam.ac.uk/data_request/cif, or by emailing data_request@ccdc.cam.ac.uk, or by contacting The Cambridge Crystallographic Data Centre, 12 Union Road, Cambridge CB2 1EZ, UK; fax: +44 1223 336033.

■ AUTHOR INFORMATION

Corresponding Author

Biprajit Sarkar − *Institut für Anorganische Chemie, Universität Stuttgart, Stuttgart D-70569, Germany; Institut für Chemie und Biochemie, Freie Universität Berlin, Berlin 14195, Germany;* orcid.org/0000-0003-4887-7277; Email: biprajit.sarkar@iac.uni-stuttgart.de

Authors

Tobias Bens − *Institut für Anorganische Chemie, Universität Stuttgart, Stuttgart D-70569, Germany; Institut für Chemie und Biochemie, Freie Universität Berlin, Berlin 14195, Germany*

Daniel Marhöfer − *Department of Chemistry and Research Center Optimas, TU Kaiserslautern, Kaiserslautern 67663, Germany*

Pit Boden − *Department of Chemistry and Research Center Optimas, TU Kaiserslautern, Kaiserslautern 67663, Germany*

Sophie T. Steiger − *Department of Chemistry and Research Center Optimas, TU Kaiserslautern, Kaiserslautern 67663, Germany*

Lisa Suntrup − *Institut für Chemie und Biochemie, Freie Universität Berlin, Berlin 14195, Germany*

Gereon Niedner-Schatteburg − *Department of Chemistry and Research Center Optimas, TU Kaiserslautern, Kaiserslautern 67663, Germany;* orcid.org/0000-0001-7240-6673

Complete contact information is available at: https://pubs.acs.org/10.1021/acs.inorgchem.3c02478

Author Contributions

T.B. and B.S. designed the project. The synthesis and complete characterization of all the complexes were performed by T.B. The photochemical/photophysical measurements and theoretical calculation were performed by D.M., P.B. and S.T.S. The data interpretation of the aforementioned methods was carried out by D.M. and G.N.S. with inputs from T.B. The manuscript was written by T.B., B.S., and D.M. with contributions from all the authors. L.S. was responsible for the single-crystal X-ray diffraction data. T.B. and D.M. contributed equally.

Notes

The authors declare no competing financial interest.

■ ACKNOWLEDGMENTS

We thank B. Förtsch for elemental analyses and Dr. W. Frey (Institut für Organische Chemie) for collecting the X-ray data sets and the support by the state of Baden-Württemberg through bwHPC and the German Research Foundation (DFG) through grant no. INST 40/575-1 FUGG (JUSTUS 2 cluster). We acknowledge the German Science Foundation (DFG, Priority Program SPP 2102 "Light-controlled reactivity of metal complexes", SA 1840/7-1 and SA 1840/7-2) for financial support.

■ REFERENCES

(1) Damrauer, N. H.; Cerullo, G.; Yeh, A.; Boussie, T. R.; Shank, C. V.; McCusker, J. K. Femtosecond Dynamics of Excited-State Evolution in $[Ru(bpy)_3]^{2+}$. *Science* **1997**, *275* (5296), 54−57.

(2) Thompson, D. W.; Ito, A.; Meyer, T. J. $[Ru(bpy)_3]^{2+*}$ and other remarkable metal-to-ligand charge transfer (MLCT) excited states. *Pure Appl. Chem.* **2013**, *85* (7), 1257−1305.

(3) Chi, Y.; Chou, P.-T. Contemporary progresses on neutral, highly emissive Os(II) and Ru(II) complexes. *Chem. Soc. Rev.* **2007**, *36* (9), 1421−1431.

(4) Kumaresan, D.; Shankar, K.; Vaidya, S.; Schmehl, R. H. Photochemistry and Photophysics of Coordination Compounds: Osmium. In *Photochemistry and Photophysics of Coordination Compounds II*; Balzani, V., Campagna, S., Eds.; *Topics in Current Chemistry*; Springer Berlin Heidelberg, 2007; pp 101−142.

(5) Flamigni, L.; Barbieri, A.; Sabatini, C.; Ventura, B.; Barigelletti, F. Photochemistry and Photophysics of Coordination Compounds: Iridium. In *Photochemistry and Photophysics of Coordination Compounds II*; Balzani, V., Campagna, S., Eds.; *Topics in Current Chemistry*; Springer Berlin Heidelberg, 2007; pp 143−203.

(6) Chi, Y.; Chang, T.-K.; Ganesan, P.; Rajakannu, P. Emissive bis-tridentate Ir(III) metal complexes: Tactics, photophysics and applications. *Coord. Chem. Rev.* **2017**, *346*, 91−100.

(7) Lee, S.; Han, W.-S. Cyclometalated Ir(III) complexes towards blue-emissive dopant for organic light-emitting diodes: fundamentals of photophysics and designing strategies. *Inorg. Chem. Front.* **2020**, *7* (12), 2396−2422.

(8) Kirgan, R. A.; Sullivan, B. P.; Rillema, D. P. Photochemistry and Photophysics of Coordination Compounds: Rhenium. In *Photo-*

https://doi.org/10.1021/acs.inorgchem.3c02478
Inorg. Chem. 2023, 62, 16182−16195

chemistry and Photophysics of Coordination Compounds II; Balzani, V., Campagna, S., Eds.; *Topics in Current Chemistry*; Springer Berlin Heidelberg, 2007; pp 45−100.
(9) Sato, S.; Ishitani, O. Photochemical reactions of fac-rhenium(I) tricarbonyl complexes and their application for synthesis. *Coord. Chem. Rev.* **2015**, *282*−*283*, 50−59.
(10) Zhao, G.-W.; Zhao, J.-H.; Hu, Y.-X.; Zhang, D.-Y.; Li, X. Recent advances of neutral rhenium(I) tricarbonyl complexes for application in organic light-emitting diodes. *Synth. Met.* **2016**, *212*, 131−141.
(11) Förster, C.; Heinze, K. Photophysics and photochemistry with Earth-abundant metals - fundamentals and concepts. *Chem. Soc. Rev.* **2020**, *49* (4), 1057−1070.
(12) Sinha, N.; Wenger, O. S. Photoactive Metal-to-Ligand Charge Transfer Excited States in $3d^6$ Complexes with Cr^0, Mn^I, Fe^{II}, and Co^{III}. *J. Am. Chem. Soc.* **2023**, *145* (9), 4903−4920.
(13) Wegeberg, C.; Wenger, O. S. Luminescent First-Row Transition Metal Complexes. *JACS Au* **2021**, *1* (11), 1860−1876.
(14) Wenger, O. S. Photoactive Complexes with Earth-Abundant Metals. *J. Am. Chem. Soc.* **2018**, *140* (42), 13522−13533.
(15) Wenger, O. S. Is Iron the New Ruthenium? *Chem.—Eur. J.* **2019**, *25* (24), 6043−6052.
(16) Chábera, P.; Liu, Y.; Prakash, O.; Thyrhaug, E.; Nahhas, A. E.; Honarfar, A.; Essén, S.; Fredin, L. A.; Harlang, T. C. B.; Kjær, K. S.; Handrup, K.; Ericson, F.; Tatsuno, H.; Morgan, K.; Schnadt, J.; Häggström, L.; Ericsson, T.; Sobkowiak, A.; Lidin, S.; Huang, P.; Styring, S.; Uhlig, J.; Bendix, J.; Lomoth, R.; Sundström, V.; Persson, P.; Wärnmark, K. A low-spin Fe(III) complex with 100-ps ligand-to-metal charge transfer photoluminescence. *Nature* **2017**, *543* (7647), 695−699.
(17) Kitzmann, W. R.; Moll, J.; Heinze, K. Spin-flip luminescence. *Photochem. Photobiol. Sci.* **2022**, *21* (7), 1309−1331.
(18) Steube, J.; Kruse, A.; Bokareva, O. S.; Reuter, T.; Demeshko, S.; Schoch, R.; Argüello Cordero, M. A.; Krishna, A.; Hohloch, S.; Meyer, F.; Heinze, K.; Kühn, O.; Lochbrunner, S.; Bauer, M. Janus-type emission from a cyclometalated iron(III) complex. *Nat. Chem.* **2023**, *15*, 468−474.
(19) Büldt, L. A.; Wenger, O. S. Chromium(0), Molybdenum(0), and Tungsten(0) Isocyanide Complexes as Luminophores and Photosensitizers with Long-Lived Excited States. *Angew. Chem., Int. Ed. Engl.* **2017**, *56* (21), 5676−5682.
(20) Tang, M.; Cameron, L.; Poland, E. M.; Yu, L.-J.; Moggach, S. A.; Fuller, R. O.; Huang, H.; Sun, J.; Thickett, S. C.; Massi, M.; Coote, M. L.; Ho, C. C.; Bissember, A. C. Photoactive Metal Carbonyl Complexes Bearing N-Heterocyclic Carbene Ligands: Synthesis, Characterization, and Viability as Photoredox Catalysts. *Inorg. Chem.* **2022**, *61* (4), 1888−1898.
(21) Sattler, W.; Ener, M. E.; Blakemore, J. D.; Rachford, A. A.; LaBeaume, P. J.; Thackeray, J. W.; Cameron, J. F.; Winkler, J. R.; Gray, H. B. Generation of Powerful Tungsten Reductants by Visible Light Excitation. *J. Am. Chem. Soc.* **2013**, *135* (29), 10614−10617.
(22) Fajardo, J.; Schwan, J.; Kramer, W. W.; Takase, M. K.; Winkler, J. R.; Gray, H. B. Third-Generation $W(CNAr)_6$ Photoreductants (CNAr = Fused-Ring and Alkynyl-Bridged Arylisocyanides). *Inorg. Chem.* **2021**, *60* (6), 3481−3491.
(23) Sattler, W.; Henling, L. M.; Winkler, J. R.; Gray, H. B. Bespoke Photoreductants: Tungsten Arylisocyanides. *J. Am. Chem. Soc.* **2015**, *137* (3), 1198−1205.
(24) Kvapilová, H.; Sattler, W.; Sattler, A.; Sazanovich, I. V.; Clark, I. P.; Towrie, M.; Gray, H. B.; Záliš, S.; Vlček, A. Electronic Excited States of Tungsten(0) Arylisocyanides. *Inorg. Chem.* **2015**, *54* (17), 8518−8528.
(25) Büldt, L. A.; Guo, X.; Vogel, R.; Prescimone, A.; Wenger, O. S. A Tris(diisocyanide)chromium(0) Complex Is a Luminescent Analog of $Fe(2,2'\text{-Bipyridine})_3^{2+}$. *J. Am. Chem. Soc.* **2017**, *139* (2), 985−992.
(26) Herr, P.; Glaser, F.; Büldt, L. A.; Larsen, C. B.; Wenger, O. S. Long-Lived, Strongly Emissive, and Highly Reducing Excited States in Mo(0) Complexes with Chelating Isocyanides. *J. Am. Chem. Soc.* **2019**, *141* (36), 14394−14402.
(27) Wegeberg, C.; Häussinger, D.; Wenger, O. S. Pyrene-Decoration of a Chromium(0) Tris(diisocyanide) Enhances Excited State Delocalization: A Strategy to Improve the Photoluminescence of $3d^6$ Metal Complexes. *J. Am. Chem. Soc.* **2021**, *143* (38), 15800−15811.
(28) Boden, P.; Di Martino-Fumo, P.; Bens, T.; Steiger, S.; Albold, U.; Niedner-Schatteburg, G.; Gerhards, M.; Sarkar, B. NIR-Emissive Chromium(0), Molybdenum(0), and Tungsten(0) Complexes in the Solid State at Room Temperature. *Chem.—Eur. J.* **2021**, *27* (51), 12959−12964.
(29) Lees, A. J. Luminescence properties of organometallic complexes. *Chem. Rev.* **1987**, *87* (4), 711−743.
(30) McHugh, T. M.; Narayanaswamy, R.; Rest, A. J.; Salisbury, K. Luminescence spectra of group 6 metal carbonyls and substituted carbonyls in frozen gas matrices at 12 K. *J. Chem. Soc., Chem. Commun.* **1979**, No. 5, 208.
(31) Stufkens, D. J. Spectroscopy, photophysics and photochemistry of zerovalent transition metal α-diimine complexes. *Coord. Chem. Rev.* **1990**, *104* (1), 39−112.
(32) Farrell, I. R.; van Slageren, J.; Záliš, S.; Vlček, A. Time-resolved emission spectra and TD-DFT excited-state calculations of $[W(CO)_4(1,10\text{-phenanthroline})]$ and $[W(CO)_4(3,4,7,8\text{-tetramethyl-}1,10\text{-phenanthroline})]$. *Inorg. Chim. Acta* **2001**, *315* (1), 44−52.
(33) Manuta, D. M.; Lees, A. J. Emission and photochemistry of $M(CO)_4$(diimine) (M = chromium, molybdenum, tungsten) complexes in room-temperature solution. *Inorg. Chem.* **1986**, *25* (9), 1354−1359.
(34) Rawlins, K. A.; Lees, A. J. Photophysical properties of $M(CO)_4$(a,a.'-diimine) (M = molybdenum, tungsten) complexes. *Inorg. Chem.* **1989**, *28* (11), 2154−2160.
(35) Servaas, P. C.; van Dijk, H. K.; Snoeck, T. L.; Stufkens, D. J.; Oskam, A. Relationship between the emission spectra and resonance Raman excitation profiles of $W(CO)_4$(a-diimine) complexes. *Inorg. Chem.* **1985**, *24* (26), 4494−4498.
(36) Wrighton, M.; Morse, D. L. Nature of the lowest excited state in tricarbonylchloro-1,10-phenanthrolinerhenium(I) and related complexes. *J. Am. Chem. Soc.* **1974**, *96* (4), 998−1003.
(37) Vlček, A., Jr. Highlights of the spectroscopy, photochemistry and electrochemistry of $[M(CO)_4(\alpha\text{-diimine})]$ complexes, M = Cr, Mo, W. *Coord. Chem. Rev.* **2002**, *230* (1−2), 225−242.
(38) Balk, R. W.; Snoeck, T.; Stufkens, D. J.; Oskam, A. (Diimine)carbonyl complexes of chromium, molybdenum, and tungsten: relationship between resonance Raman spectra and photosubstitution quantum yields upon excitation within the lowest metal to diimine charge-transfer band. *Inorg. Chem.* **1980**, *19* (10), 3015−3021.
(39) Dahlgren, R. M.; Zink, J. I. Photochemistry and spectroscopy of monosubstituted derivatives of tungsten hexacarbonyl which exhibit low-efficiency photoreactivities. *J. Am. Chem. Soc.* **1979**, *101* (6), 1448−1454.
(40) Dobson, G. R.; El Sayed, M. F. A.; Stolz, I. W.; Sheline, R. K. Photochemical Formation of Some Metal Hexacarbonyl-Acetonitrile Derivatives. *Inorg. Chem.* **1962**, *1* (3), 526−530.
(41) Graham, M. A.; Poliakoff, M.; Turner, J. J. Photochemistry of the group VI hexacarbonyls in low temperature matrices. Part I. The pentacarbonyls of chromium, molybdenum, and tungsten. *J. Chem. Soc., A* **1971**, 2939−2948.
(42) Panesar, R. S.; Dunwoody, N.; Lees, A. J. Wavelength-Dependent Photochemistry of $W(CO)_4$(en) (en = Ethylenediamine): Evidence for Distinct Chemical Reactivities from Singlet and Triplet Ligand Field Excited States. *Inorg. Chem.* **1998**, *37* (7), 1648−1650.
(43) Stolz, I. W.; Dobson, G. R.; Sheline, R. K. The Infrared Spectrum and Evidence for the Structure of a New Metal Carbonyl. *J. Am. Chem. Soc.* **1962**, *84* (18), 3589−3590.
(44) Wieland, S.; Reddy, K. B.; van Eldik, R. Ligand-field and charge-transfer photochemistry of $M(CO)_4$(1,10-phenanthroline) (M = chromium, molybdenum, tungsten). Mechanistic information from high-pressure effects. *Organometallics* **1990**, *9* (6), 1802−1806.

https://doi.org/10.1021/acs.inorgchem.3c02478
Inorg. Chem. 2023, 62, 16182−16195

(45) Wrighton, M. Photochemistry of metal carbonyls. *Chem. Rev.* **1974**, *74* (4), 401−430.
(46) Zhu, L.; Saha, S.; Wang, Y.; Keszler, D. A.; Fang, C. Monitoring Photochemical Reaction Pathways of Tungsten Hexacarbonyl in Solution from Femtoseconds to Minutes. *J. Phys. Chem. B* **2016**, *120* (51), 13161−13168.
(47) Boden, P. J.; Di Martino-Fumo, P.; Bens, T.; Steiger, S. T.; Marhöfer, D.; Niedner-Schatteburg, G.; Sarkar, B. Mechanistic and Kinetic Investigations of ON/OFF (Photo)Switchable Binding of Carbon Monoxide by Chromium(0), Molybdenum(0) and Tungsten(0) Carbonyl Complexes with a Pyridyl-Mesoionic Carbene Ligand. *Chem.—Eur. J.* **2022**, *28* (51), No. e202201038.
(48) Bens, T.; Boden, P.; Di Martino-Fumo, P.; Beerhues, J.; Albold, U.; Sobottka, S.; Neuman, N. I.; Gerhards, M.; Sarkar, B. Chromium(0) and Molydenum(0) Complexes with a Pyridyl-Mesoionic Carbene Ligand: Structural, (Spectro)electrochemical, Photochemical, and Theoretical Investigations. *Inorg. Chem.* **2020**, *59* (20), 15504−15513.
(49) Cao, L.; Huang, S.; Liu, W.; Zhao, H.; Xiong, X.-G.; Zhang, J.-P.; Fu, L.-M.; Yan, X. Thermally Activated Delayed Fluorescence from d^{10} -Metal Carbene Complexes through Intermolecular Charge Transfer and Multicolor Emission with a Monomer-Dimer Equilibrium. *Chem.—Eur. J.* **2020**, *26* (71), 17222−17229.
(50) Dierks, P.; Kruse, A.; Bokareva, O. S.; Al-Marri, M. J.; Kalmbach, J.; Baltrun, M.; Neuba, A.; Schoch, R.; Hohloch, S.; Heinze, K.; Seitz, M.; Kühn, O.; Lochbrunner, S.; Bauer, M. Distinct photodynamics of κ-N and κ-C pseudoisomeric iron(II) complexes. *Chem. Commun.* **2021**, *57* (54), 6640−6643.
(51) Hettmanczyk, L.; Spall, S. J. P.; Klenk, S.; van der Meer, M.; Hohloch, S.; Weinstein, J. A.; Sarkar, B. Structural, Electrochemical, and Photochemical Properties of Mono- and Digold(I) Complexes Containing Mesoionic Carbenes. *Eur. J. Inorg. Chem.* **2017**, *2017* (14), 2112−2121.
(52) Kleinhans, G.; Chan, A. K.-W.; Leung, M.-Y.; Liles, D. C.; Fernandes, M. A.; Yam, V. W.-W.; Fernández, I.; Bezuidenhout, D. I. Synthesis and Photophysical Properties of T-Shaped Coinage-Metal Complexes. *Chem.—Eur. J.* **2020**, *26* (31), 6993−6998.
(53) Maity, R.; Sarkar, B. Chemistry of Compounds Based on 1,2,3-Triazolylidene-Type Mesoionic Carbenes. *JACS Au* **2022**, *2* (1), 22−57.
(54) Matteucci, E.; Monti, F.; Mazzoni, R.; Baschieri, A.; Bizzarri, C.; Sambri, L. Click-Derived Triazolylidenes as Chelating Ligands: Achievement of a Neutral and Luminescent Iridium(III)-Triazolide Complex. *Inorg. Chem.* **2018**, *57* (18), 11673−11686.
(55) Nair, S. S.; Bysewski, O. A.; Kupfer, S.; Wächtler, M.; Winter, A.; Schubert, U. S.; Dietzek, B. Excitation Energy-Dependent Branching Dynamics Determines Photostability of Iron(II)-Mesoionic Carbene Complexes. *Inorg. Chem.* **2021**, *60* (12), 9157−9173.
(56) Naziruddin, A. R.; Lee, C.-S.; Lin, W.-J.; Sun, B.-J.; Chao, K.-H.; Chang, A. H. H.; Hwa8ng, W.-S. Platinum complexes bearing normal and mesoionic N-heterocyclic carbene based pincer ligands: syntheses, structures, and photo-functional attributes. *Dalton Trans.* **2016**, *45* (13), 5848−5859.
(57) Pinter, P.; Schüßlbauer, C. M.; Watt, F. A.; Dickmann, N.; Herbst-Irmer, R.; Morgenstern, B.; Grünwald, A.; Ullrich, T.; Zimmer, M.; Hohloch, S.; Guldi, D. M.; Munz, D. Bright luminescent lithium and magnesium carbene complexes. *Chem. Sci.* **2021**, *12* (21), 7401−7410.
(58) Sarkar, B.; Suntrup, L. Illuminating Iron: Mesoionic Carbenes as Privileged Ligands in Photochemistry. *Angew. Chem., Int. Ed.* **2017**, *56* (31), 8938−8940.
(59) Soellner, J.; Strassner, T. Diaryl-1,2,3-Triazolylidene Platinum-(II) Complexes. *Chem.—Eur. J.* **2018**, *24* (21), 5584−5590.
(60) Suntrup, L.; Stein, F.; Hermann, G.; Kleoff, M.; Kuss-Petermann, M.; Klein, J.; Wenger, O. S.; Tremblay, J. C.; Sarkar, B. Influence of Mesoionic Carbenes on Electro- and Photoactive Ru and Os Complexes: A Combined (Spectro-)Electrochemical, Photochemical, and Computational Study. *Inorg. Chem.* **2018**, *57* (21), 13973−13984.
(61) Suntrup, L.; Stein, F.; Klein, J.; Wilting, A.; Parlane, F. G. L.; Brown, C. M.; Fiedler, J.; Berlinguette, C. P.; Siewert, I.; Sarkar, B. Rhenium Complexes of Pyridyl-Mesoionic Carbenes: Photochemical Properties and Electrocatalytic CO_2 Reduction. *Inorg. Chem.* **2020**, *59* (7), 4215−4227.
(62) Verma, S. K.; Kumari, P.; Ansari, S. N.; Ansari, M. O.; Deori, D.; Mobin, S. M. A novel mesoionic carbene based highly fluorescent Pd(II) complex as an endoplasmic reticulum tracker in live cells. *Dalton Trans.* **2018**, *47* (44), 15646−15650.
(63) Vivancos, Á.; Jiménez-García, A.; Bautista, D.; González-Herrero, P. Strongly Luminescent Pt(IV) Complexes with a Mesoionic N-Heterocyclic Carbene Ligand: Tuning Their Photophysical Properties. *Inorg. Chem.* **2021**, *60* (11), 7900−7913.
(64) Liu, Y.; Kjaer, K. S.; Fredin, L. A.; Chábera, P.; Harlang, T.; Canton, S. E.; Lidin, S.; Zhang, J.; Lomoth, R.; Bergquist, K.-E.; Persson, P.; Wärnmark, K.; Sundström, V. A Heteroleptic Ferrous Complex with Mesoionic Bis(1,2,3-triazol-5-ylidene) Ligands: Taming the MLCT Excited State of Iron(II). *Chem.—Eur. J.* **2015**, *21* (9), 3628−3639.
(65) Brown, D. G.; Sanguantrakun, N.; Schulze, B.; Schubert, U. S.; Berlinguette, C. P. Bis(tridentate) Ruthenium-Terpyridine Complexes Featuring Microsecond Excited-State Lifetimes. *J. Am. Chem. Soc.* **2012**, *134* (30), 12354−12357.
(66) Leigh, V.; Ghattas, W.; Lalrempuia, R.; Müller-Bunz, H.; Pryce, M. T.; Albrecht, M. Synthesis, Photo-and Electrochemistry of Ruthenium Bis(bipyridine) Complexes Comprising a N-heterocyclic Carbene Ligand. *Inorg. Chem.* **2013**, *52* (9), 5395−5402.
(67) Schulze, B.; Escudero, D.; Friebe, C.; Siebert, R.; Görls, H.; Köhn, U.; Altuntas, E.; Baumgaertel, A.; Hager, M. D.; Winter, A.; Dietzek, B.; Popp, J.; González, L.; Schubert, U. S. A Heteroleptic Bis(tridentate) Ruthenium(II) Complex of a Click-Derived Abnormal Carbene Pincer Ligand with Potential for Photosensitzer Application. *Chem.—Eur. J.* **2011**, *17* (20), 5494−5498.
(68) Sinn, S.; Schulze, B.; Friebe, C.; Brown, D. G.; Jäger, M.; Altuntaş, E.; Kübel, J.; Guntner, O.; Berlinguette, C. P.; Dietzek, B.; Schubert, U. S. Physicochemical Analysis of Ruthenium(II) Sensitizers of 1,2,3-Triazole-Derived Mesoionic Carbene and Cyclometalating Ligands. *Inorg. Chem.* **2014**, *53* (4), 2083−2095.
(69) Soellner, J.; Císařová, I.; Strassner, T. Ruthenium(II) Bipyridyl Complexes with ĈC* Cyclometalated Mesoionic Carbene Ligands. *Organometallics* **2018**, *37* (24), 4619−4629.
(70) Baschieri, A.; Monti, F.; Matteucci, E.; Mazzanti, A.; Barbieri, A.; Armaroli, N.; Sambri, L. A Mesoionic Carbene as Neutral Ligand for Phosphorescent Cationic Ir(III) Complexes. *Inorg. Chem.* **2016**, *55* (16), 7912−7919.
(71) Karmis, R. E.; Carrara, S.; Baxter, A. A.; Hogan, C. F.; Hulett, M. D.; Barnard, P. J. Luminescent iridium(iii) complexes of N-heterocyclic carbene ligands prepared using the 'click reaction'. *Dalton Trans.* **2019**, *48* (27), 9998−10010.
(72) Topchiy, M. A.; Dzhevakov, P. B.; Kirilenko, N. Y.; Rzhevskiy, S. A.; Ageshina, A. A.; Khrustalev, V. N.; Paraschuk, D. Y.; Bermeshev, M. V.; Nechaev, M. S.; Asachenko, A. F. Cyclometallated 1,2,3-triazol-5-ylidene iridium(III) complexes: synthesis, structure, and photoluminescence properties. *Mendeleev Commun.* **2019**, *29* (2), 128−131.
(73) Urinda, S.; Das, G.; Pramanik, A.; Sarkar, P. Essential Role of Ancillary Ligand in Color Tuning and Quantum Efficiency of Ir(III) Complexes with N-Heterocyclic or Mesoionic Carbene Ligand: A Comparative Quantum Chemical Study. *J. Phys. Chem. A* **2018**, *122* (38), 7532−7539.
(74) Soellner, J.; Strassner, T. Cyclometalated Platinum(II) Complexes with Mesoionic Dibenzofuranyl-1,2,3-triazol-4-ylidene Ligands: Synthesis, Characterization and Photophysical Properties. *ChemPhotoChem.* **2019**, *3* (7), 554−558.
(75) Vivancos, Á.; Bautista, D.; González-Herrero, P. Luminescent Platinum(IV) Complexes Bearing Cyclometalated 1,2,3-Triazolylidene and Bi- or Terdentate 2,6-Diarylpyridine Ligands. *Chem.—Eur. J.* **2019**, *25* (23), 6014−6025.
(76) Monticelli, M.; Baron, M.; Tubaro, C.; Bellemin-Laponnaz, S.; Graiff, C.; Bottaro, G.; Armelao, L.; Orian, L. Structural and

https://doi.org/10.1021/acs.inorgchem.3c02478
Inorg. Chem. 2023, 62, 16182−16195

Luminescent Properties of Homoleptic Silver(I), Gold(I), and Palladium(II) Complexes with nNHC-tzNHC Heteroditopic Carbene Ligands. *ACS Omega* **2019**, *4* (2), 4192−4205.
(77) Bens, T.; Walter, R. R. M.; Beerhues, J.; Schmitt, M.; Krossing, I.; Sarkar, B. The Best of Both Worlds: Combining the Power of MICs and WCAs to generate Stable and Crystalline Cr^{I}-tetracarbonyl Complexes with π-Accepting Ligands. *Chem.—Eur. J.* **2023**, *29*, No. e202301205.
(78) Lee, J. J.; Yap, C. P.; Chwee, T. S.; Fan, W. Y. Highly-phosphorescent tungsten(0) carbonyl pyridyl-imidazole complexes as photosensitisers. *Dalton Trans.* **2017**, *46* (33), 11008−11012.
(79) Felder, D.; Nierengarten, J. F.; Barigelletti, F.; Ventura, B.; Armaroli, N. Highly Luminescent Cu(I)-Phenanthroline Complexes in Rigid Matrix and Temperature Dependence of the Photophysical Properties. *J. Am. Chem. Soc.* **2001**, *123* (26), 6291−6299.
(80) Lees, A. J. The Luminescence Rigidochromic Effect Exhibited by Organometallic Complexes: Rationale and Applications. *Comments Inorg. Chem.* **1995**, *17* (6), 319−346.
(81) Mohankumar, M.; Holler, M.; Meichsner, E.; Nierengarten, J.-F.; Niess, F.; Sauvage, J.-P.; Delavaux-Nicot, B.; Leoni, E.; Monti, F.; Malicka, J. M.; Cocchi, M.; Bandini, E.; Armaroli, N. Heteroleptic Copper(I) Pseudorotaxanes Incorporating Macrocyclic Phenanthroline Ligands of Different Sizes. *J. Am. Chem. Soc.* **2018**, *140* (6), 2336−2347.
(82) Fry, H. C.; Lucas, H. R.; Narducci Sarjeant, A. A.; Karlin, K. D.; Meyer, G. J. Carbon Monoxide Coordination and Reversible Photodissociation in Copper(I) Pyridylalkylamine Compounds. *Inorg. Chem.* **2008**, *47* (1), 241−256.
(83) Vlček, A., Jr.; Farrell, I. R.; Liard, D. J.; Matousek, P.; Towrie, M.; Parker, A. W.; Grills, D. C.; George, M. W. Early photochemical dynamics of organometallic compounds studied by ultrafast time-resolved spectroscopic techniquesBased on the presentation given at Dalton Discussion No. 4, 10−13th January 2002, Kloster Banz, Germany. *J. Chem. Soc., Dalton Trans.* **2002**, No. 5, 701−712.
(84) *The MERCK Index: An Encyclopedial of Chemical, Drugs and Biologicals*; Budavari, S., Ed., 11th ed.; Merck & Co, 1989.
(85) *APEX3*; Bruker AXS Inc, 2015.
(86) Sheldrick, G. M. *SHELXS-97 and SHELXL-97, Program for Crystal Structure Solution and Refinement*; University of Gottingen, 1997;.
(87) Sheldrick, G. M. *Program for Empirical Absorption Correction*; University of Göttingen, 2008;.
(88) Sheldrick, G. M. *Program for Crystal Structure Solution and Refinement*; University of Göttingen, 2014.
(89) Macrae, C. F.; Edgington, P. R.; McCabe, P.; Pidcock, E.; Shields, G. P.; Taylor, R.; Towler, M.; van de Streek, J. Mercury: visualization and analysis of crystal structures. *J. Appl. Crystallogr.* **2006**, *39* (3), 453−457.
(90) *SAINT+. Data Integration Engine*; Bruker AXS Inc., 1997−2012.
(91) Sheldrick, G. M. A short history of SHELX. *Acta Crystallogr.* **2008**, *64* (1), 112−122.
(92) Sheldrick, G. M. Crystal structure refinement with SHELXL. *Acta Cryst. C* **2015**, *71* (1), 3−8.
(93) Liu, Y. S.; de Mayo, P.; Ware, W. R. Photophysics of Polycyclic Aromatic Hydrocarbons Adsorbed on Silica Gel Surfaces. 3. Fluorescence Quantum Yields and Radiative Decay Rate Constants Derived from Lifetime Distributions. *J. Phys. Chem.* **1993**, *97* (22), 5995−6001.
(94) Wrighton, M. S.; Ginley, D. S.; Morse, D. L. Technique for the Determination of Absolute Emission Quantum Yields of Powdered Samples. *J. Phys. Chem.* **1974**, *78* (22), 2229−2233.

https://doi.org/10.1021/acs.inorgchem.3c02478
Inorg. Chem. 2023, 62, 16182−16195

3.6 Investigations on the Influence of Two Pyridyl-Mesoionic Carbene Constitutional Isomers on the Electrochemical and Spectroelectrochemical Properties of Group 6 Metal Carbonyl Complexes

Tobias Bens,[†,§] Biprajit Sarkar[†,§,*]

[†]Institut für Anorganische Chemie, Universität Stuttgart, Pfaffenwaldring 55, D-70569 Stuttgart, Germany, Email: biprajit.sarkar@iac.uni-stuttgart.de
[§]Institut für Chemie und Biochemie, Freie Universität Berlin, Fabeckstraße 34-36, 14195, Berlin, Germany.

This article was published and is reprinted with permission from MDPI:
T. Bens, B. Sarkar, *Inorganics* **2024**, *12*, 46.
DOI: 10.3390/inorganics12020046 (© 2024 Multidisciplinary Digital Publishing Institute)

The **Supporting Information** is available free of charge at https://www.mdpi.com/article/10.3390/inorganics12020046/s1.

Autor contribution: The project was designed by Biprajit Sarkar. The presented complexes were synthesized and fully characterized by Tobias Bens. All (spectro)electrochemical measurements were performed by Tobias Bens (as a part of the master thesis), including all electrochemical investigations in the presence of CO_2. The manuscript was written by Tobias Bens and Biprajit Sarkar.

inorganics

MDPI

Article

Investigations of the Influence of Two Pyridyl-Mesoionic Carbene Constitutional Isomers on the Electrochemical and Spectroelectrochemical Properties of Group 6 Metal Carbonyl Complexes

Tobias Bens [1,2] and Biprajit Sarkar [1,2,*]

[1] Institut für Anorganische Chemie, Universität Stuttgart, Pfaffenwaldring 55, 70569 Stuttgart, Germany; tobias.bens@uibk.ac.at
[2] Institut für Chemie und Biochemie, Freie Universität Berlin, Fabeckstraße 34–36, 14195 Berlin, Germany
* Correspondence: biprajit.sarkar@iac.uni-stuttgart.de

Abstract: Metal complexes of mesoionic carbenes (MICs) of the triazolylidene type and their derivatives have gained increasing attention in the fields of electrocatalysis and photochemistry. The redox activity of these metal complexes is critical for their applications in both the aforementioned fields. Easy accessibility and modular synthesis open a wide field for the design of ligands, such as bidentate ligands. The combination of an MIC with a pyridyl unit in a bidentate ligand setup increases the π acceptor properties of the ligands while retaining their strong σ donor properties. The analogy with the well-established 2,2′-bipyridine ligand allows conclusions to be drawn about the influence of the mesoionic carbene (MIC) moiety in tetracarbonyl group 6 complexes in cyclic voltammetry and (spectro)electrochemistry (SEC). However, the effects of the different connectivity in pyridyl-MIC ligands remain underexplored. Based on our previous studies, we present a thorough investigation of the influence of the two different pyridyl-MIC constitutional isomers on the electrochemical and the UV-vis-NIR/IR/EPR spectroelectrochemical properties of group 6 carbonyl complexes. Moreover, the presented complexes were investigated for the electrochemical conversion of CO_2 using two different working electrodes, providing a fundamental understanding of the influence of the electrode material in the precatalytic activation.

Keywords: mesoionic carbenes; (spectro)electrochemistry; carbonyl ligands; group 6 carbonyls; EPR spectroscopy

Citation: Bens, T.; Sarkar, B. Investigations of the Influence of Two Pyridyl-Mesoionic Carbene Constitutional Isomers on the Electrochemical and Spectroelectrochemical Properties of Group 6 Metal Carbonyl Complexes. *Inorganics* **2024**, *12*, 46. https://doi.org/10.3390/inorganics12020046

Academic Editors: Francis Verpoort and Axel Klein

Received: 23 November 2023
Revised: 26 December 2023
Accepted: 27 December 2023
Published: 29 January 2024

1. Introduction

In 2001, Sharpless and co-workers coined the term "click" chemistry to describe modular reactions with a wide scope and high yields, producing only mild inoffensive byproducts [1]. The azide–alkyne cycloaddition reaction is arguably one of the best examples of a click reaction. The thermally induced 1,3-dipolar cycloaddition between alkynes and azides results in a mixture of two regioisomers [2]. In 2002, two groups independently discovered the copper-catalyzed azide–alkyne cycloaddition reaction (CuAAC), generating exclusively the 1,4-regioisomer of 1,2,3-triazole [3,4].

The methylation of 1,2,3-triazoles leads to the formation of so-called triazolium salts in near quantitatively yields [5–7]. They represent one of the most important precursors for triazolylidenes, a class of carbenes that are better known as abnormal *N*-heterocyclic carbenes (aNHCs) or mesoionic carbenes (MICs). This classification arises from the fact that while following octet rules, no resonance structures can be drawn for MICs without charge separation, unlike their well-established *N*-heterocyclic carbene (NHC) counterparts [5,7–9]. Therefore, not surprisingly, the synthetic scope of MICs has expanded rapidly, opening up the possibility of introducing additional donor substituents, such as pyridine, to generate

Inorganics 2024, 12, 46

bidentate ligands [10–16] or post-modifications to *N*-heterocyclic olefins (NHOs) [17,18] and mesoionic imines (MIIs) [19,20], which are promising candidates for small molecule activation [5].

Suntrup et al. showed in 2017 that the insertion of a pyridyl moiety into 1,2,3-triazole- and 1,4-triazolylidene-based Re(I) carbonyl complexes drastically improves the overall π acceptor character of the ligand, while the incorporation of an MIC unit results in a greater σ donor strength compared to the well-established bpy ligand [21]. The robustness toward reductive electrochemistry provided the basis for the investigation of a series of pyridyl-MIC Re(I) complexes in the electrochemical reduction in CO_2 to generate CO with high selectivity and the study of their photophysical properties [16].

However, many of the most promising electrocatalysts explored contain expensive and rare metals, which preclude their large-scale applications [22–27]. In recent years, great efforts have been made to develop more earth-abundant photo- and electrocatalysts for the activation of small molecules based on carbenes [28–39].

Group 6 metal complexes are attractive candidates because of their natural occurrence, such as molybdenum in the active site of enzymes that convert CO_2 to formate [40].

Recent reports have shown that the isoelectronic and isostructural group 6 metal complexes of $[M(bpy)(CO)_4]$ (M = Cr, Mo, W) and $[M(L)(CO)_4]$ (L = "non-innocent" ligands) with Mo and W are capable of electrocatalytic conversion of CO_2 [28,29,33,36,37,39].

Tory et al. and Clark et al. reported the (spectro)electrochemical properties of group 6 complexes $[M(bpy\text{-}R)(CO)_4]$ (R = 5,5′ H, 5,5′ ^{t}Bu) and demonstrated their activity in CO_2 reduction on a gold (Au WE) and glassy carbon working electrode (GC WE), respectively [28,39]. The results indicate two important facts: first, the substitution of the bpy moiety results in a shift of the reduction potential for the precatalytic activation, and second, the change in the working electrode from a platinum working electrode (Pt WE) to a Au WE shifts the onset potential for electrocatalytic CO_2 reduction by +0.6 V, similar to what was reported for the group 7 electrocatalysts [25]. Based on these results, Neri et al. investigated the role of the electrode–catalyst interaction using vibrational sum frequency generation spectroscopy (VSFG), providing an insight into the mechanism at the electrode surface [36]. Cyclic voltammetric measurements with a Au WE show an equilibrium between the one-electron reduced species $[Mo(bpy)(CO)_4]^-$ and $[Mo(bpy)(CO)_3]^-$ after CO dissociation. In contrast, using a Pt WE, two-electron reduction is required to generate the precatalytically active species.

Recently, we have presented a series of two 1,4-pyidyl-MIC group 6 carbonyl complexes $[M(\mathbf{L})(CO)_4]$ (M = Cr, Mo, W) with two different constitutional isomers (**L**: **C–C** = pyridyl-4-triazolylidene [41] and **C–N** = pyridyl-1-triazolylidene [42–44]) that exhibit excellent photophysical and photochemical properties, making them suitable candidates in photo-induced small molecule activation [43–46]. For the first time, details of the influence of the two constitutional isomers were reported in the chemically and electrochemically oxidized $[Cr(\mathbf{L})CO)_4]^+$ complexes, providing detailed insights into the extraordinary σ donor properties [41]. In addition, a comprehensive study of precatalytic activation in [Rh(Cp*)] complexes for electrochemical H^+ reduction was reported, demonstrating the capability of small molecule activation with both ligands (Scheme 1) [47].

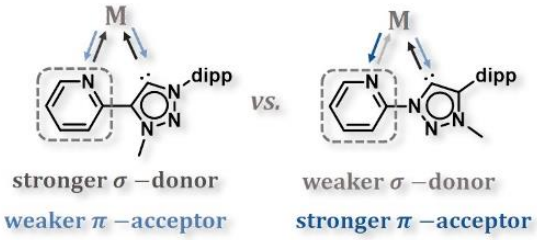

Scheme 1. Relative donor/acceptor strength of constitution isomers: **C–C** (**left**) and **C–N** (**right**).

Inorganics **2024**, *12*, 46

Based on our previous studies, we report a comprehensive electrochemical and spectroelectrochemical investigation of [M(**C–C**)(CO)$_4$] and [M(**C–N**)(CO)$_4$] [42] (M = Cr, Mo, W) to gain a fundamental understanding of the effects of the two constitutional isomers on their electronic structures and perform reactivity of the complexes in electrochemical CO_2 reduction as a function of the electrode material.

2. Results and Discussion

The triazolium salts, [H(**C–C**)](BF$_4$) [21] and [H(**C–N**)](Otf) [42], and the complexes, [M(**C–C**)(CO)$_4$] [41] and [M(**C–N**)(CO)$_4$] [42,43], were synthesized according to a previously reported protocol (Scheme 2).

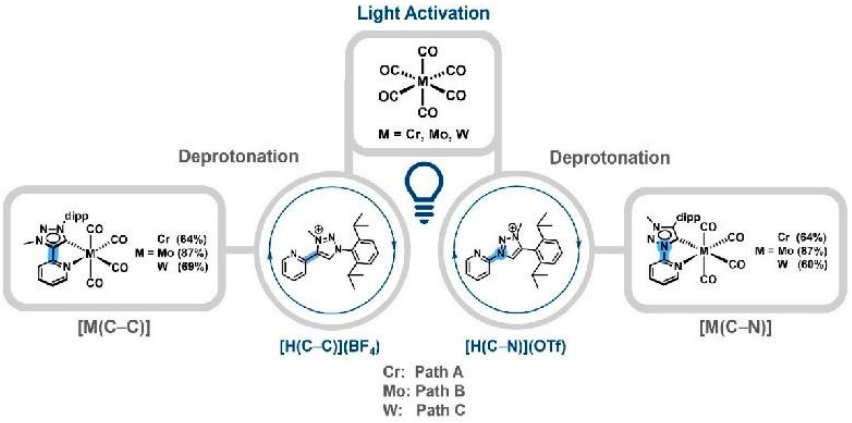

Scheme 2. Synthetic protocol for [M(**L**)CO)$_4$] (M = Cr, Mo, W; Path A [42], Path B [42], Path C [43]).

The light-induced activation of the corresponding [M(CO)$_6$] followed by the addition of [H(**C–C**)](BF$_4$) or [H(**C–N**)](OTf) and subsequent deprotonation with NEt$_3$ leads to the chromium and tungsten complexes, [M(**C–C**)(CO)$_4$] and [M(**C–N**)(CO)$_4$], after chromatographic workup and recrystallization, while in the case of molybdenum, the precursor [Mo(nbd)(CO)$_4$] (nbd = norbornadiene) was synthesized and further converted in the presence of a base to isolate [Mo(**C–C**)(CO)$_4$] or [Mo(**C–N**)(CO)$_4$], respectively.

2.1. Cyclic Voltammetry with a GC WE and EPR-SEC

The redox potentials measured from cyclic voltammetry are often, but not always, used for gauging the donor/acceptor properties of the ligands in metal complexes. A reversible metal-centered oxidation, as observed for [Cr(**C–C**)(CO)$_4$] [41] and [Cr(**C–N**)(CO)$_4$], [42] allows us to estimate the overall σ donor strength of the ligand, while a reversible ligand-centered reduction can be used to determine indirectly the π acceptor capacity of the ligand.

Previous reports from our group already established a stronger σ donor strength of the ligand in [Cr(**C–C**)(CO)$_4$] compared to [Cr(**C–N**)(CO)$_4$] [41,42]. The same trend in this regard is observed for the higher homologs, [M(**C–C**)(CO)$_4$] and [M(**C–N**)(CO)$_4$] (M = Mo, W). However, the oxidations of the respective complexes are irreversible as a consequence of the kinetic lability of the CO ligands and the possibility of forming complexes with higher coordination numbers in the oxidized complexes (Figure 1; see Supplementary Materials S6) [48,49]. The oxidation potentials follow the trend according to the ionization energy of the central metal atom (Cr > Mo > W) [50].

Inorganics **2024**, *12*, 46

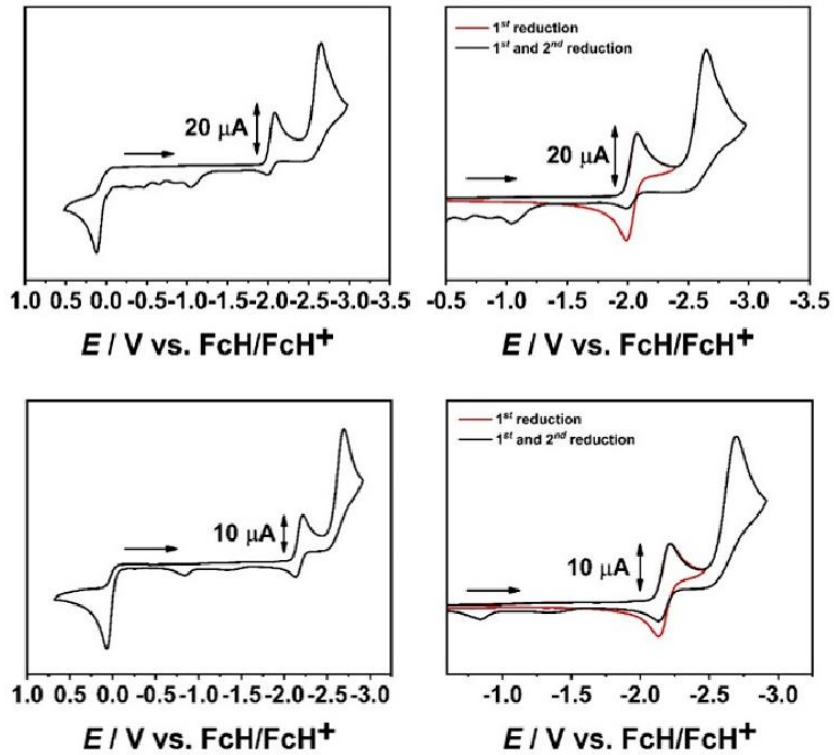

Figure 1. Cyclic voltammograms of [W(**C–C**)(CO)$_4$] (**top**) and [W(**C–N**)(CO)$_4$] (**bottom**) in CH_3CN and 0.1 M Bu_4NPF_6 at a scan rate of 100 mV/s and a glassy carbon working electrode.

All presented complexes, on the other hand, show a reversible first reduction, followed by a second irreversible reduction, whereas in the series of [M(**C–N**)(CO)$_4$], a third reduction process is observed at lower scan rates (Table 1; see Supplementary Materials S2) [42].

Table 1. Redox potentials of [M(**C–C**)(CO)$_4$] and [M(**C–N**)(CO)$_4$] (M = Cr, Mo, W) in CH_3CN and 0.1 M NBu_4PF_6 at 100 mV/s vs. FcH/FcH^+ (FcH = ferrocene) with a glassy carbon working electrode.

	1. Red./V		2. Red./V	1. Ox./V	
	$E_{1/2}^{red1}$	ΔE_p	E_p^{red2}	$E_{1/2}^{ox1}$	ΔE_p
[Cr(**C–C**)(CO)$_4$] [41]	−2.26	0.07	−2.80	−0.21	0.07
[Cr(**C–N**)(CO)$_4$] [42]	−2.16	0.07	−2.79	−0.17	0.07
[Mo(**C–C**)(CO)$_4$]	−2.21	0.07	−2.70	0.07 [a]	
[Mo(**C–N**)(CO)$_4$] [42]	−2.10	0.08	−2.68	0.08 [a]	
[W(**C–C**)(CO)$_4$]	−2.19	0.08	−2.69	0.07 [a]	
[W(**C–N**)(CO)$_4$]	−2.05	0.06	−2.65	0.12 [a]	

[a] $= E_p^{ox1}$.

The reduction potentials $E_{1/2}^{red1}$ presented in Table 1 are in good agreement with the aforementioned π acceptor properties of the constitutional isomers. In the case of [M(**C–N**)(CO)$_4$] (M = Cr, Mo, W), the first reduction is shifted to more anodic potential compared to [M(**C–C**)(CO)$_4$] (M = Cr, Mo, W), indicating the greater π acceptor ability of the **C–N** linked constitutional isomer in the complexes.

To obtain detailed insights into the electronic structure of the first reduction, electron paramagnetic resonance (spectro)electrochemistry (EPR-SEC) was performed with a Au WE in 0.1 M Bu_4NPF_6/CH_3CN (Figure 2 and Table 2; see Supplementary Materials S3).

Inorganics **2024**, *12*, 46

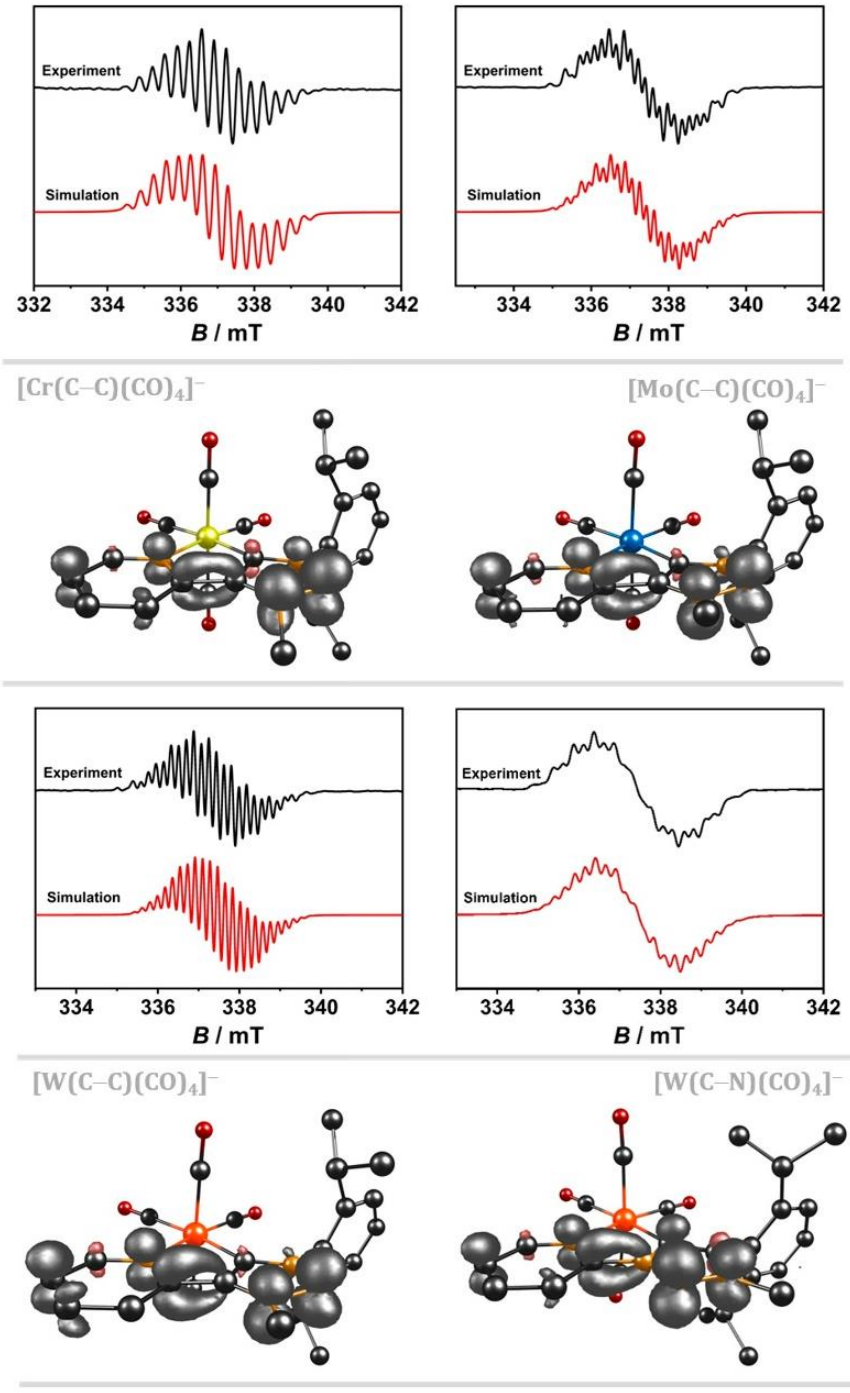

Figure 2. EPR spectrum and spin density plot (B3LYP/RIJCOSX/D3BJ/def2-TZVP, iso value = 0.006) of [Cr(**C–C**)] (**top left**), [Mo(**C–C**)] (**top right**), [W(**C–C**)] (**bottom left**), and [W(**C–N**)] (**bottom right**) in 0.1 M NBu_4PF_6/CH_3CN with a Au working electrode during the first reduction (black: experimental, red: simulation).

Table 2. EPR simulation data of $[M(\mathbf{C–N})(CO)_4]^-$ (M = Cr, Mo, W) and $[W(\mathbf{C–N})(CO)_4]^-$.

	$[\mathbf{Cr(C–C)}(CO)_4]^-$	$[\mathbf{Mo(C–C)}(CO)_4]^-$	$[\mathbf{W(C–C)}(CO)_4]^-$	$[\mathbf{W(C–N)}(CO)_4]^-$
g	2.0030	2.0033	2.0028	2.0032
AM	5.90	1.97	13.10	2.65
AN1	17.90	10.37	10.39	16.92
AN2	17.80	4.95	5.60	14.22
AN3	11.00	16.10	5.60	6.47
AN4	9.60	9.60	4.53	5.82
AH1	11.70	12.00	4.16	16.20
AH2	9.50	11.90	20.27	13.77
AH3	3.00	10.50	20.27	13.22
AH4	2.00	14.45	15.36	7.19
AH5	-	-	1.01	3.19
AH6	-	-	1.01	3.19
AH7	-	-	0.63	-
AH8	-	-	1.81	-
AH9	-	-	0.49	-
AH10	-	-	0.50	-
lwpp [a]/mT	[0 0.123]	[0 0.121]	[0 0.054]	[0 0.161]

[a] The first value corresponds to the Gaussian and the second to the Lorentzian shape.

Upon a reduction in room temperature, line-rich EPR spectra at $g = 2.003$ are observed for all complexes, showing hyperfine coupling to all four ^{14}N nuclei within the central pyridyl-MIC ligand framework (Table 2). The hyperfine coupling constants of the ^{14}N nuclei and the spin density plots of the respective complexes reveal a strong interaction of the electron spin with the N^2 and N^3 nuclei of the reduced 1,2,3-triazolylidene (MIC) moiety, and to a smaller extent, with the ^{14}N nuclei of the pyridyl-*N* and the N^1 nuclei of the MIC unit. Only in the case of $[W(\mathbf{C–C})]^-$ is a strong coupling to only one ^{14}N nucleus observed. A plausible explanation might be the stronger delocalization of the electron spin within the **C–C** isomer. The $[W(\mathbf{C–C})]^-$ complex shows ^1H hyperfine coupling to ten ^1H nuclei. In contrast, the analog $[Cr(\mathbf{C–C})(CO)_4]^-$ and $[Mo(\mathbf{C–C})(CO)_4]^-$ complexes display ^1H hyperfine coupling to four ^1H nuclei, which can be assigned to the pyridyl-*H*. The strong interaction of the electron spin within the pyridyl moiety is also present in $[W(\mathbf{C–C})(CO)_4]^-$. The complex shows a strong ^1H coupling constant to four ^1H nuclei, indicating a predominant localization within the central pyridyl-MIC framework. However, small hyperfine couplings with six additional ^1H nuclei are observed. Even though the spin density plot of $[W(\mathbf{C–C})]^-$ does not directly indicate the localization of the electron spin at the different ligand fragments, the coupling to three ^1H nuclei of the methyl group at the MIC moiety and three ^1H nuclei of the 2,6-diisopropylphenyl (=dipp) substituent are reasonable.

The influence of the constitutional isomers is shown in the EPR spectrum of $[W(\mathbf{C–C})(CO)_4]^-$ and $[W(\mathbf{C–N})(CO)_4]^-$. The analog tungsten C–N complex displays a stronger coupling of the electronic spin with the four ^{14}N nuclei in the pyridyl-MIC moiety. Consequently, the line-rich spectrum shows an increased line broadening of the isotropic signal. In contrast to its C–C counterpart, only six ^1H hyperfine couplings are observed in $[W(\mathbf{C–N})(CO)_4]^-$. This observation could indicate an increased localization of the electron spin at the MIC moiety, consequently leading to a decreased contribution of the dipp substituent. The stronger localization at the MIC moiety in the C–N linked isomer is further affirmed by the stronger ^1H hyperfine coupling to the methyl group. The EPR spectrum shows ^1H coupling constants of up to 7.19 MHz, while the **C–C** linked analog shows only weak couplings of up to 1.81 MHz. Additionally, three strong ^1H hyperfine couplings to three pyridyl-*H* are observed, confirming the significant localization at the pyridyl-MIC framework within the **C–N** isomer.

Inorganics **2024**, *12*, 46

Unfortunately, no clear trend regarding the influence of the central metal atom in the series of $[M(\mathbf{C–C})(CO)_4]^-$ and $[M(\mathbf{C–N})(CO)_4]^-$ (M = Cr, Mo, W) could be observed, despite all metal ions showing a coupling with the ligand-centered radical [42].

To further shine a light on the influence of the constitutional isomers in $[M(\mathbf{C–C})(CO)_4]$ and $[M(\mathbf{C–N})(CO)_4]$ (M = Cr, Mo, W), IR-SEC with a Au WE in 0.1 M NBu_4PF_6/CH_3CN was conducted.

2.2. IR-Spectroelectrochemistry

In contrast to cyclic voltammetry, IR spectroscopy of the complexes, $[M(\mathbf{C–C})(CO)_4]$ and $[M(\mathbf{C–N})(CO)_4]$ (M = Cr, Mo, W), under investigation is a common method for the characterization of the electronic structure due to the characteristic CO stretching frequencies.

The IR spectra of $[M(\mathbf{C–C})(CO)_4]$ and $[M(\mathbf{C–N})(CO)_4]$ in CH_2Cl_2 show four CO stretching frequencies as a consequence of the lowering of symmetry around the metal center (Table 3, Figure 3). Even though the number of bands observed in the IR spectra are identical, their positions shifted, depending on the electronic nature of the ligands and the central metal atoms.

Table 3. CO stretching frequencies of [M(**C–C**)] and [M(**C–N**)] (M = Cr, Mo, W) in CH_2Cl_2.

	$\tilde{\upsilon}$ (CO)/cm^{-1}				$\tilde{\upsilon}_{average}$ (CO)/cm^{-1}
$[Cr(\mathbf{C–C})(CO)_4]$ [41]	1998	1890	1875 (sh)	1822	1896
$[Cr(\mathbf{C–N})(CO)_4]$ [42]	1998	1890	1878 (sh)	1830	1899
$[Mo(\mathbf{C–C})(CO)_4]$	2004	1894	1876 (sh)	1827	1900
$[Mo(\mathbf{C–N})(CO)_4]$ [42]	2006	1896	1876 (sh)	1830	1902
$[W(\mathbf{C–C})(CO)_4]$	1998	1882	1870 (sh)	1826	1894
$[W(\mathbf{C–N})(CO)_4]$	2000	1884	1873 (sh)	1830	1897

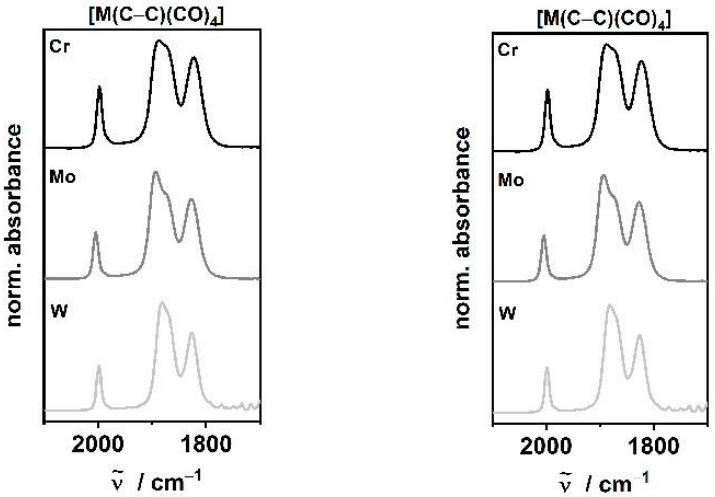

Figure 3. IR spectra of $[M(\mathbf{C–C})(CO)_4]$ [41] (**left**) and $[M(\mathbf{C–N})(CO)_4]$ [42] (**right**) in CH_2Cl_2 (M = Cr: black, Mo: grey, W: light grey).

Concerning the net electron density of the $[M(CO)_4]$ fragment with the incorporated pyridyl-MIC ligands, the averaged CO stretching frequencies presented in Table 3 further confirm the greater σ donor strength of the chelating ligand observed in $[M(\mathbf{C–C})(CO)_4]$ compared to $[M(\mathbf{C–N})(CO)_4]$.

The influence of the constitutional isomers becomes evident upon a one-electron reduction in $[M(\mathbf{C–C})(CO)_4]$ and $[M(\mathbf{C–N})(CO)_4]$ during IR-SEC (Figure 4; see Supplementary Materials S4). Within the series of $[M(\mathbf{C–N})(CO)_4]$, the observation of isosbestic points during the IR-SEC measurements is consistent with a clean conversion of the native species into

the reduced $[M(\mathbf{C}–\mathbf{N})(CO)_4]^-$ complexes. The shift of the frequencies by about 20 cm^{-1} to lower wavenumbers confirms the predominantly ligand-centered reduction and is in good agreement with our calculated changes in the CO stretching frequencies of $[M(\mathbf{C}–\mathbf{N})(CO)_4]^-$ (see Supplementary Materials S4) [41,42].

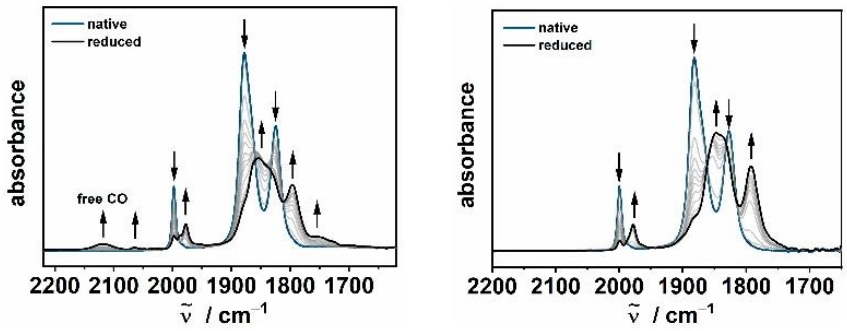

Figure 4. Changes in the IR spectra of $[W(\mathbf{C}–\mathbf{C})(CO)_4]$ (**left**) and $[W(\mathbf{C}–\mathbf{N})(CO)_4]$ (**right**) in CH_3CN/0.1 M Bu_4NPF_6 with a Au working electrode during the first reduction.

However, the picture changes upon a reduction in the other isomer. All complexes within the series show at least two new species in the IR-SEC measurements, as indicated by the formation of several new IR bands.

The most significant change can be assigned to the newly formed band at 2119 cm^{-1}. Torey et al. described a similar observation after a reduction in $[Mo(bpy)(CO)_4]$ [39]. The IR band at 2130 cm^{-1} could be assigned to adsorbed CO at the Au electrode surface. Furthermore, in-depth investigations by VSFG by *Neri* et al. confirmed the dissociative EC mechanism of CO upon a reduction in a Au WE [36]. Based on these results and our theoretical calculations (see Supplementary Materials S4), the reduced species could likely be a mixture of the one-electron-reduced $[M(\mathbf{C}–\mathbf{C})(CO)_4]^-$ species, the coordinatively unsaturated complex $[M(\mathbf{C}–\mathbf{C})(CO)_3]^-$, and/or the solvent adduct $[M(\mathbf{C}–\mathbf{C})(CH_3CN)(CO)_3]^-$, formed after subsequent CO dissociation.

In addition, a comparison of the IR spectra before and after electrolysis in the OTTLE cell clearly indicates the partial decomposition of $[M(\mathbf{C}–\mathbf{C})(CO)_4]$ after reduction, whereas only minor decomposition products are observed in the series of $[M(\mathbf{C}–\mathbf{N})(CO)_4]$ after prolonged electrolysis [42]. These results provide useful information on the stabilization of the ligand-centered radical based on the different linkage in the two constitutional isomers, as the CO cleavage observed in $[M(\mathbf{C}–\mathbf{C})(CO)_4]$ gives access to an open coordination site for potential electrocatalytic applications, such as electrochemical CO_2 reduction [28,29,33,36,37,39].

To confirm the reversibility in the series of $[M(\mathbf{C}–\mathbf{N})(CO)_4]$ and the EC mechanism observed for $[M(\mathbf{C}–\mathbf{C})(CO)_4]$ upon reduction, UV/vis/NIR-SEC measurements were performed.

2.3. UV/vis/NIR-Spectroelectrochemistry

UV/vis/NIR-SEC is a commonly employed technique to test either pure electrochemical reversibility or reversibility following an EC mechanism [51].

All presented complexes display electronic transitions in the visible to near UV region (300–550 nm), which can be assigned to metal-to-ligand charge transfers (MLCTs) with an additional contribution of the axial CO ligands in the ground state and excited state (see Supplementary Materials S6.20–S6.40) [41,42]. Within the series of $[M(\mathbf{C}–\mathbf{C})(CO)_4]$, the MLCT transitions are blue-shifted compared to $[M(\mathbf{C}–\mathbf{N})(CO)_4]$, which is in good agreement with the previously described π acceptor properties of the C–N linked constitutional isomer. However, a significant contribution of the aromatic substituent is observed in $[M(\mathbf{C}–\mathbf{N})(CO)_4]$ (see Supplementary Materials S6.40) [42].

Inorganics **2024**, *12*, 46

The electrochemical reduction in [M(**C**–**C**)(CO)$_4$] leads to broad transitions in the visible and NIR region (650–2100 nm; Figure 5 and Supplementary Materials S30 and S31). According to TD-DFT calculations, these bands can be assigned to an intra-ligand charge transfer (ILCT) from the reduced **C**–**C** linked ligand to the 2,6-diisopropylphenyl substituent and a ligand-to-ligand charge transfer (LLCT) from the reduced ligand to the axial CO ligands. The absorption bands in the 380–400 nm range are best described as metal ligand-to-ligand charge transfer (MLLCT) from the [M(CO)$_4$] fragment to the pyridyl-MIC ligand and all four CO ligands.

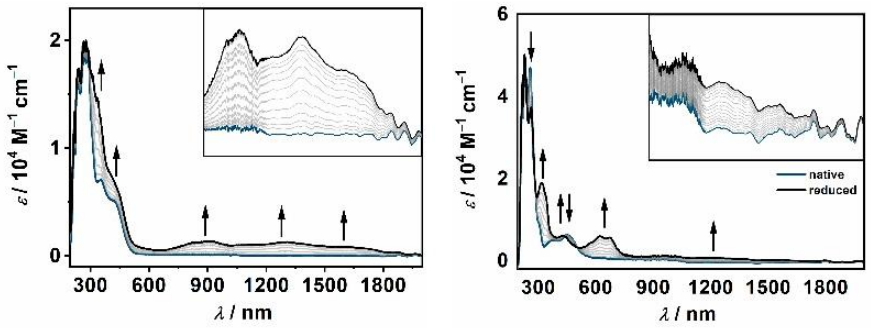

Figure 5. Changes in the UV/VIS spectra of [W(**C**–**C**)(CO)$_4$] (**left**, inset: 650–2050 nm) and [W(**C**–**N**)(CO)$_4$] (**right**, inset: 750–2090 nm) in CH_3CN/0.1 M Bu_4NPF_6 during the first reduction with a Au working electrode.

Upon a reduction in [M(**C**–**N**)(CO)$_4$], weak bands are observed in the visible and NIR region (700–2100 nm), which can be assigned to ILCTs and LLCTs from the reduced ligand to the axial CO ligands, the pyridyl-MIC moiety, and the aromatic substituent (see Supplementary Materials S6.40). Additionally, more discrete transitions are observed in the 550–700 nm region, indicating a more localized ligand-centered radical, which is in good agreement with the aforementioned EPR-SEC results. The electronic transitions in this range are best described as a mixture of ILCTs, MLLCTs, and LLCTs.

The partial degradation of [M(**C**–**C**)(CO)$_4$]$^-$ by an EC mechanism is confirmed by the decrease in absorption maxima during electrolysis in the OTTLE cell in the visible and NIR region and further supported by comparing the UV/vis/NIR spectra before and after UV/vis/NIR-SEC (see Supplementary Materials S5.10–S5.30). Only in the case of [Mo(**C**–**C**)(CO)$_4$] could the UV/vis/NIR spectrum of the starting complex be recovered completely. A similar observation was already described by Tory et al., who proposed the recoordination of the CO ligand to the metal center within the experimental setup [39]. In contrast, no degradation within the series of [M(**C**–**N**)(CO)$_4$] is detected, confirming the complete reversibility of the first ligand-centered reduction (see Supplementary Materials S5.40).

Based on our UV/vis/NIR- and IR-SEC measurements, we can conclude that the C–N linkage in [M(**C**–**N**)(CO)$_4$] results in an increased stabilization of the ligand-centered radical, while a reduction in the C–C pyridyl-MIC ligand shows an EC mechanism, leading to CO dissociation (Scheme 3).

An associative mechanism for the CO dissociation is unlikely, as it would generate 21 VE species of the already electron-rich [M(**C**–**C**)(CO)$_4$] complex. Therefore, we propose a dissociative mechanism after the first reduction, leading to 17 VE species [M(**C**–**C**)(CO)$_3$]$^-$. However, the intermediate is coordinatively unsaturated and thus accessible to solvent coordination, generating the complex [M(**C**–**C**)(CH_3CN)(CO)$_3$]$^-$.

Inorganics **2024**, *12*, 46

The electrochemical reduction in [M(**C**–**C**)(CO)$_4$] leads to broad transitions in the visible and NIR region (650–2100 nm; Figure 5 and Supplementary Materials S30 and S31). According to TD-DFT calculations, these bands can be assigned to an intra-ligand charge transfer (ILCT) from the reduced **C**–**C** linked ligand to the 2,6-diisopropylphenyl substituent and a ligand-to-ligand charge transfer (LLCT) from the reduced ligand to the axial CO ligands. The absorption bands in the 380–400 nm range are best described as metal ligand-to-ligand charge transfer (MLLCT) from the [M(CO)$_4$] fragment to the pyridyl-MIC ligand and all four CO ligands.

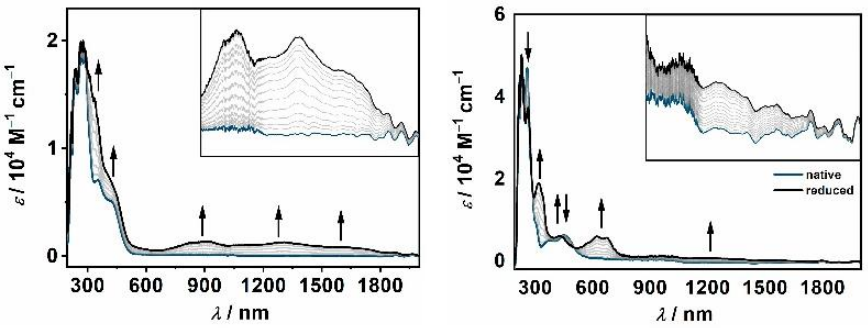

Figure 5. Changes in the UV/VIS spectra of [W(**C**–**C**)(CO)$_4$] (**left**, inset: 650–2050 nm) and [W(**C**–**N**)(CO)$_4$] (**right**, inset: 750–2090 nm) in CH_3CN/0.1 M Bu_4NPF_6 during the first reduction with a Au working electrode.

Upon a reduction in [M(**C**–**N**)(CO)$_4$], weak bands are observed in the visible and NIR region (700–2100 nm), which can be assigned to ILCTs and LLCTs from the reduced ligand to the axial CO ligands, the pyridyl-MIC moiety, and the aromatic substituent (see Supplementary Materials S6.40). Additionally, more discrete transitions are observed in the 550–700 nm region, indicating a more localized ligand-centered radical, which is in good agreement with the aforementioned EPR-SEC results. The electronic transitions in this range are best described as a mixture of ILCTs, MLLCTs, and LLCTs.

The partial degradation of [M(**C**–**C**)(CO)$_4$]$^-$ by an EC mechanism is confirmed by the decrease in absorption maxima during electrolysis in the OTTLE cell in the visible and NIR region and further supported by comparing the UV/vis/NIR spectra before and after UV/vis/NIR-SEC (see Supplementary Materials S5.10–S5.30). Only in the case of [Mo(**C**–**C**)(CO)$_4$] could the UV/vis/NIR spectrum of the starting complex be recovered completely. A similar observation was already described by Tory et al., who proposed the recoordination of the CO ligand to the metal center within the experimental setup [39]. In contrast, no degradation within the series of [M(**C**–**N**)(CO)$_4$] is detected, confirming the complete reversibility of the first ligand-centered reduction (see Supplementary Materials S5.40).

Based on our UV/vis/NIR- and IR-SEC measurements, we can conclude that the C–N linkage in [M(**C**–**N**)(CO)$_4$] results in an increased stabilization of the ligand-centered radical, while a reduction in the C–C pyridyl-MIC ligand shows an EC mechanism, leading to CO dissociation (Scheme 3).

An associative mechanism for the CO dissociation is unlikely, as it would generate 21 VE species of the already electron-rich [M(**C**–**C**)(CO)$_4$] complex. Therefore, we propose a dissociative mechanism after the first reduction, leading to 17 VE species [M(**C**–**C**)(CO)$_3$]$^-$. However, the intermediate is coordinatively unsaturated and thus accessible to solvent coordination, generating the complex [M(**C**–**C**)(CH_3CN)(CO)$_3$]$^-$.

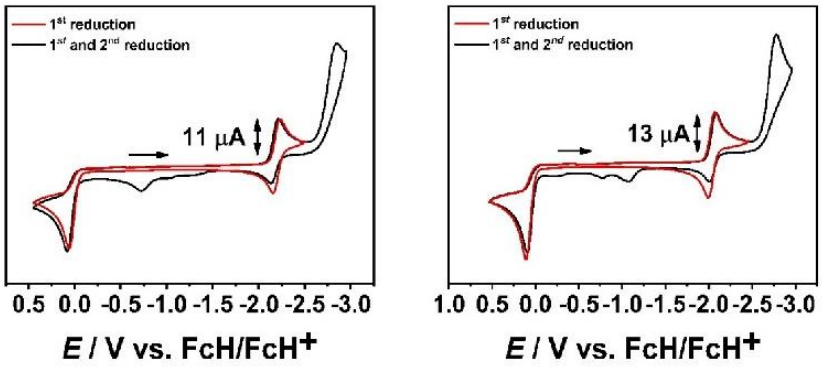

Figure 6. Cyclic voltammograms of [W(**C**–**C**)(CO)$_4$] (**left**) and [W(**C**–**N**)(CO)$_4$] (**right**) in CH_3CN and 0.1 M Bu_4NPF_6 with a scan rate of 100 mV/s and a Au electrode.

The second reduction appears completely irreversible in the series of [M(**C**–**C**)(CO)$_4$] and [M(**C**–**N**)(CO)$_4$] and is further confirmed by the appearance of additional oxidation processes in the range from −1.5 V to ± 0.0 V.

Earlier reports by Hartl and co-workers on [Mo(CO)$_4$(bpy)] showed a reversible first reduction, generating the monoanionic [Mo(CO)$_4$(bpy)]$^-$ species using a Au WE [39]. The second irreversible reduction results in the formation of the coordinatively unsaturated [Mo(CO)$_3$(bpy)]$^{2-}$ complex after CO dissociation. On sweeping back to cathodic potentials, the rapid recoordination of the CO ligand is proposed, as indicated by the near recovery of the first reversible reduction in [Mo(CO)$_4$(bpy)]$^-$.

As judged by the cyclic voltammetry for [M(**C**–**C**)(CO)$_4$] and [M(**C**–**N**)(CO)$_4$], no such intermediate could be detected after the second reduction with a Au WE, even at lower scan rates of 25 mV/s (see Supplementary Materials S2). Notably, lowering the scan rate leads to the complete disappearance of the oxidative processes between –1.5 V and ± 0.0 V. Reversible coordination of one of the pyridyl-MIC moieties after the second reduction can, therefore, not be ruled out due to its electron-rich nature [52–55].

In the presence of CO_2 under non-protic conditions, the influence of the metal center, the electrode material, and the constitutional isomers reveal their full potential in the electrochemical activation of CO_2 (Figure 7; see Supplementary Materials S7).

In the series of [M(**C**–**C**)(CO)$_4$], only the chromium complex shows a catalytic current with a GC WE after the first catalytic cycle, while no catalytic current is observed for the higher homologs. Instead, an overpotential (η = ~280 mV) [56] is observed after the second reduction, which could be a consequence of adduct formation with CO_2, leading to the deactivation of the catalysts, as previously reported by Kubiak and co-workers [37].

The second catalytic cycle in [Cr(**C**–**C**)(CO)$_4$] shows similar reactivity and is described by higher homologs. To verify whether the catalyst is a real homogenous catalyst or deposited on the electrode surface, a rinse test was performed (see Supplementary Materials S58) [57].

As judged by the experimental data, no heterogenous reactivity can be detected, which supports the CO_2 adduct formation within the series of [M(**C**–**C**)(CO)$_4$].

In contrast, in the series of [M(**C**–**N**)(CO)$_4$], a catalytic current at high potentials $E_p^{cat} > -3.0$ V is detected (see Supplementary Materials S7), which underlines that the fine-tuning of the ligand can have a major impact on catalytic performance. Unfortunately, high applied potentials for the electrocatalytic transformation of CO_2 prevented us from further product analysis. Hence, we focused on the influence of the electrode material to shift the onset potential for the electrochemical conversion of CO_2 with a Au WE (Figure 7; see Supplementary Materials S7).

Inorganics **2024**, *12*, 46

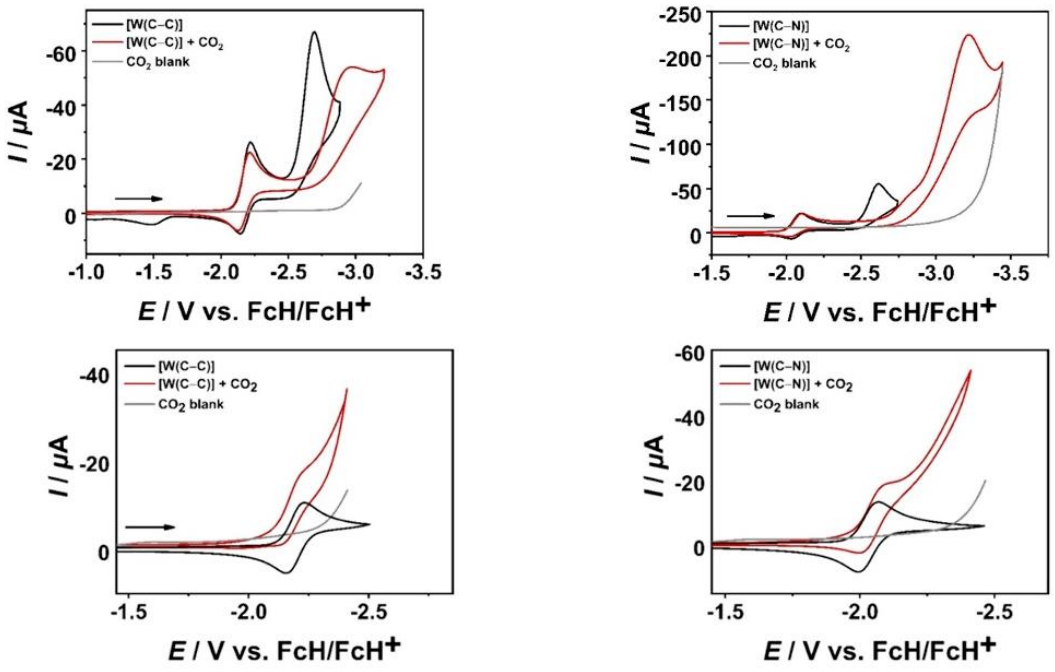

Figure 7. Cyclic voltammograms of [W(**C–C**)$(CO)_4$] (**left**) and [W(**C–N**)$(CO)_4$] (**right**) (1 mM, black) and in the presence of CO_2 (red) at 100 mV/s in CH_3CN/0.1 M Bu_4NPF_6 with a GC WE (**top**) and a Au WE (**bottom**).

According to our IR-SEC measurements, the first reduction in [M(**C–C**)$(CO)_4$] with a Au WE leads to CO dissociation, creating an open coordination site for binding CO_2. However, the weaker π acceptor properties of the C–C linked pyridyl-MIC ligand compared to its bpy counterpart shifts the onset potential to higher cathodic potential, preventing us from investigating the catalytic conversion under the experimental conditions, giving access to precatalytic activation (see Supplementary Materials S7).

To our surprise, the electrochemical conversion of CO_2 with the greater π acceptor ligand in [M(**C–N**)$(CO)_4$] results in a catalytic current close to the potential window of a saturated CO_2/CH_3CN solution, which is in conflict with our previously described IR-SEC measurements. A plausible explanation could be the formation of traces of [M(**C–N**)$(CO)_3]^-$ at the electrode surface, capable of electrocatalytically reducing CO_2, as previously described by Cowan and co-workers [36].

Analysis of the results in the electrochemical conversion of CO_2 with [M(**C–C**)$(CO)_4$] and [M(**C–N**)$(CO)_4$] using a Au WE show that the onset potential can be shifted drastically, up to +730 mV vs. a GC WE by the right choice of ligand and electrode material, as shown in the case of [W(**C–N**)$(CO)_4$].

3. Conclusions

The influence of the constitutional isomers on the redox and the spectroscopic properties of group 6 carbonyl complexes was investigated by cyclic voltammetry, EPR-, IR- and UV/vis/NIR-SEC. According to cyclic voltammetry, the different linkage of the constitutional isomers results in a greater σ donor strength of the **C–C** linked pyridyl-MIC ligand and a lower π acceptor ability compared to its **C–N** counterpart, which could be further confirmed by IR spectroscopy. The changes in the electronic structure have a tremendous influence on the redox properties of [M(**C–C**)$(CO)_4$] and [M(**C–N**)$(CO)_4$]. Based on our EPR-SEC measurements, the first ligand-centered reduction leads to an increased delocalization

of the electron spin within the **C–C** linked isomer. This observation was further supported by UV/vis/NIR-SEC measurements and TD-DFT calculations of the singly-reduced species, indicating an enhanced localization of the charge distribution in $[M(\mathbf{C–N})(CO)_4]^-$. Upon reduction, IR-SEC measurements of $[M(\mathbf{C–C})(CO)_4]$ show an EC mechanism, leading to CO dissociation using a Au WE, while in the case of $[M(\mathbf{C–N})(CO)_4]$, a complete electrochemically reversible one-electron reduction was observed. Additionally, UV/vis/NIR-SEC measurements were performed to confirm the pure reversibility of the first ligand-centered reduction or reversibility following an EC mechanism. In the case of $[Mo(\mathbf{C–C})(CO)_4]$, the initial spectra could be fully recovered, indicating reversible binding of CO following an EC mechanism. Based on these results, all presented complexes were further tested for the electrochemical conversion of CO_2 using a GC and a Au WE. Performing an electrochemical CO_2 reduction with a GC WE indicates that all complexes of the series $[M(\mathbf{C–N})(CO)_4]$ are capable of electrochemically converting CO_2 at high potentials, while the $[M(\mathbf{C–C})(CO)_4]$ complexes tend to generate CO_2 adducts after the second reduction. A change in electrode material leads to a shift of the onset potential of about +730 mV. However, the catalytic performance close to the potential window of the CO_2-saturated 0.1 M CH_3CN/Bu_4NPF_6 precluded further analysis of the product formation. Qualitatively, all presented complexes are capable of activating CO_2 by changing the working electrode from GC to Au. In this study, we were able to demonstrate that minor changes in the ligand framework, metal center, and experimental setup can have a tremendous influence on the electrochemical, spectroelectrochemical, and electrocatalytic performance in such systems.

4. Experimental Section

The synthesis of the complexes $[M(\mathbf{C–C})(CO)_4]$ and $[M(\mathbf{C–N})(CO)_4]$ (M = Cr, Mo, W) was performed according to the previously reported literature procedures [41–43,45].

4.1. General Procedures, Materials, and Instrumentation

Caution! Compounds containing azides are potentially explosive. Although we never experienced any problems during synthesis or analysis, all compounds should be synthesized in small quantities and handled with great care!

Unless otherwise noted, all reactions were carried out using standard Schlenk-line techniques under an inert atmosphere of argon (Linde Argon 4.8, purity 99.998%) or in a glovebox (Glovebox Systemtechnik, GS095218).

Commercially available chemicals were used without further purification. The solvents used for metal complex synthesis and catalysis were available from MBRAUN MB-SPS-800 solvent System and degassed by standard techniques prior to use. The identity and purity of the compounds were established via ^1H and ^{13}C NMR spectroscopy, elemental analysis, and mass spectrometry.

Solvents for cyclic voltammetry and UV/vis- and EPR-spectroelectrochemical measurements were dried and distilled under argon and degassed by common techniques prior to use. Column chromatography was performed over silica 60 M (0.04–0.063 mm).

^1H and $^{13}C\{^1H\}$ NMR spectra were recorded on a Bruker Advance 400 spectrometer at 19–22 °C. Chemical shifts are reported in ppm referenced to the residual solvent peaks [58].

The following abbreviations are used to represent the multiplicity of the signals: s (singlet), d (doublet), t (triplet), q (quartet), p (pentet), and sept (septet).

Mass spectrometry was performed on an Agilent 6210 ESI-TOF.

Elemental analyses were performed with an Elementar Micro Cube elemental analyzer.

The light-induced syntheses were performed with a LOT-QuantumDesign Arc Lamp (150 W, Xe OF).

4.2. Electrochemistry

Cyclic voltammograms were recorded with a PalmSens4 potentiostat or PAR VersaStat (Ametek), respectively, with a conventional three-electrode configuration consisting of a glassy carbon working electrode or gold working electrode, a platinum auxiliary electrode,

and a coiled silver wire as a pseudoreference electrode. The ferrocene/ferrocenium couple was used as an internal reference. All measurements were performed at room temperature at a scan rate between 25 and 1000 mVs^{-1}. The experiments were carried out in absolute Acetonitrile containing 0.1 M Bu_4NPF_6 (Sigma Aldrich, ≥99.0%, electrochemical grade) as the supporting electrolyte.

4.3. Spectroelectrochemistry

UV/vis spectra were recorded with an Avantes spectrometer consisting of a light source (AvaLight-DH-S-Bal), a UV/vis detector (AvaSpec-ULS2048), and an NIR detector (AvaSpeC-NIR256-TEC). IR spectra were recorded with a BRUKER Vertex 70 FT-IR or Nicolet 6700 FT-IR spectrometer, respectively. UV/vis-spectroelectrochemical measurements were carried out in an optically transparent thin-layer electrochemical (OTTLE) [59,60] cell (CaF_2 windows) with a gold-mesh working electrode, a platinum-mesh counter electrode, and a silver-foil pseudoreference. EPR spectra at the X-band frequency (ca. 9.5 GHz) were obtained with a Magnettech MS-5000 benchtop EPR spectrometer equipped with a rectangular TE 102 cavity and a TC HO4 temperature controller. The measurements were carried out in synthetic quartz glass tubes. For EPR spectroelectrochemistry, a three-electrode setup was employed using two Teflon-coated platinum wires (0.005 in. bare and 0.008 in. coated) as the working and counter electrodes and a Teflon-coated silver wire (0.005 in. bare and 0.007 in coated) as the pseudoreference electrode. The experiments were carried out in absolute Acetonitrile containing 0.1 M Bu_4NPF_6 as the supporting electrolyte. The same solvents used for CV measurements were used for each compound.

4.4. Calculations

The program package ORCA 4.1 was used for all DFT calculations [61]. Starting from the molecular structure obtained from X-ray diffraction, geometry optimizations were carried out using the B3LYP [62,63] function, and no symmetry restrictions were imposed during the optimization. For tungsten, relativistic effects in zero-order regular approximation (ZORA) were included [64]. All calculations were performed with an empirical Van der Waals correction (D3) [65–68]. The restricted and unrestricted DFT methods were employed for closed and open shell molecules, respectively, unless stated otherwise. Convergence criteria were set to the default for geometry optimization (OPT) and tight for SCF calculations (TIGHTSCF). Triple-ζ valence basis sets (def2-TZVP) [69] were employed for all atoms. Calculations were performed using a resolution of the identity approximation [70–76] with matching auxiliary basis sets [77,78] for geometry optimizations and numerical frequency calculations, and a RIJCOSX (combination of the resolution of the identity and chain of spheres algorithms) approximation was used for single-point calculations using the B3LYP function. Low-lying excitation energies were calculated with time-dependent DFT (TD-DFT). Solvent effects were taken into account with the conductor-like polarizable continuum model, CPCM [79]. Spin densities were calculated according to the Mulliken population analysis [80]. The absence of imaginary frequency, spin densities, molecular orbitals, and difference densities were visualized with a modified Chemcraft 1.8 program [81,82]. All molecular orbitals are illustrated with an iso value of 0.052. All calculated TD-DFT spectra are Gaussian-broadened with a bandwidth of 25 at half height unless otherwise noted.

Supplementary Materials: The following supporting information can be downloaded at https://www.mdpi.com/article/10.3390/inorganics12020046/s1.

Author Contributions: Conceptualization, T.B. and B.S.; methodology, T.B.; software, T.B.; validation, T.B. and B.S.; formal analysis, T.B. and B.S.; investigation, T.B.; resources, B.S.; data curation, T.B.; writing—original draft preparation, T.B.; writing—review and editing, B.S.; visualization, T.B.; supervision, B.S.; project administration, B.S.; funding acquisition, B.S. All authors have read and agreed to the published version of the manuscript.

Funding: We thank the state of Baden-Württemberg through bwHPC and the German Research Foundation (DFG) through grant No. INST 40/575-1 FUGG (JUSTUS 2 cluster) for their support.

Data Availability Statement: The data that support the findings of this study are available in the Supporting Material in this article.

Acknowledgments: We thank the state of Baden-Württemberg through bwHPC and the German Research Foundation (DFG) through grant No. INST 40/575-1 FUGG (JUSTUS 2 cluster) for their support.

Conflicts of Interest: There are no conflicts of interest to declare.

References

1. Kolb, H.C.; Finn, M.G.; Sharpless, K.B. Click Chemistry: Diverse Chemical Function from a Few Good Reactions. *Angew. Chem. Int. Ed.* **2001**, *40*, 2004–2021. [CrossRef]
2. Breugst, M.; Reissig, H.-U. The Huisgen Reaction: Milestones of the 1,3-Dipolar Cycloaddition. *Angew. Chem. Int. Ed.* **2020**, *59*, 12293–12307. [CrossRef]
3. Rostovtsev, V.V.; Green, L.G.; Fokin, V.V.; Sharpless, K.B. A Stepwise Huisgen Cycloaddition Process: Copper(I)-Catalyzed Regioselective "Ligation" of Azides and Terminal Alkynes. *Angew. Chem.* **2002**, *114*, 2708–2711. [CrossRef]
4. Tornøe, C.W.; Christensen, C.; Meldal, M. Peptidotriazoles on Solid Phase: [1,2,3]-Triazoles by Regiospecific Copper(I)-Catalyzed 1,3-Dipolar Cycloadditions of Terminal Alkynes to Azides. *J. Org. Chem.* **2002**, *67*, 3057–3064. [CrossRef]
5. Maity, R.; Sarkar, B. Chemistry of Compounds Based on 1,2,3-Triazolylidene-Type Mesoionic Carbenes. *JACS Au* **2022**, *2*, 22–57. [CrossRef]
6. Mathew, P.; Neels, A.; Albrecht, M. 1,2,3-Triazolylidenes as Versatile Abnormal Carbene Ligands for Late Transition Metals. *J. Am. Chem. Soc.* **2008**, *130*, 13534–13535. [CrossRef] [PubMed]
7. Schweinfurth, D.; Hettmanczyk, L.; Suntrup, L.; Sarkar, B. Metal Complexes of Click-Derived Triazoles and Mesoionic Carbenes: Electron Transfer, Photochemistry, Magnetic Bistability, and Catalysis. *Z. Anorg. Allg. Chem.* **2017**, *643*, 554–584. [CrossRef]
8. Crabtree, R.H. Abnormal, mesoionic and remote N-heterocyclic carbene complexes. *Coord. Chem. Rev.* **2013**, *257*, 755–766. [CrossRef]
9. Donnelly, K.F.; Petronilho, A.; Albrecht, M. Application of 1,2,3-triazolylidenes as versatile NHC-type ligands: Synthesis, properties, and application in catalysis and beyond. *Chem. Commun.* **2013**, *49*, 1145–1159. [CrossRef]
10. Bolje, A.; Hohloch, S.; Košmrlj, J.; Sarkar, B. Ru^{II}, Ir^{III} and Os^{II} mesoionic carbene complexes: Efficient catalysts for transfer hydrogenation of selected functionalities. *Dalton Trans.* **2016**, *45*, 15983–15993. [CrossRef] [PubMed]
11. Bolje, A.; Košmrlj, J. A Selective Approach to Pyridine Appended 1,2,3-Triazolium Salts. *Org. Lett.* **2013**, *15*, 5084–5087. [CrossRef]
12. Hohloch, S.; Suntrup, L.; Sarkar, B. Arene–Ruthenium(II) and −Iridium(III) Complexes with "Click"-Based Pyridyl-triazoles, Bistriazoles, and Chelating Abnormal Carbenes: Applications in Catalytic Transfer Hydrogenation of Nitrobenzene. *Organometallics* **2013**, *32*, 7376–7385. [CrossRef]
13. Kralj, J.; Bolje, A.; Polančec, D.S.; Steiner, I.; Gržan, T.; Tupek, A.; Stojanović, N.; Hohloch, S.; Urankar, D.; Osmak, M.; et al. Half-Sandwich Ir(III) and Os(II) Complexes of Pyridyl-Mesoionic Carbenes as Potential Anticancer Agents. *Organometallics* **2019**, *38*, 4082–4092. [CrossRef]
14. Sabater, S.; Müller-Bunz, H.; Albrecht, M. Carboxylate-Functionalized Mesoionic Carbene Precursors: Decarboxylation, Ruthenium Bonding, and Catalytic Activity in Hydrogen Transfer Reactions. *Organometallics* **2016**, *35*, 2256–2266. [CrossRef]
15. Saha, S.; Yadav, S.; Reshi, N.U.D.; Dutta, I.; Kunnikuruvan, S.; Bera, J.K. Electronic Asymmetry of an Annelated Pyridyl–Mesoionic Carbene Scaffold: Application in Pd(II)-Catalyzed Wacker-Type Oxidation of Olefins. *ACS Catal.* **2020**, *10*, 11385–11393. [CrossRef]
16. Suntrup, L.; Stein, F.; Klein, J.; Wilting, A.; Parlane, F.G.L.; Brown, C.M.; Fiedler, J.; Berlinguette, C.P.; Siewert, I.; Sarkar, B. Rhenium Complexes of Pyridyl-Mesoionic Carbenes: Photochemical Properties and Electrocatalytic CO_2 Reduction. *Inorg. Chem.* **2020**, *59*, 4215–4227. [CrossRef]
17. Hansmann, M.M.; Antoni, P.W.; Pesch, H. Stable Mesoionic N-Heterocyclic Olefins (mNHOs). *Angew. Chem.* **2020**, *132*, 5831–5836. [CrossRef]
18. Liang, Q.; Song, D. Recent advances of mesoionic N-heterocyclic olefins. *Dalton Trans.* **2022**, *51*, 9191–9198. [CrossRef] [PubMed]
19. Huang, S.; Wu, Y.; Huang, L.; Hu, C.; Yan, X. Synthesis, Characterization and Photophysical Properties of Mesoionic N-Heterocyclic Imines. *Chem. Asian J.* **2022**, *17*, e202200281. [CrossRef] [PubMed]
20. Rudolf, R.; Neuman, N.I.; Walter, R.R.M.; Ringenberg, M.R.; Sarkar, B. Mesoionic Imines (MIIs): Strong Donors and Versatile Ligands for Transition Metals and Main Group Substrates. *Angew. Chem. Int. Ed. Engl.* **2022**, *61*, e202200653. [CrossRef] [PubMed]
21. Suntrup, L.; Klenk, S.; Klein, J.; Sobottka, S.; Sarkar, B. Gauging Donor/Acceptor Properties and Redox Stability of Chelating Click-Derived Triazoles and Triazolylidenes: A Case Study with Rhenium(I) Complexes. *Inorg. Chem.* **2017**, *56*, 5771–5783. [CrossRef] [PubMed]
22. Collin, J. Electrochemical Reduction of Carbon Dioxide Mediated by Molecular Catalysts. *Coord. Chem. Rev.* **1989**, *93*, 245–268. [CrossRef]

23. Gonell, S.; Massey, M.D.; Moseley, I.P.; Schauer, C.K.; Muckerman, J.T.; Miller, A.J.M. The Trans Effect in Electrocatalytic CO_2 Reduction: Mechanistic Studies of Asymmetric Ruthenium Pyridyl-Carbene Catalysts. *J. Am. Chem. Soc.* **2019**, *141*, 6658–6671. [CrossRef] [PubMed]
24. Hawecker, J.; Lehn, J.-M.; Ziessel, R. Electrocatalytic reduction of carbon dioxide mediated by $Re(bipy)(CO)_3Cl$ (bipy = 2,2′-bipyridine). *J. Chem. Soc., Chem. Commun.* **1984**, *6*, 328–330. [CrossRef]
25. Smieja, J.M.; Kubiak, C.P. $Re(bipy\text{-}tBu)(CO)_3Cl$-improved Catalytic Activity for Reduction of Carbon Dioxide: IR-Spectroelectrochemical and Mechanistic Studies. *Inorg. Chem.* **2010**, *49*, 9283–9289. [CrossRef]
26. Todorova, T.K.; Huan, T.N.; Wang, X.; Agarwala, H.; Fontecave, M. Controlling Hydrogen Evolution during Photoreduction of CO_2 to Formic Acid Using $Rh(R\text{-}bpy)(Cp^*)Cl^+$ Catalysts: A Structure-Activity Study. *Inorg. Chem.* **2019**, *58*, 6893–6903. [CrossRef] [PubMed]
27. Windle, C.D.; Perutz, R.N. Advances in molecular photocatalytic and electrocatalytic CO_2 reduction. *Coord. Chem. Rev.* **2012**, *256*, 2562–2570. [CrossRef]
28. Clark, M.L.; Grice, K.A.; Moore, C.E.; Rheingold, A.L.; Kubiak, C.P. Electrocatalytic CO_2 reduction by $M(bpy\text{-}R)(CO)_4$ (M = Mo, W.; R = H, *t*Bu) complexes. Electrochemical, spectroscopic, and computational studies and comparison with group 7 catalysts. *Chem. Sci.* **2014**, *5*, 1894–1900. [CrossRef]
29. Franco, F.; Cometto, C.; Sordello, F.; Minero, C.; Nencini, L.; Fiedler, J.; Gobetto, R.; Nervi, C. Electrochemical Reduction of CO_2 by $M(CO)_4$ (diimine) Complexes (M = Mo, W): Catalytic Activity Improved by 2,2′-Dipyridylamine. *ChemElectroChem* **2015**, *2*, 1372–1379. [CrossRef]
30. Franco, F.; Pinto, M.F.; Royo, B.; Lloret-Fillol, J. A Highly Active N-Heterocyclic Carbene Manganese(I) Complex for Selective Electrocatalytic CO_2 Reduction to CO. *Angew. Chem. Int. Ed.* **2018**, *57*, 4603–4606. [CrossRef]
31. Friães, S.; Realista, S.; Gomes, C.S.B.; Martinho, P.N.; Royo, B. Click-Derived Triazoles and Triazolylidenes of Manganese for Electrocatalytic Reduction of CO_2. *Molecules* **2021**, *26*, 6325. [CrossRef]
32. Gonell, S.; Lloret-Fillol, J.; Miller, A.J.M. An Iron Pyridyl-Carbene Electrocatalyst for Low Overpotential CO_2 Reduction to CO. *ACS Catal.* **2021**, *11*, 615–626. [CrossRef]
33. Grice, K.A.; Saucedo, C. Electrocatalytic Reduction of CO_2 by Group 6 $M(CO)_6$ Species without "Non-Innocent" Ligands. *Inorg. Chem.* **2016**, *55*, 6240–6246. [CrossRef]
34. Huang, C.; Liu, J.; Huang, H.-H.; Ke, Z. Recent progress in electro- and photo-catalytic CO_2 reduction using N-heterocyclic carbene transition metal complexes. *Polyhedron* **2021**, *203*, 115147. [CrossRef]
35. Machan, C.W.; Stanton, C.J.; Vandezande, J.E.; Majetich, G.F.; Schaefer, H.F.; Kubiak, C.P.; Agarwal, J. Electrocatalytic Reduction of Carbon Dioxide by $Mn(CN)(2,2'\text{-bipyridine})(CO)_3$: CN Coordination Alters Mechanism. *Inorg. Chem.* **2015**, *54*, 8849–8856. [CrossRef]
36. Neri, G.; Donaldson, P.M.; Cowan, A.J. The Role of Electrode-Catalyst Interactions in Enabling Efficient CO_2 Reduction with $Mo(bpy)(CO)_4$ As Revealed by Vibrational Sum-Frequency Generation Spectroscopy. *J. Am. Chem. Soc.* **2017**, *139*, 13791–13797. [CrossRef] [PubMed]
37. Sieh, D.; Lacy, D.C.; Peters, J.C.; Kubiak, C.P. Reduction of CO_2 by Pyridine Monoimine Molybdenum Carbonyl Complexes: Cooperative Metal-Ligand Binding of CO_2. *Chem. Eur. J.* **2015**, *21*, 8497–8503. [CrossRef]
38. Smieja, J.M.; Sampson, M.D.; Grice, K.A.; Benson, E.E.; Froehlich, J.D.; Kubiak, C.P. Manganese as a Substitute for Rhenium in CO_2 Reduction Catalysts: The Importance of Acids. *Inorg. Chem.* **2013**, *52*, 2484–2491. [CrossRef] [PubMed]
39. Tory, J.; Setterfield-Price, B.; Dryfe, R.A.W.; Hartl, F. $[M(CO)]_4$ (2,2′-bipyridine)] (M = Cr, Mo, W) Complexes as Efficient Catalysts for Electrochemical Reduction of CO_2 at a Gold Electrode. *ChemElectroChem* **2015**, *2*, 213–217. [CrossRef]
40. Reda, T.; Plugge, C.M.; Abram, N.J.; Hirst, J. Reversible interconversion of carbon dioxide and formate by an electroactive enzyme. *Proc. Natl. Acad. Sci. USA* **2008**, *105*, 10654–10658. [CrossRef] [PubMed]
41. Bens, T.; Walter, R.R.M.; Beerhues, J.; Schmitt, M.; Krossing, I.; Sarkar, B. The Best of Both Worlds: Combining the Power of MICs and WCAs to generate Stable and Crystalline Cr^I-tetracarbonyl Complexes with π-Accepting Ligands. *Chem. Eur. J.* **2023**, *29*, e202301205. [CrossRef]
42. Bens, T.; Boden, P.; Di Martino-Fumo, P.; Beerhues, J.; Albold, U.; Sobottka, S.; Neuman, N.I.; Gerhards, M.; Sarkar, B. Chromium(0) and Molydenum(0) Complexes with a Pyridyl-Mesoionic Carbene Ligand: Structural, (Spectro)electrochemical, Photochemical, and Theoretical Investigations. *Inorg. Chem.* **2020**, *59*, 15504–15513. [CrossRef]
43. Boden, P.; Di Martino-Fumo, P.; Bens, T.; Steiger, S.; Albold, U.; Niedner-Schatteburg, G.; Gerhards, M.; Sarkar, B. NIR-Emissive Chromium(0), Molybdenum(0), and Tungsten(0) Complexes in the Solid State at Room Temperature. *Chem. Eur. J.* **2021**, *27*, 12959–12964. [CrossRef] [PubMed]
44. Boden, P.J.; Di Martino-Fumo, P.; Bens, T.; Steiger, S.T.; Marhöfer, D.; Niedner-Schatteburg, G.; Sarkar, B. Mechanistic and Kinetic Investigations of ON/OFF (Photo)Switchable Binding of Carbon Monoxide by Chromium(0), Molybdenum(0) and Tungsten(0) Carbonyl Complexes with a Pyridyl-Mesoionic Carbene Ligand. *Chem. Eur. J.* **2022**, *28*, e202201038. [CrossRef] [PubMed]
45. Bens, T.; Marhöfer, D.; Boden, P.; Steiger, S.T.; Suntrup, L.; Niedner-Schatteburg, G.; Sarkar, B. A Different Perspective on Tuning the Photophysical and Photochemical Properties: The Influence of Constitutional Isomers in Group 6 Carbonyl Complexes with Pyridyl-Mesoionic Carbenes. *Inorg. Chem.* **2023**, *62*, 16182–16195. [CrossRef] [PubMed]

46. Tang, M.; Cameron, L.; Poland, E.M.; Yu, L.-J.; Moggach, S.A.; Fuller, R.O.; Huang, H.; Sun, J.; Thickett, S.C.; Massi, M.; et al. Photoactive Metal Carbonyl Complexes Bearing N-Heterocyclic Carbene Ligands: Synthesis, Characterization, and Viability as Photoredox Catalysts. *Inorg. Chem.* **2022**, *61*, 1888–1898. [CrossRef] [PubMed]
47. Bens, T.; Walter, R.R.M.; Beerhues, J.; Lücke, C.; Gabler, J.; Sarkar, B. Isolation, Characterization and Reactivity of Key Intermediates Relevant to Reductive (Electro)catalysis with Cp*Rh Complexes Containing Pyridyl-MIC (MIC=Mesoionic Carbene) Ligands. *Chem. Eur. J.* **2024**, *30*, e202302354. [CrossRef] [PubMed]
48. Bohnenberger, J.; Schmitt, M.; Feuerstein, W.; Krummenacher, I.; Butschke, B.; Czajka, J.; Malinowski, P.J.; Breher, F.; Krossing, I. Completing the triad: Synthesis and full characterization of homoleptic and heteroleptic carbonyl and nitrosyl complexes of the group VI metals. *Chem. Sci.* **2020**, *11*, 3592–3603. [CrossRef] [PubMed]
49. Vlček, A., Jr. Highlights of the spectroscopy, photochemistry and electrochemistry of [M(CO)4(α-diimine)] complexes, M=Cr, Mo, W. *Coord. Chem. Rev.* **2002**, *230*, 225–242. [CrossRef]
50. Huheey, J.E.; Keiter, E.A.; Keiter, R.L. *Huheey—Anorganische Chemie*; Walter de Gruyter: Berlin, Germany; Boston, MA, USA, 2008; ISBN 978-3-11-030433-6.
51. Kaim, W.; Fiedler, J. Spectroelectrochemistry: The best of two worlds. *Chem. Soc. Rev.* **2009**, *38*, 3373–3382. [CrossRef]
52. Crawley, M.R.; Kadassery, K.J.; Oldacre, A.N.; Friedman, A.E.; Lacy, D.C.; Cook, T.R. Rhenium(I) Phosphazane Complexes for Electrocatalytic CO_2 Reduction. *Organometallics* **2019**, *38*, 1664–1676. [CrossRef]
53. Knebel, W.J.; Angelici, R.J. Kinetic and Equilibrium Studies of Bi- and Tridentate Chelate Ring-Opening Reactions of Metal Carbonyl Complexes. *Inorg. Chem.* **1974**, *13*, 632–637. [CrossRef]
54. Knebel, W.J.; Angelici, R.J. Mechanism of Chelate Ring-Opening in Metal Carbonyl Complexes. *Inorg. Chem.* **1974**, *13*, 627–631. [CrossRef]
55. Lee, C.-C.; Ke, W.-C.; Chan, K.-T.; Lai, C.-L.; Hu, C.-H.; Lee, H.M. Nickel(II) Complexes of Bidentate N-Heterocyclic Carbene/Phosphine Ligands: Efficient Catalysts for Suzuki Coupling of Aryl Chlorides. *Chem. Eur. J.* **2007**, *13*, 582–591. [CrossRef] [PubMed]
56. Elgrishi, N.; Chambers, M.B.; Wang, X.; Fontecave, M. Molecular polypyridine-based metal complexes as catalysts for the reduction of CO_2. *Chem. Soc. Rev.* **2017**, *46*, 761–796. [CrossRef] [PubMed]
57. Lee, K.J.; McCarthy, B.D.; Dempsey, J.L. On decomposition, degradation, and voltammetric deviation: The electrochemist's field guide to identifying precatalyst transformation. *Chem. Soc. Rev.* **2019**, *48*, 2927–2945. [CrossRef] [PubMed]
58. Budavari, S. (Ed.) *The Merck-Index: An Encyclopedia of Chemicals, Drugs, and Biologicals*, 11th ed.; 3. print; Centennial ed.; Merck & Co., Inc.: Rahway, NJ, USA, 1991; ISBN 091191028X.
59. Krejčik, M.; Daněk, M.; Hartl, F. Simple construction of an infrared optically transparent thin-layer electrochemical cell: Applications to the redox reactions of ferrocene, $Mn_2(CO)_{10}$ and $Mn(CO)_3$(3,5-di-t-butyl-catecholat)$^-$. *J. Electroanal. Chem. Interfacial* **1991**, *317*, 179. [CrossRef]
60. Klein, J.; Stuckmann, A.; Sobottka, S.; Suntrup, L.; van der Meer, M.; Hommes, P.; Reissig, H.-U.; Sarkar, B. Ruthenium Complexes with Strongly Electron-Donating Terpyridine Ligands: Effect of the Working Electrode on Electrochemical and Spectroelectrochemical Properties. *Chem. Eur. J.* **2017**, *23*, 12314–12325. [CrossRef]
61. Neese, F. The ORCA program system. *WIREs Comput. Mol. Sci.* **2012**, *2*, 73–78. [CrossRef]
62. Becke, A.D. Density-functional thermochemistry. III. The role of exact exchange. *J. Chem. Phy.* **1993**, *98*, 5648–5652. [CrossRef]
63. Lee, C.; Yang, W.; Parr, R.G. Development of the Colle-Salvetti correlation-energy formula into a functional of the electron density. *Phys. Rev. B* **1988**, *37*, 785–789. [CrossRef] [PubMed]
64. van Wüllen, C. Molecular density functional calculations in the regular relativistic approximation: Method, application to coinage metal diatomics, hydrides, fluorides and chlorides, and comparison with first-order relativistic calculations. *J. Chem. Phy.* **1998**, *109*, 392–399. [CrossRef]
65. Grimme, S. Semiempirical GGA-type density functional constructed with a long-range dispersion correction. *J. Comput. Chem.* **2006**, *27*, 1787–1799. [CrossRef] [PubMed]
66. Grimme, S. Accurate description of van der Waals complexes by density functional theory including empirical corrections. *J. Comput. Chem.* **2004**, *25*, 1463–1473. [CrossRef] [PubMed]
67. Grimme, S.; Antony, J.; Ehrlich, S.; Krieg, H. A consistent and accurate ab initio parametrization of density functional dispersion correction (DFT-D) for the 94 elements H-Pu. *J. Chem. Phy.* **2010**, *132*, 154104-1–154104-19. [CrossRef] [PubMed]
68. Grimme, S.; Ehrlich, S.; Goerigk, L. Effect of the damping function in dispersion corrected density functional theory. *J. Comput. Chem.* **2011**, *32*, 1456–1465. [CrossRef] [PubMed]
69. Weigend, F.; Ahlrichs, R. Balanced basis sets of split valence, triple zeta valence and quadruple zeta valence quality for H to Rn: Design and assessment of accuracy. *Phys. Chem. Chem. Phys.* **2005**, *7*, 3297–3305. [CrossRef]
70. Izsák, R.; Neese, F. An overlap fitted chain of spheres exchange method. *J. Chem. Phy.* **2011**, *135*, 144105-1–144105-11. [CrossRef]
71. Neese, F. An improvement of the resolution of the identity approximation for the formation of the Coulomb matrix. *J. Comput. Chem.* **2003**, *24*, 1740–1747. [CrossRef]
72. Neese, F.; Olbrich, G. Efficient use of the resolution of the identity approximation in time-dependent density functional calculations with hybrid density functionals. *Chem. Phy. Lett.* **2002**, *362*, 170–178. [CrossRef]
73. Neese, F.; Wennmohs, F.; Hansen, A.; Becker, U. Efficient, approximate and parallel Hartree–Fock and hybrid DFT calculations. A 'chain-of-spheres' algorithm for the Hartree–Fock exchange. *Chem. Phys.* **2009**, *356*, 98–109. [CrossRef]

74. Petrenko, T.; Kossmann, S.; Neese, F. Efficient time-dependent density functional theory approximations for hybrid density functionals: Analytical gradients and parallelization. *J. Chem. Phy.* **2011**, *134*, 054116-1–054116-14. [CrossRef] [PubMed]
75. Vahtras, O.; Almlöf, J.; Feyereisen, M.W. Integral approximations for LCAO-SCF calculations. *Chem. Phy. Lett.* **1993**, *213*, 514–518. [CrossRef]
76. Whitten, J.L. Coulombic potential energy integrals and approximations. *J. Chem. Phy.* **1973**, *58*, 4496–4501. [CrossRef]
77. Eichkorn, K.; Treutler, O.; Öhm, H.; Häser, M.; Ahlrichs, R. Auxiliary basis sets to approximate Coulomb. *Chem. Phy. Lett.* **1995**, *242*, 652–660. [CrossRef]
78. Eichkorn, K.; Weigend, F.; Treutler, O.; Ahlrichs, R. Auxiliary basis sets for main row atoms and transition metals and their use to approximate Coulomb potentials. *Theor. Chem. Acc.* **1997**, *97*, 119–124. [CrossRef]
79. Barone, V.; Cossi, M. Quantum Calculation of Molecular Energies and Energy Gradients in Solution by a Conductor Solvent Model. *J. Phys. Chem. A* **1998**, *102*, 1995–2001. [CrossRef]
80. Mulliken, R.S. Electronic Population Analysis on LCAO–MO Molecular Wave Functions. I. *J. Chem. Phy.* **1955**, *23*, 1833–1840. [CrossRef]
81. Zhurko, G.A. *Chemcraft-Graphical Program for Visualization of Quantum Chemistry Computations*; Version 1.8; Chemcraft: Ivanovo, Russia, 2023.
82. Hanwell, M.D.; Curtis, D.E.; Lonie, D.C.; Vandermeersch, T.; Zurek, E.; Hutchison, G.R. Avogadro: An advanced semantic chemical editor, visualization, and analysis platform. *J. Cheminform.* **2012**, *4*, 17. [CrossRef]

3.7 Isolation, Characterization and Reactivity of Key Intermediates Relevant to Reductive (Electro)catalysis with Cp*Rh Complexes containing Pyridyl-MIC (MIC = Mesoionic Carbene) Ligands

Tobias Bens,[†,§] Robert R. M. Walter,[†] Julia Beerhues,[†,§,^] Clemens Lücke, [†] Julia Gabler,[†#] Biprajit Sarkar[†,§,*]

[†]Institut für Anorganische Chemie, Universität Stuttgart, Pfaffenwaldring 55, D-70569 Stuttgart, Germany, Email: biprajit.sarkar@iac.uni-stuttgart.de
[§]Institut für Chemie und Biochemie, Freie Universität Berlin, Fabeckstraße 34-36, 14195, Berlin, Germany.
[^]Current Address: Institute of Chemical Research of Catalonia (ICIQ), Barcelona Institute of Science and Technology (BIST), Av. Països Catalans 16, 43007 Tarragona, Spain.
[#]Julia Gabler passed away in January 2023

This article was published and is reprinted with permission from WILEY-VCH:
T. Bens, R. R. M. Walter, J. Beerhues, C. Lücke, J. Gabler, B. Sarkar, *Chem. Eur. J.* **2024**, *30*, e202302354.
DOI: 10.1002/chem.202302354 (© WILEY-VCH Verlag GmbH & Co. KGaA, Weinheim).

The **Supporting Information** is available free of charge at https://chemistry-europe.onlinelibrary.wiley.com/doi/full/10.1002/chem.202302354.

Autor contribution: The project was designed by Biprajit Sarkar. The presented complexes were synthesized and fully characterized by Tobias Bens together with Julia Gabler during her internship. All (spectro)electrochemical measurements were realized by Tobias Bens. The electrochemical proton reduction was investigated by Tobias Bens and Julia Gabler as a part of her internship. All calculations were performed by Tobias Bens. X-Ray diffraction analysis was carried out by Robert R. M. Walter, Julia Beerhues and Clemens Lücke. The manuscript was written by Tobias Bens and Biprajit Sarkar.

Check for updates

Chemistry–A European Journal

Research Article
doi.org/10.1002/chem.202302354

Chemistry Europe
European Chemical Societies Publishing

www.chemeurj.org

VIP Very Important Paper

Special Collection

Isolation, Characterization and Reactivity of Key Intermediates Relevant to Reductive (Electro)catalysis with Cp*Rh Complexes Containing Pyridyl-MIC (MIC = Mesoionic Carbene) Ligands

Tobias Bens,[a, b] Robert R. M. Walter,[a] Julia Beerhues,[a, b, c] Clemens Lücke,[a] Julia Gabler+,[a] and Biprajit Sarkar*[a, b]

Dedicated to Julia Gabler, a wonderful soul, who departed far too soon.

In recent years, metal complexes of pyridyl-mesoionic carbene (MIC) ligands have been reported as excellent homogeneous and molecular electrocatalysts. In combination with group 9 metals, such ligands form highly active catalysts for hydrogenation/transfer hydrogenation/hydrosilylation catalysis and electrocatalysts for dihydrogen production. Despite such progress, very little is known about the structural/electrochemical/spectroscopic properties of crucial intermediates for such catalytic reactions with these ligands: solvato complexes, reduced complexes and hydridic species. We present here a comprehensive study involving the isolation, crystallographic characterization, electrochemical/spectroelectrochemical/theoretical investigations, and in-situ reactivity studies of all the aforementioned crucial intermediates involving Cp*Rh and pyridyl-MIC ligands. A detailed mechanistic study of the precatalytic activation of [RhCp*] complexes with pyridyl-MIC ligands is presented. Intriguingly, amphiphilicity of the [RhCp*]-hydride complexes was observed, displaying the substrate dependent transfer of H^+, H or H^-. To the best of our knowledge, this study is the first of its kind targeting intermediates and reactive species involving metal complexes of pyridyl-MIC ligands and investigating the interconversion amongst them.

Introduction

In the past decades, great efforts in the field of electrocatalysis have been made to design highly efficient and stable electrocatalysts to generate renewable energy-based alternatives to fossil fuels from energy-poor feedstocks into energy-rich molecular resources.[1,2,3] However, the nontrivial multi-electron transformation to the high-energetic catalytic active species is an extraordinarily complex subject.[4–7] The investigation of fragile and short-lived intermediates remains challenging and has received growing attention for the design of suitable precatalysts in the selective generation of the molecular active species.[5–7,8]

One of the most promising and well-established precatalysts in the electrochemical generation of H_2, as a suitable energy source, are the stable and facile accessible [RhCp*] (Cp* = pentamethylcyclopentadienyl) complexes with bidentate chelating ligands, such as polypyridine[2,3,9–18] or diphosphine ligands.[19] The mechanistic proposal from Kölle and Grätzel in 1987, involved a two-electron reduction from Rh(III) to Rh(I) and subsequent protonation to form the [RhCp*] hydride species, which undergoes protonolysis to H_2.[13]

Nearly 30 years later, the group of Miller and Blakemore reinvestigated the rhodium(III)hydride formation in polypyridine [RhCp*] complexes (**I**, Scheme 1, top).[11,15,16] Addition of a H^+ source to the reduced [RhCp*] complex (**II**, Scheme 1) results in the protonation of the Cp* moiety to form η^4–pentametyhlcyclopentadiene (Cp*H) capable to generate H_2. Theoretical calculations by Blakemore and Goddard, provided detailed insights into a tautomerization mechanism between the metal-bound hydride complex [HRhCp*] (**III**, Scheme 1) and the Cp* protonated [RhCp*H] (**IV**, Scheme 1)

[a] T. Bens, R. R. M. Walter, Dr. J. Beerhues, C. Lücke, J. Gabler,+ Prof. Dr. B. Sarkar
Institut für Anorganische Chemie
Universität Stuttgart
Pfaffenwaldring 55, D-70569 Stuttgart (Germany)
E-mail: biprajit.sarkar@iac.uni-stuttgart.de

[b] T. Bens, Dr. J. Beerhues, Prof. Dr. B. Sarkar
Institut für Chemie und Biochemie
Freie Universität Berlin
Fabeckstraße 34–36, 14195, Berlin (Germany)

[c] Dr. J. Beerhues
Current Address:
Institute of Chemical Research of Catalonia (ICIQ)
Barcelona Institute of Science and Technology (BIST)
Av. Països Catalans 16, 43007 Tarragona (Spain)

[+] deceased, January 20, 2023

Supporting information for this article is available on the WWW under https://doi.org/10.1002/chem.202302354

This manuscript is part of a special collection on 3rd International Conference on Organometallics and Catalysis (ICOC-2023).

Chemistry–A European Journal | Research Article
doi.org/10.1002/chem.202302354
Chemistry Europe
European Chemical Societies Publishing

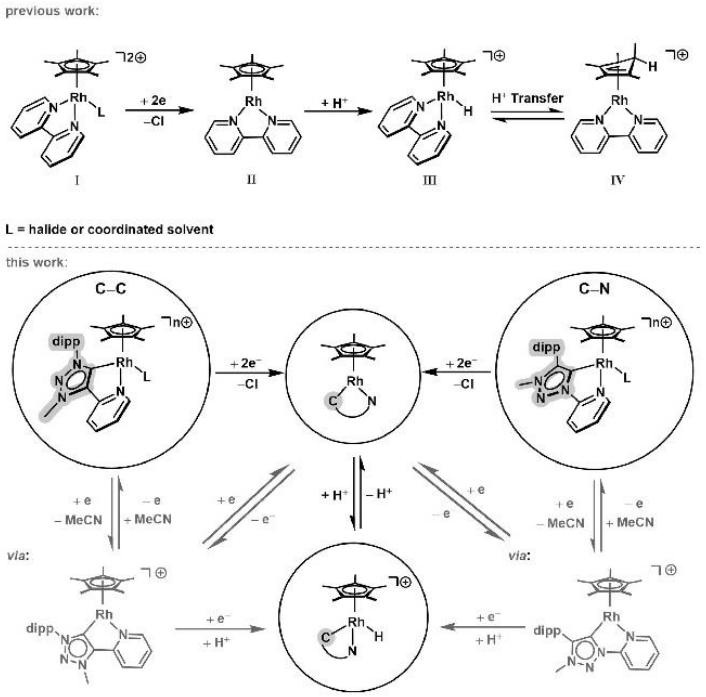

Scheme 1. Reported [RhCp*] hydride formation (top) in electrochemical H^+ reduction and presented work (bottom) for the precatalytic activation in electrocatalytically H_2 generation.

complex, as a function of the acidity of the proton source and the electronic structure of the corresponding ligands. In the presence of a weak acid, proton migration from the metal center into the Cp* ligand occurs. In agreement with the experimental finding, a stronger acid is required to evolve H_2. The direct addition of a strong acid, on the other hand, results in a rapid H_2 formation starting from the metal hydride complex, which is formed subsequently after addition to the reduced complexes.[11] In contrast, the modulation of the electronic properties by exchanging the polypyridine ligands with electron-rich 1,2-bis-(diphenylphosphino)benzene favors a metal-bound hydride complex, which show a remarkable stability.[19]

In 2015, our group reported a robust pyridyl mesoionic carbene (MIC) [CoCp*] complex for electrochemical H^+ reduction with acetic acid. The complex showed a low overpotential of 130 mV and turnover frequencies (TOF) of $4\times10^2\ s^{-1}$ with an outstanding turnover number (TON) of 650 000 at −1.54 V.[20] Additionally, Rh complexes of pyridyl-MIC ligands have been reported to be efficient hydrogenation and hydrosilylation catalysts[21] and Cp*Ir complexes with similar ligands are active transfer hydrogenation catalysts.[22] Metal complexes of pyridyl-MIC ligands were also shown to be efficient CO_2 reduction electrocatalysts.[23] For all of the aforementioned catalytic processes, the solvato, the reduced and the hydridic species are crucial intermediates. Recently, a [RhCp*] hydride complexes with a bis-NHC ligand (NHC = *N*-heterocyclic carbene) has been reported for the catalytic reduction of NAD^+ to NADH (= nicotinamide adenine dinucleotide) and crystallographically characterized.[24] However, very little information is available on their isolation and characterization, in particular with single crystal X-ray diffraction, and reactivity studies of such intermediates for complexes of pyridyl-MIC containing ligands.[25]

The ligands (**C–C** = pyridyl-4-triazolylidene[26] and **C–N** = pyridyl-1-triazolylidene)[27] presented in this work show similar overall π−acceptor properties and a highly increased overall σ−donor strength compared to the well-established bpy ligand. These properties are essential for electrocatalysis to maintain the low potential for the precatalytic activation, while increasing the electron density at the metal center to generate a highly active catalytic center.

Therefore, the high activity of the pyridyl-MIC complexes in electrocatalysis/reductive homogeneous catalysis and the aforementioned results motivated us to investigate the precatalytic activation of pyridyl-MIC containing [RhCp*] in the electrocatalytic H_2 formation with acetic acid. The combination of reaction-oriented electrochemistry with species-focused spectroscopy (spectroelectrochemistry, SEC) provides a detailed analysis of single and multiple electron-transfer processes.[4,28,29] Additionally, theoretical calculations and the isolation of highly reactive intermediates allows us to propose a mechanism for the precatalytic activation in pyridyl-MIC [RhCp*] complexes. The isolation, full characterization including single crystal X-ray diffraction, and reactivity studies of the chlorido, solvato,

Chemistry–A European Journal | Research Article
doi.org/10.1002/chem.202302354
Chemistry Europe
European Chemical Societies Publishing

hydridic and reduced complexes with the help of synthetic, crystallographic, electrochemical, spectroelectrochemical and theoretical methods are presented below.

Results and Discussion

Synthesis and Characterization

The synthesis of [Rh(**C**–**C**)Cl](PF$_6$) and [Rh(**C**–**N**)Cl](PF$_6$) was performed according to a modified silver(I)-transmetalation route reported by Bolje *et al.* for related d^6 metal complexes (**A**, Scheme 2).[30] The triazolium salt, [H(**C**–**C**)](BF$_4$) or [H(**C**–**N**)](PF$_6$), was dissolved in CH_3CN, Ag_2O was added and the suspension stirred for 3 days at room temperature under exclusion of light. After filtration and evaporation of the remaining solvent, [RhCp*Cl$_2$]$_2$ was added and dissolved in CH_2Cl_2. After three days, KPF_6 was added for salt-metathesis and the crude product was extracted with H_2O to remove the excess of salts, yielding orange crystals of [Rh(**C**–**C**)Cl](PF$_6$) (77%) or [Rh(**C**–**N**)Cl](PF$_6$) (91%) suitable for single crystal X-ray diffraction analysis (Figure 1).

To obtain the corresponding acetonitrile adducts [Rh(**C**–**C**)MeCN](PF$_6$)$_2$ and [Rh(**C**–**N**)MeCN](PF$_6$)$_2$ for detailed mechanistic studies, [Rh(**C**–**C**)Cl](PF$_6$) or [Rh(**C**–**N**)Cl](PF$_6$) was dissolved in CH_3CN and $AgPF_6$ was added (**B**, Scheme 2).[31]

The reaction mixture was stirred overnight under the exclusion of light, filtered and the concentrated solution was overlaid with *n*-hexane or first Et_2O, followed by *n*-hexane (1:1) yielding >99% of yellow crystals suitable for X-ray diffraction analysis (Figure 1).

Motivated by the work of Kölle and Blakemore, we tried to convert [Rh(**C**–**C**)Cl](PF$_6$) and [Rh(**C**–**N**)Cl](PF$_6$) with Na(Hg) in THF to access [Rh(**C**–**C**)] and [Rh(**C**–**N**)]. For these reactions, a color change from orange to deep green and purple, respectively, was observed.[17–19] However, after two hours, the reaction mixture changed to a dark brown solution, pointing to decomposition of the corresponding complexes, while some of the starting complexes remained in the crude products. Therefore, we changed our strategy using two equivalents of KC_8 in THF at −40 °C.[32] After warming up to room temperature over a two-hour period, the color-intense solution was filtered and the solvent was evaporated to complete dryness. Some drops of THF and an excess of *n*-hexane were added to the crude product, filtered and stored at −40 °C in the deep freezer for one month. We were able to collect deep purple single crystals of [Rh(**C**–**N**)] suitable for X-ray diffraction analysis (10%, Figure 1), while all crystallization attempts for [Rh(**C**–**C**)] at different temperatures and with different solvents failed.

To clarify, whether a [RhCp*] hydride complex is formed or the H^+ migrated [Rh(Cp*H)] complex, [Rh(**C**–**C**)Cl](PF$_6$) and [Rh(**C**–**N**)Cl](PF$_6$) was converted with an aqueous solution of NaOOCH/HCOOH (pH = 4.8) as hydride transferring agent, similar to a reported protocol.[15] In contrast to the direct protonation of [Rh(**C**–**C**)] and [Rh(**C**–**N**)], which did not work out, the synthesis with an aqueous solution of NaOOCH/HCOOH resulted in a clean conversion to the metal-bound hydrido complex [Rh(**C**–**C**)H](PF$_6$) and [Rh(**C**–**N**)H](PF$_6$) complexes (**D**, Scheme 2). Diffusion of *n*-hexane into a concentrated THF solution of [Rh(**C**–**N**)H](PF$_6$) yielded 43% of orange crystals suitable for X-ray diffraction analysis (Figure 1), while the

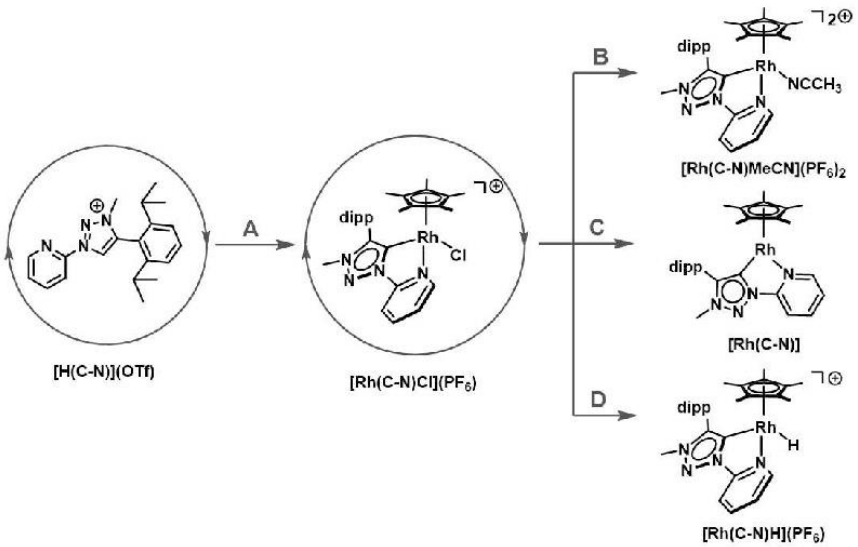

Scheme 2. Synthetic strategy for [Rh(**C**–**N**)Cl](PF$_6$), [Rh(**C**–**N**)MeCN](PF$_6$)$_2$, [Rh(**C**–**N**)] and [Rh(**C**–**N**)H](PF$_6$). Path **A**: [H(**C**–**N**)](PF$_6$), Ag_2O, CH_3CN, rt, 3 d; [RhCp*Cl$_2$]$_2$, CH_2Cl_2, rt, 3 d; KPF_6. Path **B**: [Rh(**C**–**N**)Cl](PF$_6$), $AgPF_6$, CH_3CN, rt, overnight. Path **C**: [Rh(**C**–**N**)Cl](PF$_6$), KC_8, THF, −40 °C to rt, 2 h. Path **D**: [Rh(**C**–**N**)Cl](PF$_6$), NaOOCH/HCOOH (pH = 4.8), 85 °C, 2 h. The same conditions were applied for [Rh(**C**–**C**)Cl](PF$_6$), [Rh(**C**–**C**)MeCN](PF$_6$)$_2$, [Rh(**C**–**C**)] and [Rh(**C**–**N**)H](PF$_6$), except for path **D** with an increased reaction time from 2 h to an overnight reaction.

Chemistry–A European Journal | Research Article
doi.org/10.1002/chem.202302354
Chemistry Europe
European Chemical Societies Publishing

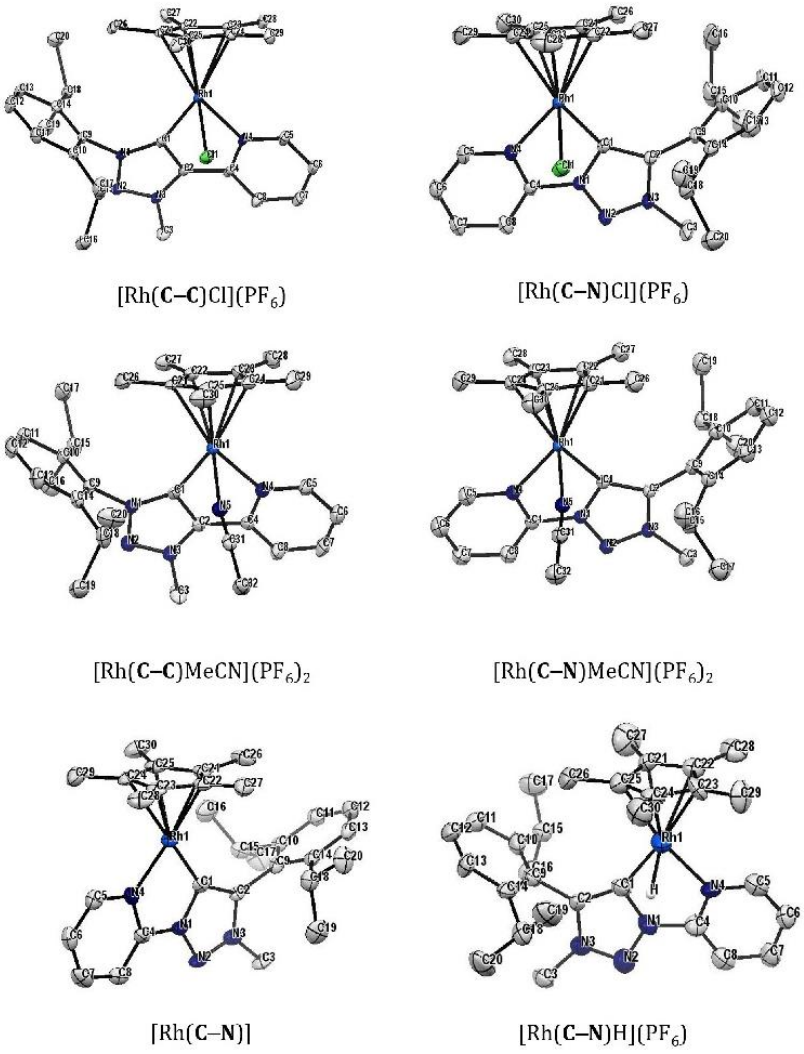

Figure 1. ORTEP representation of top left: [Rh(**C**–**C**)Cl](PF$_6$), top right: [Rh(**C**–**N**)Cl](PF$_6$), center left: [Rh(**C**–**C**)MeCN](PF$_6$)$_2$, center left: [Rh(**C**–**N**)MeCN](PF$_6$)$_2$, center right: [Rh(**C**–**N**)MeCN](PF$_6$)$_2$, bottom left: [Rh(**C**–**N**)] and bottom right: [Rh(**C**–**N**)H](PF$_6$) (carbon-hydrogens and counter ions are omitted for clarity). Ellipsoids are drawn with 50% probability.

crystalline material (40%) obtained for [Rh(**C**–**C**)H](PF$_6$) was not suitable for X-ray diffraction analysis.

The $^{13}C\{^1H\}$ NMR spectra of the presented complexes show characteristic doublet signals in the range of 170–160 MHz with Rh-MIC coupling constants between $J_{Rh,MIC}$ = 53–48 Hz.[24,33]

In the molecular structures in the crystal, the rhodium center in the complexes [Rh(**C**–**C**)Cl](PF$_6$), [Rh(**C**–**N**)Cl](PF$_6$), [Rh(**C**–**C**)MeCN](PF$_6$)$_2$ and [Rh(**C**–**N**)MeCN](PF$_6$)$_2$ display a three-legged piano-stool type geometry (Figure 1). The complexes show a η^5 mode from the Cp* ligand to the rhodium center with a metal-carbon bond length between 2.136(4)–2.227(1) Å. The angles between the planes of the Cp* ligand and the plane of the pyridyl-MIC coordination pocket at the rhodium center ((C1-N1-C4-N4) for [Rh(**C**–**N**)Cl](PF$_6$) and [Rh(**C**–**N**)MeCN](PF$_6$)$_2$ or (C1-C2-C4-N4) for [Rh(**C**–**C**)Cl](PF$_6$) and [Rh(**C**–**C**)MeCN](PF$_6$)$_2$, respectively) are in the range between 49.1°–56.7°, similar to those of [RhCp*(bpy)Cl]$^+$.[34] The complexes show a η^5 mode from the Cp* ligand to the rhodium center with a metal-carbon bond length between 2.136(4)–2.227(1) Å. The angles between the planes of the Cp* ligand and the plane of the pyridyl-MIC coordination pocket at the rhodium center ((C1-N1-C4-N4) for [Rh(**C**–**N**)Cl](PF$_6$) and [Rh(**C**–**N**)MeCN](PF$_6$)$_2$ or (C1-C2-C4-N4) for [Rh(**C**–**C**)Cl](PF$_6$) and [Rh(**C**–**C**)MeCN](PF$_6$)$_2$, respectively) are in the range between 49.1°–56.7°, similar to those of [RhCp*-(bpy)Cl]$^+$.[34] In contrast, an almost orthogonal geometry of the Cp* plane and the plane within the pyridyl-MIC coordination

Chemistry–A European Journal | Research Article doi.org/10.1002/chem.202302354 | Chemistry Europe European Chemical Societies Publishing

pocket (C1-N1-C4-N4) are observed in [Rh(**C**–**N**)H](PF$_6$) and [Rh(**C**–**N**)] (Figure 1).

In the case of the hydrido complex [Rh(**C**–**N**)H](PF$_6$), the angle between the two planes is 83.5°, whereas the [Rh(**C**–**N**)] complex displays an angle of 86.0°. The drastic change in the geometry around the rhodium center results in the elongation of the Rh-Cp* bond distance between 0.025 Å and 0.051 Å (Table 1, see SI, **3**).

The comparison of the piano-stool complexes with the almost orthogonal oriented complexes indicates a significant delocalization from the rhodium center to the pyridyl-MIC ligand in [Rh(**C**–**N**)] and [Rh(**C**–**N**)H](PF$_6$). The increased π−backbonding results in a decrease of the metal-pyridyl-*N* and metal-MIC bond distances. The Rh-N bond lengths decreases from 2.120(3)–2.140(3) Å to 2.122(9) Å for [Rh-(**C**–**N**)H](PF$_6$) and 2.006(5) Å for [Rh(**C**–**N**)], while the Rh–C(MIC) bond distances shorten from 2.051(1)–2.063(3) Å to 2.015(1) Å and 1.960(6) Å, respectively. Additionally, the formally reduced [Rh(**C**–**N**)] complex reveals an increase in the electron-density in the chelating C1-N1-C4-N4 framework (Table 1), indicated by the changes from partially C–N double bond character (~1.37 Å) to an increased C–N single-bond character (~1.40 Å) and *vice versa*. Only minimal changes in the intra-ligand (pyridyl-MIC) bond distances are observed other than those directly involved in the chelating pocket (see SI, Table S2 and S3). These data are thus an indication of a predominantly rhodium-based reduction, changing the formally Rh^{+III} center to a formally Rh^{+I} center.

Table 1. Selected bond lengths of [Rh(C–C)Cl](PF$_6$), [Rh(C–C)MeCN](PF$_6$)$_2$, [Rh(C–N)Cl](PF$_6$), [Rh(C–N)MeCN](PF$_6$)$_2$, [Rh(C–N)H](PF$_6$) and [Rh(C–N)].

	Bond lengths / Å	
Atoms	[Rh(C–C)Cl](PF$_6$)	[Rh(C–C)MeCN](PF$_6$)$_2$
Rh1-C1	2.052(3)	2.057(4)
C1-C2	1.388(4)	1.388(5)
C2-C4	1.454(4)	1.451(5)
C4-N4	1.357(4)	1.362(4)
N4-Rh1	2.120(3)	2.137(3)
Rh1-C21	2.175(3)	2.158(3)
Rh1-C22	2.150(3)	2.136(4)
Rh1-C23	2.173(3)	2.177(4)
Rh1-C24	2.201(3)	2.199(4)
Rh1-C25	2.191(3)	2.198(4)
	[Rh(C–N)Cl](PF$_6$)	[Rh(C–N)MeCN](PF$_6$)$_2$
Rh1-C1	2.051(1)	2.063(3)
C1-N1	1.370(2)	1.373(4)
N1-C4	1.405(1)	1.407(5)
C4-N4	1.332(2)	1.327(5)
N4-Rh1	2.133(2)	2.140(3)
Rh1-C21	2.143(1)	2.139(4)
Rh1-C22	2.143(1)	2.155(4)
Rh1-C23	2.227(1)	2.156(4)
Rh1-C24	2.213(1)	2.221(4)
Rh1-C25	2.138(1)	2.205(4)
	[Rh(C–N)H](PF$_6$)	[Rh(C–N)]
Rh1-C1	2.015(1)	1.960(6)
C1-N1	1.403(1)	1.394(7)
N1-C4	1.423(1)	1.374(7)
C4-N4	1.342(1)	1.369(7)
N4-Rh1	2.122(9)	2.006(5)
Rh1-C21	2.260(1)	2.192(6)
Rh1-C22	2.244(1)	2.245(6)
Rh1-C23	2.203(2)	2.241(5)
Rh1-C24	2.175(2)	2.241(6)
Rh1-C25	2.158(2)	2.245(6)

Hydride Reactivity

Transition-metal hydride complexes play a key role in the electrocatalytic H_2 formation.[2,3,9–11,35,36] The reactive intermediates can act as transferring reagent for H^+, H· or H^- and are of particular interest in the design of the electrocatalyst. However, the investigation of the hydride species remains challenging due to the high reactivity and instability in coordinating solvents. Hence, the isolation of the diamagnetic [Rh-(**C**–**C**)H](PF$_6$) and [Rh(**C**–**N**)H](PF$_6$) allows us to shine light on the reactivity of the metal bound hydride species (Scheme 3, see SI **7**).

In the ^{1}H NMR spectrum, both the hydride complexes show a metal-bound hydride signal at −11.46 ppm ($J_{Rh,H}$ = 22.0 Hz) and −11.48 ppm ($J_{Rh,H}$ = 23.1 Hz), respectively, similar to the hydride shift reported for electron-rich diphosphine ligands (see SI, **2.50** and **2.60**).[19] There is no evidence for the H^+ migration into the Cp* ligand, (even under variable temperature conditions) which would result in three inequivalent methyl resonances (see SI, Figure S10).[15,16] The strong σ−donating properties of the MIC-moieties lead to an increased electron density at formally Rh^{+III} centers, favoring the formation of the metal-bound [HRhCp*] complexes instead of the protonated [RhCp*H] complexes.

Further investigations by IR spectroscopy clearly confirm the metal-bound hydride species with a Rh-H stretching at $\tilde{\nu}$(Rh-H) = 1956 cm^{-1} for [Rh(**C**–**C**)H](PF$_6$) and at 1953 cm^{-1} for [Rh-(**C**–**N**)H](PF$_6$) (see SI, Figure S12 and S15). The Rh–H stretching frequencies are located between the earlier reported bpy and diphosphine based [Rh(Cp*)] hydride analogues, elucidating the synergy between reactivity and stability.[19,37]

The addition of $NaBH_4$ to the Rh-hydrides results in the formation of [Rh(**C**–**N**)] and [Rh(**C**–**C**)] (see SI, **7.10**) under evolution of H_2. The ^{1}H NMR shows a strong high field shift of the aromatic signals up to 6.53 ppm, confirming the strongly reduced character of the pyridyl-MIC ligands and the H^+ reactivity in [Rh(**C**–**N**)] and [Rh(**C**–**C**)].

Treatment of [Rh(**C**–**C**)H](PF$_6$) and [Rh(**C**–**N**)H](PF$_6$) with TEMPO (=(2,2,6,6-tetramethylpiperidin-1-yl)oxyl)) at room temperature results in a rapid formation of a EPR-active 17 VE species (Figure 2, see SI, **7.20**).

Chemistry–A European Journal | Research Article doi.org/10.1002/chem.202302354 | Chemistry Europe European Chemical Societies Publishing

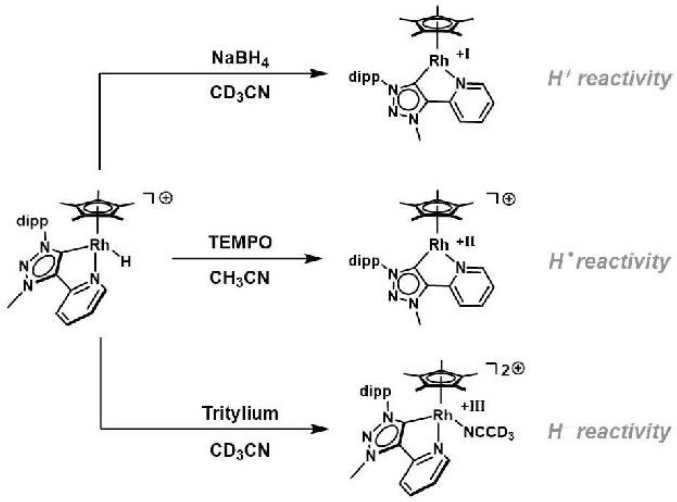

Scheme 3. Reactivity of [Rh(**C**–**C**)H](PF$_6$) as a H$^+$, H$^\cdot$ or H$^-$ in CD$_3$CN at room temperature. The same reaction conditions were applied for [Rh(**C**–**N**)H](PF$_6$) (see experimental section).

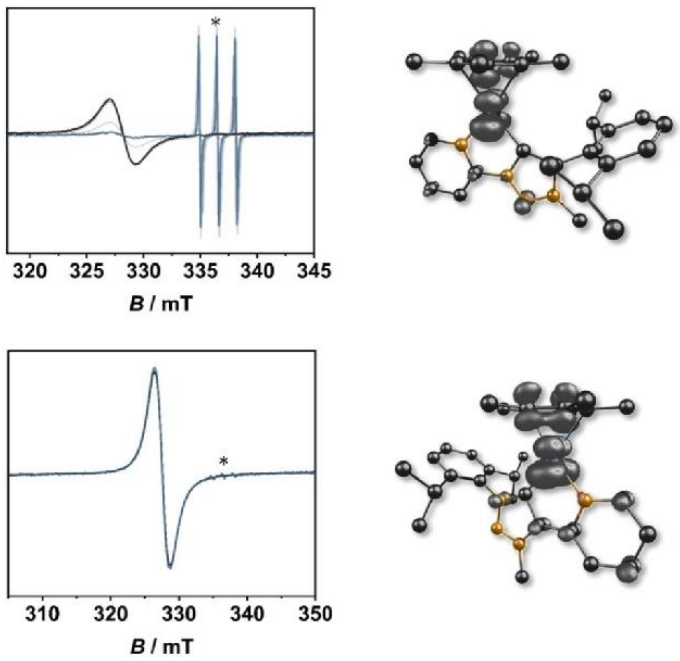

Figure 2. EPR spectra of [Rh(**C**–**N**)]$^+$ (top left) and [Rh(**C**–**C**)]$^+$ (bottom left) generated after addition of TEMPO to a CH$_3$CN solution of [Rh(**C**–**N**)H](PF$_6$) or [Rh(**C**–**C**)H](PF$_6$), respectively, over a 10 minute period (* = unreacted TEMPO) at room temperature (g = 2.06) and spin density plot of [Rh(**C**–**N**)]$^+$ (top right) and [Rh(**C**–**C**)]$^+$ (bottom right) (Rh = 46% for both complexes) with PBE0/RIJCOSX/D3BJ/def2-TZVP (iso value = 0.006).

The isotropic signal at a g-value of 2.06 for both complexes at room temperature is characteristic for a Rh(II) species.[36,38] Upon cooling, the EPR signal diminishes, most likely as consequence of dimerization of two EPR-active species. The EPR signal can be recovered by allowing the sample to warm up to room temperature again, further supporting the dimerization of the EPR-active intermediate. The isolation of the respective Rh(II) species failed due to the lack of stability during the crystallization attempts in the glovebox, indicated by a color

Chemistry–A European Journal | Research Article doi.org/10.1002/chem.202302354 | Chemistry Europe European Chemical Societies Publishing

change from a purple-grey to a colorless solution with a colorless precipitate.

In the case of $[Rh(\mathbf{C}–\mathbf{C})]^+$ a rhombic signal could be detected at low temperatures with $g_1 = 2.16$, $g_2 = 2.05$ and $g_3 = 1.98$ at −100 °C. The high g−anisotropy of $\Delta g = 0.11$ supports the strong metal contribution of the radical species (see SI, **7.20**), which is also reflected in the spin density plot of the coordinatively unsaturated $[Rh(\mathbf{C}–\mathbf{C})]^+$ (Rh = 46%) compared to the coordinatively saturated solvent adduct $[Rh(\mathbf{C}–\mathbf{C})MeCN]^+$(Rh = 1%). The above results indicate that the dimerization of the formally Rh^{II} based species is slower for $[Rh(\mathbf{C}–\mathbf{C})]^+$ in comparison to $[Rh(\mathbf{C}–\mathbf{N})]^+$.

The amphiphilic reactivity of $[Rh(\mathbf{C}–\mathbf{C})H](PF_6)$ and $[Rh(\mathbf{C}–\mathbf{N})H](PF_6)$ motivated us to further investigate the hydride transfer reactivity with $Ph_3C(PF_6)$ (=tritylium) in CD_3CN at room temperature (see SI, **7.30**). In the case of $[Rh(\mathbf{C}–\mathbf{N})H](PF_6)$, a clean conversion to triphenylmethane ($Ph_3C–\underline{H}$ = 5.61 ppm) under the formation of $[Rh(\mathbf{C}–\mathbf{N})MeCN\text{-}d_3](PF_6)_2$ was observed, while the reaction of $[Rh(\mathbf{C}–\mathbf{C})H](PF_6)_2$ with $Ph_3C(PF_6)$ leads to a mixture of $[Rh(\mathbf{C}–\mathbf{C})(MeCN\text{-}d_3)](PF_6)_2$, triphenylmethane, the starting material and an unknown species without any detectable metal-hydride signal in the ^1H NMR spectrum. Thus, the Rh-hydride complexes present here can act as either H^+, $H^\cdot$ or H^- transfer reagents displaying their true ambivalent nature.

The estimation of the pK_a values, bond dissociation free energies (BDFE) and hydricities (ΔG^0_H) was performed according to the correlation reported by Waldie *et al.* on the basis of the reduction potentials of the parent complexes in $[Rh(\mathbf{C}–\mathbf{C})MeCN](PF_6)$ and $[Rh(\mathbf{C}–\mathbf{C})MeCN](PF_6)$ (see cyclic voltammetry).[39]

The comparatively low pK_a values of 22.0 kcal/mol for $[Rh(\mathbf{C}–\mathbf{C})H]^+$ and 20.3 kcal/mol in the case of $[Rh(\mathbf{C}–\mathbf{N})H]^+$ emphasize a strong stabilization of the respective Rh(I) species by the excellent σ−donor and π−acceptor properties pyridyl-MIC ligands. The higher π−acceptor capacity of the C–N linked pyridyl-MIC ligand compared to its C–C linked counterpart likely results in an advantageous distribution of the electron density between the orthogonal oriented C–N ligand and the electron donating Cp* moiety in $[Rh(\mathbf{C}–\mathbf{N})]$.[40] In contrast, the analogues cyclometallated pyridyl-phenyl [RhCp*] hydride complexes reported by Norton *et al.* show pK_a values of 30.3 kcal/mol in acetonitrile.[36] The anionic nature of the cyclometallated ligand probably results in a destabilization of the Rh(I) species compared to the neutral pyridyl-MIC ligand.

The greater σ−donor properties of the C–C linked pyridyl-MIC ligand compared to the C–N linked constitutional isomer lead to a slightly lower BDFE in in $[Rh(\mathbf{C}–\mathbf{C})H]^+$ with 49.6 kcal/mol and 50.0 kcal/mol in $[Rh(\mathbf{C}–\mathbf{N})H]^+$ indicating an increased stabilization of the respective Rh(II) species.

However, these results should be taken with care as an identical hydricity of $\Delta G^0_{H^-} = 56.2$ kcal/mol is assigned for both complexes following the correlation by Waldie *et al.*. Future studies in our laboratories will focus on the direct determination of the experimental pK_a values, BDFE and $\Delta G^0_{H^-}$.

Cyclic Voltammetry

The electrochemical activation of polypyridine [RhCp*] complexes has been intensively studied over the past decades.[2,3,9–13,15,16,18] A 2e$^-$ reduction of Rh^{III} to Rh^I and the corresponding re-oxidation back to the Rh^{III} species is usually observed in these systems.

In contrast to previous reports on polypyridine [RhCp*] complexes, the 2e$^-$ reduction of $[Rh(\mathbf{C}–\mathbf{C})Cl](PF_6)$ and $[Rh(\mathbf{C}–\mathbf{N})Cl](PF_6)$ at $E^{red}_{p,c} = -1.46$ V and $E^{red}_{p,c} = -1.34$ V generates two new species in the re-oxidation cycle along with a shift of the anodic potential at $E^{ox1'}_{p,a} = -1.19$ V and $E^{ox2'}_{p,a} = -1.05$ V for $[Rh(\mathbf{C}–\mathbf{C})Cl](PF_6)$, and $E^{ox2'}_{p,a} = -1.12$ V and $E^{ox2'}_{p,a} = -1.03$ V for $[Rh(\mathbf{C}–\mathbf{N})Cl](PF_6)$, respectively (Figure 3).

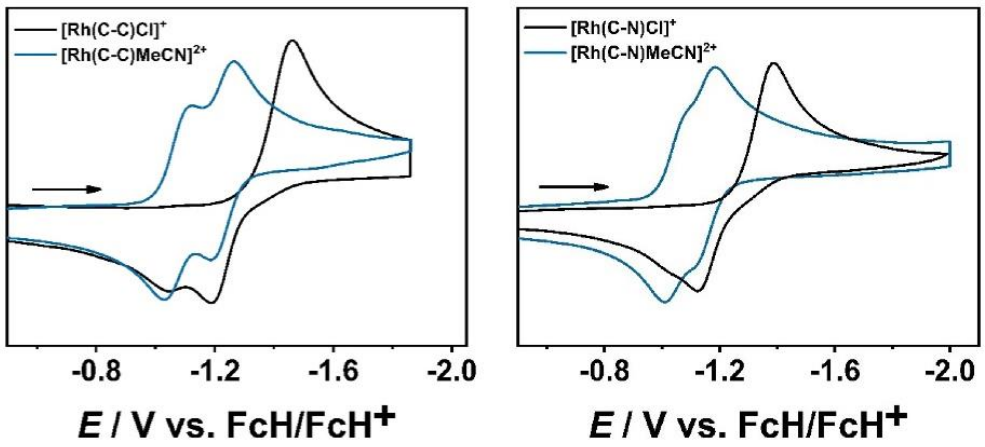

Figure 3. Comparison of the cyclic voltammograms of $[Rh(\mathbf{C}–\mathbf{C})Cl](PF_6)$ and $[Rh(\mathbf{C}–\mathbf{C})MeCN](PF_6)_2$ (left) and $[Rh(\mathbf{C}–\mathbf{N})Cl](PF_6)$ and $[Rh(\mathbf{C}–\mathbf{N})MeCN](PF_6)_2$ (right) in CH_3CN and 0.1 M Bu_4NPF_6 with a scan rate of 100 mV/s.

Chemistry–A European Journal | Research Article
doi.org/10.1002/chem.202302354
Chemistry Europe
European Chemical Societies Publishing

The first 2e$^-$ reduction is shifted according to the overall π−acceptor capacities of the two ligands, described earlier by our group.[27,40] The C–C linked ligand displays a weaker π−acceptor ability, compared to its C–N linked counterpart. After 2e$^-$ reduction, subsequent chloride dissociation takes place, leading to the formation of the respective [Rh(**C**–**C**)] and [Rh(**C**–**N**)] complexes. The drastic structural reorganization initiates an electronic re-distribution from the predominantly pyridyl-MIC centered electron to the central metal atom, formally generating a Rh^{+I} metal center.

Reversing the scan direction shows two distinct one-electron oxidations. According to our assumption, the first oxidation can be assigned to a Rh(I)/Rh(II) redox couple. The Rh(I)/Rh(II) redox couple of the respective complexes is shifted according to the overall σ−donor strength of the respective ligands.[40] The higher overall σ−donor properties of the C–C linked ligand leads to a greater destabilization of the rhodium-centered orbitals, as indicated by the cathodic shift at $E_{1/2}^{ox1'} = -1.18$ V. In contrast, the weaker σ−donor strength of the C–N linked counterpart results in an anodic shift of the metal-centered oxidation at $E_{1/2}^{ox1'} = -1.11$ V.

The second oxidation at $E_{p,a}^{ox2'} = -1.03$ V, for the C–C linked complex, and at $E_{p,a}^{ox2'} = -1.01$ V, for the C–N linked counterpart, display nearly identical oxidation potentials. Therefore, the second oxidation can be assigned to the Rh(II)/Rh(III) redox couple, resulting in the respective solvato complexes.

With the acetonitrile adducts in hand, we examined the electrochemical transformation in cyclic voltammetry (Figure 3, see SI, **4.30**). Both complexes show two separated one-electron reduction processes. The high peak-to-peak separation ($\Delta E_{p,c}^{red1} = 90$ mV) of the first reduction at $E_{p,c}^{red1} = -1.06$ V, for both complexes, provides first indications of a structural reorganization accompanied by the loss of the acetonitrile ligand after the first metal-centered reduction (for details, see **4.** and **5.**).

In contrast, the second reduction at $E_{1/2}^{red2} = -1.24$ V, for [Rh(**C**–**C**)MeCN](PF$_6$)$_2$, and $E_{1/2}^{red2} = -1.15$ V, for [Rh(**C**–**C**)MeCN](PF$_6$)$_2$, display a smaller peak-to-peak separation of $\Delta E_{1/2}^{red2} = 70$ mV for both complexes. The second reduction potential follows the same trend in the π−acceptor properties of the ligands, as earlier described for the respective chlorido [RhCp*] complexes. The decreased peak-to-peak separation indicates a minor structural reorganization and further supports the partially loss of the acetonitrile ligand.

Furthermore, complex [Rh(**C**–**N**)] was investigated by cyclic voltammetry (Figure 4). Starting from an initial potential of −1.73 V, the Rh(I)/Rh(II) and Rh(II)/Rh(III) redox couple are in good agreement with the reduction processes observed for [Rh(**C**–**N**)MeCN](PF$_6$)$_2$. This match also further confirms the dissociation of the solvent molecule upon one electron reduction of the acetonitrile complexes as discussed above.

All complexes show a further third irreversible reduction at $E_{p,c}^{red3} = -2.69$ V for [Rh(**C**–**C**)] and $E_{p,c}^{red3} = -2.81$ V for [Rh(**C**–**N**)], respectively.

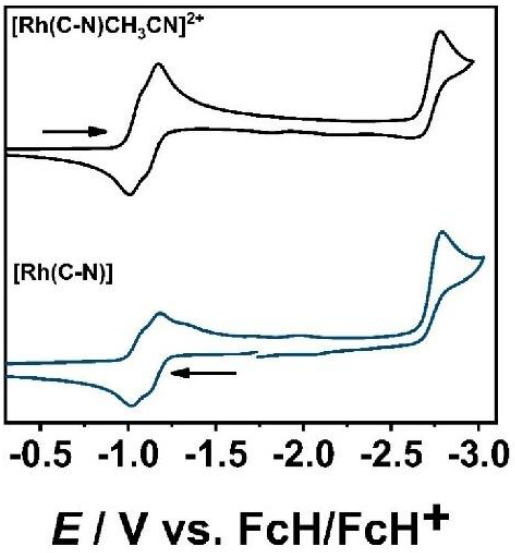

Figure 4. Comparison of [Rh(**C**–**N**)MeCN](PF$_6$)$_2$ (top, black) and [Rh(**C**–**N**)] (bottom, blue) in CH_3CN and with 0.1 M Bu_4NPF_6 with a scan rate of 100 mV/s.

Electrochemical H^+ Reduction

To investigate the precatalytic activation in the electrochemical H^+ reduction, all complexes were tested in presence acetic acid (=AcOH) as proton source (Figure 5, see SI, **8**). The two-electron reduced forms of the solvent complexes [Rh(**C**–**C**)MeCN](PF$_6$)$_2$ and [Rh(**C**–**N**)MeCN](PF$_6$)$_2$ are excellent candidates to provide useful insights in the precatalytic activation to generate the corresponding [RhCp*] hydride complexes.

In the presence of acetic acid, the first reduction, which results in the loss of acetonitrile remains intact (Figure 5). However, addition of one equivalent of the acid shifts the second reduction to more anodic potential, indicating the formation of new species at −1.21 V for [Rh(**C**–**C**)MeCN](PF$_6$)$_2$ and −1.14 V for [Rh(**C**–**N**)MeCN](PF$_6$)$_2$, which undergo an additional reduction at −2.11 V and −1.97 V, respectively.

However, the addition of more equivalents shifts the potential only slightly to more anodic potential (−1.18 V for [Rh(**C**–**C**)MeCN](PF$_6$)$_2$ and −1.11 V for [Rh(**C**–**N**)MeCN](PF$_6$)$_2$) without significantly influencing the current. In contrast, the current at −1.97 V constantly increases, indicating the catalytic conversion of H^+ in presence of the catalysts.

The stepwise addition of five equivalents shows an interesting trend: one-electron reduction of Rh^{III} to Rh^{II} turns into a two-electron reduction, as indicated by the increased current, while the Rh^{II}/Rh^{I} redox couple is no longer apparent. This observations emphasize a rapid CE mechanism or a proton-coupled electron transfer (PCET) after the first reduction and subsequent loss of acetonitrile.[41] We have performed tentative calculations of TOF for these catalysts at low proton concentrations (see section 8, SI). However, as the catalytic current with these

Chemistry–A European Journal | Research Article
doi.org/10.1002/chem.202302354
Chemistry Europe
European Chemical Societies Publishing

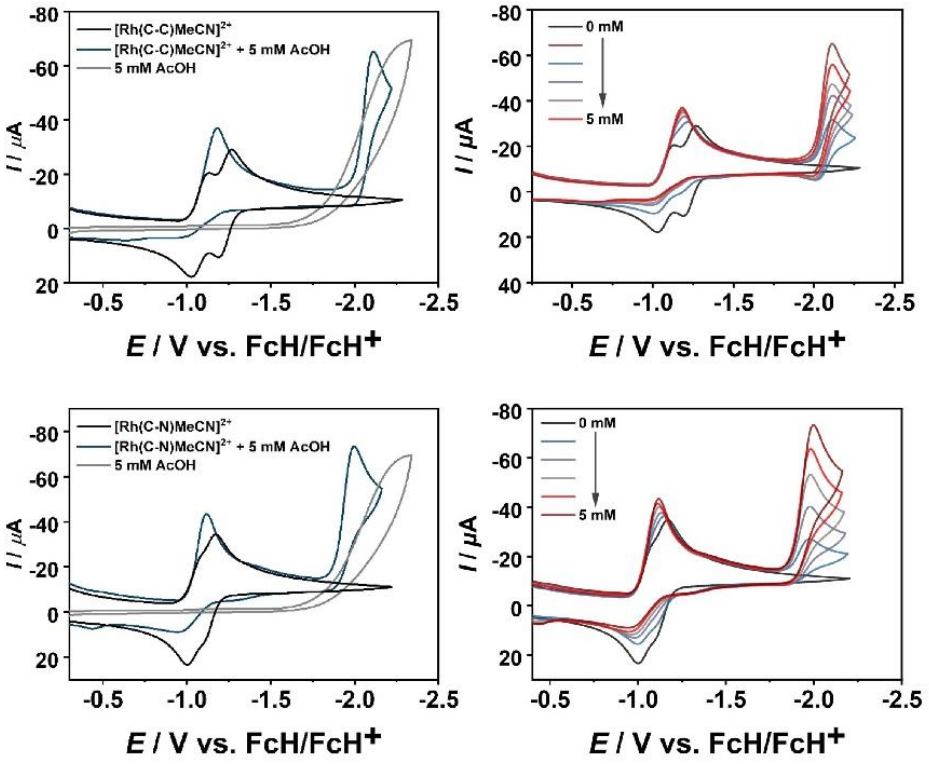

Figure 5. Electrochemical H^+ reduction with [Rh(**C**–**C**)MeCN]$(PF_6)_2$ (top) and [Rh(**C**–**N**)MeCN]$(PF_6)_2$ (bottom) (1 mM) in CH_3CN and 0.1 M Bu_4NPF_6 with a scan rate of 100 mV/s (left: black = without AcOH, grey = only AcOH, green = with 10 mM AcOH) and at low concentrations of AcOH (right).

complexes are almost in the region of the background current of the direct reduction of the protons at the electrode surfaces (see control measurements, section 8, SI), these values should be taken with caution.

Taking all the data together, the first reduction results in the dissociation of the acetonitrile ligand, generating the coordinatively unsaturated Rh(II) complexes, which can undergo a either a CE mechanism or a PCET to form the respective [RhCp*]-hydride complexes.

An additional electron-transfer is required to initiate the electrocatalytic H^+ reduction. Unfortunately, the [RhCp*]-hydride complexes are not sufficiently stable under the electrochemical conditions, indicated by a drastically color changes after couple of minutes, even under fully inert conditions (see SI, **4.50** and **4.60**). Therefore, we turned our focus to UV/vis/NIR (spectro−)electrochemistry (UV/vis/NIR-SEC).

UV/vis/NIR (Spectro−)electrochemistry

UV/vis/NIR SEC is a powerful technique to detect short-lived intermediates in electron-transfer processes. In combination with (TD)-DFT calculations, detailed mechanistic insights can be provided to understand the precatalytic formation.[4,12,28,29]

The well-separated multi-electron processes makes [Rh(**C**–**C**)MeCN]$(PF_6)_2$ a good candidate to study in UV/vis/NIR-SEC. The complex displays a featureless UV/vis spectrum with several mixed metal-ligand-to-ligand charged transfer (MLLCT) and ligand-to-metal-charge transfer (LMCT) bands, indicated by the bright yellow color of the complex (see SI, **6.40**), while the chloride containing complex features an additional metal-chloride-to-ligand charge transfer band (MXLCT).

Upon reduction to [Rh(**C**–**C**)], the UV/vis/NIR spectrum shows intense absorption bands in the visible and near-infrared range around 823 nm, 589 nm and 436 nm, which can be assigned to different MLCT bands from the rhodium center with small contribution of the Cp* ligand to the pyridyl-MIC ligand (Figure 6, see SI, **6.80**). The two-electron reduction is accordingly accompanied by a color change from light yellow to dark green. The same trend in this regard is observed in the case of complex [Rh(**C**–**N**)MeCN]$(PF_6)_2$. Upon reduction, [Rh(**C**–**N**)] turns dark purple in color and a blue-shift of the MLCT bands is observed. The chloride containing complexes display identical absorption spectra after two-electron reduction as the ones described above and are in good agreement with the previously described electrochemical data.

During the reduction of [Rh(**C**–**C**)MeCN]$(PF_6)_2$ in SEC experiments, an intermediate could be detected. Our TD-DFT

Chemistry–A European Journal | Research Article doi.org/10.1002/chem.202302354 | Chemistry Europe European Chemical Societies Publishing

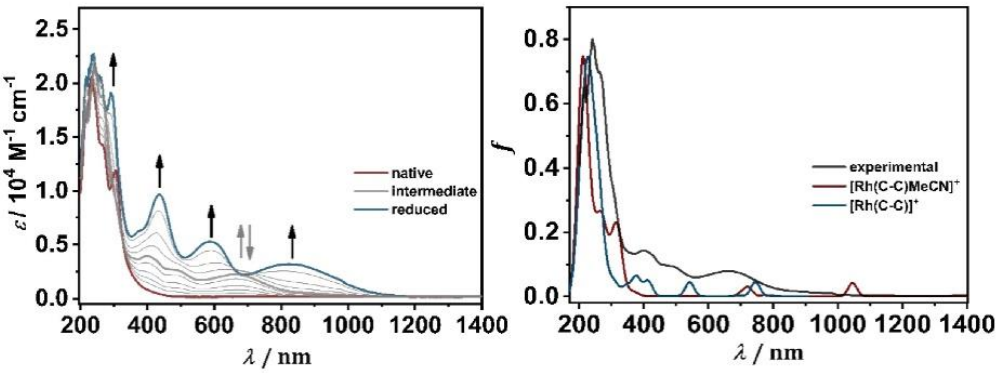

Figure 6. Changes in the UV/vis/NIR spectra of [Rh(**C**–**C**)MeCN]$(PF_6)_2$ in CH_3CN/0.1 M Bu_4NPF_6 during the first two reductions with a Au working electrode (left) and calculated spectra (right, PBE0/RIJCOSX/D3BJ/def2-TZVP, FWHM = 32) of [Rh(**C**–**C**)MeCN]$^+$ (red), [Rh(**C**–**C**)]$^+$ (blue) in comparison with experimental intermediate (black, normalized).

calculations confirm the formation of the coordinatively unsaturated [Rh(**C**–**C**)]$^+$ complex (Figure 6, right: blue), instead of the solvent coordinated [Rh(**C**–**C**)MeCN]$^+$ complex (Figure 6, right: red), as indicated by the characteristic absorption bands between 380–600 nm. This is in good agreement with the aforementioned EPR spectra of [Rh(**C**–**C**)]$^+$ and [Rh(**C**–**N**)]$^+$ (Figure 2). The absorption bands observed for [Rh(**C**–**C**)]$^+$ display similar features as described for [Rh(**C**–**C**)]. The blue-shift is a consequence of the change in the formal oxidation state of the rhodium center from Rh(I) to Rh(II). To compensate the electron deficiency at the rhodium center, the Cp* ligand contributes stronger to the electronic transitions (see SI, **6.40** and **6.80**). The comparison of the spectra before and after bulk electrolysis reveals that even after the chemical transformation due to ligand dissociation, the initial spectra could be restored after SEC for all studied complexes. In the case of the chloride containing [RhCp*] complexes, it is reasonable to predict the formation of [Rh(**C**–**C**)MeCN]$(PF_6)_2$ and [Rh(**C**–**N**)MeCN]$(PF_6)_2$ after SEC due to chloride dissociation and solvent coordination.

However, according to our spectroelectrochemical data, the coordination of the chloride takes place when sweeping back to the anodic potential (see SI, **5.10** and **5.20**). This observation could have a drastic impact on electrocatalysis, as the chloride, in the vicinity of the reduced [RhCp*] complex, can influence the preequilibrium during electrochemical H^+ reduction.

No intermediates in the visible spectrum could be detected during the reduction process in the presence of acetic acid, likely confirming a rapid CE mechanism or PCET in the electrochemical generation of [Rh(**C**–**C**)H](PF_6) and [Rh(**C**–**N**)H](PF_6) (Figure 7). The absorption spectra show a characteristic metal-hydride-to-ligand charge transfer (MHLCT) at 430 nm and 444 nm, respectively, which are in good agreement with our TD-DFT calculations (PBE0/RIJCOSX/D3BJ/def2-TZVP, see SI, **6.6** and **6.7**).

With the [RhCp*] hydride complexes and the reduced complexes in hand, we compared the electrochemically generated species with the chemically isolated complexes (Figure 8, see SI, **5.50**).

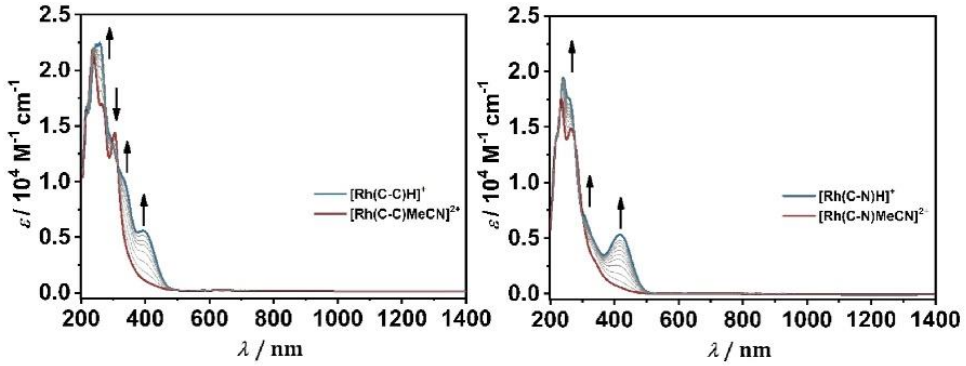

Figure 7. Changes in the UV/vis/NIR spectra of [Rh(**C**–**C**)MeCN]$(PF_6)_2$ (left) and [Rh(**C**–**N**)MeCN]$(PF_6)_2$ (right) in CH_3CN/0.1 M Bu_4NPF_6 during the two reductions in presence of excess AcOH with a Au working electrode.

Chemistry–A European Journal | Research Article doi.org/10.1002/chem.202302354 | Chemistry Europe European Chemical Societies Publishing

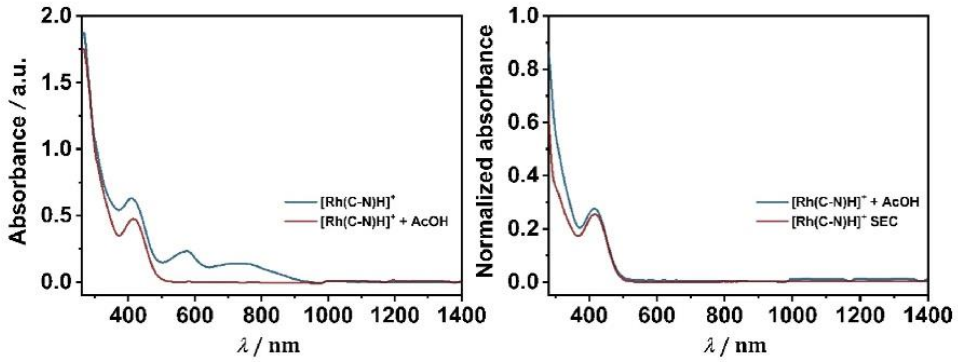

Figure 8. Left: UV/vis/NIR spectra of [Rh(**C**–**N**)H](PF$_6$) (blue) and after addition of an excess AcOH in CH$_3$CN (red). Right: Comparison of the UV/vis/NIR spectra of the chemically isolated [Rh(**C**–**N**)H](PF$_6$) (blue) and after bulk electrolysis with an Au working electrode in presence of an excess AcOH (red) in CH$_3$CN/0.1 M Bu_4NPF_6.

In the case of [Rh(**C**–**N**)], the absorption spectrum of the isolated complex shows the same transitions as observed for the electrochemically generated species, while the isolated [Rh(**C**–**N**)H](PF$_6$) complex shows a mixture of [Rh(**C**–**N**)] and [Rh(**C**–**N**)H](PF$_6$) generated during SEC. Addition of excess acetic acid exclusively generates the [RhCp*] hydride complex indicating an equilibrium between [Rh(**C**–**N**)] and the weakly bound hydride in [Rh(**C**–**N**)H](PF$_6$).

To our surprise, the electrochemically and chemically generated spectra of [Rh(**C**–**C**)] are not identical in acetonitrile. However, changing the solvent to THF results in a good fit of both spectra (see SI, **5.51**). A plausible explanation might be solvent effects causing degradation in presence of light.

In the case of [Rh(**C**–**C**)H](PF$_6$), the chemically isolated complex and the electrochemically generated species fit well, beside the presence of a second unknown species, which diminish upon addition of acetic acid. Unfortunately, our spectroscopic and electrochemcial data do not provide any convincing evidence to assign the nature of the unknown species due to the absence of additional hydride signals in the ^{1}H NMR.

Conclusions

In summary, we have presented the first isolation and a thorough characterization through crystallographic, spectroscopic and (spectro)electrochemical methods of solvato, hydrido, and reduced species of Cp*Rh complexes with pyridyl-mesoionic carbene ligands. A detailed mechanistic study of the precatalytic activation of pyridiyl-MIC [RhCp*] complexes is presented (Scheme 4). Cyclic voltammetric studies, combined with UV/vis/NIR-SEC measurements and theoretical calculations reveal a two-electron reduction process (Scheme 4, $\mathbf{E^1}$ and $\mathbf{E^2}$) to generate the coordinatively unsaturated [RhCp*] complexes after ligand dissociation, which are the first of their kinds to be isolated and fully characterized.

In presence of acetic acid, a PCET is observed after the first reduction generating the [RhCp*] hydride complexes (Scheme 4, $\mathbf{E^2}$). The data presented here are of fundamental importance for the mechanistic understanding of a range of reductive electrocatalytic and homogeneous catalytic processes with metal complexes of pyridyl-MIC ligands. The utility of such complexes in several electrocatalytic processes, including a synthetic strategy to reduce their overpotential, and a detailed mechanistic understanding thereof are currently under investigation in our laboratories.

Experimental Section

General Procedures, Materials, and Instrumentation

Caution! Compounds containing azides are potentially explosive. Although we never experienced any problems during synthesis or analysis, all compounds should be synthesized only in small quantities and handled with great care! Unless otherwise noted, all reactions were carried out using standard Schlenk-line-techniques under an inert atmosphere of argon (Linde Argon 4.8, purity 99.998%). Commercially available chemicals were used without further purification. The solvents used for metal complex synthesis and catalysis were available from MBRAUN MB-SPS-800 solvent System and degassed by standard techniques prior to use. The identity and purity of compounds were established via ^{1}H and ^{13}C NMR spectroscopy, elemental analysis and mass spectrometry. Solvents for cyclic voltammetry and UV/vis- and EPR-spectroelectrochemical measurements were dried and distilled under argon and degassed by common techniques prior to use. Column chromatography was performed over silica 60 M (0.04–0.063 mm). ^{1}H and ^{13}C{^{1}H} NMR spectra were recorded on a Bruker Avance 500 spectrometer at 19–22 °C. Chemical shifts are reported in ppm referenced to the residual solvent peaks.[42] The following abbreviations are used to represent the multiplicity of the signals: s (singlet), d (doublet), t (triplet), q (quartet), p (pentet), sept (septet), hept (heptet). Mass spectrometry was performed on an Agilent 6210 ESI-TOF. Elemental analyses were performed with an Elementar Micro Cube elemental analyser.

Chemistry–A European Journal
Research Article
doi.org/10.1002/chem.202302354
Chemistry Europe
European Chemical Societies Publishing

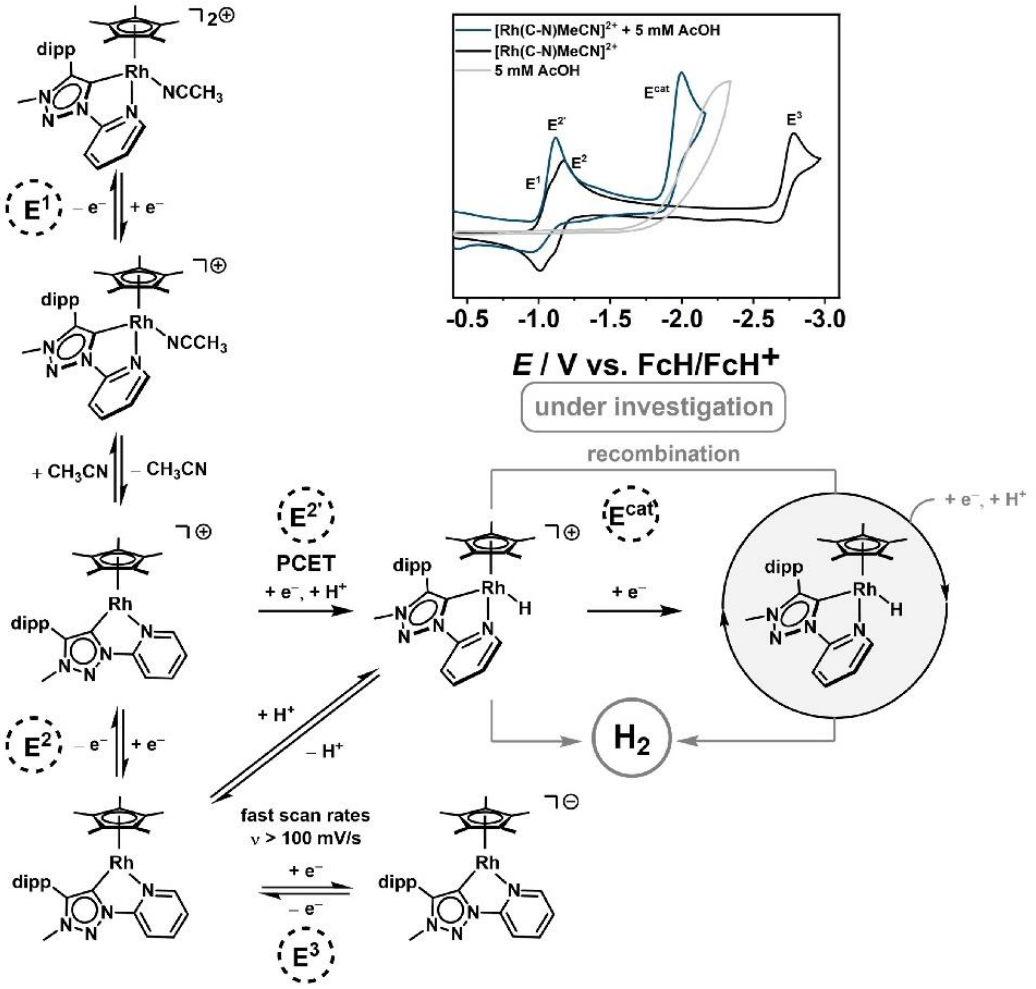

Scheme 4. Proposed precatalytic activation of [Rh(**C**–**N**)MeCN]$(PF_6)_2$ in CH_3CN/0.1 M Bu_4NPF_6 with a GC working electrode.

X-ray Diffraction

Deposition Numbers 2075636 (for [Rh(**C**–**C**)Cl](PF_6)), 2133478 (for [Rh(**C**–**C**)MeCN]$(PF_6)_2$), 2075640 (for [Rh(**C**–**N**)Cl](PF_6)), 2133502 (for [Rh(**C**–**N**)MeCN]$(PF_6)_2$), 2173197 (for [Rh(**C**–**N**)H](PF_6)), 2127781 (for [Rh(**C**–**N**)]) contain the supplementary crystallographic data for this paper. These data are provided free of charge by the joint Cambridge Crystallographic Data Centre and Fachinformationszentrum Karlsruhe Access Structures service. X-ray data were collected on a BRUKER Smart AXS, BRUKER D8 Venture or Bruker Kappa Apex2duo system. Data were collected at 100(2) or 140(2) K, respectively, using graphite-monochromatic Mo K_α radiation (λ_α =0.71073 Å). The strategy for the data collection was evaluated by using the APEX2 or Smart software. The data were collected by standard "ω scan techniques" or "$\omega - \varphi$ scan techniques" and were scaled and reduced using APEX2, SAINT+, and SADABS software. The structures were solved by direct methods using SHELXL-97 or intrinsic phasing using SHELXL-2014/7 and refined by full matrix least-squares with SHELXL-2014/7, refining on F^2. Non-hydrogen atoms were refined anisotropically. If it is noted, bond length and angles were measured with Mercury, version 3.8.[43]

Electrochemistry

Cyclic voltammograms were recorded with a PalmSens4 potentiostat with a conventional three-electrode configuration consisting of a glassy carbon working electrode, a platinum auxiliary electrode, and a coiled silver wire as a pseudo reference electrode. The (decamethyl)ferrocene/(decamethyl)ferrocenium couple was used as internal reference. All measurements were performed at room temperature with a scan rate between 25 and 1000 mVs^{-1}. The experiments were carried out in absolute acetonitrile containing 0.1 M Bu_4NPF_6 (Sigma Aldrich, ≥99.0 %, electrochemical grade) as the supporting electrolyte. For electrocatalysis a solution of acetic acid (1 M) in acetonitrile was added to a 1 mM solution of the complex in steps of 5 μL or 25 μL and measured with all scan rates mentioned above. (Decamethyl)ferrocene/(decamethyl)ferrocenium couple (1 mg, 1 mM) was added as internal reference.

Chemistry–A European Journal | Research Article doi.org/10.1002/chem.202302354 | Chemistry Europe European Chemical Societies Publishing

Spectroelectrochemistry

UV/vis spectra were recorded with a J&M TIDAS spectrometer and the IR spectra were performed with a Bruker FT-IR Spectrometer INVENIO. The spectroelectrochemical measurements were carried out in an optically transparent thin-layer electrochemical (OTTLE)[44] cell (CaF_2 windows) with a gold-mesh working electrode, a platinum-mesh counter electrode, and a silver-foil pseudo reference. The spectroelectrochemical experiments were carried out in absolute acetonitrile containing 0.1 M Bu_4NPF_6 as the supporting electrolyte. The same solvents as for the CV measurements were used for each compound.

EPR Spectroscopy

EPR spectra at the X-band frequency (ca. 9.5 GHz) were obtained with a Magnetech MS-5000 benchtop EPR spectrometer equipped with a rectangular TE 102 cavity and a TC HO4 temperature controller. The measurements were carried out in synthetic quartz glass tubes. The low temperature EPR-spectra were performed up to −175 °C.

Calculations

The program package ORCA 4.1. was used for all DFT calculations.[45] Starting from the molecular structure obtained from X-ray diffraction geometry optimizations were carried out using the PBE0[46] functional and no symmetry restrictions were imposed during the optimization. All calculations were performed with empirical Van der Waals correction (D3).[47] The restricted and unrestricted DFT methods were employed for closed and open shell molecules respectively unless stated otherwise. Convergence criteria were set to default for geometry-optimization (OPT), and tight for SCF calculations (TIGHTSCF). Triple-ζ–valence basis sets (def2-TZVP)[48] were employed for all atoms. Calculations were performed using resolution of the identity approximation[49] with matching auxiliary basis sets[50] for geometry optimizations and numerical frequency calculations and the RIJCOSX (combination of the resolution of the identity and chain of spheres algorithms) approximation for single point calculations using the PBE0 functional.[46] Low-lying excitation energies were calculated with time-dependent DFT (TD-DFT). Solvent effects were taken into account with the conductor-like polarizable continuum model, CPCM.[51] Spin densities were calculated according to the Mulliken population analysis.[52] The absence of imaginary frequency Spin densities, molecular orbitals and difference densities were visualized with the modified Chemcraft 1.8 program.[53] All molecular orbitals are illustrated with an iso value of 0.052. All calculated TD-DFT spectra are Gaussian broadened with a band width of 25 at half height.

Synthesis and Characterization

Synthesis of [Rh(C–C)Cl](PF$_6$)

According to a modified synthetic procedure from Bolje *et al.*,[30] [H(**C–C**)](BF$_4$)[26] (0.87 g, 0.213 mmol), KCl (0.16 g, 2.125 mmol) and Ag_2O (0.17 g, 0.748 mmoL) was dissolved in 20 mL CH_3CN and stirred for 3 days at room temperature under exclusion of light. The solution was filtered and the remaining solvent was evaporated. [RhCp*Cl$_2$]$_2$ (0.07 g, 0.113 mmol) was added and dissolved in CH_2Cl_2. The reaction mixture was stirred for 3 days at room temperature under exclusion of light. An excess of KPF_6 (0.16 g, 0.850 mmol) was added and the reaction mixture was rigorous stirred for 20 min. The orange solution was filtered through Celite and extracted with 3 x H_2O (50 mL). The organic phase was separated and dried over Na_2SO_4. Additional crystallization from slow diffusion of *n*-hexane/Et_2O (1 : 1) into a concentrated solution of [Rh(**C–C**)Cl](PF$_6$) in CH_2Cl_2 yielded orange crystals (120 mg, 0.162 mmol, 77 %) suitable for X-ray diffraction analysis. In case of an insufficient conversion, purification by column chromatography (aluminum oxide, activated with 5 w% water; CH_2Cl_2/CH_3CN 100:0→1:1) resulted in pure [Rh(**C–C**)Cl](PF$_6$).

^{1}H NMR (500 MHz, $CDCl_3$) δ =8.77 (d, J=5.5 Hz, 1H), 8.10–8.03 (m, 2H), 7.59 (t, J=7.8 Hz, 1H), 7.54 (td, J=5.4, 2.8 Hz, 1H), 7.44 (dd, J=7.8, 1.1 Hz, 1H), 7.39 (dd, J=7.8, 1.1 Hz, 1H), 4.60 (s, 3H), 3.28 (hept, J=6.4 Hz, 1H), 2.58 (hept, J=6.4 Hz, 1H), 1.43 (s, 15H), 1.37 (d, J=6.6 Hz, 3H), 1.31 (d, J=6.6 Hz, 3H), 1.26 (d, J=6.6 Hz, 3H), 0.81 (d, J=6.9 Hz, 3H) ppm; **^{13}C{^{1}H} NMR** (126 MHz, $CDCl_3$) δ =170.31 (d, J=53.2 Hz, 1 C, MIC-Rh), 152.21, 148.45, 147.05, 146.66, 145.41, 139.34, 134.42, 131.72, 125.63, 125.63, 124.24, 124.05, 121.72, 97.72 (d, J=7.0 Hz, 5 C, Rh-Cp*), 39.22, 28.66, 27.88, 27.20, 25.55, 21.90, 21.80, 9.01 ppm; **MS (ESI-ToF)**: m/z found: 593.1944, calcd: 593.1913 ($C_{18}H_{22}ClN_4Rh^+$); **Elemental analysis** calcd. (%) for $C_{30}H_{39}ClF_6N_4PRh$: C 48.76, H 5.32, N 7.58; found: C 48.78, H 5.39, N 7.52.

Synthesis of [Rh(C–N)Cl](PF$_6$)

According to a modified synthetic procedure from Bolje *et al.*,[13] [H(**C–N**)](OTf)[15] (0.10 g, 0.213 mmol), KCl (0.16 g, 2.125 mmol) and Ag_2O (0.17 g, 0.748 mmoL) was dissolved in 20 mL CH_3CN and stirred for 3 days at room temperature under exclusion of light. The solution was filtered and the remaining solvent was evaporated. [RhCp*Cl$_2$]$_2$ (0.07 g, 0.113 mmol) was added and dissolved in CH_2Cl_2. The reaction mixture was stirred for 3 days at room temperature under exclusion of light. An excess of KPF_6 (0.16 g, 0.850 mmol) was added and the reaction mixture was rigorous stirred for 20 min. The orange solution was filtered through Celite and extracted with 3×H_2O (50 mL). The organic phase was separated and dried over Na_2SO_4. Additional crystallization from slow diffusion of *n*-hexane into a concentrated solution of [Rh(**C–N**)Cl](PF$_6$) in CH_2Cl_2 yielded orange crystals (142 mg, 0.192 mmol, 91 %) suitable for X-ray diffraction analysis. In case of an insufficient conversion, purification by column chromatography (aluminum oxide, activated with 5 w% water; CH_2Cl_2/CH_3CN 100:0→1:1) resulted in pure [Rh(**C–N**)Cl](PF$_6$).

^{1}H NMR (500 MHz, $CDCl_3$) δ δ 8.67–8.64 (m, 1H), 8.27 (ddd, J=8.2, 1.3, 0.7 Hz, 1H), 8.19 (ddd, J=8.3, 7.6, 1.5 Hz, 1H), 7.73 (ddd, J=7.5, 5.6, 1.3 Hz, 1H), 7.60 (t, J=7.8 Hz, 1H), 7.42 (dd, J=7.9, 1.1 Hz, 1H), 7.38 (dd, J=7.8, 1.0 Hz, 1H), 4.01 (s, 3H), 3.09 (hept, J=6.7 Hz, 1H), 2.82 (hept, J=6.7 Hz, 1H), 1.55 (s, 12H), 1.37 (d, J=6.6 Hz, 2H), 1.29 (d, J=6.6 Hz, 2H), 1.25 (d, J=6.6 Hz, 2H), 0.86 (d, J=6.9 Hz, 2H) ppm; **^{13}C{^{1}H} NMR** (126 MHz, $CDCl_3$) δ =163.47 (d, J=49.7 Hz, 1 C, MIC-Rh), 151.07, 150.45, 150.32, 150.30, 145.69, 145.65, 141.60, 132.23, 127.24, 124.54, 124.13, 122.29, 115.54, 98.36 (d, J=7.2 Hz, 5 C, Rh-Cp*), 38.27, 30.55, 30.30, 25.49, 25.34, 24.55, 23.48, 9.45 ppm; **MS (ESI-ToF)**: m/z found: 593.1915, calcd: 593.1918 ($C_{18}H_{22}ClN_4Rh^+$); **Elemental analysis** calcd. (%) for $C_{30}H_{39}ClF_6N_4PRh$: C 48.76, H 5.32, N 7.58; found: C 48.32, H 5.48, N 7.20.

Synthesis of [Rh(C–C)MeCN](PF$_6$)$_2$

[Rh(**C–C**)Cl](PF$_6$) (0.03 g, 0.052 mmol) was dissolved in 3 mL CH_3CN and $AgPF_6$ (0.01 g, 0.057 mmol) was added. The reaction mixture was stirred overnight at room temperature under exclusion of light and filtered through Celite. The solvent was reduced to 1 mL and overlaid with Et_2O yielding yellow crystals of [Rh(**C–C**)MeCN](PF$_6$)$_2$ (0.04 g, 0.052 mmol, >99 %) suitable for X-ray diffraction analysis.

^{1}H NMR (250 MHz, CD_3CN) δ =8.93 (dd, J=5.6, 0.7 Hz, 1H), 8.31 (ddd, J=8.1, 7.6, 1.5 Hz, 1H), 8.22–8.15 (m, 1H), 7.85–7.76 (m, 1H),

Chemistry–A European Journal | Research Article doi.org/10.1002/chem.202302354 | Chemistry Europe European Chemical Societies Publishing

7.71 (d, J=7.8 Hz, 1H), 7.56 (td, J=7.8, 1.2 Hz, 2H), 4.56 (s, 3H), 2.70 (hept, J=6.8 Hz, 1H), 2.47 (hept, J=6.8 Hz, 1H), 1.96 (s, 3H), 1.44 (s, 15H), 1.37 (d, J=6.7 Hz, 3H), 1.30 (d, J=6.6 Hz, 6H), 0.87 (d, J=6.8 Hz, 3H) ppm; **^{13}C{^{1}H} NMR** (63 MHz, CD_3CN) δ =166.98 (d, J=51.5 Hz, 1 C, Rh-MIC),154.76, 149.51, 147.66, 147.64, 147.32, 146.44, 142.01, 134.81, 133.52, 128.35, 128.35, 126.01, 125.74, 123.31, 123.30, 101.54 (d, J=7.3 Hz, 5 C, Rh-Cp*), 40.67, 29.82, 29.04, 27.45, 26.03, 22.16, 21.96, 9.64 ppm; **MS (ESI-ToF)**: m/z found: found: 593.1913, calcd: 593.1913 ($C_{30}H_{39}ClN_4Rh^+$); 557.2146, calcd: 557.2230 ($C_{30}H_{39}N_4Rh^+$); **Elemental analysis** calcd. (%) for $C_{32}H_{42}F_{12}N_4P_2Rh$: C 43.21, H 4.76, N 7.87; found: C 42.83, H 4.68, N 7.80.

Synthesis of [Rh(C–N)MeCN](PF$_6$)$_2$

[Rh(**C**–**N**)Cl](PF$_6$) (0.03 g, 0.052 mmol) was dissolved in 3 mL CH_3CN and $AgPF_6$ (0.01 g, 0.057 mmol) was added. The reaction mixture was stirred overnight at room temperature under exclusion of light and filtered through Celite. The solvent was reduced to 1 mL and overlaid with Et_2O yielding yellow crystals of [Rh(**C**–**N**)MeCN](PF$_6$)$_2$ (0.04 g, 0.052 mmol, >99 %) suitable for X-ray diffraction analysis.

^{1}H NMR (700 MHz, CD_3CN) δ =8.82 (dd, J=5.6, 0.9 Hz, 1H), 8.45 (ddd, J=8.2, 7.7, 1.5 Hz, 1H), 8.33 (ddd, J=8.2, 1.3, 0.7 Hz, 1H), 7.93 (ddd, J=7.7, 5.6, 1.3 Hz, 1H), 7.73–7.69 (m, 1H), 7.55 (d, J=8.2 Hz, 1H), 7.51 (d, J=7.7 Hz, 1H), 4.06 (s, 3H), 2.70 (hept, J=6.6 Hz, 1H), 2.65 (hept, J=6.6 Hz, 1H), 1.96 (s, 2H), 1.53 (s, 15H), 1.36 (d, J=6.7 Hz, 3H), 1.30 (d, J=6.6 Hz, 3H), 1.25 (d, J=6.8 Hz, 3H), 0.94 (d, J=6.8 Hz, 3H) ppm; **^{13}C{^{1}H} NMR** (176 MHz, CD_3CN) δ =160.57 (d, J=48.3 Hz, 1 C, Rh-MIC), 152.86, 151.53, 150.95, 150.85, 147.41, 147.39, 144.70, 133.55, 138.39, 125,98, 125.98, 125.42, 122.36 166.36, 116.35, 101.97 (d, J=7.6 Hz, 5 C, Rh-Cp*), 39.72, 31.53, 31.40, 25.84, 25.63, 24.84, 23.67, 9.89 ppm; **MS (ESI-ToF)**: m/z found: 557.2158, calcd: 557.2230 ($C_{30}H_{39}N_4Rh^+$); **Elemental analysis** calcd. (%) for $C_{32}H_{42}F_{12}N_4P_2Rh$: C 43.21, H 4.76, N 7.87; found: C 43.03, H 4.68, N 7.80.

Synthesis of [Rh(C–C)H](PF$_6$)

[Rh(**C**–**C**)Cl](PF$_6$) (0.05 g, 0.087 mmol) was added in a 10 mL Schlenk-tube and rigorously stirred until a fine powder was formed. Subsequently, 3 mL of an aqueous NaOOCH/HCOOH (excess, pH= 4.8) was added and the fine suspension was refluxed at 85 °C overnight. The yellow suspension was filtered and washed extensively with degassed H_2O and dried overnight at 40 °C. The yellow solid was transferred in the synthetic glovebox and dissolved CD_3CN (for NMR) or THF (for crystallization) and filtered through a syringe filter. The THF solution was overlaid with *n*-hexane yielding crystalline material of [Rh(**C**–**C**)H](PF$_6$) (0.03 g, 0.035 mmol, 40% isolated yield, >98 % NMR yield). Unfortunately, the obtained crystals were not suitable for X-ray diffraction analysis and all our attempts to obtain single crystals failed.

^{1}H NMR (500 MHz, CD_3CN) δ =8.74 (dq, J=5.7, 1.0 Hz, 1H), 8.09–8.05 (m, 2H), 7.64 (t, J=7.8 Hz, 1H), 7.52–7.48 (m, 2H), 7.45 (dd, J=7.8, 1.3 Hz, 1H), 4.49 (s, 3H), 2.73–2.65 (m, 1H), 2.67 (hept, J=6.8 Hz, 1H), 2.63 (hept, J=6.8 Hz, 1H), 1.56 (d, J=0.8 Hz, 15H, *through space coupling of Cp* with Hydride*), 1.39 (d, J=6.8 Hz, 3H), 1.32 (d, J=6.8 Hz, 3H), 1.24 (d, J=6.7 Hz, 3H), 0.89 (d, J=6.9 Hz, 3H), −11.46 (d, J=22.0 Hz, 1H) ppm; **^{13}C{^{1}H} NMR** (126 MHz, CD_3CN) δ (ppm) =155.19, 149.46, 147.57, 146.86, 143.30, 138.73, 135.48, 132.81, 125.70, 125.29, 125.17, 122,07, 98.42 (d, J=5.2 Hz, 5 C, Rh-Cp*), 40.07, 29.76, 29.40, 27.17, 25.63, 22.30, 22.28, 10.13 ppm; **MS (ESI-ToF)**: m/z found: 593.2301, calcd: 593.2303 ($C_{30}H_{40}N_4Rh^+$); 557.2135, calcd: 557.2230 ($C_{30}H_{39}N_4Rh^+$); **Elemental analysis** calcd. (%) for $C_{32}H_{42}F_{12}N_4P_2Rh$: C 51.14, H 5.72, N 7.98; found: C 49.90, H 5.64, N 7.56.

Note: The ^{1}H NMR shows no equilibrium with [Rh(**C**–**C**)]. Some traces of acidic impurities in the CD_3CN might shift the equilibrium to [Rh(**C**–**C**)H](PF$_6$).

Synthesis of [Rh(C–N)H](PF$_6$)

[Rh(**C**–**N**)Cl](PF$_6$) (0.05 g, 0.087 mmol) was added in a 10 mL Schlenk-tube and rigorously stirred until a fine powder was formed. Subsequently, 3 mL of an aqueous NaOOCH/HCOOH (excess, pH= 4.8) was added and the fine suspension was refluxed at 85 °C for two hours. The yellow suspension was filtered and washed extensively with degassed H_2O and dried overnight at 40 °C. The yellow solid was transferred in the synthetic glovebox and dissolved CD_3CN (for NMR) or THF (for crystallization) and filtered through a syringe filter. The THF solution was overlaid with *n*-hexane yielding yellow single crystals of [Rh(**C**–**N**)H](PF$_6$) suitable for X-ray diffraction analysis (0.03 g, 0.037 mmol, 43 % isolated yield, >98 % NMR yield).

^{1}H NMR (500 MHz, CD_3CN) δ =8.62 (d, J=5.6 Hz, 1H), 8.20 (d, J=3.8 Hz, 2H), 7.66–7.60 (m, 2H), 7.47 (d, J=7.9 Hz, 1H), 7.42 (d, J=7.8 Hz, 1H), 3.94 (s, 3H), 2.83 (hept, J=6.8 Hz, 1H), 2.58 (hept, J=6.9 Hz, 1H), 1.64 (d, J=0.8 Hz, 15H, *through space coupling of Cp* with Hydride*), 1.37 (d, J=6.7 Hz, 3H), 1.28 (d, J=6.7 Hz, 3H), 1.21 (d, J=6.7 Hz, 3H), 0.96 (d, J=6.9 Hz, 3H), −11.48 (d, J=23.1 Hz, 1H) ppm; **^{13}C{^{1}H} NMR** (126 MHz, CD_3CN) δ =168.72 (d, J=48.5 Hz, 1 C, Rh-MIC), 153.50, 151.53, 150.62, 150.60, 146.70, 146.65, 141.17, 132.80, 126.55, 125.12, 124.99, 123.87, 114.97, 98.77 (d, J=5.2 Hz, 5 C, Rh-Cp*), 39.00, 31.66, 31.56, 25.33, 24.97, 24.54, 24.34, 10.33 ppm; **MS (ESI-ToF)**: m/z found: 593.1985, calcd: 593.2303 ($C_{30}H_{40}N_4Rh^+$); 557.2185, calcd: 557.2230 ($C_{30}H_{39}N_4Rh^+$); **Elemental analysis** calcd. (%) for $C_{32}H_{42}F_{12}N_4P_2Rh$: C 51.14, H 5.72, N 7.98; found: C 51.04, H 5.79, N 7.65.

Note: The ^{1}H NMR shows no equilibrium with [Rh(**C**–**N**)]. Some traces of acidic impurities in the CD_3CN might shift the equilibrium to [Rh(**C**–**N**)H](PF$_6$).

Synthesis of [Rh(C–C)]

[Rh(**C**–**C**)Cl](PF$_6$) (0.05 g, 0.087 mmol) was dissolved in 5 mL THF and stored overnight at −40 °C. Upon addition of KC_8 (0.03 g, 0.182 mmol), the color changed immediately from orange to intense green. The reaction mixture was stirred for two hours at room temperature and filtered through a syringe filter. The solvent was evaporated and the crude product was dissolved in some drops of THF and *n*-hexane, filtered and stored at −40 °C for one month yielding a green solid (0.04 g, 0.068 mmol, 78%). Unfortunately, we were not able to isolate single crystals suitable for X-ray diffraction analysis in various solvents and different temperatures. The obtained ^{1}H and ^{13}C NMR spectrum was generated by addition of $NaBH_4$ to [Rh(**C**–**C**)H](PF$_6$) in CD_3CN at room temperature after one hour, since some reducing reagent was presented in the crude product (>98 %, NMR yield).

^{1}H NMR (500 MHz, CD_3CN) δ =8.70 (dd, J=6.3, 1.0 Hz, 1H), 7.61–7.58 (m, 1H), 7.58–7.54 (m, 1H), 7.42 (d, J=7.8 Hz, 2H), 7.27–7.22 (m, 1H), 6.52 (td, J=6.5, 1.3 Hz, 1H), 4.43 (s, 3H), 2.69 (hept, J=6.8 Hz, 2H), 1.58 (s, 15H), 1.31 (d, J=6.9 Hz, 6H), 0.97 (d, J=6.8 Hz, 6H); **^{13}C{^{1}H} NMR** (126 MHz, CD_3CN) δ =150.53, 148.63, 146.15, 140.65, 137.64, 129.89, 123.27, 120.23, 118.95, 116.63, 89.74 (d, J=5.6 Hz, 5 C, Rh-Cp*), 37.63, 27.75, 23.70, 21.71, 9.12 ppm; **MS (ESI-ToF)**: m/z found: 559.2286, calcd: 559.2281 ($C_{30}H_{40}N_4Rh^+$).

Chemistry–A European Journal | Research Article doi.org/10.1002/chem.202302354 | Chemistry Europe European Chemical Societies Publishing

Synthesis of [Rh(C–N)]

[Rh(**C**–**N**)Cl](PF$_6$) (0.05 g, 0.087 mmol) was dissolved in 5 mL THF and stored overnight at −40 °C. Upon addition of KC_8 (0.03 g, 0.182 mmol), the color changed immediately from orange to intense purple. The reaction mixture was stirred for two hours at room temperature and filtered through a syringe filter. The solvent was evaporated and the crude product was dissolved in some drops of THF and *n*-hexane, filtered and stored at −40 °C for one month yielding a purple crystal (0.01 g, 0.009 mmol, 10%) suitable for X-ray diffraction analysis. The obtained ^{1}H NMR spectrum was generated by addition of $NaBH_4$ to [Rh(**C**–**N**)H](PF$_6$) in CD_3CN at room temperature after 10 minutes, since some reducing reagent was presented in the crystalline product (>95%, NMR yield). Unfortunately, we were not able to record a reasonable ^{13}C NMR.

^{1}H NMR (500 MHz, CD_3CN) δ =8.77 (dd, J=6.4, 0.7 Hz, 1H), 7.63 (d, J=8.2 Hz, 1H), 7.57–7.52 (m, 1H), 7.41 (d, J=7.7 Hz, 3H), 6.75 (td, J=6.8, 1.2 Hz, 1H), 3.61 (s, 3H), 2.81 (hept, J=6.6 Hz, 2H), 1.68 (s, 15H), 1.29 (d, J=6.8 Hz, 6H), 1.01 (d, J=6.9 Hz, 6H) ppm; **MS (ESI-ToF)**: m/z found: 279.1132, calcd: 279.6149 ($C_{30}H_{40}N_4Rh^{2+}$).

Performance of the Hydride Reactivity Experiments

Reactivity with $NaBH_4$: The respective [RhCp*] hydride complex was dissolved in CD_3CN and $NaBH_4$ was added at room temperature. The yellow reaction mixture changed rapidly to a deep purple (for [Rh(**C**–**N**)H](PF$_6$)) or dark green (for [Rh(**C**–**N**)H](PF$_6$)) solution under the evolution of gas. The reaction mixture was stirred for additional 10 min and transferred in a young NMR tube using a syringe filter.

Reactivity with TEMPO: The respective [RhCp*] hydride complex was dissolved in CH_3CN and TEMPO (approx. 0.9 eq.) (=(2,2,6,6-tetramethylpiperidin-1-yl)oxyl)) was added at room temperature. The reaction mixture was stirred until the TEMPO was completely dissolved and directly transferred in the EPR tube.

Reactivity with Tritylium: The respective [RhCp*] hydride complex was dissolved in CD_3CN and [$(C_6H_5)_3C$](PF$_6$) was added (>1 eq). The reaction mixture was stirred for 10 min and transferred in a young NMR tube.

† Electronic supplementary information (ESI) available: Synthetic procedures, NMR spectra, X-ray crystallographic data, electrochemistry, spectroelectrochemistry, reactivity studies and computational details.

Acknowledgements

We thank Cindy Odenwald and Ivan Shestov for the synthetic support during their internship, Barbara Förtsch for elemental analyses, Dr. Wolfgang Frey (Institut für Organische Chemie) for collecting the X-ray data sets and the support by the state of Baden-Württemberg through bwHPC and the German Research Foundation (DFG) through grant no INST 40/575-1 FUGG (JUSTUS 2 cluster). Funded by the Deutsche Forschungsgemeinschaft [DFG, German Research Foundation – Project-IDs 358283783 – SFB 1333/2 2022. Open Access funding enabled and organized by Projekt DEAL.

Conflict of Interests

There are no conflicts to declare.

Data Availability Statement

The data that support the findings of this study are available in the supplementary material of this article.

Keywords: mesoionic carbenes · (spectro-)electrochemistry · RhCp* · ambiphilic hydride · precatalyst activation

[1] a) J. D. Blakemore, A. Gupta, J. J. Warren, B. S. Brunschwig, H. B. Gray, *J. Am. Chem. Soc.* **2013**, *135*, 18288; b) S. Cosnier, H. Gunther, *J. Electroanal. Chem.* **1991**, *315*, 307; c) N. Elgrishi, B. D. McCarthy, E. S. Rountree, J. L. Dempsey, *ACS Catal.* **2016**, *6*, 3644; d) R. Francke, B. Schille, M. Roemelt, *Chem. Rev.* **2018**, *118*, 4631; e) R. Ruppert, S. Herrmann, E. Steckhan, *Tetrahedron Lett.* **1987**, *28*, 6583; f) E. Steckhan, S. Herrmann, R. Ruppert, E. Dietz, M. Frede, E. Spika, *Organometallics* **1991**, *10*, 1568; g) T. K. Todorova, T. N. Huan, X. Wang, H. Agarwala, M. Fontecave, *Inorg. Chem.* **2019**, *58*, 6893; h) S. Enthaler, J. von Langermann, T. Schmidt, *Energy Environ. Sci.* **2010**, *3*, 1207; i) C. Finn, S. Schnittger, L. J. Yellowlees, J. B. Love, *Chem. Commun.* **2012**, *48*, 1392; j) E. E. Benson, C. P. Kubiak, A. J. Sathrum, J. M. Smieja, *Chem. Soc. Rev.* **2009**, *38*, 89; k) W.-H. Wang, Y. Himeda, J. T. Muckerman, G. F. Manbeck, E. Fujita, *Chem. Rev.* **2015**, *115*, 12936.
[2] S. Cosnier, A. Deronzier, N. Vlachopoulos, *J. Chem. Soc., Chem. Commun.* **1989**, *17*, 1259.
[3] S. Fukuzumi, T. Kobayashi, T. Suenobu, *ChemSusChem* **2008**, *1*, 827.
[4] W. Kaim, J. Fiedler, *Chem. Soc. Rev.* **2009**, *38*, 3373.
[5] D. A. Kurtz, J. L. Dempsey, *Inorg. Chem.* **2019**, *58*, 16510.
[6] J. A. Widegren, R. G. Finke, *J. Mol. Catal. A* **2003**, *198*, 317.
[7] V. Artero, M. Fontecave, *Chem. Soc. Rev.* **2013**, *42*, 2338.
[8] a) A. Jutand, *Chem. Rev.* **2008**, *108*, 2300; b) J. Liu, L. Lu, D. Wood, S. Lin, *ACS Cent. Sci.* **2020**, *6*, 1317.
[9] W. C. Henke, D. Lionetti, W. N. G. Moore, J. A. Hopkins, V. W. Day, J. D. Blakemore, *ChemSusChem* **2017**, *10*, 4589.
[10] J. A. Hopkins, D. Lionetti, V. W. Day, J. D. Blakemore, *Organometallics* **2019**, *38*, 1300.
[11] S. I. Johnson, H. B. Gray, J. D. Blakemore, W. A. Goddard, *Inorg. Chem.* **2017**, *56*, 11375.
[12] W. Kaim, R. Reinhardt, S. Greulich, J. Fiedler, *Organometallics* **2003**, *22*, 2240.
[13] U. Kölle, B.-S. Kang, P. Infelta, P. Comte, M. Grätzel, *Chem. Ber.* **1989**, *122*, 1869.
[14] Y. Peng, M. V. Ramos-Garcés, D. Lionetti, J. D. Blakemore, *Inorg. Chem.* **2017**, *56*, 10824.
[15] C. L. Pitman, O. N. L. Finster, A. J. M. Miller, *Chem. Commun.* **2016**, *52*, 9105.
[16] L. M. A. Quintana, S. I. Johnson, S. L. Corona, W. Villatoro, W. A. Goddard, M. K. Takase, D. G. VanderVelde, J. R. Winkler, H. B. Gray, J. D. Blakemore, *PNAS USA* **2016**, *113*, 6409.
[17] J. D. Blakemore, E. S. Hernandez, W. Sattler, B. M. Hunter, L. M. Henling, B. S. Brunschwig, H. B. Gray, *Polyhedron* **2014**, *84*, 14.
[18] U. Kölle, M. Grützel, *Angew. Chem. Int. Ed. Engl.* **1987**, *26*, 567.
[19] E. A. Boyd, D. Lionetti, W. C. Henke, V. W. Day, J. D. Blakemore, *Inorg. Chem.* **2019**, *58*, 3606.
[20] M. van der Meer, E. Glais, I. Siewert, B. Sarkar, *Angew. Chem.* **2015**, *127*, 13997.
[21] a) T. V. Q. Nguyen, W.-J. Yoo, S. Kobayashi, *Angew. Chem. Int. Ed. Engl.* **2015**, *54*, 9209; b) T. V. Q. Nguyen, W.-J. Yoo, S. Kobayashi, *Adv. Synth. Catal.* **2016**, *358*, 452; c) S. N. Sluijter, C. J. Elsevier, *Organometallics* **2014**, *33*, 6389; d) K. Farrell, H. Müller-Bunz, M. Albrecht, *Organometallics* **2015**, *34*, 5723.
[22] a) I. D. Alshakova, M. Albrecht, *ACS Catal.* **2021**, *11*, 8999; b) A. Bolje, S. Hohloch, M. van der Meer, J. Košmrlj, B. Sarkar, *Chem. Eur. J.* **2015**, *21*, 6756; c) R. Maity, A. Mekic, M. van der Meer, A. Verma, B. Sarkar, *Chem. Commun.* **2015**, *51*, 15106; d) Z. Mazloomi, R. Pretorius, O. Pàmies, M. Albrecht, M. Diéguez, *Inorg. Chem.* **2017**, *56*, 11282; e) Á. Vivancos, M.

Chemistry–A European Journal | Research Article doi.org/10.1002/chem.202302354 | Chemistry Europe European Chemical Societies Publishing

Albrecht, *Organometallics* **2017**, *36*, 1580; f) Á. Vivancos, M. Beller, M. Albrecht, *ACS Catal.* **2018**, *8*, 17.
[23] a) F. Franco, M. F. Pinto, B. Royo, J. Lloret-Fillol, *Angew. Chem.* **2018**, *130*, 4693; b) T. Scherpf, C. R. Carr, L. J. Donnelly, Z. S. Dubrawski, B. S. Gelfand, W. E. Piers, *Inorg. Chem.* **2022**, *61*, 13644; c) F. Stein, M. Nößler, A. S. Hazari, L. Böser, R. Walter, H. Liu, E. Klemm, B. Sarkar, *Chem. Eur. J.* **2023**, *29*, e202300405; d) L. Suntrup, F. Stein, J. Klein, A. Wilting, F. G. L. Parlane, C. M. Brown, J. Fiedler, C. P. Berlinguette, I. Siewert, B. Sarkar, *Inorg. Chem.* **2020**, *59*, 4215.
[24] V. Ganesan, J. J. Kim, J. Shin, K. Park, S. Yoon, *Inorg. Chem.* **2022**, *61*, 5683.
[25] a) G. Guisado-Barrios, M. Soleilhavoup, G. Bertrand, *Acc. Chem. Res.* **2018**, *51*, 3236; b) R. Maity, B. Sarkar, *JACS Au* **2022**, *2*, 22; c) Á. Vivancos, C. Segarra, M. Albrecht, *Chem. Rev.* **2018**, *118*, 9493.
[26] L. Suntrup, S. Klenk, J. Klein, S. Sobottka, B. Sarkar, *Inorg. Chem.* **2017**, *56*, 5771.
[27] T. Bens, P. Boden, P. Di Martino-Fumo, J. Beerhues, U. Albold, S. Sobottka, N. I. Neuman, M. Gerhards, B. Sarkar, *Inorg. Chem.* **2020**, *59*, 15504.
[28] C. W. Machan, *Curr. Opin. Electrochem.* **2019**, *15*, 42.
[29] C. W. Machan, M. D. Sampson, S. A. Chabolla, T. Dang, C. P. Kubiak, *Organometallics* **2014**, *33*, 4550.
[30] A. Bolje, S. Hohloch, D. Urankar, A. Pevec, M. Gazvoda, B. Sarkar, J. Košmrlj, *Organometallics* **2014**, *33*, 2588.
[31] C. White, A. Yates, P. M. Maitlis, *Inorg. Synth.* **29**, *1992*, 228.
[32] M. L. Clark, K. A. Grice, C. E. Moore, A. L. Rheingold, C. P. Kubiak, *Chem. Sci.* **2014**, *5*, 1894.
[33] a) M. Poyatos, E. Mas-Marzá, J. A. Mata, M. Sanaú, E. Peris, *Eur. J. Inorg. Chem.* **2003**, *2003*, 1215; b) M. Poyatos, W. McNamara, C. Incarvito, E. Clot, E. Peris, R. H. Crabtree, *Organometallics* **2008**, *27*, 2128; c) M. Poyatos, M. Sanaú, E. Peris, *Inorg. Chem.* **2003**, *42*, 2572.
[34] L. Dadci, H. Elias, U. Frey, A. Hoernig, U. Koelle, A. E. Merbach, H. Paulus, J. S. Schneider, *Inorg. Chem.* **1995**, *34*, 306.
[35] a) C. Caix, S. Chardon-Noblat, A. Deronzier, J.-C. Moutet, S. Tingry, *J. Organomet. Chem.* **1997**, *540*, 105; b) K. M. Waldie, F. M. Brunner, C. P. Kubiak, *ACS Sustainable Chem. Eng.* **2018**, *6*, 6841.
[36] Y. Hu, J. R. Norton, *J. Am. Chem. Soc.* **2014**, *136*, 5938.
[37] W. C. Henke, Y. Peng, A. A. Meier, E. Fujita, D. C. Grills, D. E. Polyansky, J. D. Blakemore, *PNAS USA* **2023**, *120*, e2217189120.
[38] D. A. Smith, D. E. Herbert, J. R. Walensky, O. V. Ozerov, *Organometallics* **2013**, *32*, 2050.
[39] K. M. Waldie, A. L. Ostericher, M. H. Reineke, A. F. Sasayama, C. P. Kubiak, *ACS Catal.* **2018**, *8*, 1313.
[40] T. Bens, R. R. M. Walter, J. Beerhues, M. Schmitt, I. Krossing, B. Sarkar, *Chem. Eur. J.* **2023**, *29*, e202301205.
[41] a) S. Hammes-Schiffer, *Acc. Chem. Res.* **2001**, *34*, 273; b) S. Hammes-Schiffer, A. V. Soudackov, *J. Phys. Chem. B* **2008**, *112*, 14108; c) J. J. Warren, T. A. Tronic, J. M. Mayer, *Chem. Rev.* **2010**, *110*, 6961; d) D. R. Weinberg, C. J. Gagliardi, J. F. Hull, C. F. Murphy, C. A. Kent, B. C. Westlake, A. Paul, D. H. Ess, D. G. McCafferty, T. J. Meyer, *Chem. Rev.* **2012**, *112*, 4016.
[42] S. Budavari, *An encyclopedia of chemicals, drugs, and biologicals*, (Ed.) The Merck index., Merck, Rahway, N.J., U.S.A., **1991**.
[43] a) *APEX3*, Bruker AXS Inc, Madison, Wisconsin, USA, **2015**; b) C. F. Macrae, P. R. Edgington, P. McCabe, E. Pidcock, G. P. Shields, R. Taylor, M. Towler, J. van de Streek, *J. Appl. Crystallogr.* **2006**, *39*, 453; c) SAINT+, *Data Integration Engine*, Bruker AXS Inc., Madison, Wisconsin, USA, 1997–2012, v. 8.27b©; d) G. M. Sheldrick, *SHELXS-97 and SHELXL-97, Program for Crystal Structure Solution and Refinement*, University of Gottingen, Göttingen, Germany, **1997**; e) G. M. Sheldrick, *Program for Empirical Absorption Correction*, University of Göttingen, Göttingen, Germany, **2008**; f) G. M. Sheldrick, *Program for Crystal Structure Solution and Refinement*, University of Göttingen, Göttingen, Germany, **2014**; g) G. M. Sheldrick, *Acta Crystallogr.* **2008**, *A64*, 112; h) G. M. Sheldrick, *Acta Crystallogr.* **2015**, *C71*, 3.
[44] a) J. Klein, A. Stuckmann, S. Sobottka, L. Suntrup, M. van der Meer, P. Hommes, H.-U. Reissig, B. Sarkar, *Chem. Eur. J.* **2017**, *23*, 12314; b) M. Krejčik, M. Daněk, F. Hartl, *J. Electroanal. Chem.* **1991**, *317*, 179.
[45] F. Neese, *Comput. Mol. Sci.* **2012**, *2*, 73.
[46] C. Adamo, V. Barone, *J. Chem. Phys.* **1999**, *110*, 6158.
[47] a) S. Grimme, *J. Comput. Chem.* **2004**, *25*, 1463; b) S. Grimme, *J. Comput. Chem.* **2006**, *27*, 1787; c) S. Grimme, J. Antony, S. Ehrlich, H. Krieg, *J. Chem. Phys.* **2010**, *132*, 154104; d) S. Grimme, S. Ehrlich, L. Goerigk, *J. Comput. Chem.* **2011**, *32*, 1456.
[48] F. Weigend, R. Ahlrichs, *Phys. Chem. Chem. Phys.* **2005**, *7*, 3297.
[49] a) R. Izsák, F. Neese, *J. Chem. Phys.* **2011**, *135*, 144105; b) F. Neese, *J. Comput. Chem.* **2003**, *24*, 1740; c) F. Neese, G. Olbrich, *Chem. Phys. Lett.* **2002**, *362*, 170; d) F. Neese, F. Wennmohs, A. Hansen, U. Becker, *Chem. Phys.* **2009**, *356*, 98; e) T. Petrenko, S. Kossmann, F. Neese, *J. Chem. Phys.* **2011**, *134*, 54116; f) O. Vahtras, J. Almlöf, M. W. Feyereisen, *Chem. Phys. Lett.* **1993**, *213*, 514; g) J. L. Whitten, *J. Chem. Phys.* **1973**, *58*, 4496.
[50] a) K. Eichkorn, O. Treutler, H. Öhm, M. Häser, R. Ahlrichs, *Chem. Phys. Lett.* **1995**, *242*, 652; b) K. Eichkorn, F. Weigend, O. Treutler, R. Ahlrichs, *Theor. Chem. Acc.* **1997**, *97*, 119.
[51] V. Barone, M. Cossi, *J. Phys. Chem. A* **1998**, *102*, 1995.
[52] R. S. Mulliken, *J. Chem. Phys.* **1955**, *23*, 1833.
[53] G. A. Zhurko, *Chemcraft-Graphical Program for Visualization of Quantum Chemistry Computations*, Ivanovo, Russia, **2023**.

Manuscript received: July 24, 2023
Accepted manuscript online: September 28, 2023
Version of record online: November 20, 2023